Particles in Europe 2025

Conference program and proceedings

17 - 19 September 2025, Ostend, Belgium

PiE Particles in Europe

VLIZ

Flanders Hydraulics

Flanders State of the Art

natural sciences .be

SEQUOIA Tools and Research for Particle Intelligence

Particles in Europe 2025

Conference program and proceedings

17 - 19 September 2025, Ostend, Belgium

Editors
Dr. Nore Praet
VLIZ, Belgium

Ir. Yves Plancke
Flanders Hydraulics, Belgium

Published by
Flanders Marine Institute, Flanders Hydraulics, Institute of Natural Sciences and Sequoia Scientific Inc.

D/2025/3241/238 https://dx.doi.org/10.48607/346

Cover photo: © The Government of Flanders, Department of Mobility and Public Works, Flanders Hydraulics

Welcome

Welcome to Oostende!

It is with great enthusiasm that we introduce the 8th Particles in Europe (PiE) conference (#PiE2025).

Over 50 participants – researchers, students, practitioners – gather along the Belgian coast, for three days of presentations, discussions and networking.

Let's embrace this opportunity to explore all fascinating facets of particle research. With PiE, we aspire to build a better network of particle experts from different institutes and companies worldwide.

Enjoy the conference, the reading of this book of abstracts and the vibrant city of Ostend, also known as the "Queen of the Seaside Towns".

Innovocean Space © VLIZ (Bart De Smet)

Introduction

The Particles in Europe (PiE) Conference 2025 takes place from 16 to 19 September in Flanders Marine Institute (VLIZ), located in Ostend, Belgium.

The seed of bringing PiE to Belgium was planted in Crete 2 years ago during the 2023 PiE conference.
More than 3000 km from here, Belgium scientist Nore Praet, working at Flandres Marine Institute, and Yves Plancke, working at Flanders Hydraulics, met each other and discovered that they were working on similar topics, surprisingly without knowing each other.

This inspiring encounter resulted in 2024 in the organization of the first Particles in Belgium (PiB) one-day-meeting where more than 40 researches from different Belgian institutes came together to share their work on particle dynamics.

The success of this local event sparked the ambition to aim higher. Several Belgian institutes — including Flanders Marine Institute, Flanders Hydraulics, and the Institute of Natural Sciences — joined forces to bring *Particles in Europe* for the first time to Belgium. Thanks to the support of Ole, CEO of Sequoia, the PiE2025 conference has now become a reality.

Information

When?

PiE2025 will take place from Wednesday **17 to** Friday **19 September 2025**,
with an icebreaker on Tuesday evening 16 September 2025.

Where?

PiE2025 will be held at the InnovOcean Campus, the main building of Flanders Marine Institute (VLIZ), Jacobsenstraat 1, 8400 Ostend, Belgium.

What?

PiE2025 brings together some of the leading experts in aquatic particles from around the world. This interdisciplinary conference is not limited to specific technology or field of study, serving as a hotspot for all those passionate about measuring, monitoring, modelling or imaging plankton, sediment or microplastic particles across oceans, estuaries, rivers, lakes and beyond. Following topics will be handled during the conference:

- Innovations in Ocean Observation and Sensing Technologies — Session 1
- Particle Dynamics and Transport in Coastal and Shelf Seas — Session 2 and 4
- Microplastics and Anthropogenic Particles in Marine Systems — Session 3
- Methods for Particle and Sediment Characterization — Session 5

Organizing institutes

Flanders Marine Institute

The Flanders Marine Institute (VLIZ) is the coordination and information platform for marine and coastal research in Flanders. It also promotes and supports the international image of Flemish marine scientific research and international marine education as a partner in various projects and networks. The marine research areas are the ocean and seas, the coast and the tidal systems. The target groups for knowledge accumulation are the marine research community as well as educational institutions, the general public, policymakers and industry (within the scope of the blue economy). VLIZ is housed in the InnovOcean Campus on the East Bank of Ostend.

More information can be found on www.vliz.be

Flanders Hydraulics

Flanders Hydraulics (FH) is a centre of expertise for research and advice on hydraulic, nautical, sediment-related and hydrological topics. As a scientific institute and technical support service, FH is a division of the department of Mobility and Public Works of the Government of Flanders. Flanders Hydraulics supports the preparation and execution of the policy of the Government of Flanders by providing comprehensive, scientifically sound knowledge, knowledge products and advice on water systems.
Besides activities on behalf of the policy domain Mobility and Public Works, Flanders Hydraulics develops activities for other entities within the Government of Flanders, for other domestic and foreign government services and for the private sector. Research projects for third parties are facilitated by Flanders Hydraulics Public Agency.

More information can be found on www.waterbouwkundiglaboratorium.be

Institute of Natural Sciences

The Institute of Natural Sciences (RBINS) is a research institute with more than 200 scientists and dozens of scientific collaborators covering a wide range of disciplines from biology, taxonomy and oceanography to geology, paleontology and anthropology. RBINS supports national and international decision-makers with scientific expertise. Within oceanography, sustainable management of marine areas such as the North Sea, heavily impacted by human activities, is thus a case-in-point of RBINS Blue Growth approach: maintain the balance between developing economic activities and preserving the marine ecosystems.

More information can be found on www.naturalsciences.be/en

Sequoia Scientific Inc.

In 1995, Sequoia invented the LISST series of aquatic science instruments for submersible and field measurements of suspended particles. Since then, more than 40 different types of instruments have been developed, prototyped, or manufactured by Sequoia, including a new series of hyperspectral instruments for aquatic optics since 2021. Today, thousands of Sequoia instruments are in use, helping ocean and freshwater scientists and managers around the world better understand our oceans and the aquatic environment. Sequoia started the PiE conference series in 2008 and has organized a PiE conference somewhere in Europe every other year since then, always in collaboration with one or several local organizers.

More information can be found on www.sequoiasci.com

Organizing committee

Dr. Nore Praet (VLIZ)

Nore is a postdoctoral researcher (marine geologist) at VLIZ. Nore received her PhD degree in 2020 from Ghent University. During her PhD, she reconstructed the seismological history of Alaska through the study of lake sediments using a combination of multibeam bathymetric, subsurface seismic and sediment core data. After her PhD, her research focus transitioned to analysing suspended particles (turbidity) in Belgian coastal waters. Within the framework of the finished TIMBERS and ongoing TURBEAMS projects, she gained experience in acquiring and processing multibeam water column data and in-situ sensor data.

Ir. Yves Plancke (Flanders Hydraulics)

Yves is an expert research engineer (VUB, 2002) at Flanders Hydraulics. He is involved (project leader, research engineer, revisor) in a large number of studies focusing on hydrodynamics, sediment transport and morphology, mainly in the Schelde-estuary. The combination of research tools (field measurements, physical scale model, numerical model and expertise) form a crucial aspect in his research philosophy. Beside his work at Flanders Hydraulics, he is guest lecturer at the University of Hasselt and the Antwerp Maritime Academy.

Dr. Michael Fettweis (Institute of Natural Sciences)

Michael has worked for more than 35 years in oceanography and engineering, from which 8 years at a consultancy company (IMDC) and the rest in academic research (KULeuven and since 1999 at RBINS). His expertise is the dynamics of fine-grained particles caused by physical and biological processes along the land-ocean transition. It includes the interaction of organic and mineral particles in suspension, flocculation, sinking and transport, and the coastal ocean carbon cycle. In 2019 he received the JJ Mehta award for outstanding contributions to observations and insights on coastal cohesive sediments transport.

Dr. Ole Mikkelsen (Sequoia)

Ole initially aimed to become a theoretical physicist, inspired by Stephen Hawking. However, a phenomenal high school geography teacher led me instead to study physical geography in college. Visits to Sequoia during his PhD. (1998-2001) and postdocs in Canada (2002-2005) and the UK (2005-2007) led to his hiring by Sequoia in 2007. His PhD. work included pioneering studies on flocculation time scales, remote sensing estimates of particle concentration and a new settling velocity model. He relocated to Seattle to work for Sequoia in 2007, continuing work on randomly shaped particles, leading to publications in Applied Optics. He left Sequoia in 2013 but returned as President in 2019 after Yogi retired.

Sponsorship

DEME is a leading contractor in the fields of offshore energy, environmental remediation, dredging and marine infrastructure. DEME also engages in concessions activities in offshore wind, marine infrastructure, green hydrogen, and deep-sea mineral harvesting. The company can build on nearly 150 years of experience and is a front runner in innovation and new technologies. DEME's vision is to work towards a sustainable future by offering solutions for global challenges: climate change, a growing population and urbanization, increasing maritime trade and environmental issues. With a team of more than 5,800 highly skilled professionals and one of the most advanced fleets in the world, DEME is well-positioned to tackle even the most complex projects. DEME realized a turnover of 4.1 billion euro with an EBITDA of 764 million euro in 2024.

For more information, please visit www.deme-group.com

Jan De Nul shapes water, land and energy around the world, addressing some of the most important challenges of our time. From the rising sea level to the energy transition, from polluted soil to sustainable construction: we engineer solutions that future-proof our world, known for their complexity and high stakes. Our Can-Do people focus on four areas of expertise: Offshore Energy, Dredging Solutions, Construction Projects and Planet Redevelopment. Together, we all work towards one shared goal: to improve the global quality of life for generations to come. We often say 'impossible is not possible'. True to our engineering DNA, there is little we like more than solving a good problem. To do so, we count on our own fleet of vessels, cranes, vehicles, machines and installations, equipped with ultra-capable technology able to meet evolving contexts and client needs. But most importantly, we can count on our team of 9,000 Can-Do people.

For more information, please visit www.jandenul.com

Table of Contents

Keynote speakers

Particle dynamics in marine environments: processes, patterns, and applications | Brent Law

Brent A. Law is a Research Scientist at the Bedford Institute of Oceanography, Department of Fisheries and Oceans, Canada. He holds a BSc. in Biology and Chemistry, MSc. in Oceanography, and a PhD in Geological Oceanography from Dalhousie University. His PhD thesis was titled "Quantifying the transport of aquaculture particulate waste". Areas of interest include the flocculation, deposition, erosion and transport of marine fine-grained sediments and sediment transport modelling. He has been funded to lead research projects related to the far field effects of aquaculture (DFO, IMR Norway), environmental impacts of offshore oil and gas and interaction of sediment with spilled oil (DFO, NRCan), optics and acoustics of sediments in-situ and related modelling (US ONR), and the erosional and depositional dynamics of tidal flats (DFO, US ONR, NS Dept. of Energy).

Particle dynamics in coastal ecosystems | Teresa Serra

Teresa Serra has worked throughout her career in coastal areas, lakes, reservoirs, ponds, rivers, and wetlands. Her primary area of study is the transport of suspended particles in natural aquatic environments, specifically how hydrodynamics—such as waves, currents, or turbulence—drive these particles. She has also worked in laboratory settings, trying to mimic field processes, or also in mesocosm studies with the purpose to approximate more realistic scenarios. Actually, her main research interest is to evaluate the processes of sediment and microplastic transport in coastal and river areas and also, determine the impact of microplastics on aquatic environments. She studies the transport of microplastic particles associated with hydrodynamics and their interaction with suspended sediments. Her latest research has also focused on the buffering function of aquatic vegetation, ponds, and lagoons to lessen microplastic pollution (you can find more details about her recent research and a list of the recent publications at https://www.udg.edu/ca/projectes/plastikhum). It has been investigated how various processes (gravity currents, passive sedimentation, turbulence, infiltration, etc.) move sediments and microplastics both horizontally and vertically in aquatic systems. Additionally, she has investigated the ways in which various forms of bed roughness impact the longitudinal movement of sediments, particles, and microplastics.

Particles in Europe 2025

Conference program

17 - 19 September 2025, Ostend, Belgium

SEPTEMBER 16th 2025 (TUESDAY)

19:00 – 21:00	**Icebreaker Reception** - Generously sponsored by Jan de Nul

SEPTEMBER 17th 2025 (WEDNESDAY)

08:00 – 09:00	**Registration**
09:00 – 09:05	**Welcome, introduction of organizers, brief mention of sponsors and exhibitors, practicalities/ logistics**
09:05 – 09:15	**Sponsor Presentations: Jan de Nul; Deme**
09:15 – 09:20	**1 minute - poster pitches**
SESSION 1A: Innovations in Ocean Observation and Sensing Technologies. Chair: Yves Plancke	
09:20 – 09:45	30 YEARS OF MEASURING SUSPENDED PARTICLES **Yogi Agrawal, Ole Mikkelsen**, Kirby Simon
09:45 – 10:05	AN OPTICAL SENSOR FOR AUTONOMOUS DETECTION OF PARTICULATE INORGANIC CARBON (PIC) CONCENTRATION IN SEAWATER **Qiming Sun**, Georges Fournier, Filip Beunis, Kristiaan Neyts, Jordan Toullec, Peter Chaerle, Olga Chepurnova, David Dana, Chuck Pottsmith, Wayne Slade, Wim Vyverman, and Griet Neukermans
10:05 – 10:25	DEVELOPMENT OF A NEW IN-SITU HYPERSPECTRAL TRANSMISSOMETER FOR OCEAN IOP CLOSURE Kirby Simon, **Ole Mikkelsen**
10:25 – 10:45	PARTICLE MEASUREMENTS TWO WAYS WITH ORIGIN 600 **Tom Comerford**, Matt Saunders, Eleanor Stanton, Tom Culverhouse
10:45 – 11:10	**COFFEE BREAK; POSTERS & EXHIBITORS**
SESSION 1B: Innovations in Ocean Observation and Sensing Technologies. Chair: Yves Plancke	
11:10 – 11:30	FROM PIXELS TO PATTERNS: HIGH-THROUGHPUT IMAGE CLASSIFICATION AND MORPHOMETRY THROUGH A NEW PI-10 IMAGING PIPELINE **Jonas Mortelmans**, Wout Decrop, Hanneloor Heynderickx, André Cattrijsse, Mark Depaepe, Lodewijk Van Walraven, James Scott, Dick van Oevelen, Klaas Deneudt, Carlota Muñiz

11:30 – 11:50	DESIGN AND IMPLEMENTATION OF AN AUTOMATED IMAGE CLASSIFICATION WORKFLOW FOR PHYTOPLANKTON MONITORING **Decrop Wout**, Rune Lagaisse, Mortelmans Jonas, Carlota Muñiz, Deneudt Klaas
11:50 – 12:10	ADVANCING COASTAL ECOSYSTEM MONITORING: A MULTI-SENSOR APPROACH FOR NEAR REAL-TIME BIOGEOCHEMICAL MAPPING AT HIGH TEMPORAL AND SPATIAL RESOLUTION **Clémence Goyens**, Alexandre Castagna, Qiming Sun, Rafael Rasse, Eva Scrivner, Heidi Dierssen, Nils Haëntjes, Hannelore Theetaert, Silke Verbrugge, Thanos Gkritzalis & Griet Neukermans
12:10 – 12:30	TOWARDS 3D TURBIDITY BY CORRELATING MULTIBEAM SONAR AND IN-SITU SENSOR DATA: THE TURBEAMS APPROACH **Thomas Vandorpe**, Nore Praet, Peter Urban, Benjamin Van Roozendael, Marc Roche, Koen Degrendele, Thomas Hermans
12:30 – 12:50	INTRA-ANNUAL VARIABILITY OF MARINE FLOC MORPHOLOGY IN SOUTHERN NORTH SEA COASTAL WATERS USING IN-SITU HIGH-RESOLUTION UNDERWATER IMAGING AND THE SANDI PYTHON PACKAGE **Louise Delhaye**, Céline Taymans, Paul van Kan and Michael Fettweis
12:50 – 13:45	**LUNCH**
SESSION 2: Particle Dynamics and Transport in Coastal and Shelf Seas I. Chair: Ole Mikkelsen	
13:45 – 14:10	**KEYNOTE:** PARTICLE DYNAMICS IN MARINE ENVIRONMENTS: PROCESSES, PATTERNS, AND APPLICATIONS **Brent Law**
14:10 – 14:30	CONCENTRATION AND COMPOSITION OF SUSPENDED PARTICULATE MATTER ALONG NEARSHORE TO OFFSHORE TRANSECTS **Michael Fettweis**
14:30 – 14:50	VERTICAL DYNAMICS OF SUSPENDED PARTICULATE MATTER AND CHLOROPHYLL-A IN A WELL-MIXED COASTAL TURBID SYSTEM **Saumya Silori**, Xavier Desmit, Rolf Riethmüller, Markus Schartau, Nathan Terseleer, Michael Fettweis
14:50 – 15:10	MULTI-SENSOR OBSERVATIONS OF SUSPENDED PARTICULATE MATTER IN A TIDAL COASTAL ENVIRONMENT **Benjamin Van Roozendael**, Matthias Baeye, Duc Tran, Romaric Verney, Michael Fettweis
15:10 – 15:40	**COFFEE BREAK; POSTERS & EXHIBITORS**

SESSION 3: Microplastics and Anthropogenic Particles in Marine Systems. Chair: Wayne Slade	
15:40 – 16:00	EXPLORING (MICRO)PLASTIC POLLUTION IN EUROPEAN PORTS: ANTWERP AND ROTTERDAM CASE STUDIES **Xiebe Stiers**, Mariana N. Miranda, Gert Everaert, Ana I. Catarino
16:00 – 16:20	MICROPLASTIC POLLUTION IN THE INNER RÍA DE AROUSA: SEASONAL VARIABILITY AND TRANSPORT PATHWAYS FROM RIVERINE, URBAN, AND INDUSTRIAL SOURCES **Marisela Des**, Juan Santos-Echeandía, Patricia Bernardez, Maite de Castro, Jesús Gago, Moncho Gómez-Gesteira
16:20 – 16:40	UNDERSTANDING THE SETTLING BEHAVIOR OF MICROPLASTICS WITH FINE SEDIMENTS Vania Ruiz-Gonzalez, **Sophie Defontaine**, Isabel Jalón-Rojas
16:40 – 17:00	TRANSPORT OF ALIEN PARTICLES IN SAND BEDS MOBILISED BY WAVES **Otto Neshamar**, Dominic van der A, Jos Derksen, Tom O'Donoghue

SEPTEMBER 18th 2025 (THURSDAY)

08:30 – 09:00	**Registration**
SESSION 4A – Particle Dynamics and Transport in Coastal and Shelf Seas II. Chair: Michael Fettweis	
09:00 – 09:25	**KEYNOTE:** PARTICLE DYNAMICS IN COASTAL ECOSYSTEMS **Teresa Serra**
09:25 – 09:45	SEASONAL CHARACTERISTICS OF FLOCCULATION AND BIO-FLOCCULATION ACROSS THE BELGIAN NEAR-SHORE REGION **Chih-Hao Hsu**, Koenraad Muylaert, Christian Schwarz
09:45 – 10:05	TIDAL DYNAMICS OF IN SITU PSD IN THE SOUTHERN GERMAN BIGHT AND THE WESER ESTUARY **Julián E. Cortese**, Marius Becker, Frank Kösters, Anna Zorndt, and Chirstian Winter
10:05 – 10:25	ZOOPLANKTON AND PHYTOPLANKTON TIME SERIES ANALYSIS FOR THE BELGIAN NORTH SEA **Annika Eske**, Ilias Semmouri, Jonas Mortelmans, Colin Janssen, Carlota Muñiz, Klaas Deneudt, Pascal I. Hablützel
10:25 – 10:55	**COFFEE BREAK; POSTERS & EXHIBITORS**

SESSION 4B – Particle Dynamics and Transport in Coastal and Shelf Seas II. Chair: Michael Fettweis	
10:55 – 11:15	THE ROLE OF SEDIMENT TRANSPORT DYNAMICS IN OCEAN-BASED CLIMATE CHANGE MITIGATION TECHNOLOGIES **Chloe Leach**, Jaclyn E Cetiner, Hailey Hayes, Thi Tran, M. Grace Andrews, Emilia Jankowska, Cheyenne Moreau, Devon B. Cole
11:15 – 11:35	EFFECTS OF SPM CONCENTRATION, COMPOSITION, SIZE CHARACTERISTICS AND OPTICAL PROPERTIES ON HYPERSPECTRAL REFLECTANCE SIGNATURES IN A COASTAL ESTUARY **Eurico D'Sa**, Ishan Joshi, Christopher Osburn, Bingqing Liu
11:35 – 11:55	A VISUAL SURVEY OF THE ATLANTIC: PARTICLE SIZE DISTRIBUTIONS FROM THE IMAGING SENSORS **Marika Takeuchi**, Zonghua Liu, Mojtaba Masoudi, Thanga Thevar, Sarah L.C. Giering
12:00 – 12:15	**Walk to the MSO (Marine Station Oostende)**
12:15 – 13:15	**LUNCH**
13:15 – 14:00	**Visit VLIZ Marine Robotics Centre**
14:00 – 14:30	**Bus to Wetenschapspark, Oostende** - Generously sponsored by DEME
14:30 – 15:30	**Visit Flanders Maritime Laboratory**
15:30 – 16:00	**Bus to Brugge** - Generously sponsored by DEME
16:00 – 18:30	**Guided city walk and boat tour** - Generously sponsored by DEME
18:30 – 22:30	**Conference dinner at Halve Maan Brewery** **with presentation of the Eva and Yogi Agrawal Award**
22:30 – 23:00	**Walk from brewery to bus parking**
23:00 – 23:30	**Bus to Ostend**

SEPTEMBER 19th 2025 (FRIDAY)

SESSION 5A – Methods for Particle and Sediment Characterization. Chair: Nore Praet	
09:00 – 09:20	USE OF A LAGRANGIAN PARTICLE MODEL TO CHARACTERISE A NEW ACOUSTIC BACKSCATTER PROFILER **Andy Smerdon**, Dominic van der A, Tom O'Donoghue
09:20 – 09:40	ON ACOUSTIC BACKSCATTER SYSTEMS (ABS) CALIBRATION FOR SUSPENDED SEDIMENT CONCENTRATION ESTIMATION IN TURBULENT FLOWS **Guillaume Fromant**, Maxime Lernould, Benoît Becquet, Ghislain Poncin, Fabien Flahaut, Georges Stienne
09:40 – 10:00	THE COMPLEXITY OF CALIBRATING INDIRECT SEDIMENT MEASUREMENT TECHNIQUES IN THE SCHELDE-ESTUARY **Yves Plancke**, Sven Smolders
10:00 – 10:20	COMPARING THE DETERMINATION OF SUSPENDED SOLIDS CONCENTRATION (SSC) BY USE OF OPTICAL BACKSCATTER (OBS) AND ACOUSTIC BACKSCATTER (ABS) SENSORS **Alisa Spriet**, Jelle Malschaert, Pieter Mallants, Kris Van Troos, Jan Claus
10:20 – 10:50	**COFFEE BREAK; POSTERS & EXHIBITORS**
SESSION 5B – Methods for Particle and Sediment Characterization. Chair: Nore Praet	
10:50 – 11:10	ASSESSMENT OF THE SETTLING VELOCITY MEASUREMENT PROCEDURES OF SEDIMENT PARTICLES IN LABORATORY CONDITIONS **Kris Dumont**, Lander Bruylandt, Thomas Neirinckx, Renaat De Sutter, Bernard Malherbe, Jan Fordeyn
11:10 – 11:30	UNDERSTANDING THE OPTICAL BEHAVIOUR AND SPECTRAL SIGNATURE OF DREDGING-INDUCED PLUMES IN COASTAL WATERS **Liesbeth De Keukelaere**, David Doxaran, Robrecht Moelans, Niels Verdoodt, Els Knaeps
11:30 – 11:50	A BIO-GEO-OPTICALLY CONSISTENT PARTICLE MODEL FOR OPTICAL INVERSION **Xiaodong Zhang**, Deric Gray, Ping Yang
11:50 – 12:10	DEVELOPING OPTICAL FINGERPRINTING FRAMEWORK FOR COASTAL PARTICLE SOURCE IDENTIFICATION **Eero Asmala**, Joonas Virtasalo, Marine Poizat, Kristian Spilling, Karoliina Koho
12:10 – 12:25	**Walk to Fort Napoleon**
12:25 – 13:25	**LUNCH and End of PiE2025**

POSTERS

SUNDANSE: Innovative sediment management project in the Danube and Black Sea system

Sven Smolders, Mihaela Timofti, Sorina Pacuraru, Mihai Dragomir, Andrei Stanisteanu, Alexandru Ionescu, Maxim Arseni, Madalina Calmuc, Nina Lazar, Daniel Constantin, Oriane Georges

Toward Robust Calibration of the Point Source Integrated Cavity Absorption Meter (PSICAM): Scattering Effects and Solid Absorption Standard Evaluation

Chris Strait, Alberto Tonizzo, Wayne Slade, Kirby Simon, Chuck Pottsmith, **Michael Twardowski**

Riding the Eddies: Lagrangian Insights into Mesoscale Eddy Impacts on the East Greenland Current and Surrounding Sea Ice

Leandro Ponsoni, Rafael Gonçalves-Araujo, Dani Flocco, Borja Aguiar-Gonzales, Wieter Boone, and E(ddies)GC research group

In Search of Carbon Pathways in the North Sea and the Belgian Coastal Zone

Evgeny Ivanov, Jean-François Grailet, Marilaure Grégoire

The comparison of in situ and in lab instruments to determine particle size distribution

Yves Plancke, Dorota Szwoch, Ellen Bastiaensen

Particles in Europe 2025

Posters

17 - 19 September 2025, Ostend, Belgium

SUNDANSE: Innovative sediment management project in the Danube and Black Sea system

Sven Smolders[a], Mihaela Timofti[b], Sorina Pacuraru[b], Mihai Dragomir[c], Andrei Stanisteanu[c], Alexandru Ionescu[c], Maxim Arseni[b], Madalina Calmuc[d], Nina Lazar[d], Daniel Constantin[d], Oriane Georges[e]

[a] Flanders Hydraulics, Department of Mobility and public Works, Flemish Government, Berchemlei 115, 2140 Antwerp, Belgium;

[b] Dunarea de Jos University of Galati, Faculty of Science and Environment, Department of Chemistry, Physics and Environment & REXDAN Research Infrastructure, Domneasca Street no. 47, Galati, Romania;

[c] Marine Research SRL, Copilului Street No. 6-12 Tronson 2 Birou 5 Sc E Et 2 Sector 1, Bucuresti 012178, Romania

[d] Dunarea de Jos University of Galati, REXDAN Research Infrastructure, Domneasca Street no. 47, Galati, Romania;

[e] F6S Network Ireland Limited, Work Hub, 77 Camden Street Lower Dublin, Dublin 2, D02 XE80 Ireland.

SUNDANSE: Innovative sediment management project in the Danube and Black Sea system

Sven Smolders[a], Mihaela Timofti[b], Sorina Pacuraru[b], Mihai Dragomir[c], Andrei Stanisteanu[c], Alexandru Ionescu[c], Maxim Arseni[b], Madalina Calmuc[d], Nina Lazar[d], Daniel Constantin[d], Oriane Georges[e]

[a]Flanders Hydraulics, Department of Mobility and public Works, Flemish Government, Berchemlei 115, 2140 Antwerp, Belgium;
[b]Dunarea de Jos University of Galati, Faculty of Science and Environment, Department of Chemistry, Physics and Environment & REXDAN Research Infrastructure, Domneasca Street no. 47, Galati, Romania;
[c]Marine Research SRL, Copilului Street No. 6-12 Tronson 2 Birou 5 Sc E Et 2 Sector 1, Bucuresti 012178, Romania
[d]Dunarea de Jos University of Galati, REXDAN Research Infrastructure, Domneasca Street no. 47, Galati, Romania;
[e]F6S Network Ireland Limited, Work Hub, 77 Camden Street Lower Dublin, Dublin 2, D02 XE80 Ireland.
Corresponding author: Sven Smolders; sven.smolders@mow.vlaanderen.be

Introduction

The Danube River has played a vital role in supporting both human and animal life for centuries. Since the late 19th century, human interventions have significantly altered the natural flow of the river to optimize its utility. These interventions have included actions such as straightening the riverbed, constructing hydropower plants, collecting freshwater, establishing nuclear power plants, engaging in agriculture, and facilitating navigation. The combined effects of climate change and extensive river regulation have led to a significant disruption in the natural balance of sediment in the Danube River, increasing flood risks, altering hydropower production, decreasing navigability of the river, and affecting in biodiversity within the Danube Basin. SUNDANSE is a European Horizon project that aims to:

- carry out a conceptual Driver- Pressure-State-Impact-Response with multiple levels of analysis (catchment level, water body level, etc.) to understand and address environmental issues of the uniqueness of Danube river lighthouse
- realize maps for observation of critical points for excessive sedimentation and/or excessive erosion, sediment transport and flow restoration
- perform innovative actions of measurements using cutting-edge portable on-vessel equipment prototypes for the direct analysis of microplastics and toxicity
- achieve an advance numerical prediction model of sediment transport process in the Danube River basin, to have a comprehensive overview of river dynamics
- develop an Innovative Sediment Management Framework for enhanced and sustainable sediment management within the Danube River basin

- produce an Action plan and Roadmap for associated regions to upscale demonstrated sustainable and effective solutions for sediment management
- fulfil interconnections synergies with DanubeSediment and SIMONA projects and ICDPR initiatives
- improve the trans-national and cross-sectorial cooperation, contributing to a better governance in region and to implementation of EU strategi

Different work packages in SUNDANSE

SUNDANSE will develop a Sediment Management Handbook, supported by numerical models, that can be applied to the Danube tributary and other rivers. This handbook will provide a comprehensive guide to address the complexities of sediment dynamics within the Danube River ecosystems. It will feature cutting-edge strategies and technologies and promote nature-based solutions, erosion-resistant materials, predictive modelling tools and adaptive monitoring systems. The handbook will cover concepts from green infrastructure to dynamic river restoration and will offer practical insights into mitigating extreme erosion and excessive sedimentation while enhancing ecological balance. The Sediment Management Handbook will be accompanied by an Action Plan and a Roadmap to achieve the mission's ambitions.

To support the development of the handbook and to evaluate the impact of measures on the sediment quantity and quality and water quality, an open-source Sediment Management Prediction tool will be developed. To support this, a methodology will be developed and validated, consisting of detailed hydrodynamic and sediment transport models of three selected locations (3 use cases) along the Danube River. Scenario analysis will be used to assess different sediment management strategies. Furthermore, one of the locations will also be modelled in a physical scale model. The results of the physical scale model will be used to further validate the numerical model results. The combined results of the physical scale model and the numerical model will be compared and allow for accurate predictions of the effectiveness of the various proposed sediment management strategies.

SUNDANSE will improve the continuous monitoring of the Danube River and perform dedicated measurements of the bathymetry. These measurements will be used to perform and

validate the sediment management prediction tool and to complete a database of the Danube River. The following measurements are foreseen:

- Bathymetry measurement using single beam and multibeam bathymetric measurements.
- Sediment quality and quantity monitoring measuring microplastics, additives, metals with toxic potential, and biological and microbiological analysis.
- Determination of suspended sediment

All measurements and monitoring activities will contribute to an open access database of measured data that will eventually become part of databases such as ICDPR, SIMONA, SEDNET, and EMODnet.

To support the sediment management handbook, SUNDANSE will demonstrate sediment management solutions in use cases at three different locations:

- Location 1 - Serbia: Impact of sediment management solutions in the Danube-Tisa-Danube hydrosystem (Hs DTD), which connects the Danube and Tisa rivers through Vojvodina and represents a unique hydrotechnical system will be investigated. The main purposes of this hydrosystem are: drainage, irrigation, water supply, acceptance of used water, navigation, acceptance of water from the territory of neighboring countries, forestry , fishing, tourism and recreation.To ensure navigation conditions, dredging works are necessary. Sediment quality monitoring will be carried out with different dynamics of sampling / testing of surface sediment (0-20 cm).
- Location 2 - Romania: Impact of sediment management solutions downstream Corabia (rkm 626) to Turnu Magurele (rkm 597). The sector of the Danube River downstream of the port of Corabia has three critical points for navigation, two at Calnovat (rkm 617-614 and rkm 613-610) and one at Semovit (rkm 609-607). Water level data has been collecting at various points in this sector for many years. In periods of high-water levels, the entire sector is subject to deposition of sediments. Deposition of sediment is in the middle of the river, erosion occurs near the banks while from rkm 616-6056 the river O. Calnovat divides the Danube unto two arms with different discharge distribution.
- Location 3 - Bulgaria: Sediment and flow management from Ruse (rkm 480) to Tutrakan (rkm 444). The Danube sector proposed from rkm 480 to rkm 444, is characterised by many islands (Aleko, Gostinu, Lungu, Mishka, Brashlyan, Vâjâetoarea). One critical point, rkm 458-453. The discharge distribution on the arms has major influence on the

sediment transport. While deposition is identified in the middle of the riverbed, near the banks erosion phenomena occur.

All measures proposed by SUNDANSE are in line with the "Joint Statement on Inland Navigation and Environmental Sustainability in the Danube River Basin" with the main goal of preserving the sediment balance and improving the environmental status of the river, according to Danube Sediment Management Guidance, 2019. The river sectors targeted by SUNDANSE innovation actions are a major source of drinking water and supports agriculture. It serves as a resource for hydropower plants and the nuclear power plant (Cernavoda, RO). The lower Danube contains the maritime Danube also, facing significant sedimentation issues, and experiencing locations with extreme erosion. It serves as the main corridor for passenger and cargo transportation.

Two types of solutions are considered: hydrotechnical works and reduction of the impact of IWT vessels on erosion:

- Hydrotechnical works will be designed for all use cases. The pilot will start with measuring the bathymetric conditions of the site to identify the specifies of the location and to detail the design of the sediment management solutions. Among the solutions considered for this location are chevrons, shore/bank protections against erosion, shore/bank protection against flooding, and groynes. The proposed solutions aim to ensure optimal navigation conditions and sediment flow on the river, considering the needs of the users. The above-mentioned works will be dimensioned so that no additional dredging works will be necessary. Geotubes will be used as basis for the hydrotechnical solutions. A geotube is a large, tube-shaped bag with independent sections made of porous, weather-resistant geotextile and filles with for example sand as ballast. The assembly forms an artificial structure, such as a breakwater, chevron, or a shore/bank protection. The geotube is a sustainable solution as they are able to hold the sand in place and require less maintenance and dredging activities because of the works, hence being less environmentally taxing than traditional solutions.

- Reduction of the impact of IWT vessels on erosion: complementary to the hydrotechnical solutions, SUNDANSE will evaluate the impact of IWT vessels on erosion in the use case in Romania. The IWT sector is one of the key users of the Danube River for the transport of people and goods. Inland vessels can have several significant influences on suspended sediments in rivers and water bodies. These influences are primarily due to the advancing at different speeds regimes, turbulence, and wave generated by vessels during

navigation. While navigating, vessels create turbulence and disturb the riverbed, resuspending sediment particles that have settled on the bottom. By reducing the waves generated by IWT vessels, the impact on erosion can be greatly reduced. To achieve a reduced impact of IWT on the river sedimentation SUNDANSE will measure the correlation between the wave height generated by IWT vessels and the impact on erosion by dedicated measurements. This correlation is then used to determine the impact of wave height reduction on the sediment based on which SUNDANSE will develop solutions and guidelines for wave height reduction of IWT vessels.

Bathymetric survey campaign of different use cases

For each use case at least two bathymetric survey campaigns will be held. These data will be used for validation of sediment transport in the numerical models of each use case.

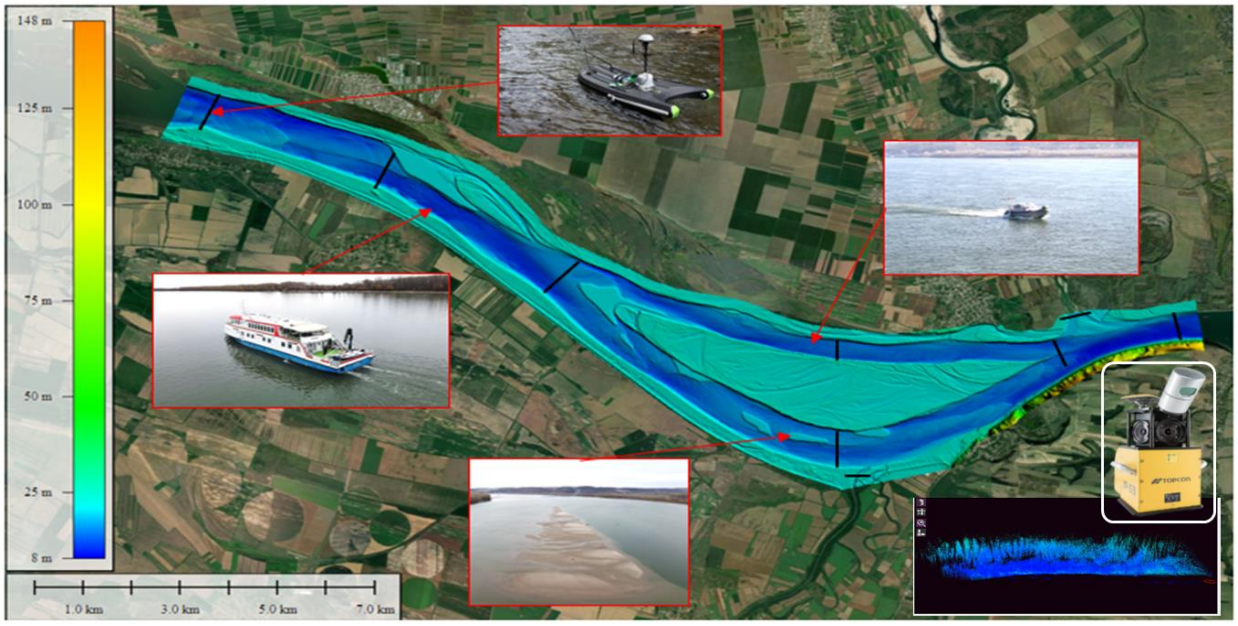

Figure 1. Bathymetric survey of Romanian Use Case.

The survey campaign integrates complex data from different types of equipment, conducted using the Kongsberg EM2040 and Geoswath 250 kHz multibeam echosounders (for riverbed mapping), Topcon HR GNSS receivers (for accurate land surveying), and the Topcon IP-S3 mobile system mounted on a boat. All surveyed data allows for the creation of a highly accurate Digital Terrain Model (DTM), providing a comprehensive view of both land and underwater features and shapes. The data collected from these systems is first processed to create individual datasets: bathymetric data (from the sonar systems) and topographic data (from the GNSS and

LiDAR systems). These datasets are then aligned and merged using georeferencing techniques, ensuring consistency across the land-river interface. Once the data is integrated, specialized software tools are used to generate the DTM, which can be further analyzed to extract critical topographic and bathymetric features. These models can be used for various purposes, such as designing a numerical model of the Danube River (Corabia–Turnu Măgurele part), assessing erosion and sedimentation, planning underwater excavation, and understanding sediment movement and exposure to safe navigation challenges.

Sediment monitoring

SUNDANSE will combine long term sediment monitoring with short term measurements to provide sufficient data for the activities in the project. The measurements and monitoring activities are done with four goals in mind:

- Validate effectiveness of solutions
- Determine effect of human activities
- Validate numerical models
- Collect data for database

To achieve these goals, a wide variety of parameters is to be measured, for which some portable analysers will be developed and/or validated. The measurements consist of, but are not limited to:

- Sediment quantity and quality: Measurements of sediment quantity will be made using portable sensors based on laser or radio frequency The sediment quality is analysed by considering chemical pollutants, microplastics, toxicity, and biodiversity.
- Microplastics: Eden Tech has developed a portable prototype microplastics analyser which will be tested and demonstrated in the SUNDANSE project. Machine learning algorithms will be developed for automated extraction of information from the near infrared (NIR) data. These algorithms will enable precise classification, counting, and sizing of microplastics, streamlining the process. Validation of the portable analyser is done using FT-IR and/or micro-FT-IR analysis on the samples collected from the use cases. The performance will be meticulously evaluated to confirm its accuracy, sensitivity, and reliability.
- Toxicity: a field-operable dispatchable fibre-optic-based biosensor system was developed to measure remotely collected specimens of sediment at the point-of-site. This system is a biosensor that uses genetically-engineered bacterial bioreporters (such as for genotoxicity, cell toxicity, membrane toxicity, quorum sensing, etc.) who are the bio specific entities that will react in the presence of whichever toxicant is found in the

sediment. The large advantage of this system is that these fibre optic probes do not need the sediment to be acid-treated and the signal does not suffer from the interference of the sediment itself. Thus, we will collect the sediment suspend in the water, dip the fibre probes into it and the biosensor will be triggered by any and all bioavailable toxicants leaching out of the sediment specimen.

- Biodiversity: In lotic ecosystems (such as the Danube River ecosystem) the assessment of water and sediment quality using several types of bioindicators is indicated. Benthic fauna will be chosen as indicator organisms that facilitate the determination of water quality in accordance with the water framework directive (WFD). The analysis and determination of aquatic macrophytes will be performed to determine phytoremediation potential of the location in which it is performed monitoring and measurements activities.
- Hydrometry: Where the Danube is divided into two arms, it is important to know the discharge of water, current speed and direction of each of the two arms. These parameters have a direct influence on the sediment's movements and will be measured.
- Underwater Mass Spectrometry (UMS): Using a field portable membrane-inlet mass spectrometer with a standard mass range of up to 200 amu. The device is suitable for continuous in-situ monitoring of dissolved gasses, light hydrocarbons, volatile and other organic compounds, and methyl mercury. The UMS will be deployed in standalone application on vehicle-based platforms, including REXDAN and drones.

The UDJG research vessel, REXDAN, will sail upstream and downstream the total length of the Danube River to conduct continuous measurements on sediment quantity and quality as well as water quality. Facilities on the vessel includes sampling and preserving samples laboratory, preparing samples laboratory, physicochemical analysis laboratory, aquatic ecology laboratory, and bathymetry systems. Thanks to the vessel guest quarters and meeting facilities, SUNDANSE will be able to organize workshops and host researchers and stakeholders onboard.

Acknowledgements

This research is part of the project `**Innovative sediment management framework for a SUstainNable DANube black Sea system (SUNDANSE)'**, co-funded by the European Union. Views and opinions expressed are however those of the author(s) only and do not necessarily reflect those of the European Union or the European Climate, Infrastructure and Environment Executive Agency. Neither the European Union nor the granting authority can be held responsible for them.

References

https://sundanseproject.eu/

Toward Robust Calibration of the Point Source Integrated Cavity Absorption Meter (PSICAM): Scattering Effects and Solid Absorption Standard Evaluation

Chris Strait[a], Alberto Tonizzo[a], Wayne Slade[a], Kirby Simons[b], Chuck Pottsmith[b], Michael Twardowski[a]

[a] Harbor Branch Oceanographic Institute, Florida Atlantic University, 5600 US Highway 1N, Ft. Pierce, FL 34946, USA

[b] Sequoia Scientific, Bellevue, WA, USA

Toward Robust Calibration of the Point Source Integrated Cavity Absorption Meter (PSICAM): Scattering Effects and Solid Absorption Standard Evaluation

Chris Strait[a], Alberto Tonizzo[a], Wayne Slade[a], Kirby Simons[b], Chuck Pottsmith[b], Michael Twardowski[a]

[a]Harbor Branch Oceanographic Institute, Florida Atlantic University, 5600 US Highway 1N, Ft. Pierce, FL 34946, USA
[b]Sequoia Scientific, Bellevue, WA, USA
Corresponding author: Chris Strait; cstrait2017@fau.edu

Abstract – The Point Source Integrated Cavity Absorption Meter (PSICAM) is used both in the lab and at sea due to its compact size. Accurate absorption measurements require prior knowledge of an absorption standard to account for the reflectivity of the integrating sphere, as even small changes in reflectivity can significantly impact results. Currently, nigrosine dye is used for this purpose because of its strong absorption across the visible spectrum. However, its poor temporal stability and sensitivity to pH variations make it difficult to use reliably in the field, where access to an accurate spectrophotometer may be limited. To address this, a solid absorption standard is proposed to improve the determination of the sphere reflectivity. Traditional calibration of the PSICAM requires solutions that closely match the sample's absorption coefficient, due to the influence of absorption on photon path lengths within the sphere. To overcome this, Monte Carlo ray tracing was used to develop and evaluate a correction scheme that enables accurate adjustment for these effects in PSICAM measurements. The influence of scattering on absorption measurements across the range of natural water conditions was also assessed.

Riding the Eddies: Lagrangian Insights into Mesoscale Eddy Impacts on the East Greenland Current and Surrounding Sea Ice

Leandro Ponsoni[a], Rafael Gonçalves-Araujo[b], Dani Flocco[c], Borja Aguiar-Gonzales[d], Wieter Boone[a], and E(ddies)GC research group

[a] **Flanders Marine Institute (VLIZ), Ostend, Belgium**
[b] **Section for Oceans and Arctic, National Institute of Aquatic Resources, Technical University of Denmark, Kgs. Lyngby, Denmark**
[c] **Dipartimento di Scienze della Terra, dell' Ambiente e delle Risorse, Università degli Studi di Napoli "Federico II", Napoli, Italy**
[d] **Oceanografía Física y Geofísica Aplicada (OFYGA), ECOAQUA, Universidad de Las Palmas de Gran Canaria, Las Palmas, Canary Islands, Spain**

In Search of Carbon Pathways in the North Sea and the Belgian Coastal Zone

Evgeny Ivanov, Jean-François Grailet, Marilaure Grégoire

MAST-AGO, University of Liège, Belgium

In Search of Carbon Pathways in the North Sea and the Belgian Coastal Zone

Evgeny Ivanov[a], Jean-François Grailet[a], Marilaure Grégoire[a]

[a]MAST-AGO, University of Liège, Belgium

Corresponding author: Evgeny Ivanov; evgeny.ivanov@uliege.be

Introduction

Despite constituting only a small fraction of the global ocean surface, shelf seas, such as the North Sea account for 80 – 90% of the total carbon stored annually in marine sediments (Hedges and Keil, 1995). Thanks to enhanced primary productivity and shallow depths, they are one of the essential tools for the Blue Economy. Most of the carbon in the North Sea (>80%) accumulates in the deep (up to 700m) Norwegian Trench (Diesing et al., 2021), suggesting that a big portion of detritus, produced in the Southern Bight, follows long-term circulation patterns along the European coast, eventually reaching the Trench through continuous cycles of resuspension and redeposition, influenced by tidal phases and meteorological conditions. The remaining fraction of the buried detritus in the North Sea accumulates mostly in small depo-hotspots, such as Helgoland Mud area, and scattered across the domain.

Methods

This study investigates carbon pathways in the North Sea using a coupled ocean model. The physical setup includes a hydrodynamic model ROMS, a wave model SWAN and a sediment model CSTMS, coupled with a biogeochemical Fennel model and a diagenetic model OmexDia, linking benthic and pelagic realms. The model is forced by the atmospheric model MAR, developed at the University of Liège, for period 1993 – 2100, under the IPCC spp370 scenario.

Results

The paths of organic detritus are assessed under both current and future climates for moderate-term scenarios (~15 years), to provide insights into their dynamics and consequences for the sequestration in the marine sediments. Additional attention is paid to the mud fields near Knokke and their capacity for long-term carbon storage.

References

Diesing, M., Thorsnes, T., & Bjarnadóttir, L. R. (2021). Organic carbon densities and accumulation rates in surface sediments of the North Sea and Skagerrak. Biogeosciences, 18(6), 2139-2160.

Hedges, J. I., & Keil, R. G. (1995). Sedimentary organic matter preservation: an assessment and speculative synthesis. *Marine chemistry*, *49*(2-3), 81-115.

The comparison of in situ and in lab instruments to determine particle size distribution

Yves Plancke[a,b], Dorota Szwoch[c], Ellen Bastiaensen[a,d]

[a] **Flanders Hydraulics, Berchemlei 115, 2140 Antwerpen, Belgium**
[b] **Hasselt University, Agoralaan gebouw H, 3590 Diepenbeek, Belgium**
[c] **University of Warsaw, Krakowskie Przedmieście 26/28, 00-927 Warsaw, Poland**
[d] **Vrije Universiteit Brussel, Pleinlaan 2, 1050 Elsene, Belgium**

The comparison of in situ and in lab instruments to determine particle size distribution

Yves Plancke[a,b], Dorota Szwoch[c], Ellen Bastiaensen[a,d]

[a]Flanders Hydraulics, Berchemlei 115, 2140 Antwerpen, Belgium
[b]Hasselt University, Agoralaan gebouw H, 3590 Diepenbeek, Belgium
[c]University of Warsaw, Krakowskie Przedmieście 26/28, 00-927 Warsaw, Poland
[d]Vrije Universiteit Brussel, Pleinlaan 2, 1050 Elsene, Belgium

Corresponding author: Yves Plancke, Yves.Plancke@mow.vlaanderen.be

Introduction

The analysis of grain size distribution can be conducted through both laboratory and in situ direct assessments. The distinct conditions present during these two measurement approaches require specific properties from the survey instruments. Each approach offers its own set of advantages and limitations. While laboratory analysis provides exceptionally high result resolution, the examined sediment is inevitably subjected to some level of alteration during sample collection, transport, and storage. On the other hand, in-situ measurements yield notably lower resolution, yet they enable the assessment of a sediment's grain size distribution in its unaltered, natural state.

Evaluating the performance of two in-situ and two laboratory devices under controlled laboratory conditions mitigates the influence of external factors on the outcomes. This approach enables the precise identification of performance disparities among the tested instruments. The derived results will play a pivotal role in shaping the selection of the optimal measurement methodology for future studies while also facilitating the comparative analysis of outcomes acquired through various devices.

This paper presents the results of a comprehensive comparison of four instruments available at Flanders Hydraulics (Flemish Government) employed for analyzing grain size distribution. The primary goals encompass the examination of result disparities between in-situ and laboratory devices as well as the evaluation of performance differences among instruments of the same application, potentially indicating advancements in newer devices. This entails evaluating their performance against standard samples with known characteristic grain sizes, assessing their applicability and suitability across various sediment types and identifying the limitations of each instrument.

Methods - instruments

All four of the tested instruments employ the laser diffraction method to capture particle-size distribution, also referred to as volume distribution. This technique, introduced in the 1970s, swiftly emerged as the predominant optical method for size distribution determination. Table 1 and Figure 1 give an overview of the 4 instruments used in this study, giving information on their measurement principle and their range of sediment sizes.

Table 1 - Overview of different instruments used within the comparative study

Instrument	***Manufacturer***	***Measurement principle***	***Range [µm]***
Mastersizer 2000[1]	Malvern Panalytical	Laboratory set-up Laser diffraction, Mie scattering Detection systems Red light (forward scattering, side scattering, back scattering) and blue light: wide angle forward and back scattering 32-ring Ring Detector	0.02 - 2000
Bettersizer 2600[2]	Bettersize Instr. Ltd	Laboratory set-up Laser Diffraction and Dynamic Imaging, combination of Fourier and inverse Fourier design 92-ring Ring Detector	0.02 - 2600
LISST-100X[3]	Sequoia Sci Inc.	In situ + in laboratory set-up Forward scattering (laser diffraction @ 670 nm) 32-ring Ring Detector Optical path length 50 mm, can be reduced using PRM	2.5 - 500
LISST-200X[4]	Sequoia Sci Inc.	In situ + in laboratory set-up Small-angle forward scattering (laser diffraction @ 670 nm) 32-ring custom photodiode Ring Detector + 4 large angle detectors 25 mm optical path	1.0 - 500

[1] https://www.malvernpanalytical.com/en/support/product-support/mastersizer-range/mastersizer-2000
[2] https://www.bettersizeinstruments.com/products/bettersizer-2600-laser-particle-size-analyzer
[3] https://www.sequoiasci.com/product/lisst-100x/
[4] https://www.sequoiasci.com/product/lisst-200x/

Figure 1. General view of the instruments: Mastersizer 2000 (top-left) and Bettersizer 2600 (top-right);LISST-100X (bottom-left), LISST-200X (bottom-right)

Methods - sediment

To ensure reliability and thoroughness of the results, tests were performed employing both reference ("standards") and field samples. Standard sediments (see Table 2 for its characteristics) represent the least complex type, characterized by uniform composition and certified grain size parameters. Field samples, on the other hand, originate as natural sediments from the Schelde estuary, and are characterized by larger variation in particle size distribution.

Table 2 - Overview of standard sediments; D10, D50 and D90 values are given in [µm]

Name	Soil type	D10	D50	D90
M 500	silt	-	3	-
M 400	silt	3	12	26
Silverbond M10	silt	4	23	60
Silverbond M6	silt	5	30	95
AF 100	fine sand	-	130	-
M 31	fine sand	-	360	-

Results

Figure 2 presents the results for the reference samples. Relative differences in median grain (D50) are shown with the certificate D50 as reference. In general relative differences remain smaller than ± 20%, although both LISST instruments show larger deviations for silt. Best results are found using the Bettersizer 2600 (average relative difference < +1%), followed by the Mastersizer 2000 (average relative difference ~ -5%), while both LISST-instruments result in an underestimation the median grain size (-22% and -11% respectively for LISST-100X and 200X).

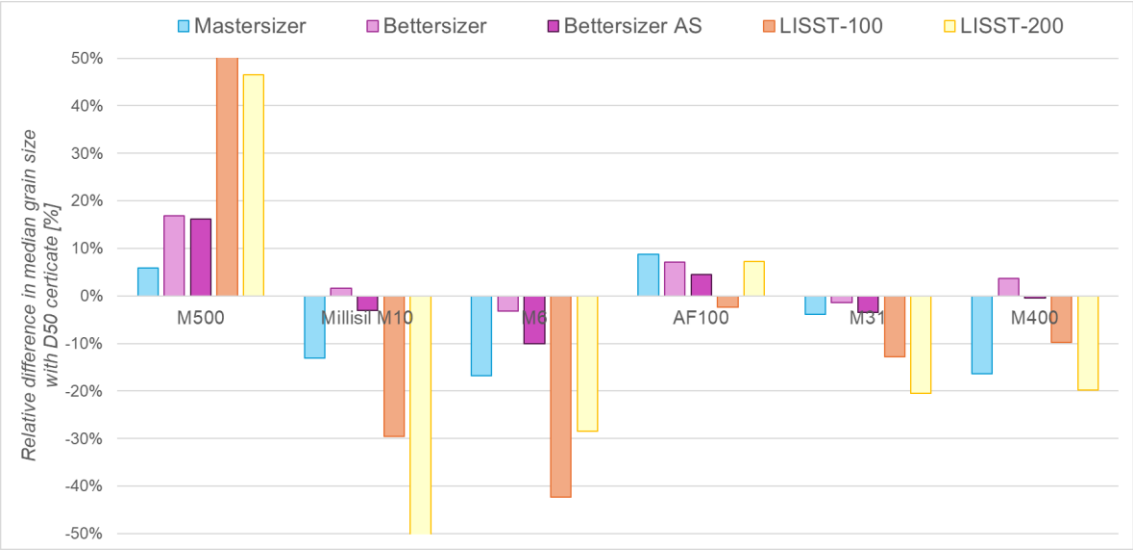

Figure 2. Relative difference in median grain size from different instruments for reference sediments (reference = D50 certificate)

Figure 3 presents the results for the field samples collected from the Schelde estuary. All samples consist of fine and medium sand. Because the exact median grain size of the field samples is not known, the comparison is made only relative to the different instruments. Again it is found that D50-values from both LISST-instruments are lower than both lab instruments, while the Bettersizer results in the largest values. Differences between the instruments can be as high as 100 µm (Ritthem 4, Bettersizer vs. LISST-200), which is quite significant. Further research is needed focusing on the full particle size distribution, in order to determine what causes these large differences.

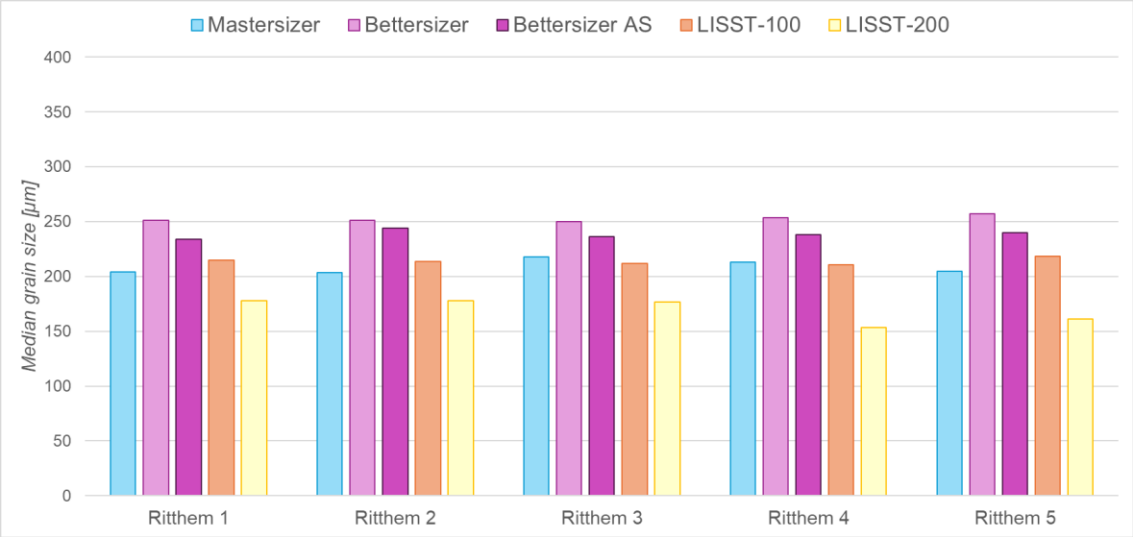

Figure 3. Median grain size from different instruments for field samples

Conclusion

A comparison between different instruments that measure the particle size distribution was performed in laboratory conditions. Both standard and field samples were used in the comparison. It was found that differences with D50-certificate values were smaller (+1% and -5%) for both lab instruments (Bettersizer, Mastersizer), while the in situ instruments (LISST-100X and 200X) resulted in larger differences (-22% and -11%). A similar pattern was found for the field samples with both LISST-instruments resulting in smaller D50 values. An important observation is that in situ instruments have a lab set-up, but they were not designed for this purpose. It was found that performing the lab experiments with these instruments, using a flow-through chamber or mixing chamber, was sub-optimal. It was found that not all sediments were brought in a homogenous suspension. This may partially explain the underestimation of D50 for the field samples, but it does not account for the discrepancies observed with the standard sediments. Further research is needed focusing on the full particle size distribution that was collected during the experiments.

Acknowledgement

The measurements were made possible with the help of different colleagues, both in the preparation phase (Engineering & Development) as during the execution of the measurements (in particular sediment lab colleagues).

Particles in Europe 2025

Proceedings

17 - 19 September 2025, Ostend, Belgium

30 Years of Measuring Suspended Particles

Yogi Agrawal, Ole Mikkelsen, Kirby Simon

Sequoia Scientific, Inc., 2700 Richards Road # 107, Bellevue, WA 98005, USA

30 Years of Measuring Suspended Particles

Yogi Agrawal[a], Ole Mikkelsen[a], Kirby Simon[a]

[a]Sequoia Scientific, Inc., 2700 Richards Road # 107, Bellevue, WA 98005, USA

Corresponding author: Ole Mikkelsen; ole.mikkelsen@sequoiasci.com

Introduction

Water flowing on the Earth's surface almost invariably carries sediments. Rivers carry sediments eroded from land and into receiving water bodies such as lakes or the sea. Here, sediments are reworked via resuspension or deposition processes, from the coastal zone to the deep sea, creating landforms, bedforms and deposits. Rivers further are the main source of microplastics discharge into lakes and the sea, where it may impact on aquatic life and interact with other types of particles, e.g., oil and sediment. Pollution and spills of many types, e.g., oil, occur both on land and in the aquatic environment and similarly affect aquatic life and human activities. Plankton is abundant in all aquatic systems and a crucial source of food for higher trophic level organisms everywhere. Harmful Algae Blooms greatly impact on the fauna and water bodies where they occur. All these particles; sediment, microplastics, oil, plankton, and others can interact with each other, forming various types of aggregates or conglomerates, which almost inevitably change the hydrodynamic behavior of the particles and/or makes them susceptible to ingestion by animals such as filter feeders, suspension feeders and others.

Despite these and many other areas of importance, in-situ measurements of particles in water remained relatively rare until the 1980's when optical transmissometers, acoustic backscatter sensors and fluorometers became more widely available. However, it wasn't until the development of commercial laser diffraction instruments and submersible camera systems in the 1990's that high-resolution particle size distributions became measurable in waters from the surface to the deep oceans. In this paper, we briefly review the evolution of laser diffraction instruments, novel applications, and advances and limits of the science of suspended particle measurements.

The Early Years

Early sediment sensor technologies began with the Lamont-Thorndike nephelometer, which used photographic film to capture scattered light from particles but lacked automation. The discovery of deep-sea storms in the 1970s prompted the development of more efficient devices, such as the transmissometer (Bartz et al., 1978), which measured light attenuation due to particles in water. Later, simpler turbidity sensors like the OBS became common (Downing et al., 1981), measuring

backscattered light, though both transmissometers and turbidity sensors required calibration due to reliance on particle area concentration (e.g., Sutherland et al., 2000; Bundgaard et al., 2018).

Photographic sensors were also used to observe flocs and marine aggregates, but their application remained limited. Acoustic backscatter sensors emerged in the HEBBLE experiment, delivering qualitative concentration profiles based on scattering strength, though calibration was hindered by unknown particle sizes (Lynch et al., 1991). Efforts continued to refine acoustic methods for measuring sediment concentrations, focusing on overcoming limitations posed by grain size variability and rapid acoustic attenuation at higher frequencies.

Sequoia then introduced the LISSTs based on laser diffraction starting in 1995, followed in 2010 by digital in-line holography in the form of the LISST-Holo, now LISST-Holo2. The laser diffraction method is fundamentally rooted in the theory of light scattering by particles. Consequently, the calibrations are not subject to drift with grain size as the nephelometers, transmissometers, turbidity meters or acoustic backscatter devices.

The basic principle of LISSTs are as follows (Figure 1): A highly collimated and clean beam is generated by use of a single-mode fiber laser source. A small part of the laser power is split off as a 'reference' laser power (*Lref*), to compensate for short or long-term drift in laser output. The collimated beam passes through two highly polished windows (*TW* and *RW*), which are coated on the air side, but not on the water side. Laser light scatters from particle sin the sample volume, *SV*. The receiving lens (*FL*) focuses the laser beam to the ring detector (*RD*), capturing scattered light. The focused laser spot has diffraction-limited diameter ~ 15 nm. It passes through the hole in the ring detector and is sensed by a photodiode (*DP*). Its measured power constitutes the optical transmission. The optical transmission is used to de-attenuate scattered energy on the rings before inversion.

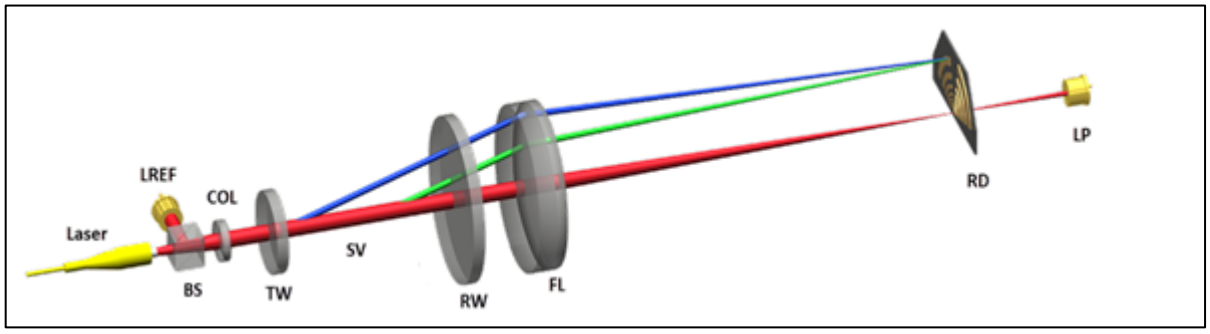

Figure 1. The optics of LISST instruments. A fiber laser is collimated (COL) and transmitted through transmit window TW into sample volume SV. Scattered light enters receive window RW and is focused by receive lens FL to the multi-ring detector RD. A hole at center of RD passes the focal spot through and is sensed by photodiode DP. The distance between windows TW and RW is the optical path in water; it can be shortened in high turbidity situations.

All scattered energy, i.e. the sum of scattering by micro-scratches on glass surfaces and by particles is sensed by ring detectors. The scattering from micro scratches is measured with ultra-filtered water. It creates a background Z on the ring detectors. With particles in water, the measured energy D on rings becomes:

$$D = G\,\tau\,[\,\underline{\mathbf{K}}\,V + Z];$$

where G is the overall electronic gain, τ is the optical transmission, V is the volume distribution and $\underline{\mathbf{K}}$ is the kernel matrix. The volume distribution is:

$$V = \underline{\mathbf{K}^{-1}}\,[D / G\,\tau - Z] \qquad (1)$$

An error in the measurement of background light Z on detector rings can bias the volume distribution V up or down. Thus, a careful measurement of Z is vital.

A modified Chahine algorithm is employed for inverting the corrected scattering V of Eq. (1). This algorithm is described by Agrawal and Pottsmith (2000). It is an iterative technique assuring non-negative particle size distributions.

Impacts

While LISSTs were originally developed for sediment transport research, and about half of all LISST papers are mainly on sediment research, other researchers were quick to adapt them (Table 1).

Table 1. Frequency of select keywords in known LISST publications (as of June 2025) indicating relative popularity of LISST use.

Keyword	**Frequency**
Sediment	53%
Optics	23%
Sediment AND Rivers	18%
Estuaries	17%
Flocs	14%
Sediment AND Ocean	13%
Oil OR Dispersant	13%

Plankton OR Primary Productivity OR Algae	6%
Cohesive Sediment	5%
Microplastic	3%
Marine snow	1%
Biogeochemistry	1%
Stormwater	1%
Hydropower	1%

For example, almost 13% of all papers and reports published with LISST data are on oil spill and oil dispersant use or research (Simon & Mikkelsen, 2024). The U.S. Environmental Protection Agency's (EPA) National Oil and Hazardous Substances Pollution Contingency Plan (NCP) outlines requirements for oil spill monitoring in the United States. These requirements have been put in place because a full assessment of an oil spill, including the location, spread, type and condition of the oil, and the effectiveness of the dispersant, is vital when making decisions about dispersant use. In particular, the NCP requires monitoring of in-situ oil droplet size distribution for droplet sizes from 2.5 to 2,000 micrometers, but predominantly in sizes up to 100 micrometers. The droplet size distribution may serve as an indicator of the effectiveness of dispersant operations. Effective dispersants yield a greater proportion of small droplets than large droplets. For subsea spills, larger droplets rise to the surface faster and can coalesce—forming slicks or sheens. Smaller droplets, however, remain suspended longer in the water column and are subject to water fate and transport processes, such as biodegradation, dissolution and aggregation.

Using data to target the use of dispersants during an oil spill response reduces the risks that oil discharges and response technologies pose to the environment. This is crucial in minimizing the environmental impact of oil spills and ensures a comprehensive and effective response to oil spills. For instance, during the response effort in the aftermath of the 2010 Deepwater Horizon accident, the EPA mandated LISST use for droplet monitoring within a few days after the accident.

Another topic nobody thought of in 1995 when LISSTs were introduced is microplastics. LISSTs have a proven track record amongst microplastics researchers, as evidenced by the talk of Dr.

Teresa Serra, one of our keynote speakers. Microplastic particle distributions from disposable masks, interactions between oil droplets and microplastics, and microplastic concentration, distribution and abundance in urban drainage systems have been studied using LISSTs. This has highlighted the environmental impacts of microplastics and contributed to improved understanding of the distribution and enrichment of microplastics in many different aquatic environments.

Other microplastic studies have been concerned with the effects of environmental aging on microplastics, understanding microplastic vertical migration, and measuring microplastic concentrations in water and ice, giving insights into the enrichment and distribution of microplastics during ice formation thus microplastics transport pathways in cold regions. While only 3% of all LISST papers are on microplastics, all of these have been published since 2020. Microplastic papers make up 8% of LISST publications since 2020.

In primary productivity studies, LISST data on particle size and concentration have aided the assessment of phytoplankton abundance and distribution, essential for more accurate estimates of primary productivity. They have also helped improving satellite-based remote sensing techniques and provided insights into particle aggregation and flocculation processes influencing suspended particulate matter dynamics and light conditions, affecting primary productivity. Finally, LISSTs data have been used to correlate particle size with chlorophyll concentrations and other biological metrics, offering a more comprehensive understanding of the biological pump and carbon sequestration processes.

A more ‘classical’ example of LISST use is its use in flocculation studies: About 15% of published papers with LISST results focus on flocculation studies. LISSTs’ versatility allows the study of floc dynamics from the surface to 6,000 m depth and they have been used to estimate flocculation time scales in situ and in the lab, investigate the influence of turbulence on flocculation, determine floc fractal dimensions and floc settling velocities, investigate how bed shear stress affects floc sizes and volumes, develop models for sediment transport purposes in rivers, estuaries and the ocean, study oil-mineral aggregates in connection with oil spill research, elucidate the aggregation and settling of dying algae, measure the primary particle size distribution of flocs in situ, investigate organic content impact on flocculation and sediment transport and study aggregation processes in (harmful) algae blooms, and dredging and deep-sea mining plumes (Sequoia Scientific, 2025).

Advances and Limitations

Scattering by irregular particles: Particles in water are rarely spheres. How does laser diffraction instruments see irregular grains? Some progress has been made to deal with shape by empirical

definition of the kernel matrix **K**. A series of experiments was performed to empirically determine the forward scattering properties of irregular terrigenous particles. Light scattering was measured at the bottom of a settling column. Motion in the column was suppressed by stratification. A thin layer of particles was placed at the top of the column at start of experiment. As particles rained down to the laser across the bottom of the column, their forward scattering signatures were measured with LISST optics. The particles settled according to their hydraulic size. The angular scattering was measured continuously over approximately 48 hours. For settling times that corresponded to specific hydraulic sizes (via. Stokes law), the light scattering signatures E were recorded. Irregular shaped particles appear optically to be about a ¼Φ (approx. factor of 1.19) larger than their hydrodynamic size (Agrawal et al., 2008).

Elongated particles: A common occurrence in field data is the appearance of a sawtooth pattern in scattering over rings. Such patterns usually arise due to presence in the laser beam of particles with a strong preferred direction, e.g. fibers. The diffraction pattern of a fiber is elongated yet centered on the central hole. The long axis of the pattern is oriented normal to long axis of the fiber, and it is not azimuthally symmetric. Only rings in one quadrant may see this scattering, producing a sawtooth pattern in scattering across rings. This is illustrated in Figure 2.

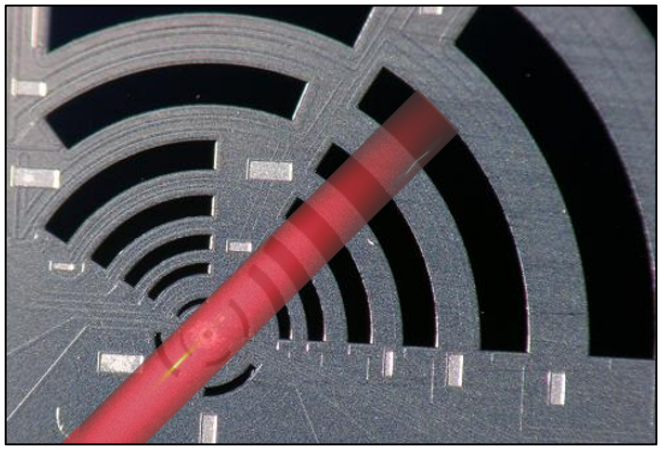

Figure 2. Diffraction pattern of a fiber overlaid on the multi-ring detector of LISST instruments.

The inversion method does not account for such variations. Scattering by flocs is also problematic for the method since no generally agreed formulation for light scattering is available for flocs. As a result, an ‘equivalent irregular grain’ is again the interpretation. Koestner et al (2024) looked at the scattering from highly stringy particles and compared the sizes from laser diffraction to sizes from a LISST-Holo2 and found excellent agreement between median diameters from many different particles. So, the effect may be considered minimal.

Speed: Laser diffraction is fast. LISST data can be processed and displayed in real-time on board the instrument, allowing for immediate adaptation of, e.g. sampling strategy as well as telemetry of fully processed data on, e.g. ocean observatory systems

Errors in estimation of the size distribution and concentration can arise from several factors and should be understood by the user.

Errors due to poor backgrounds or fouling: This error may be caused by inadequate attention to the acquisition of a background measure of light on detectors *Z*, usually due to poor cleaning of the windows. The error becomes more significant in low particle concentrations when the background is of similar magnitudes to the scattering signal. In very clear water it is advisable to use an *in-situ* background, where the measurement with the highest optical transmission is used as the background.

Density effects: The existence of microstructure from density differences can cause scintillation-like steering of the laser beam (Mikkelsen et al., 2008). Also, in laboratory use, ignoring mixing of water during testing can cause temperature stratification and consequent beam-steering. Thermal boundary layer forming on glass windows immediately after instrument insertion can lead to lead scintillation-like fluctuations.

Small number statistics: It can be readily estimated that at small concentrations, only a few particles of a particular size may be present in the laser sample volume. This is typical for large grains. In such situations, individual PSD's may exhibit high variability for the large grain concentrations. Averaging solves the problem, but at the expense of time-resolution.

Resolution of the inverse method: Due to the imperfect knowledge of the kernel matrix for all types of particles, the inverse method is set for relatively low resolution in PSD. PSD can be sharpened by increasing the number of iterations.

Multiple scattering: In highly dense particle situations that typically arise in fluvial use, optical transmission across the sample volume may drop below 30%. In such cases, multiple scattering may start to affect the size distribution, shifting it up one size bin, and possibly inventing fine particles.

Conclusion

Laser diffraction is used in many very different applications: Research in microplastics, ocean optics, plankton, oil spill research and more were never envisioned when Sequoia started in 1995. The method has some basic limitations but is fundamentally sound and the physics is very well understood. Above all, it is fast and accurate.

References

Agrawal YC, Pottsmith HC (2000) Instruments for particle size and settling velocity observations in sediment transport. Marine Geology 168(14), 89-114.

Agrawal YC, Whitmire A, Mikkelsen OA, Pottsmith HC (2008) Light scattering by random shaped particles and consequences on measuring suspended sediments by laser diffraction. Journal of Geophysical Research Oceans 113.

Bartz R, Zaneveld RJV, Pak HA (1978) Transmissometer For Profiling And Moored Observations In Water. Ocean Optics V 102–109, doi:10.1117/12.956856.

Bundgaard K, Lumborg U, Nyborg L, Jakobsen BH (2019) Challenges of optical backscatter monitoring in mixed sediment environments. Terra et Aqua 154, 22-29.

Downing JP, Sternberg RW, Blister CR (1981) New instrumentation for the investigation of sediment suspension processes in the shallow marine environment, Marine Geology 41(1-4), 19-34.

Koestner D, Foster R, El-Habashi A, Cheatham S (2024) Measurements of the inherent optical properties of aqueous suspensions of microplastics. Limnology & Oceanography Letters. doi:10.1002/lol2.10387.

Lynch J, Gross T, Brumley BH (1991) Sediment concentration profiling in HEBBLE using a 1-MHz acoustic backscatter system. Marine Geology 99 (3-4), 361-385

Mikkelsen OA, Milligan TG, Hill PS, Chant RJ, Jago CF, Jones SE, Krivtsov V, Mitchelson-Jacob G (2008). The influence of schlieren on in situ optical measurements used for particle characterization. Limnology & Oceanography: Methods 6, 133–143.

Sequoia Scientific (2025): https://www.sequoiasci.com/library/technical-papers/?fwp_papers_topic=flocculation. Accessed 9 June 2025.

Simon K, Mikkelsen O (2024) Submersible Optical Sensors – Instrumentation for HAB, Oil Spill and Remote Sensing Research. Sea Technology 65, 17–21.

Sutherland TF, Lane PM, Amos CL, Downing J (2000) The calibration of optical backscatter sensors for suspended sediment of varying darkness levels. Marine Geology 162, 587–597.

An Optical Sensor for Autonomous Detection of Particulate Inorganic Carbon (PIC) Concentration in Seawater

Qiming Sun[a,c], Georges Fournier[b], Filip Beunis[c], Kristiaan Neyts[c], Jordan Toullec[a], Peter Chaerle[d], Olga Chepurnova[d], David Dana[e], Chuck Pottsmith[e], Wayne Slade[f], Wim Vyverman[d], and Griet Neukermans[a,g]

[a] MarSens Research Group, Biology Department, Ghent University, Krijgslaan 281 – S8, 9000 Ghent, Belgium
[b] DRDC Valcartier Research Centre, Québec, Québec, G3J1X5, Canada
[c] LCP group, ELIS Department, Ghent University, Technologiepark 126, 9052 Ghent, Belgium
[d] BCCM/DCG, Biology Department, Ghent University, Krijgslaan 281 – S8, 9000 Ghent, Belgium
[e] Sequoia Scientific, Inc., 2700 Richards Road, Suite 107, Bellevue, Washington 98005, USA
[f] Florida Atlantic University, 777 Glades Rd, Boca Raton, Florida 33431, USA
[g] Flanders Marine Institute, Jacobsenstraat 1, 8400 Oostende, Belg

Development of a New In-Situ Hyperspectral Transmissometer for Ocean IOP Closure

Kirby Simon, Ole Mikkelsen

Sequoia Scientific, Inc., 2700 Richards Road, Suite 107, Bellevue, WA 98005, United States

Development of a New In-Situ Hyperspectral Transmissometer for Ocean IOP Closure

Kirby Simon[a], Ole Mikkelsen[a]

[a]Sequoia Scientific, Inc., 2700 Richards Road, Suite 107, Bellevue, WA 98005, United States

Corresponding author: Kirby Simon; kirby.simon@sequoiasci.com

Introduction

Measurements from ocean color satellites are used to monitor phytoplankton blooms, oil spills, atmosphere-ocean carbon cycling, and other phenomena (Dierssen et al., 2023; Werdell et al., 2018) and are therefore critical to understanding the health of our oceans. Instruments on these satellites typically measure remote sensing reflectance $R_{rs}(\lambda)$, which depends on the inherent optical properties (IOPs) of the water, or more specifically the absorption, scattering, and attenuation properties. Robust and accurate in-water measurements of these IOPs are therefore critical to the accuracy of data products from ocean color satellites, as these IOP measurements enable (1) data simulation with realistic assumptions and measurements to baseline model development and (2) model refinement and ocean color data product validation.

As the next generation of ocean color satellites, such as NASA's PACE (Plankton, Aerosol, Cloud, ocean Ecosystem) and GLIMR (Geostationary Littoral Imaging and Monitoring Radiometer) missions, move from multispectral measurement capabilities to high-resolution hyperspectral capabilities, in-situ instrumentation for IOP measurements must follow suit. In-situ hyperspectral absorption and scattering sensors have been developed in recent years, including by our team at Sequoia, however instruments measuring attenuation are still either single- or multi-spectral or do not meet the wavelength range and resolution requirements to match hyperspectral satellite measurements. We are developing a hyperspectral transmissometer (Hyper-c) to directly meet the needs of next-generation ocean color satellites for IOP closure in support of model and data product development and validation, while also adding complementary measurement capabilities to expand the utility of the sensor to broader biogeochemistry and environmental monitoring research.

Methods

We designed the Hyper-c instrument breadboard in Zemax OpticStudio, performing optical simulations of different lens and LED configurations to maximize the spectral range, optical throughput, and other characteristics. We then assembled the instrument breadboard using commercially available components in the configuration shown in Figure 1. Key components included a broadband LED source, lenses to collimate and focus the light, a linear variable filter

(LVF) to selectively scan through source wavelengths, and a fiber-coupled spectrometer to collect and measure the transmitted light. A 10-cm pathlength cuvette was fabricated to hold the sample between the transmit and receive optics for measurement.

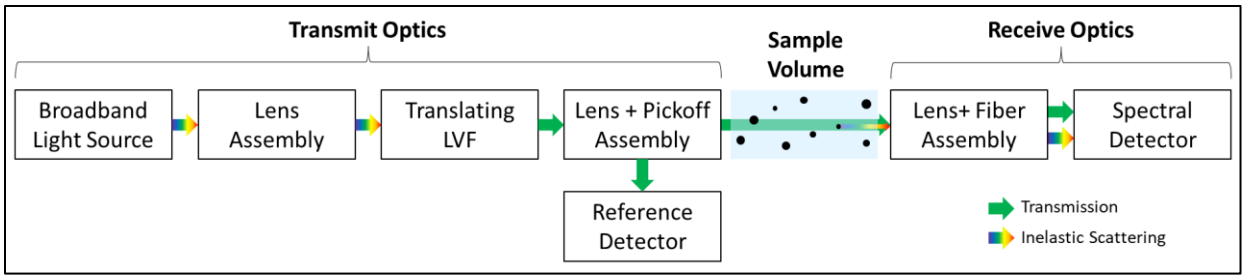

Figure 1. Block diagram of the Hyper-c breadboard with key parts and subsystems labeled. Wavelengths were selected for measurement by translating the LVF to pass specific wavelengths of light. The light transmitted through the sample was fiber-coupled to a spectrometer for measurement. There was no reference detector in the initial breadboard, but one will be incorporated into the next instrument for monitoring source output power to correct for LED drift.

For a given measurement, we used an LED warm-up time of 60 seconds and kept the LED powered on for the entire scan. The LED power was kept at its minimum setting for all attenuation measurements and was increased to its maximum setting when performing inelastic scattering measurements. To scan through wavelengths with the Hyper-c, we manually translated the LVF in 2-mm increments using a linear stage and performed a measurement at each position, resulting in 18 discrete measurements across a spectral range of approximately 389 nm to 722 nm. We used a 0.24 ms spectrometer exposure time for attenuation measurements (set to maximize the dynamic range of the spectrometer based on the highest peak intensity measured across the scanned wavelengths without saturating any pixels in clean water) and 100 averages. We varied these values for the inelastic scattering measurements. All spectra were dark subtracted to account for stray light or other artifacts.

To calculate the beam attenuation coefficient for the Hyper-c breadboard at each wavelength, we followed the IOCCG Protocol Series (2019) for beam transmission and attenuation. Assuming a constant source output, we used equation 20 from the protocol (reprinted below as Equation 1) to calculate beam attenuation as a function of wavelength $c(\lambda)$, where r_t is the pathlength in meters (0.1 m for the Hyper-c breadboard), $V_D(\lambda)$-$V_D^{dark}(\lambda)$ is the background-subtracted measurement of the sample of interest, $V_{D,w}(\lambda)$-$V_{D,w}^{dark}(\lambda)$ is the background subtracted measurement of clean water, and $c_w(\lambda)$ is the beam attenuation coefficient of pure water calculated using pure water absorption and scattering values from the absorption IOCCG Protocol Series (2018) and Pegau et al. (2003), respectively, as recommended in the attenuation IOCCG Protocol Series (2019).

$$c(\lambda) = -\frac{1}{r_t}\ln\left(\frac{V_D(\lambda) - V_D^{dark}(\lambda)}{V_{D,w}(\lambda) - V_{D,w}^{dark}(\lambda)}\right) + c_w(\lambda) \quad [1]$$

The values for $V_D(\lambda)$-$V_D^{dark}(\lambda)$ and $V_{D,w}(\lambda)$-$V_{D,w}^{dark}(\lambda)$ were the background-subtracted measurements of the sample and water blank, respectively, with the wavelength λ being the approximate peak of the LED emission at a given LVF position. Due to the manual nature of the LVF scanning process, minor discrepancies from measurement-to-measurement were accounted for by integrating signal over ±2 nm around the peak LED wavelength for a given LVF position.

We used a PerkinElmer Lambda 365+ spectrophotometer for benchmarking the Hyper-c attenuation measurements. We used a 10-cm pathlength fused quartz cuvette, a scan range of 370 nm to 730 nm (1-nm slit width), and a scan speed of 240 nm/min. Each measurement was referenced to a clean water blank, so the reported absorbance values were due to the non-water (chlorophyll or antacid) components in solution.

For sample preparation, we used ultrapure, degassed water filtered through a Barnstead GenPure Pro system (Thermo Fisher Scientific). We used an off-the-shelf antacid (Kroger, Regular Strength) to make a dilution series, adding 5 mL of the antacid stock to 195 mL of water to create a 2.5% concentrated initial solution. We diluted this solution (50 mL solution into 150 mL water) several times for approximate concentrations of 0.635%, 0.156%, 0.039%, and 0.010% and let the samples sit at room temperature for at least 1 hour. Before an individual measurement, we mixed the sample for at least 15 seconds to resuspend settled particles.

We extracted chlorophyll from spinach leaves for additional measurements, crushing the leaves with a mortar and pestle and soaking the crushed leaves in isopropyl alcohol (99%) for a minimum of 24 hours. After soaking, we filtered the solution through a 0.2 um filter, leaving behind only the dissolved chlorophyll as our concentrated stock solution. To make a dilution series, we added 2 mL of the stock solution (100%) to 198 mL of water for the initial dilution (1%), then continued the dilution to 0.1% and 0.01% concentrations (20 mL solution to 180 mL water). Similar to the antacid dilutions, we let these samples sit after the initial dilution and then briefly mixed the sample before a given measurement.

Results

The two highest concentration antacid solutions (2.5% and 0.625%) resulted in significant signal attenuation across the 10-cm pathlength of the instruments such that no detectable optical signal was measured by the spectrophotometer or Hyper-c. For the three lower concentrations (0.156%, 0.039%, and 0.010%), we found a linearly decreasing trend in absorbance with increasing wavelength with no clear spectral features across the spectral profile. The measured absorbances ranged from 2.598 (maximum absorbance from 0.156% solution) down to 0.190 (minimum absorbance from 0.010% solution) across the three samples (Figure 2). We found a similar trend when measuring the same samples with the Hyper-c breadboard, where the calculated beam

attenuation coefficient decreased as a function of increasing wavelength with minimal spectral features. The calculated beam attenuation coefficients ranged from approximately 106.43 m^{-1} (maximum from 0.156% solution) down to 5.40 m^{-1} (minimum from 0.010% solution).

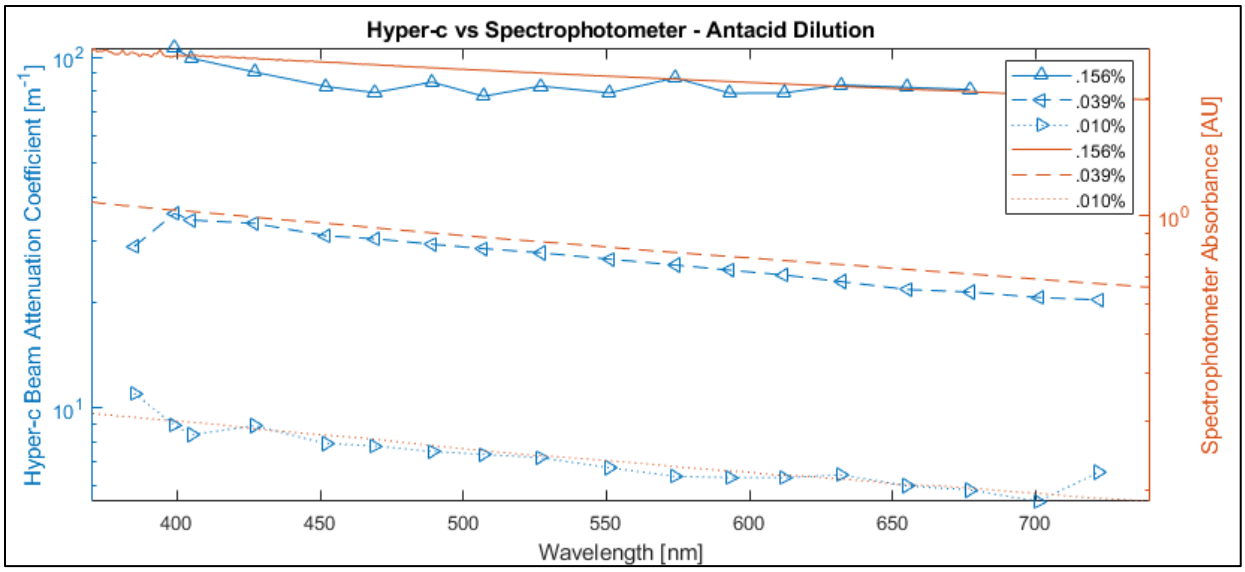

Figure 2. Comparison between Hyper-c breadboard (blue) and spectrophotometer (orange) measurements of antacid dilution samples at the same concentrations.

The lowest concentration chlorophyll sample (0.01%) was too diluted such that the transmitted signal was indistinguishable from the clean water background. For the two higher concentration solutions, the measured absorbances from the spectrophotometer ranged from 2.741 (maximum from 1.0% solution) to 0.002 (minimum from 0.1% solution) while the beam attenuation coefficients measured by the Hyper-c ranged from 63.76 m^{-1} to 0.33 m^{-1} (Figure 3).

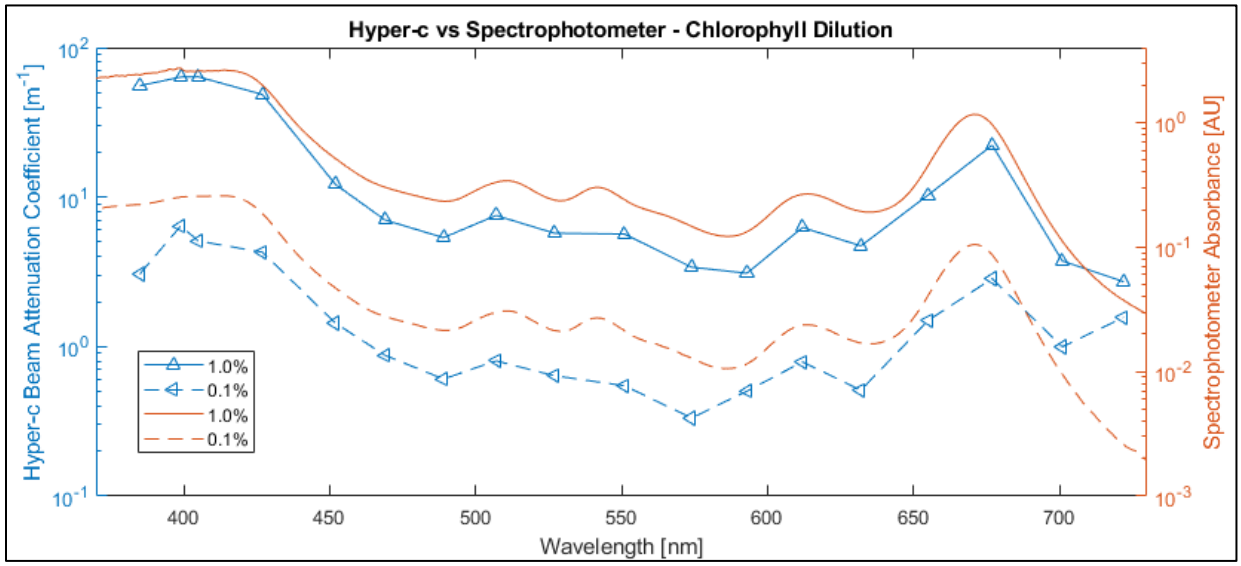

Figure 3. Comparison between Hyper-c breadboard (blue) and spectrophotometer (orange) measurements for chlorophyll dilution samples at the same concentrations.

We attempted chlorophyll fluorescence measurements with the Hyper-c breadboard as a demonstration of complementary capabilities that can enhance the utility of the sensor. We focused on exciting the sample with light near the chlorophyll absorption maximum (around 400 nm), which coincided with the peak emission of the LED (406 nm), to stimulate fluorescence emission between 650-750 nm. We translated the LVF in 1 mm increments to seven different positions around the 406 nm LED emission peak, performing a measurement at each position for a given sample and set of conditions. Additionally, we added a bandpass filter (400 nm center wavelength, 40 nm full-width-half-max) after the transmit optics to eliminate any light leakage through the LVF at off-band wavelengths that could interfere with the fluorescence signal.

We made a solution of chlorophyll in water using the extracted chlorophyll stock, adding approximately 1 mL of the stock to 50 mL of water. We attempted fluorescence measurements at a low LED power and short exposure time (0.1 ms), however no fluorescence was detectable. We increased the LED power to its maximum, at which point fluorescence was detectable by eye near the front of the sample holder, however still no fluorescence was measured at the detector. We then added another 2 mL of chlorophyll stock to the sample and increased the exposure time of the detector. At 100 ms exposure time we began to measure the chlorophyll fluorescence signal, with the signal intensity continuing to increase with exposure time (Figure 4).

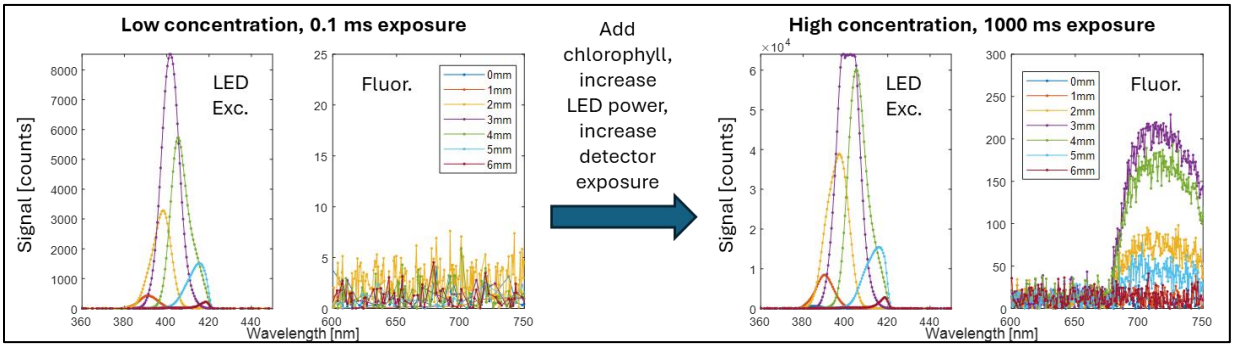

Figure 4. Measurements demonstrating successful detection of chlorophyll fluorescence with the Hyper-c breadboard. After initially not detecting fluorescence in the sample (left pair), we added more chlorophyll extract to the sample, increased the LED power, and increased the spectrometer exposure time (right pair) at which point the chlorophyll fluorescence signature between 650-750 nm was detected. Each set of spectra includes the excitation profile of the LED emission (left plot) and the spectral region for the target chlorophyll fluorescence feature (right plot) for each LVF position scanned.

After demonstrating fluorescence measurements, we attempted to measure Raman scattering with the Hyper-c breadboard. We placed an additional bandpass filter (450 nm center wavelength, 40 nm full-width-half-max) into the optical assembly in front of the receive optics to block direct emission from the LED from saturating the detector. We chose the filter to correspond with Raman emission from pure water due to O-H stretching, which shows up between 2900-3800 cm^{-1}. Using the LED peak emission wavelength (406 nm) for excitation, we calculated the target Raman signal to occur approximately between 460 nm and 478 nm

(converting Raman shift in cm^{-1} to wavelength). We performed measurements on pure water at the maximum LED power, increasing the spectrometer exposure time with successive measurements. We began to measure the target Raman signal at exposure times of 500 ms, with the signal intensity increasing with increasing exposure time (Figure 5).

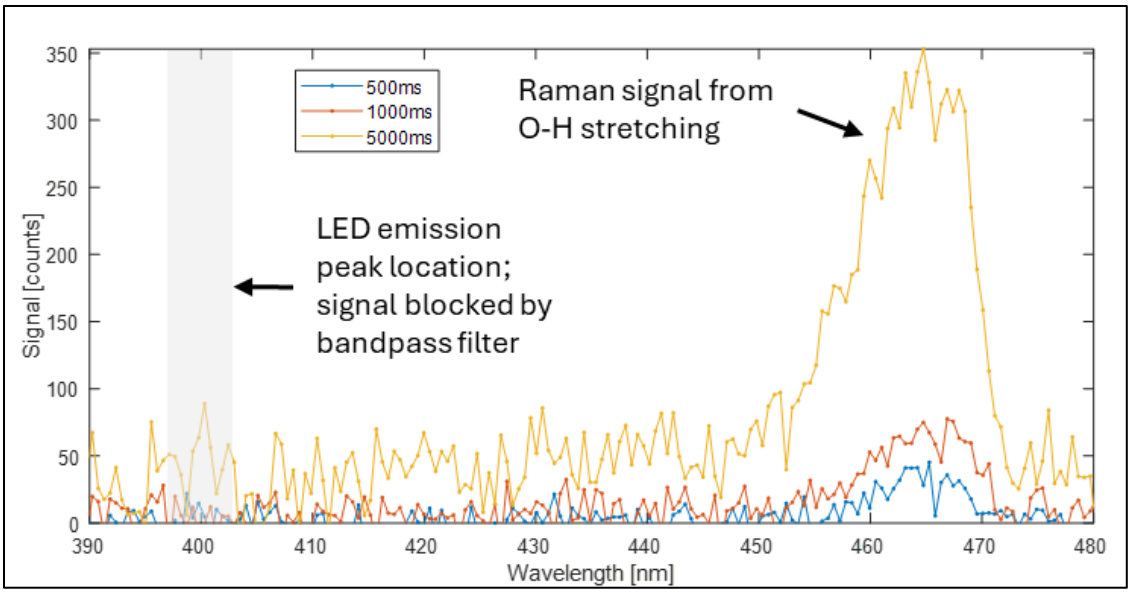

Figure 5. Measurements of pure water showing the Raman signal of the O-H stretching band present at exposure times as low as 500 ms using the maximum LED power. Unlike the fluorescence measurements above, the LED emission is blocked from the detector here by an extra bandpass filter added to the optical assembly.

Discussion

Values measured by the Hyper-c and spectrophotometer cannot be compared as 1:1, as the spectrophotometer detector geometry (detector size, acceptance angle) is unknown and total-internal-reflection by the cuvette walls can result in more scattered light transmitting to the detector than what the Hyper-c would see (IOCCG Protocol Series, 2019). Therefore, comparison of the exact values reported by the sensors is less important than the spectral shape of the measurements and relative magnitude changes with concentration steps. Importantly, the absorbance measurements from the spectrophotometer and the beam attenuation measurements from the Hyper-c breadboard are in good agreement in terms of both (1) capturing the spectral shape of the profile and (2) relative changes in signal across different sample concentrations.

The measured absorbance profile of the chlorophyll matches that of chlorophyll *a*, with major peaks in absorbance located between approximately 400-420 nm and 650-680 nm, two minor peaks between 500-550 nm, and another minor peak between 600-620 nm. The Hyper-c captures all of five of these peaks, both in terms of spectral position and relative intensities, despite the poor resolution of the spectral scan due to the manual nature of the measurement process. Variations in the Hyper-c signal at the edges of the spectral range are attributed to a combination

of low LED output at those wavelengths and, for the signals above 700 nm, the relative increase in water absorption with wavelength.

The measured absorbance and beam attenuation profiles for the antacid dilutions also agreed in spectral shape, although there were few discerning spectral features across the spectra. Similar to the chlorophyll measurements, spectral features at the upper and lower wavelength bounds of the Hyper-c are attributed to low LED output and water absorption. Importantly, the relative changes in signal between concentration steps are similar between the two instruments. From the 0.156% solution to the 0.039% solution, the average absorbance decreased by a factor of 0.33 and the average beam attenuation decreased by 0.37. From the 0.039% solution to the 0.010% solution, the averages values decreased by a factor of 0.27 (spectrophotometer) and 0.29 (Hyper-c).

Inelastic scattering measurements with the Hyper-c have several potential benefits. Raman and fluorescence both provide additional information about the chemical makeup of the sample under investigation, and when combined with hyperspectral beam attenuation a more comprehensive picture of the water chemistry is captured. Historically, multiple fluorometers have been needed to measure different fluorophores (e.g., chlorophyll *a*, chlorophyll *b*, phycocyanin, oil) where each fluorometer is tailored to a specific excitation/emission wavelength pair to match the fluorophore of interest. The Hyper-c, however, could measure multiple fluorophores by scanning through different excitation wavelengths and capturing a full fluorescence spectrum at each excitation wavelength. Additionally, independently measuring hyperspectral attenuation and fluorescence can aid in the deconvolution of overlapping spectral features, such as the overlapping absorption and fluorescence peaks of chlorophyll *a* between 600-700 nm, that may exist in samples with complex chemistries. Finally, Raman measurements can be used as an in-field quantitative calibration, including for fluorescence (Lawaetz et al., 2009). Combined, the co-benefits of inelastic scattering measurements made by the Hyper-c stand to expand its capabilities while simultaneously increasing the accuracy of the attenuation measurements.

Conclusion

We developed a hyperspectral transmissometer (Hyper-c) breadboard and demonstrated its ability to measure optical transmission and beam attenuation from ultraviolet to near-infrared wavelengths to meet the needs of next-generation hyperspectral remote sensing missions. We validated the sensor performance by measuring a dilution series of two different samples (antacid and chlorophyl) ranging from high (>100 m^{-1}) to low (<1 m^{-1}) concentrations. We benchmarked these measurements against a commercial spectrophotometer, demonstrating qualitatively good agreement between (1) the spectral shape of the attenuation profile (Hyper-c) and absorbance profile (spectrophotometer) and (2) the relative changes in signal across different sample concentrations between the two instruments. Additionally, we demonstrated inelastic scattering

measurements with the Hyper-c breadboard, performing both Raman and fluorescence measurements with minor modifications to the optical configuration of the sensor. Combining hyperspectral beam attenuation measurements with complementary Raman and fluorescence stands to make the Hyper-c a novel sensor with broad applicability to optical oceanography, biogeochemistry, environmental monitoring, and other areas of research in aquatic sciences. We are continuing to develop the Hyper-c with the goal of commercializing the sensor in 2027/2028.

Acknowledgements

This work was funded by the National Aeronautics and Space Administration (NASA) Small Business Innovation Research (SBIR) program under award 80NSSC24PB439. The views and opinions of the authors expressed here do not necessarily state or reflect those of the US government or any agency thereof.

References

Dierssen, H. M., Gierach, M., Guild, L. S., Mannino, A., Salisbury, J., Uz, S. S., Scott, J., Townsend, P. A., Turpie, K., Tzortziou, M., Urquhart, E., Vandermeulen, R. & Werdell, P. J. (2023). Synergies Between NASA's Hyperspectral Aquatic Missions PACE, GLIMR, and SBG: Opportunities for New Science and Applications. *Journal of Geophysical Research: Biogeosciences, 128(10)*. https://doi.org/10.1029/2023jg007574

IOCCG Protocol Series (2018). Inherent Optical Property Measurements and Protocols: Absorption Coefficient, Neeley, A. R. and Mannino, A. (eds.), IOCCG Ocean Optics and Biogeochemistry Protocols for Satellite Ocean Colour Sensor Validation, Volume 1.0, IOCCG, Dartmouth, NS, Canada. http://dx.doi.org/10.25607/OBP-119

IOCCG Protocol Series (2019). Beam Transmission and Attenuation Coefficients: Instruments, Characterization, Field Measurements and Data Analysis Protocols. Boss, E., Twardowski, M., McKee, D., Cetinić, I. and Slade, W. IOCCG Ocean Optics and Biogeochemistry Protocols for Satellite Ocean Colour Sensor Validation, Volume 2.0, edited by A. Neeley and I. Cetinić, IOCCG, Dartmouth, NS, Canada. http://dx.doi.org/10.25607/OBP-458

Lawaetz, A. J. & Stedmon, C. A. (2009). Fluorescence Intensity Calibration Using the Raman Scatter Peak of Water. *Applied Spectroscopy, 63(8)*, 936–940. https://doi.org/10.1366/000370209788964548

Pegau, S., Zaneveld, J.R.V., & Mueller, J.L. (2003). Inherent Optical Property Measurement Concepts: Physical Principles and Instruments, in *Ocean Optics Protocols for Satellite Ocean Color Sensor Validation, Revision 4, Volume IV: Inherent Optical Properties: Instruments, Characterizations, Field Measurements and Data Analysis Protocols*, NASA/TM-2003-211621/Rev4-Vol. IV, edited by J.L. Mueller, G.S. Fargion, and C.R. McClain, pp. 1-14, NASA Goddard Space Flight Center, Greenbelt, Maryland.

Werdell, P. J., McKinna, L. I. W., Boss, E., Ackleson, S. G., Craig, S. E., Gregg, W. W., Lee, Z., Maritorena, S., Roesler, C. S., Rousseaux, C. S., Stramski, D., Sullivan, J. M., Twardowski, M. S., Tzortziou, M. & Zhang, X. (2018). An overview of approaches and challenges for retrieving marine inherent optical properties from ocean color remote sensing. *Progress in Oceanography, 160*, 186–212. https://doi.org/10.1016/j.pocean.2018.01.001

Particle measurements two ways with Origin 600

Tom Comerford , Matt Saunders , Eleanor Stanton , Tom Culverhouse

Sonardyne International

Particle measurements two ways with Origin 600

Tom Comerford [a], Matt Saunders [a], Eleanor Stanton [a], Tom Culverhouse [a]

[a] Sonardyne International,
Corresponding author: Tom Comerford, thomas.comerford@sonardyne.com

Introduction

Two recently added features of Sonardyne's Origin 600 ADCP have enabled enhanced particle measurements. Firstly, the ability to connect multiple external sensors to the ADCP allows sensor data to be live-processed in the Edge environment, and output via the Origin 600's integrated acoustic modem. This was demonstrated *in situ* using a Sequoia LISST-200X particle size analyser (among other sensors), with the live results hosted on a remotely accessible server. Secondly, the Origin 600's echosounder mode allows for acoustic characterization of individual scatterers while also providing current measurements, by interleaving narrowband echosounder pings with broadband ADCP pings. In both cases, using the Origin 600 for gathering particle measurements enables direct comparison with ADCP data products, such as mean current speed and wave measurements, which can be calculated *in situ* using the Edge computing environment. In this work, we describe both methods, using data from trial deployments.

External sensor integration

To demonstrate external sensor connectivity, an Origin 600 was deployed in a seabed lander which also contained a Sequoia LISST-200X particle size analyser, a CONTROS HydroC CO_2 sensor, and a Seabird HydroCAT-EP V2 CTD. The sensors were connected to the ADCP via an Origin E-Mux, which passes the serial output of each sensor into the Edge computing environment on the ADCP. The frame was deployed in Mayflower Marina, in Plymouth, UK, at a depth of approximately 30 metres. A schematic of the deployment is shown in Figure 1.

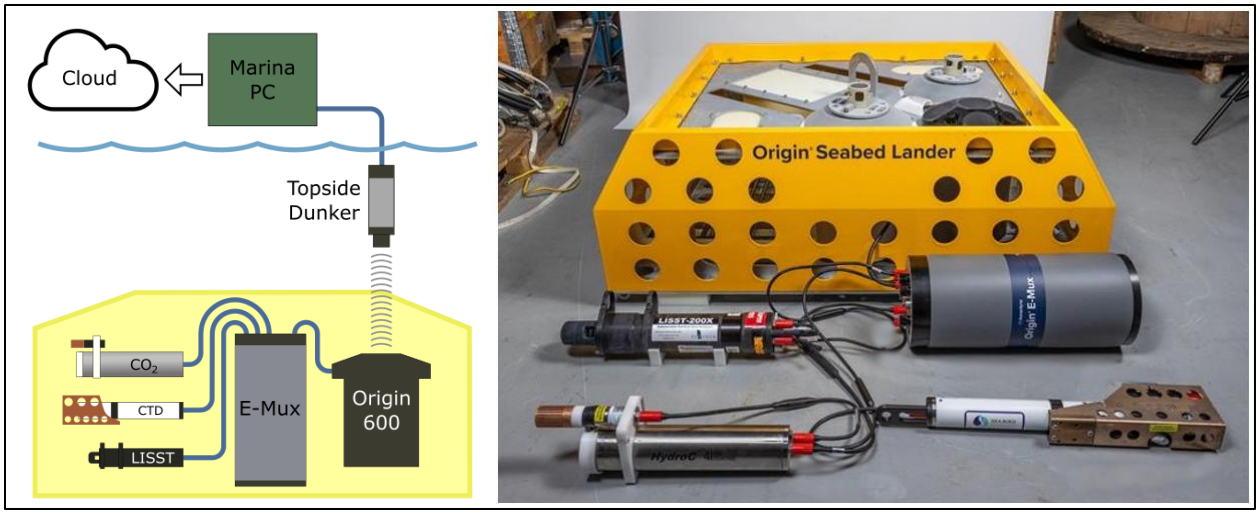

Figure 1. Schematic and photo of sensors, E-Mux, ADCP, and seabed lander.

The Edge environment enables processing of ADCP data in real time, via the use of user-specified applications, loaded onto the instrument as part of its configuration. For this demonstration, the app produced a measurement of the mean current speed and bearing using the ADCP data, in addition to reporting average CO_2 partial pressure, conductivity, depth, and the mean and standard deviation of particle size from the three external sensors. Results were output as a NMEA-format string, which was transmitted by the integrated modem every 5 minutes. These messages were received by a topside acoustic modem, which output the strings to a connected computer with network access. A remotely accessible cloud-based web frontend extracted values from the NMEA strings and displayed live plots of timeseries for each output parameter. An example is shown in Figure 2 below, where the display is configured to show the mean current speed (as measured by the Origin 600) and particle size (as measured by the LISST-200X).

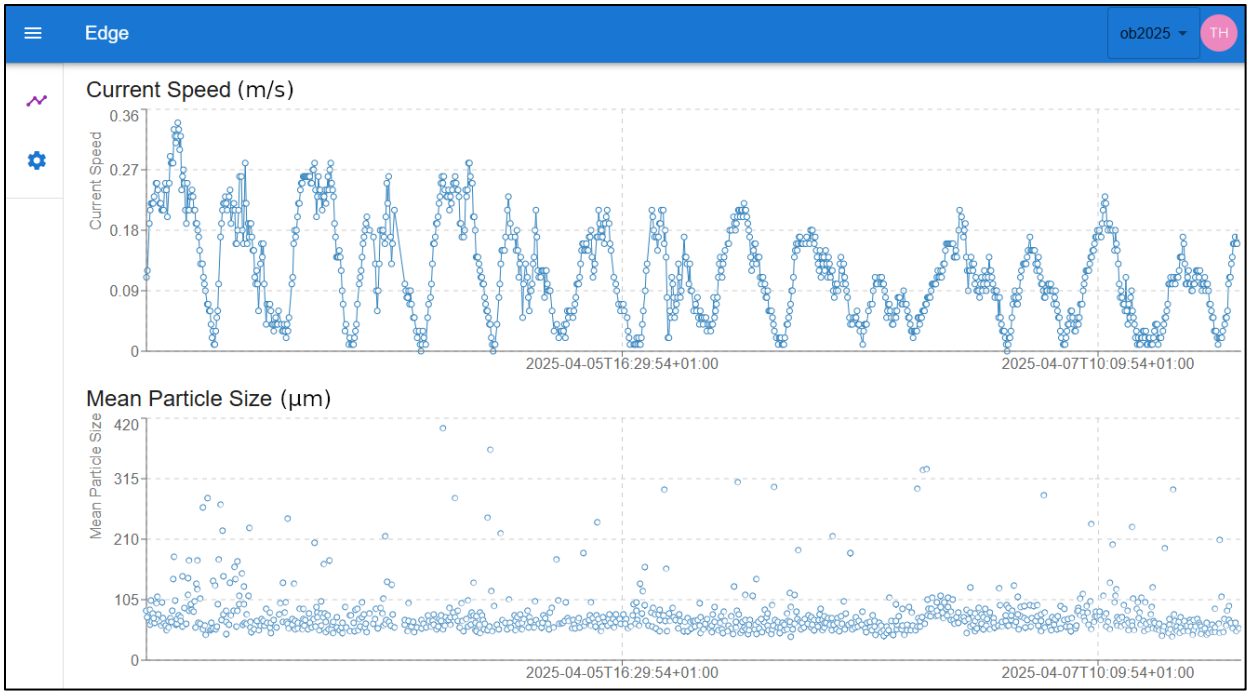

Figure 2: Screenshot from data portal, showing timeseries of current speed measured by the ADCP (top) and mean particle size measured by the LISST-200X (bottom).

This deployment demonstrates how the Origin 600 and Edge can serve as a system for *in situ* data fusion and live monitoring of multiple sensors.

Echosounder mode

In order to measure water velocities, ADCPs typically emit acoustic pulses with durations around 1 millisecond, and covering a range of frequencies. When in echosounder mode, the Origin 600 emits pulses at its carrier frequency (625 kHz), and with a duration that can be configured by the operator. The measured acoustic backscatter from these pulses produces profiles of backscatter intensity with much higher spatial resolution than the ADCP pings.

In the data presented below, a pulse length of 50 µs is used, corresponding to a spatial length of approximately 7.5 cm. The results are recorded in Sonardyne's B-gram format, which records data in 5000 bins, each with a width of 1.2 cm. Echosounder measurements are recorded on a linear scale, which can be converted to volume backscatter strength results (in dB re. 1 m^2/m^3), with reference to a calibration using a tungsten carbide sphere (Turner-Dockery et al., in prep.).

The data presented below was gathered at a seaweed aquaculture facility near Hitra, Norway, where the ADCP was deployed in a seabed lander at approximately 25 metres depth, and gathered data with 2 Hz interleaved ADCP and echosounder pings (i.e. 4 Hz combined). This deployment was part of the BEDLAM project to evaluate the use of Origin echosounder data at

two aquaculture sites, in collaboration with SINTEF Ocean, and funded by the AquaExcel3.0 transnational access program.

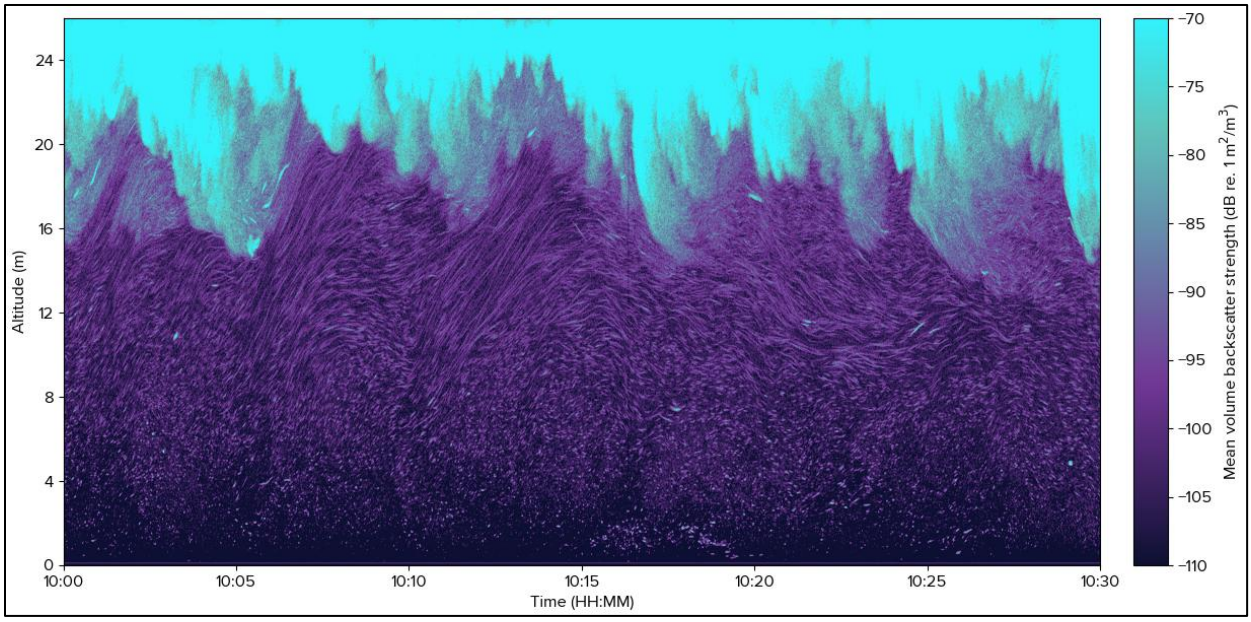

Figure 3: Heatmap of mean volume backscatter strength measured by the O600's vertical beam over a 30-minute period.

Figure 3 above shows a heatmap of the mean volume backscatter strength from the vertical echosounder beam, over a 30-minute period containing the largest waves of the deployment. The top edge of the plot is dominated by backscatter from the surface and entrained air from the waves. At lower altitudes, we see long-period bulk movement of suspended particles tracing internal wave motion. The effect of waves upon the scattering environment can be shown by comparing with data from a relatively quiescent period, as done in Figure 4 and Figure 5 below.

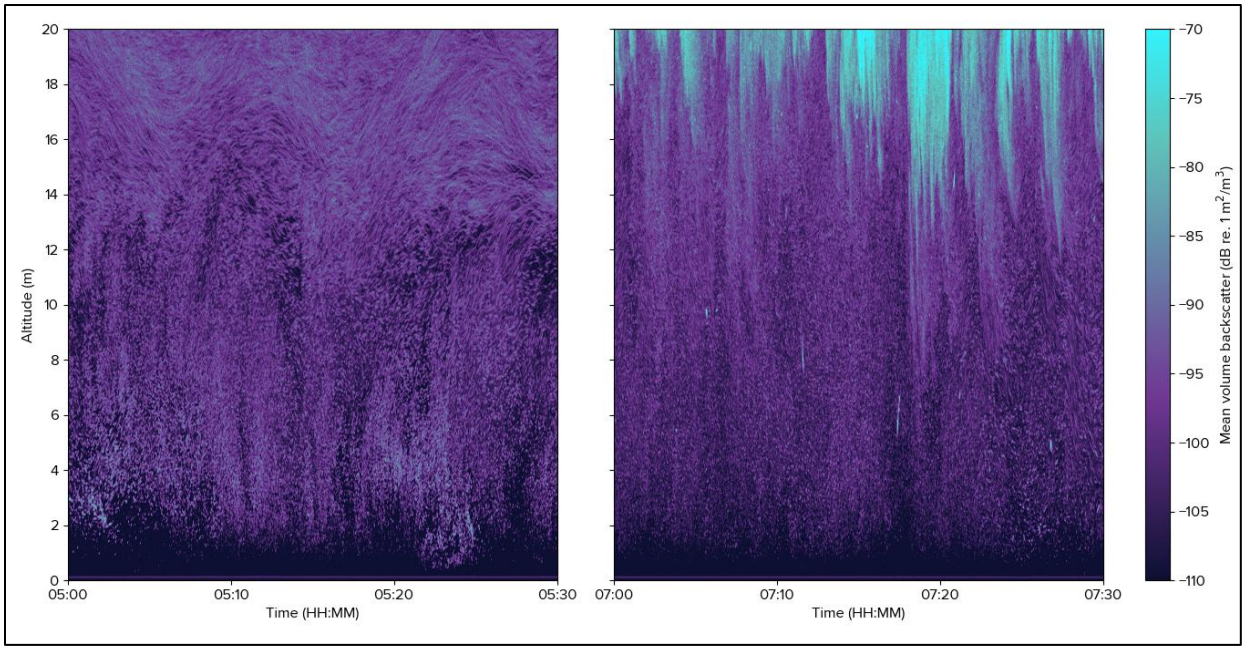

Figure 4: Heatmaps of mean volume backscatter strength for two different time periods, each lasting 30 minutes. Note that the water surface is excluded from this altitude range. In the left-hand plot, the maximum recorded wave height was 0.09 m; in the right, it was 0.80 m.

Figure 4 shows mean volume backscatter data for two 30-minute periods, two hours apart. In the intervening period, the maximum recoded wave height increased from 0.09 to 0.80 cm, as derived from the ADCP results. Despite the lack of surface waves in the left-hand plot, the scatterers at 15-19 m altitude can be seen tracing the motion of long-period internal waves, whereas this region is dominated by the effects of surface waves in the right-hand plot. While the regions below 10 m altitude appear to be little effected by the surface waves, this can be quantified by examining histograms of the backscatter strength, as in Figure 5.

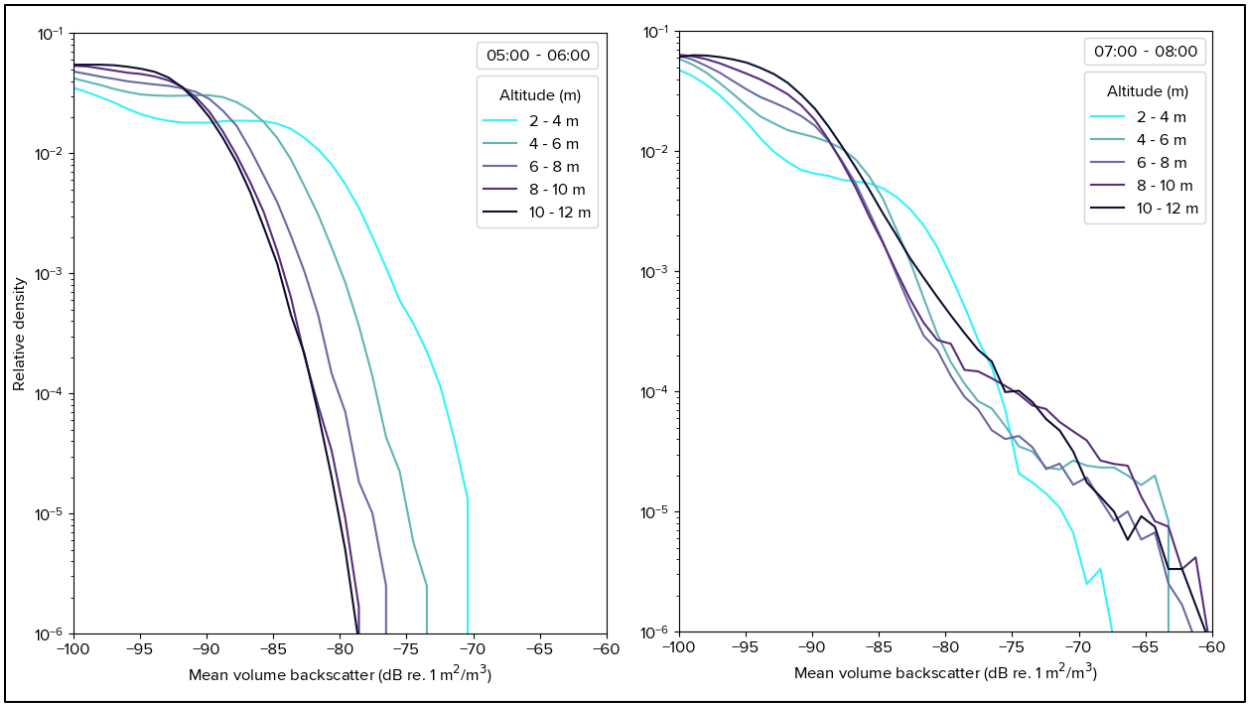

Figure 5: Histograms of mean volume backscatter strength for the same times shown in Figure 4. Each line corresponds to a different 2-metre altitude bin.

In Figure 5 above, the mean volume backscatter data was split into five 2-metre depth bins between 2 and 12 metres altitude. The left- and right-hand plots match to the time periods of the corresponding plots in Figure 4. We can see that the increase in wave activity is correlated with an increase in the density of large scatterers (s_v > -75 dB), even at low altitudes, where there was no apparent effect in the heatmaps, and where the effect of wave motion should be negligible.

Conclusion

In this work we have demonstrated how the Origin 600 can be used to perform measurements of marine particles, by using external sensors or the ADCP's echosounder functionality. In both cases, the particle measurements were combined and compared with the standard ADCP measurements – namely mean current and wave results. While not shown here, it is also possible to combine all of these methods together, using the Edge computing environment to gather external sensor data, echosounder measurements, and process ADCP results simultaneously.

References

Turner-Dockery, C., Williamson, B., Scott, B., & Culverhouse, T. (in prep.). A calibration procedure for Sonardyne's Origin 600 ADCP-Echosounder.

From pixels to patterns: high-throughput image classification and morphometry through a new PI-10 imaging pipeline

Jonas Mortelmans[a], Wout Decrop[a], Hanneloor Heynderickx[a], André Cattrijsse[a], Mark Depaepe[b], Lodewijk Van Walraven[c, d], James Scott[e], Dick van Oevelen[f], Klaas Deneudt[a], Carlota Muñiz[a]

[a] Flanders Marine Institute (VLIZ) InnovOcean Campus, Jacobsenstraat 1, 8400 Ostend, Belgium.

[b] VLOOT dab, Sir Winston Churchillkaai 2, 8400 Oostende, Belgium.

[c] Wageningen University and Research (WUR), Wageningen Marine Research, P.O. Box 57, 1780 AB Den Helder, the Netherlands

[d] Rijkswaterstaat (RWS), Postbus 2232, 3500 GE Utrecht. The Netherlands.

[e] Centre for Environment, Fisheries and Aquaculture Science (CEFAS), Pakefield Road, Lowestoft NR33 0RP, the United Kingdom.

[f] Department of Estuarine and Delta Systems, Royal Netherlands Institute for Sea Research (NIOZ), PO Box 140, 4400 AC, Yerseke, the Netherlands

From pixels to patterns: high-throughput image classification and morphometry through a new PI-10 imaging pipeline

Jonas Mortelmans[a], Wout Decrop[a], Hanneloor Heynderickx[a], André Cattrijsse[a], Mark Depaepe[b], Lodewijk Van Walraven[c, d], James Scott[e], Dick van Oevelen[f], Klaas Deneudt[a], Carlota Muñiz[a]

[a] Flanders Marine Institute (VLIZ) InnovOcean Campus, Jacobsenstraat 1, 8400 Ostend, Belgium.
[b] VLOOT dab, Sir Winston Churchillkaai 2, 8400 Oostende, Belgium.
[c] Wageningen University and Research (WUR), Wageningen Marine Research, P.O. Box 57, 1780 AB Den Helder, the Netherlands
[d] Rijkswaterstaat (RWS), Postbus 2232, 3500 GE Utrecht. The Netherlands.
[e] Centre for Environment, Fisheries and Aquaculture Science (CEFAS), Pakefield Road, Lowestoft NR33 0RP, the United Kingdom.
[f] Department of Estuarine and Delta Systems, Royal Netherlands Institute for Sea Research (NIOZ), PO Box 140, 4400 AC, Yerseke, the Netherlands

Corresponding author: Jonas Mortelmans; jonas.mortelmans@vliz.be

Introduction

Plankton are ubiquitous and their importance to marine food webs are thoroughly documented. Many plankters are especially vulnerable to climate-driven changes: their phenology, range, and body size change with climate having consequences for the biological carbon pump and higher trophic interactions. Plankton size structure, from individual body length to community-level size spectra, affects trophic efficiency and predator-prey dynamics. Finally, being a chain in the marine food web, plankters are essential for ocean's health and resilience.

The Belgian part of the North Sea (BPNS), a small but dynamic marine coastal area, is hosting a rich planktonic community shaped by strong seasonal cycles, riverine inputs, eutrophication, and climate variability. Historically, plankton monitoring in the BPNS has relied on net sampling and manual microscopy, labour-intensive methods, relatively limited in resolution and prone to observer bias. Recent decades have seen a rapid shift in marine observation capabilities, particularly through the development of automated, high-resolution imaging technologies able to yield size and biomass estimations. A particularly interesting new and emerging technology is the Plankton Imager 10 (Pi-10, developed by the Centre for Environment Fisheries and Aquaculture Science (CEFAS) and Plankton Analytics), a line-scan imaging system. The Pi-10 is a standalone, automated imaging instrument designed for continuous, in situ monitoring of plankton and particles in a flow-through system processing around 1m³ per 29 minutes.

In this study, we present a modular and reproducible workflow for processing images acquired with the PI-10. The pipeline integrates convolutional neural network (CNN)-based classification, morphological feature extraction, and standardized data publication via Darwin Core Archives. Special attention is given to the extraction of size-related metrics such as equivalent spherical diameter, eccentricity, and major/minor axis lengths, allowing trait-based ecological interpretation. Its high-frequency, high-volume data collection makes it an ideal tool for studying fine-scale ecological processes and for contributing to the development of digital ocean twins.

Methods

The Pi-10 (fig. 1) captures high-resolution images of particles as they pass through a flow cell. A downward-facing line-scan camera records up to 70,000 lines per second with 2048 × 10 µm resolution. These lines are concatenated based on the water flow and yields regions of interest (ROIs). Images are transmitted via fiber optic cable to the onboard Pi-PC for real-time processing and storage. The system can detect up to 100,000 regions of interest (ROIs) per minute based on a user dependant size cutoff level (for zooplankton ecology, typically set at a threshold of 200µm; but can be as low as 20µm). The PI-10 is mounted within a temperature- and humidity-controlled metal frame and part of the ships' underway data acquisition system, easily linked to metadata/data streams. On RV Simon Stevin, water intake is at 0.6 m depth—ideal for surface monitoring.

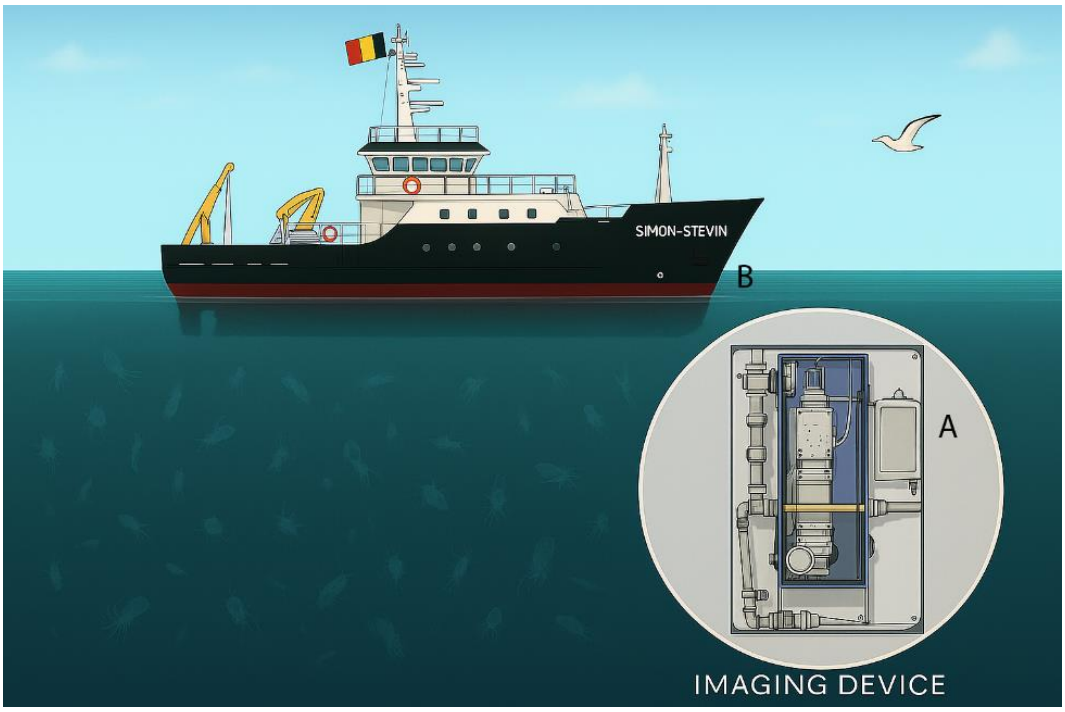

Fig. 1. Illustration of the RV Simon Stevin (B) and PI-10 sensor (A)

Results

Data was collected during 9 cruises between March 2025 and July 2025 aboard the RV Simon Stevin in the southern North Sea (Fig. 2) and yielded 1.2 billion images of which 60 million are saved and 1 million are validated manually for testing and model accuracy estimates (example seen in Fig. 3).

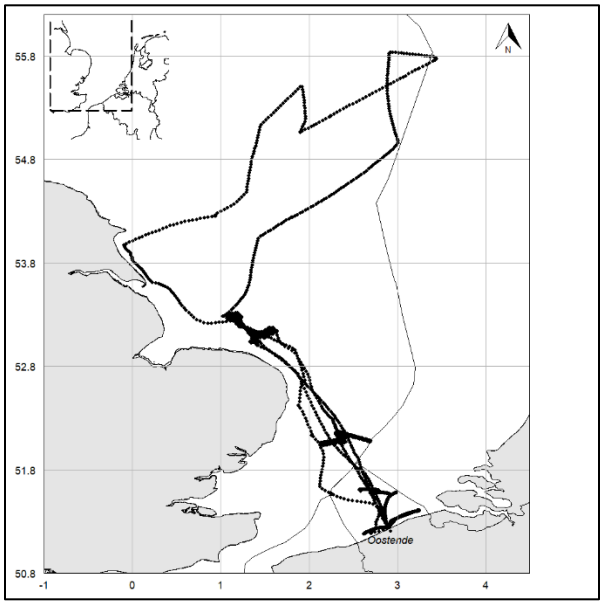

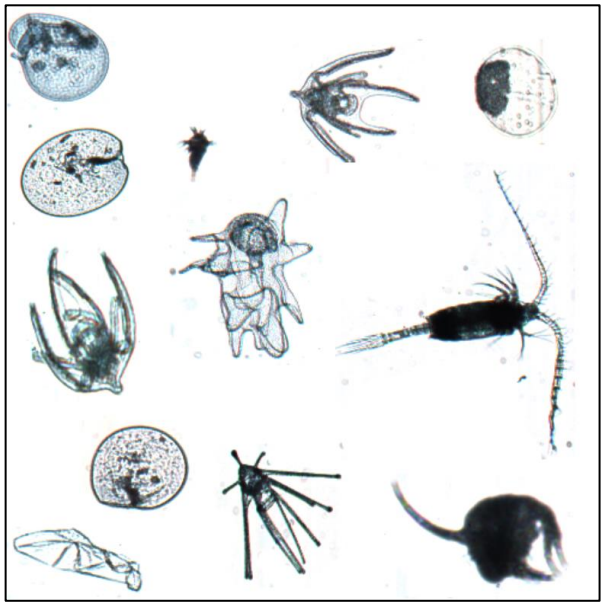

Fig 2. Transects on which the PI-10 was deployed. Fig 3. Representation of most common taxa visualised by the PI-10

The here published PI-10 image processing pipeline integrates a modular script designed to handle data ingestion, classification, validation, and standardised output, with all code openly published (Mortelmans et al., 2025). Upon acquisition, raw .tar archives are securely stored on a VLIZ server. The pipeline begins with a preview stage in which 200 randomly selected .tif images are classified. Archives containing >30% predicted "bubbles" are flagged as low quality and excluded, saving processing time by leveraging the model's high precision for this class. In total, ten output types are subsequently generated, including: (1)_background, containing the background image of a .tar file, essential for quick assessment of the metadata; (2) _gpstag, containing a timestamp and GPS coordinates for each ROI in the .tar; (3) _hitsmisses, to keep track of the fraction imaged; it counts the amount of hits and misses, in each minute of the .tar file; (4) _image_properties; an extension to store all metrics on a certain ROI (e.g., eccentricity, ESD, major, minor, ...); (6) _predictions_relative, a file containing the result of the CNN-algorithm; (7) _topspecies, an extension to _predictions_relative, to store the best fitting class to each ROI, according to a user defined threshold; (8) _validated, the result of a validations; (9) _merged, combined the different outputs; (10) _dwca, compiles the validated dataset into a

Darwin Core Archive (DwC-A), structured for interoperability with biodiversity data platforms such as EurOBIS. The DwC-A contains an Event Core (sampling metadata), Occurrence Core (species records linked to WoRMS taxonomy), and an eMoF extension for environmental parameters like temperature and salinity; but also include total estimated biomass. Final archives are published in the Marine Data Archive (MDA) with a DOI, ensuring traceability and open access. All datasets are discoverable through IMIS, VLIZ's ISO-19115-compliant metadata catalogue.

The PI-10 zooplankton image classifier uses a Convolutional Neural Network (CNN) based on the FlowCam phytoplankton model developed in the iMagine project (Decrop *et al.*, 2025), here trained on 350,000 annotated PI-10 images provided by Van Walraven *et al.* (2025). The PI-10 classifier adopts this architecture, reusing the AI platform, OSCAR services, and FAIR metadata standards. The classifier's output performance varies across taxonomic groups (Fig 4, 5). Certain classes, such as *Noctiluca*, bubbles, and straight diatoms, are identified with high accuracy and precision, exhibiting minimal false positives even at low confidence thresholds. In contrast, classes like Appendicularia and Calanoida show high recall but low precision, with frequent misclassification of other taxa into these categories. Finally, several taxa, such as *Phaeocystis*, are poorly resolved by the model (Fig. 4, 5).

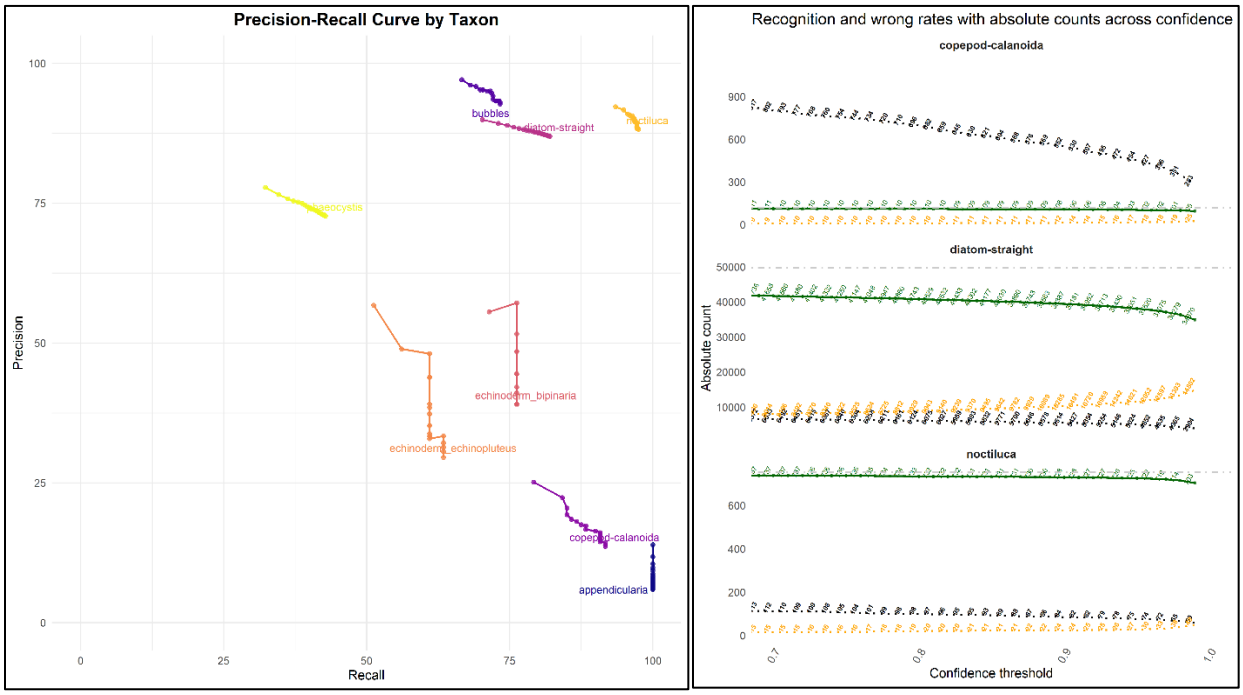

Fig 4. Precision-recall curves for main biological taxa. Fig 5. Recovery rates of correct and false predictions (three taxa only). Green: correctly identified ROIs. Yellow: wrongly identified ROIs. Black: False predictions.

Discussion

A key strength of the PI-10 pipeline lies not only in its taxonomic classification capabilities but also in its integration of standardized size measurements for every detected particle. This goes beyond the focus of many image-based biodiversity tools, which often concentrate solely on species detection. Size and morphological traits offer critical ecological context and play an essential role in functional ecology and ecosystem modeling (e.g., Benedetti et al., 2018). Quantifying size structure is particularly important because it directly reflects community dynamics, which influence trophic interactions, grazing pressure, and biogeochemical fluxes (Hirai et al., 2020; Lombard et al., 2019). Moreover, accurate size data enables biomass estimation and functional trait analyses that link organism size to physiological processes, feeding strategies, and motility patterns. Finally, size-based indicators derived from imaging systems are increasingly used in marine ecosystem monitoring and biodiversity assessments (Benedetti et al., 2021). It is obvious, the size-measurements of in situ particles here provided are essential.

The performance of the CNN classifier across specific taxa is variable. For instance, distinguishing between morphologically similar or irregular taxa remains challenging. This reflects a broader trade-off between automation and expert validation effort; especially seen in the result of the currently published classifiers. For taxa, alike *Noctiluca* or straight diatoms, it can easily be argued to skip human validation entirely (see fig. 4 and 5). The model holds high accuracy and precision, exhibiting minimal false positives even at low confidence thresholds. For other taxa, Appendicularia or Calanoida, are correctly identified even at low confidence thresholds; but hold many false positives. Finally, taxa like *Phaeocystis*, the model has both accuracy and precision low. For these two groups of taxa, manual validation remains essential. Despite automation significantly reducing manual annotation workload (Luo et al., 2018), the risk of misclassification, especially for key ecological indicators, necessitates continued expert validation.

To further advance the PI-10 pipeline, model improvement efforts should focus on integrating temporal context, such as seasonal variability in plankton communities. This could involve seasonal model retraining or transfer learning approaches. Moreover, there is strong potential for linking image-derived traits to ecosystem indicators (e.g., biodiversity indices, bloom risk alerts, or ecosystem health assessments) as highlighted in recent studies (Lombard et al., 2019; Ohman et al., 2019; Irisson et al., 2022). A promising direction involves real-time or in situ deployment, with onboard image classification modules enabling near-instant data feedback for adaptive sampling or early warning systems (Irisson et al., 2022; Pitois et al., 2025). Such technological advances can improve responsiveness in oceanographic research and monitoring, while also

supporting integration with satellite and modeling frameworks (Ohman et al., 2019). The automation of ecological interpretation from plankton images remains an emerging but essential frontier in this field (Lombard et al., 2019).

Conclusion

This work assesses the practicalities and on-board implementation of the Pi-10 on the RV Simon Stevin, exploring its integration with the ship's existing underway system, while generating the first collection of high-resolution PI-10 imagery and annotations for the Belgian part of the North Sea. A fully open-access data processing pipeline and classification framework is presented combining geotagged imaging, deep learning (CNN-based), image-based metrics and a multi-label taxonomic system. This initiative represents a step toward automated, real-time data collection and downstream ecological assessments in coastal systems - with its applicability well beyond the BPNS. By quantifying plankton, and suspended particles as a whole, size at high resolution critical insights into community structure are detected - making size not just a descriptor, but a key ecological indicator of change.

References

Barth, A. J., Pinckney, J. L., Krask, J., Smith, E., & Stone, J. (2025). Storm in a bottle: An experimental investigation of how extreme precipitation impacts phytoplankton communities. *bioRxiv*. https://doi.org/10.1101/2025.05.20.655176

Benedetti, F., Gasparini, S., & Irisson, J.-O. (2018). The seasonal and inter-annual fluctuations of plankton abundance and community structure in the Northwestern Mediterranean Sea. *Progress in Oceanography*, 162, 1–12.

Benedetti, F., Righetti, D., & Irisson, J.-O. (2021). Major restructuring of marine plankton assemblages under global warming. *Nature Communications*, 12, 5229.

Decrop, W., Deneudt, K., Heredia, I., Calatrava Arroyo, A., Lagaisse, R., & Muñiz, C. (in preparation). *Design and implementation of an automated image classification workflow for phytoplankton monitoring*.

Hirai, J., Tsuda, A., & Suzuki, K. (2020). Global gradients in species richness of marine plankton functional groups. *Journal of Plankton Research*, 45(6), 832–845

Irisson, J.-O., Kraft, K., & Velhonoja, O. (2022). Towards operational phytoplankton recognition with automated high-throughput microscopy and machine learning. *Frontiers in Marine Science*, 9, 867695.Lagaisse et al., 2025

Lombard, F., Boss, E., Waite, A. M., Uitz, J., Stemmann, L., Sosik, H. M., et al. (2019). Globally consistent quantitative observations of planktonic ecosystems. Front. Mar. Sci. 6. doi: 10.3389/fmars.2019.00196
Luo, T., Suikkanen, S., & Tamminen, T. (2018). Automated plankton image classification using deep learning. *Frontiers in Marine Science*, 5, 370

Mortelmans, J., Decrop, W., Heynderickx, H., Cattrijsse, A., Depaepe, M., Van Walraven, L., Scott, J., van Oevelen, D., Deneudt, K., & Muñiz, C. (n.d.). *From pixels to patterns: High-throughput image classification and morphometry through a new PI-10 imaging pipeline*.

Ohman, M. D., Davis, R. E., Sherman, J. T., Grindley, K. R., Whitmore, B. M., Nickels, C. F., & Ellen, J. S. (2018). Zooglider: An autonomous vehicle for optical and acoustic sensing of zooplankton. Limnology and Oceanography: Methods, 17(1), 69–86. https://doi.org/10.1002/lom3.10301

Pitois, S.G., Blackwell R.E., Close H., Eftekhari N., Giering, S.L.C, Masoudi M., Payne E., Ribeiro J, Scot, J. (2025). RAPID: real-time automated plankton identification dashboard using Edge AI at sea. Frontiers in Marine Science 11. https://doi.org/10.3389/fmars.2024.1513463

Van Walraven, L., Scott, J., Pitois, S., CEFAS team, Hoekendijk, J., Hovenkamp, P., Jak, R. and van Oevelen, D., 2025. A large (50k+) and FAIR training set for the Plankton Imager (Pi-10) for the Greater North Sea and NW Atlantic, based on a flexible classification protocol.

Design and Implementation of an Automated Image Classification Workflow for Phytoplankton Monitoring

Decrop Wout[a], Rune Lagaisse[b], Mortelmans Jonas[a], Carlota Muñiz[a], Deneudt Klaas[a]

[a]Flanders Marine Institute (VLIZ), InnovOcean site, Jacobsentstraat 1, 8400 Oostende, Belgium
[b]UGent Sint-Pietersnieuwstraat 25, 9000 Gent, Belgium

Design and Implementation of an Automated Image Classification Workflow for Phytoplankton Monitoring

Decrop Wout[a], Rune Lagaisse[b], Mortelmans Jonas[a], Carlota Muñiz[a], Deneudt Klaas[a]

[a]Flanders Marine Institute (VLIZ), InnovOcean site, Jacobsentstraat 1, 8400 Oostende, Belgium
[b]UGent Sint-Pietersnieuwstraat 25, 9000 Gent, Belgium
Corresponding author: Wout Decrop; wout.decrop@vliz.be

Introduction – Phytoplankton plays a pivotal role in both marine and freshwater ecosystems. They provide over 45 percent of the global net primary production, play a pivotal role in the global carbon and nutrient cycles and they fuel entire aquatic foodwebs through their photosynthetic activity (Ducklow et al., 2001; Hays et al., 2005; Pierella Karlusich et al., 2020). Moreover, phytoplankton has the ability to quickly respond to environmental and anthropogenic disturbances through their short generation times. The Water Directive Framework and the Marine Strategy Framework directive recognize phytoplankton as an indicator for monitoring aquatic ecosystem health. (European Commission, 2008) (EEC, 1991). Marine and freshwater plankton represent a highly diverse group of organisms, both taxonomically and morphologically, spanning numerous phyla and tens of thousands of species (Sournia et al., 1991; De Vargas et al., 2015). They are generally small in size, going from less than 1 µm up to 1 mm (Winder & Sommer, 2012). Traditionally, phytoplankton identification has relied on expert taxonomists manually classifying specimens under a microscope. This process is not only time-consuming and resource-intensive but also demands highly skilled specialists to distinguish subtle morphological differences between taxa (Benfield et al., 2007).
To address these issues, researchers are increasingly adopting specially designed high-throughput digital imaging systems. These systems, such as the Video Plankton Recorder (Sournia et al., 1991; Ollevier et al., 2022) and the FlowCam (Sieracki et al., 1998), are employed both in situ and in laboratory settings respectively. These next-generation imaging systems significantly speed up analysis time in the lab by capturing thousands of particles in a matter of minutes. While these systems generate vast volumes of plankton image data, the lack of automated, reliable classification techniques means that manual image classification is still necessary, creating a bottleneck in the processing workflow (Kerr et al., 2020; Sosa-Trejo et al., 2023). Recent studies have turned to automated methods, particularly Convolutional Neural Networks (CNNs) (Krizhevsky et al. 2012), to perform plankton image classification.

Despite the promising advantages of deep learning on phytoplankton images, according to Lumini and Nanni (2019), challenges persist for three main reasons: (i) plankton images are often low-resolution, making classification difficult even for human experts; (ii) the wide range of phylogenetic species in plankton images presents specific challenges for taxonomy; and (iii) class imbalance between datasets and data drift between training and test sets.

In this study, phytoplankton images were captured using FlowCam technology (Fluid Imaging Technologies) and annotated by a human expert. This automated high-throughput device combines the principles of flow cytometry, microscopy, and imaging to generate high-resolution images of particles in liquid samples. As part of the LifeWatch observatory, FlowCam instruments are routinely deployed to monitor microphytoplankton communities in the Belgian Part of the North Sea. This long-term monitoring program yields approximately 300,000 to 400,000 annotated particle images annually, contributing to a continuously expanding archive of quality-controlled biodiversity data. Based on this archive, a curated subset was created for training purposes. The resulting training dataset consists of 95 common taxa from the Belgian Part of the North Sea (BPNS).

In this work, we focus on developing and evaluating a deep learning model for phytoplankton image classification, leveraging high-throughput FlowCam data to address the challenges of automated taxonomic identification and support scalable ecological monitoring. The model was initialized using pre-trained weights from the EfficientNetV2B0 architecture, a member of the EfficientNetV2 family developed by the Google Brain team (Tan and Le, 2021). The model predicts the five most probable classes along with their associated confidence scores. The model reached an accuracy of 86.3% and a top-5 accuracy of 98.8%.

To encourage reproducibility, transparency, and further research, we make the complete image library, the sampled training dataset, and the fully trained classifier openly available. The raw FlowCam image collection, containing phytoplankton observations from the Belgian Part of the North Sea, is accessible via the VLIZ Marine Data Archive Flanders Marine Institute. The annotated subset used for training the model has been published on Zenodo (Decrop et al., 2024), along with the final version of the trained classifier (Decrop and Lagaisse, 2025).

These contributions were developed in the context of the IMAGINE project, which supports open and modular tools for ecological monitoring. The classification pipeline is compatible with the IMAGINE infrastructure and is already available as a module in the IMAGINE Marketplace (https://dashboard.cloud.imagine-ai.eu/marketplace). This framework includes alternative annotation tools that complement or can replace internal systems, providing flexibility for future developments and external use.

Methods

Here, we describe a data acquisition and image processing procedure that includes preprocessing, segmentation, classification, and postprocessing for the accurate identification of 95 classes of phytoplankton using CNNs.

Time series are built as part of the LifeWatch marine observatory in the Belgian Part of the North Sea (BPNS). Several fixed stations are visited regularly using the RV Simon Stevin. A grid of nine coastal stations is sampled on a monthly basis, while eight offshore stations are sampled seasonally. Samples are collected on board using an Apstein net with a 55 µm mesh size and preserved in Lugol's iodine solution. In the laboratory, samples are analyzed using a VS-4 FlowCAM system at 4X magnification, capturing particles in the 55–300 µm size range. Image classification is performed using an automated classifier, followed by manual validation. Since May 2017, this dataset has provided microplankton and phytoplankton data—primarily comprising diatoms, dinoflagellates, and ciliates—for the BPNS. The lab protocol and pipelines are described here Lagaisse (2024); Lagaisse et al. (2025).

Raw FlowCam output data consisting of image collages and a number of .txt files with lab based parameters and measurements are processed via in-house Python data pipeline. The manufacturers VisualSpreadsheet software was used solely for FlowCam operation and data acquisition during the lab run. Raw and binary images are not saved during the FlowCam run; instead, only the image collages created at the end of the run are retained and used for downstream processing and identification. Individual Regions Of Interest (ROIs) are extracted from the image collages based on the coordinates (width and height) from the raw textual data file, using custom Python code. The background of the ROIs remains untouched. These single ROIs are then uploaded to an internal processing database to enable en-masse prediction and subsequent human annotation.

The dataset consists of 95 classes, you can see an overview of the distribution of images training set in Figure 1.

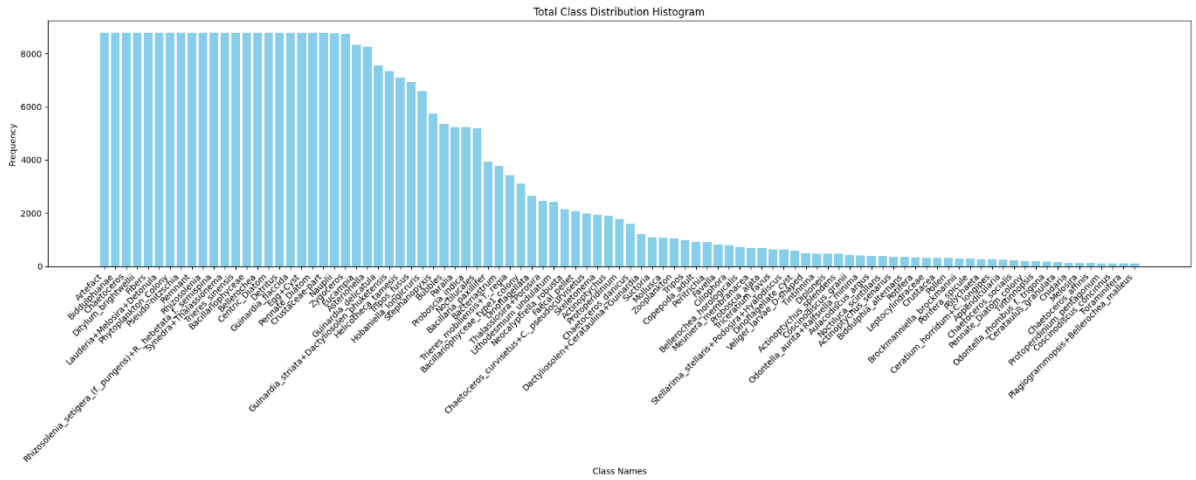

Figure 1. Histogram showing the class distribution across the full phytoplankton dataset.

To balance representation and maintain a realistic distribution, we applied minimum and maximum caps on the number of samples per class, setting the range between 100 and 8800 images. This approach was chosen after several iterations to avoid overfitting on classes with very few samples while preventing dominant classes from overwhelming the model. Through trial and error, this capped distribution provided the best trade-off between model robustness and generalization performance.

The model used for automated image classification is based on EfficientNetV2B0, a deep convolutional neural network known for its use of residual connections to facilitate the training of very deep architectures. EfficientNetV2B0 is part of the EfficientNetV2 family developed by the Google Brain team (Tan and Le, 2021).

Once trained, the classifier produces a ranked list of the top five predicted phytoplankton species for each input image, along with associated confidence scores. These scores represent the model's certainty in each prediction, calculated as softmax probabilities from the final classification layer. Presenting the top five predictions enables users to evaluate multiple plausible labels, which is especially important in ecological datasets where visual similarities between species can introduce ambiguity. The confidence scores also allow users to assess the reliability of each prediction and guide decisions for further expert verification or automated downstream analysis.

Results

The model achieved a Top-1 accuracy of 86.34%, meaning that the correct class was the model's most confident prediction in the vast majority of cases. The Top-5 accuracy increased substantially to 98.76%, suggesting that for almost all samples, the correct label was among the five most probable predictions. This highlights the model's reliability, particularly in scenarios where ranking the most likely classes is sufficient.

Table 1. Grouped classification performance metrics across different Top-K values (percentages)

Group	Metric	Top-1	Top-2	Top-3	Top-4	Top-5
Accuracy	Accuracy	86.34	94.59	97.12	98.19	98.76
Precision	Weighted Precision	86.24	94.61	97.13	98.20	98.77
	Micro Precision	86.34	94.59	97.12	98.19	98.76
	Macro Precision	81.08	92.91	95.93	97.44	98.18
Recall	Weighted Recall	86.34	94.59	97.12	98.19	98.76
	Micro Recall	86.34	94.59	97.12	98.19	98.76
	Macro Recall	77.62	89.39	93.55	95.44	96.64
F1 Score	Weighted F1	86.25	94.57	97.11	98.19	98.76
	Micro F1	86.34	94.59	97.12	98.19	98.76
	Macro F1	78.76	90.84	94.56	96.32	97.35

Table 1 provides a comprehensive overview of the Top-K classification metrics, including accuracy, precision, recall, and F1-score, using micro, macro, and weighted averaging strategies.

• Micro-averaged metrics aggregate contributions from all classes and are generally more influenced by performance on frequent classes. These scores were high across all metrics, with Top-1 micro precision, recall, and F1-score all reaching 86.34%.

• Macro-averaged metrics compute unweighted means across all classes and are more sensitive to class imbalance. At Top-1, macro precision was 81.08%, macro recall was 86.34%, and macro F1-score was 78.76%, indicating solid generalization to both frequent and infrequent classes.

• Weighted metrics fall between the two, accounting for label imbalance while preserving per-class performance. For Top-1 predictions, weighted precision, recall, and F1-score were 86.24%, 86.34%, and 86.34%, respectively—closely tracking the micro scores and indicating balanced overall performance.

As expected, all evaluation metrics improved as the number of considered top predictions (K) increased. For instance, the Top-3 weighted F1-score was 97.12 %, and the Top-5 weighted F1-score rose to 98.76%. These results confirm that the model often assigns high probabilities to the correct class, even when it is not ranked first.

As shown in Figure 2, increasing the probability threshold results in a higher proportion of correct predictions, while also reducing the total number of predictions made.

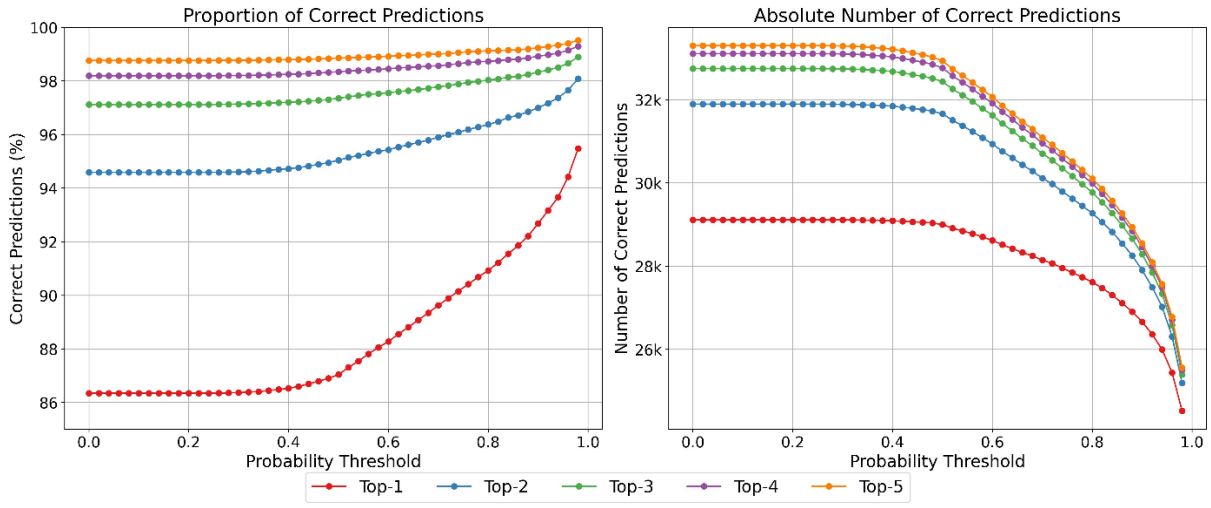

Figure 2. Progression of correct predictions across increasing probability thresholds. Left: Proportion of correct predictions. Right: Absolute number of correct predictions. Each curve corresponds to a different Top-k setting.

Discussion

These results indicate that the model is highly reliable in predicting the correct class within its top few guesses and performs especially well when broader prediction tolerance is allowed. The alignment between micro and weighted scores reflects the model's robustness across the full dataset. The slightly lower macro scores suggest variability in performance among classes, especially those with fewer samples.

The balance between precision and recall, as indicated by the F1 scores, confirms that the model maintains a good trade-off between identifying the correct classes and avoiding false positives. This supports the model's suitability for practical applications, particularly in scenarios where identifying the top few likely classes is sufficient.

Figure 2 illustrates a key trade-off: increasing the probability threshold improves prediction certainty but reduces the number of samples considered. Including more candidate predictions (e.g., Top-2 or Top-3) improves the correct prediction rate while discarding fewer data points. This highlights a practical tuning parameter depending on the intended application—favoring either higher confidence or broader coverage.

This pattern reflects the challenge of class imbalance and taxonomic complexity in plankton image classification and suggests that model improvements—either through data augmentation, hierarchical classification, or targeted data collection—may be beneficial for rare or difficult taxa.

The strong performance at Top-3 and Top-5 levels aligns well with practical workflows in marine ecology, where model predictions can serve as decision support for expert taxonomists. Presenting multiple likely taxa can accelerate annotation while retaining human oversight.
A crucial aspect of this work is the open and free access provided to the entire image library, the annotated training dataset, and the fully trained classifier model. Making these resources publicly available supports reproducibility, transparency, and further research. This accessibility enables other researchers to benchmark and improve upon the classification models, fostering collaboration and accelerating advances in plankton image analysis.
Furthermore, the integration of the classifier and datasets within the Imagine infrastructure enhances the accessibility and usability of these tools. The Imagine platform offers a modular marketplace where the classifier module is available alongside complementary tools, including annotation software that can serve as an alternative to internal systems. This feature is particularly important to address reviewer concerns and to promote standardized, scalable workflows in plankton image annotation and classification.

Conclusion

Improved automated classification of phytoplankton images has significant ecological implications. By accelerating the processing of microscopy data, such models enable more timely detection of plankton blooms, biodiversity shifts, and other critical ecological changes in response to environmental stressors such as climate change, eutrophication, or pollution events. The classifier's strong performance, particularly at Top-3 and Top-5 prediction levels, demonstrates its potential as a valuable tool in operational monitoring pipelines. Rather than replacing expert taxonomists, it offers a means of prioritizing and guiding expert validation, increasing throughput without sacrificing scientific rigor.
Moreover, the public availability of the image dataset, model weights, and source code fosters transparency and reproducibility, enabling researchers worldwide to replicate, validate, and build upon this work. The model only needs a labeled training set to start retraining models, which can be created through many different labeling methods. The integration within the Imagine infrastructure further supports the development of modular, standardized workflows for large-scale marine image annotation and analysis. Looking forward, future research could address remaining challenges such as class imbalance, inter-class similarity, and domain adaptation to microscopy variations.
Altogether, this work represents a significant step toward scalable, accessible, and high-performance plankton image analysis, opening new possibilities for long-term ecological monitoring and global marine biodiversity research.

References

Benfield, M. C., Grosjean, P., Culverhouse, P. F., Irigoien, X., Sieracki, M. E., Lopez-Urrutia, A., et al. (2007). Rapid: research on automated plankton identification. Oceanography 20, 172–187

De Vargas, C., Audic, S., Henry, N., Decelle, J., Mah ´e, F., Logares, R., et al. (2015). Eukaryotic plankton diversity in the sunlit ocean. Science 348, 1261605

[Dataset] Decrop, W. and Lagaisse, R. (2025). Pre-trained phytoplankton species classifier model. doi:10.5281/zenodo.15269453

[Dataset] Decrop, W., Lagaisse, R., Jonas, M., Muyle, J., Amadei Mart´ınez, L., and Deneudt, K. (2024). Lifewatch observatory data: phytoplankton annotated trainingset by flowcam imaging in the belgian part of the north sea (version v1). doi:10.5281/zenodo.10554845

Ducklow, H. W., Steinberg, D. K., and Buesseler, K. O. (2001). Upper ocean carbon export and the biological pump. Oceanography 14, 50–58

[Dataset] Flanders Marine Institute (VLIZ) (2024). Lifewatch observatory data: phytoplankton observations by flowcam imaging in the belgian part of the north sea. doi:10.14284/650

Hays, G. C., Richardson, A. J., and Robinson, C. (2005). Climate change and marine plankton. Trends in ecology & evolution 20, 337–344

Kerr, T., Clark, J. R., Fileman, E. S., Widdicombe, C. E., and Pugeault, N. (2020). Collaborative deep learning models to handle class imbalance in flowcam plankton imagery. Ieee Access 8, 170013–170032

Krizhevsky, A., Sutskever, I., and Hinton, G. E. (2012). Imagenet classification with deep convolutional neural networks. Advances in neural information processing systems 25

[Dataset] Lagaisse, R. (2024). Lifewatch belgium: Flowcam sampling and lab protocol for imaging microphytoplankton in the belgian part of the north sea. https://www.protocols.io/view/lifewatch-belgium-flowcam-sampling-and-lab-protoco-6qpvr8e6zlmk/v1. Flanders Marine Institute, DOI: 10.17504/protocols.io.6qpvr8e6zlmk/v1

Lagaisse, R., Dillen, N., Bakeev, D., Decrop, W., Focke, P., Mortelmans, J., et al. (2025). Advancing long-term phytoplankton biodiversity assessment in the north sea using an imaging approach. Manuscript submitted for review to *Scientific Data*, Manuscript #SDATA-25-02770

Lumini, A. and Nanni, L. (2019). Deep learning and transfer learning features for plankton classification. Ecological informatics 51, 33–43

Ollevier, A., Mortelmans, J., Vandegehuchte, M. B., Develter, R., De Troch, M., and Deneudt, K. (2022). A video plankton recorder user guide: Lessons learned from in situ plankton imaging in shallow and turbid coastal waters in the belgian part of the north sea. Journal of Sea Research 188, 102257

Pierella Karlusich, J. J., Ibarbalz, F. M., and Bowler, C. (2020). Phytoplankton in the tara ocean. Annual Review of Marine Science 12, 233–265

Sieracki, C. K., Sieracki, M. E., and Yentsch, C. S. (1998). An imaging-in-flow system for automated analysis of marine microplankton. Marine Ecology Progress Series 168, 285–296

Sosa-Trejo, D., Bandera, A., Gonz ´alez, M., and Hern ´andez-Le ´on, S. (2023). Vision-based techniques for automatic marine plankton classification. Artificial Intelligence Review 56, 12853–12884

Sournia, A., Chrdtiennot-Dinet, M.-J., and Ricard, M. (1991). Marine phytoplankton: how many species in the world ocean? Journal of Plankton Research 13, 1093–1099

Tan, M. and Le, Q. (2021). Efficientnetv2: Smaller models and faster training. In International conference on machine learning (PMLR), 10096–10106

Advancing Coastal Ecosystem Monitoring: A Multi-Sensor Approach for Near Real-Time Biogeochemical Mapping at High Temporal and Spatial Resolution

Clémence Goyens[a], Alexandre Castagna[a], Qiming Sun[a], Rafael Rasse[a], Eva Scrivner[b], Heidi Dierssen[b], Nils Haëntjes[c], Hannelore Theetaert[d], Silke Verbrugge[d], Thanos Gkritzalis[d] & Griet Neukermans[a,d].

[a] Ghent University, MarSens Research Group, Campus De Sterre, Krijgslaan 281/S8, B-9000 Ghent, Belgium
[b] University of Connecticut, Department of Marine Sciences, 1080 Shennecossett Road, Groton, CT 06340, USA
[c] University of Maine, School of Marine Sciences, 5706 Aubert Hall, Orono, USA
[d] VLIZ (Flanders Marine Institute), InnovOcean Campus, Jacobsenstraat 1, 8400 Oostende, Belgium

Towards 3D turbidity by correlating multibeam sonar and in-situ sensor data: the TURBEAMS approach.

Thomas Vandorpe[a], Nore Praet[a], Peter Urban[b], Benjamin Van Roozendael[c], Marc Roche[d], Koen Degrendele[d], Thomas Hermans[b]

[a] **Flanders Marine Institute (VLIZ), Jacobsenstraat 1, 8400 Oostende, Belgium**
[b] **Ghent University, Department of Geology, Krijgslaan 281 S8, 9000 Gent, Belgium**
[c] **Royal Belgian Institute of Natural Sciences (RBINS), Rue Vautier 29, 1000 Brussel, Belgium**
[d] **FPS Economy - Continental Shelf Service, Bd Roi Albert II, 1000 Brussels, Belgium**

Towards 3D turbidity by correlating multibeam sonar and in-situ sensor data: the TURBEAMS approach.

Thomas Vandorpe[a], Nore Praet[a], Peter Urban[b], Benjamin Van Roozendael[c], Marc Roche[d], Koen Degrendele[d], Thomas Hermans[b]

[a]Flanders Marine Institute (VLIZ), Jacobsenstraat 1, 8400 Oostende, Belgium
[b]Ghent University, Department of Geology, Krijgslaan 281 S8, 9000 Gent, Belgium
[c]Royal Belgian Institute of Natural Sciences (RBINS), Rue Vautier 29, 1000 Brussel, Belgium
[d]FPS Economy - Continental Shelf Service, Bd Roi Albert II, 1000 Brussels, Belgium

Corresponding author: Thomas Vandorpe; thomas.vandorpe@vliz.be

Introduction

Turbidity (or the cloudiness of water) is related to the concentration and type of suspended particles in the water column. These particles may be either of planktonic (both zoo- and phytoplankton) or sedimentological origin (resuspension of surface-bound sediments). Combined they form a cloud of suspended particulate matter (SPM) which affects light penetration in coastal waters.

SPM is regularly monitored in the BPNS using a large suite of instruments. Ocean color satellite imagery is typically used to determine SPM concentrations over vast areas, but is restricted to the surface layer of the water column (Eleveld et al., 2008, Dogliotti et al., 2015). Within the water column, turbidity and SPM have been monitored either in 1D (moorings, ship-based samples, tripods on the seafloor, …) or in 2D (Acoustic Doppler Current Profiler, ADCP, transects)(Fettweis and Lee, 2017, Van Lancker and Baeye, 2015). SPM variability in coastal environments is highly dynamic and forms complex pattern (Fettweis et al., 2014) that are best captured by comprehensive 3D measurements.

A possible solution lies in multibeam sonars which, next to seafloor bathymetry data, are able to deliver a 3D dataset of backscatter values in the water column (Simmons et al., 2017, Fromant et al., 2021, Simmons et al., 2010, Van Dijk et al., 2024), which can be converted to yield a 3D estimate of SPM concentrations in the water column of the BPNS (Praet et al., 2023). However, the relationship between the acoustic return signal of the MBES and the variable character of SPM is still insufficiently resolved.

To address this issue, Praet et al. (2023) recommended a better monitoring of the varying SPM properties. Images of SPM might prove to be pivotal in this regard, as they provide a direct snapshot of suspended particles and can contain a number of unexplored quantitative parameters. Several types of imaging devices, standard practice in long-term plankton monitoring programs, can yield these images.

In order to address the abovementioned issues and the lack of proficient processing capabilities of water column data in the currently-available software, the TURBEAMS project aims to

1. Develop adequate and purpose-built open-access software able of handling, visualizing and exporting MBES water column backscatter data.
2. Provide 3D SPM and turbidity information using MBES water column backscatter data by correlating the acoustic return signal to a diverse set of in-situ turbidity and SPM measurements.
3. Investigate the potential of images for the characterization of SPM in the BPNS: can we extract quantitative SPM information from these images and can plankton imaging instruments be used for sedimentological studies too?

Methods

Within the TURBEAMS project, an empirical approach is used: Kongsberg Discovery EM2040 300 kHz MBES water column data are gathered and concurrent in-situ optical, visual and acoustic data are obtained using a wide variety of sensors. Other acoustic data consist of Kongsberg Discovery EK80 single beam (SBES) data acquired over a wide range of frequencies (38, 70, 120, 200 and 333 kHz) and Teledyne Workhorse ADCP data (600 kHz). Ping interference of the different acoustic sources is avoided using a ping synchronization system. Optical data include grainsize data obtained with the Sequoia LISST-200X and turbidity data obtained using a Wetlabs ECO NTU OBS sensor. Water samples allow turbidity measurements using Hach turbidimeters (2100Qis and TL2360) and SPM measurements through filtration. Furthermore, 1L water samples were selected at specific stations and timings for subsequent analysis with imaging instruments (ZooScan, FlowCam and Flow cytometer) in the lab. As these imaging sensors cover a different size range, integrating these complementary devices allows us to investigate the suspended particle spectrum from a few micrometers to several centimeters. Data are obtained by performing tidal measurements at three well-studied stations with the BPNS: MOW01, W05 and W08 and by sailing transects between these stations (**Fout! Verwijzingsbron niet gevonden.**).

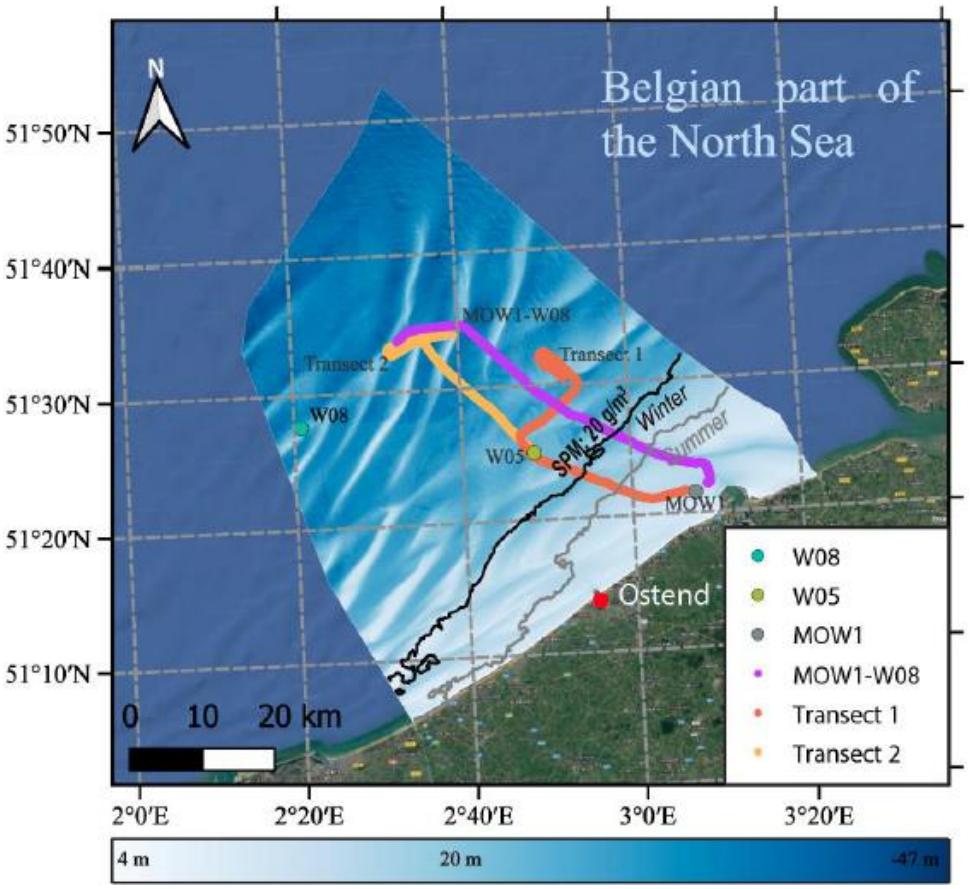

Figure 1: Stations and transects of which data have been gathered during TURBEAMS (Mawet, 2024)

The ZooScan (Hydroptic) is a waterproof scanner that visualizes and analyses zooplankton and other particles larger than ~150 µm ESD using scanner technology (Grosjean et al., 2004). The FlowCam VS-4 benchtop model (Yokogawa Fluid Imaging Technologies) automatically visualizes and quantifies particles (55-300 µm) in a moving fluid combining principles of flow cytometry, microscopy and image analysis (Sieracki et al., 1998). The CytoSense (Cytobuoy) flow cytometer (FCM) is based on the principle of imaging flow cytometry (Dubelaar et al., 1999) and outputs optical scattering, fluorescence and imaging data of each particle (1-800 µm) that passes the laser. We have built our own learning dataset for the classification of all unidentifiable non-biological particles, previously incorrectly classified as “detritus”. In this learning dataset, we have morphologically subdivided the “detritus” group for the ZooScan and FlowCam images based on their shape and color (Figure 2). Automatic classification of the images is obtained using the existing and updated learning datasets, after which a series of quantitative parameters (e.g. number of particles, size characteristics and ratio plankton/sediment) were exported from the EcoTaxa and MongoDB databases.

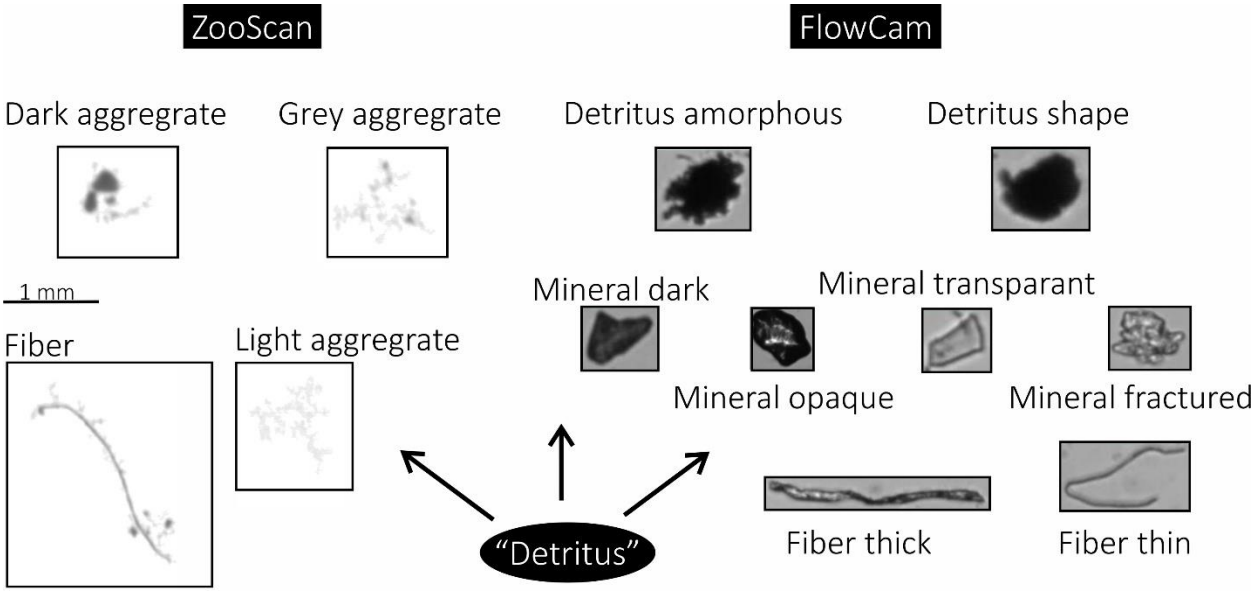

Figure 2: "Detritus" classification of Zooscan and FlowCam images

Several Machine learning (ML) approaches (Robin, 2023, Hermans, 2017) have been tested to derive correlations between acoustic volume backscatter values (MBES, ADCP and EK80 data) and SPM or turbidity measurements obtained from OBS and LISST values. An XG-boost (extreme gradient) model was compared to a multi-linear regression model to evaluate the added value of multi-frequency data. In addition, a probabilistic neural network (PNN; (Robin, 2023)) model was trained to quantify the uncertainty.

Results & discussion

1. MBES processing software

An open-source python-based software, named PING, that allows to efficiently load, visualize and export large datasets of MBES- and SBES water column data has been developed. Within PING, cross-calibration of the MBES water column data with calibrated SBES data from the same frequency allows for correcting sensitivity differences between different beams (Figure 3). The corrected water column images are a powerful tool for detecting spatial SPM variability, sediment plumes or other relevant features present within the water column. Detection is currently performed on individual images, stacks of multiple images and the visualization of relevant 2D profiles of the center beam(s), allowing to quickly visualize a large dataset. Export options within PING are being developed and will contain 3D formats.

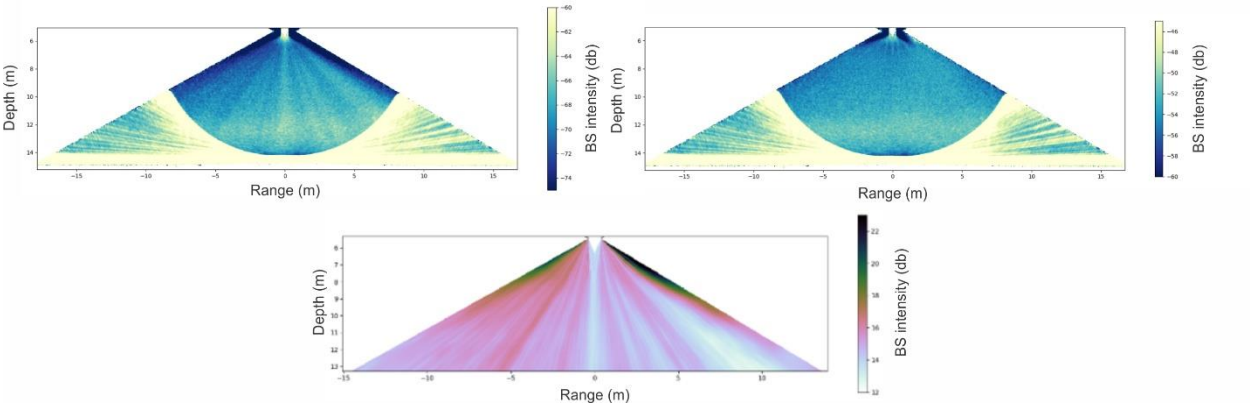

Figure 3: Left: Uncorrected water column image displaying line-like artifacts caused by different beam sensitivities. Middle: Correction beam pattern to be applied on the uncorrected image. Right: Corrected water column image. See Urban et al. (in prep) for more information.

2. Machine learning methods to obtain optimal correlations

Before training our models using ML approaches, the data had to undergo several processing steps, one of which is feature scaling. Machine learning algorithms do not perform well on input attributes with very different scales, as features with larger numerical ranges dominate the learning process. Therefore, standardization of the values has been conducted (Mawet, 2024).

Two important results were obtained based on our initial approaches. First, XG-boost performed better than multilinear regression, especially in the higher and lower turbidity ranges. The reason lies in its capacity to deal with non-linear trends. While the PNN approach also yielded satisfying results including an estimation of uncertainty, XG-boost appears to outperform PNN for all tested datasets (Figure 4). Optimizing hyperparameters is necessary to maximize the performance of both ML algorithms. Second, the use of multi-frequency in XG-boost models improves the prediction of both OBS and LISST data considerably, with r^2 values exceeding 0.95 for all frequencies combined (Figure 5).

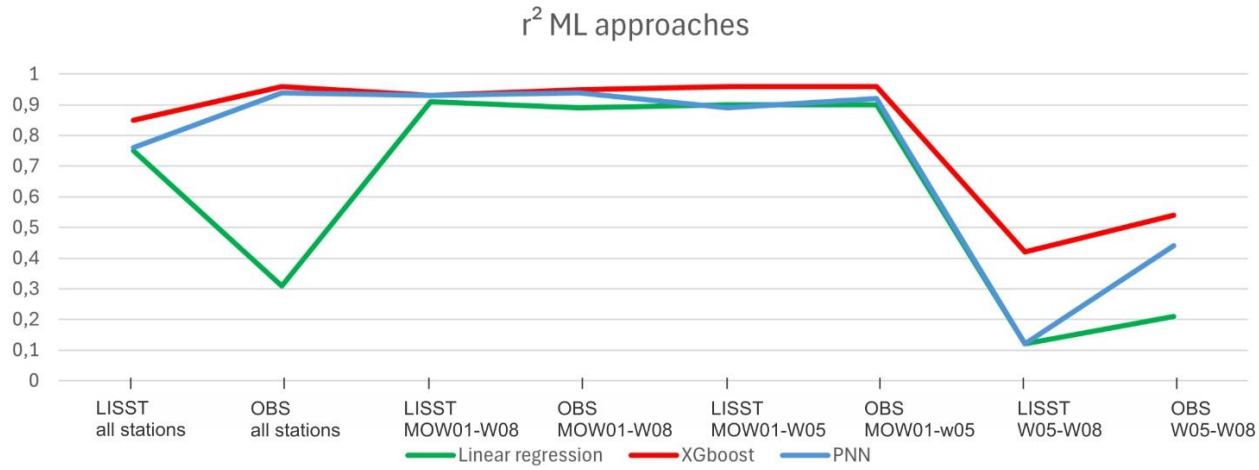

Figure 4: Correlation coefficients (r^2) between multibeam water column data and LISST/OBS data for different scenarios..

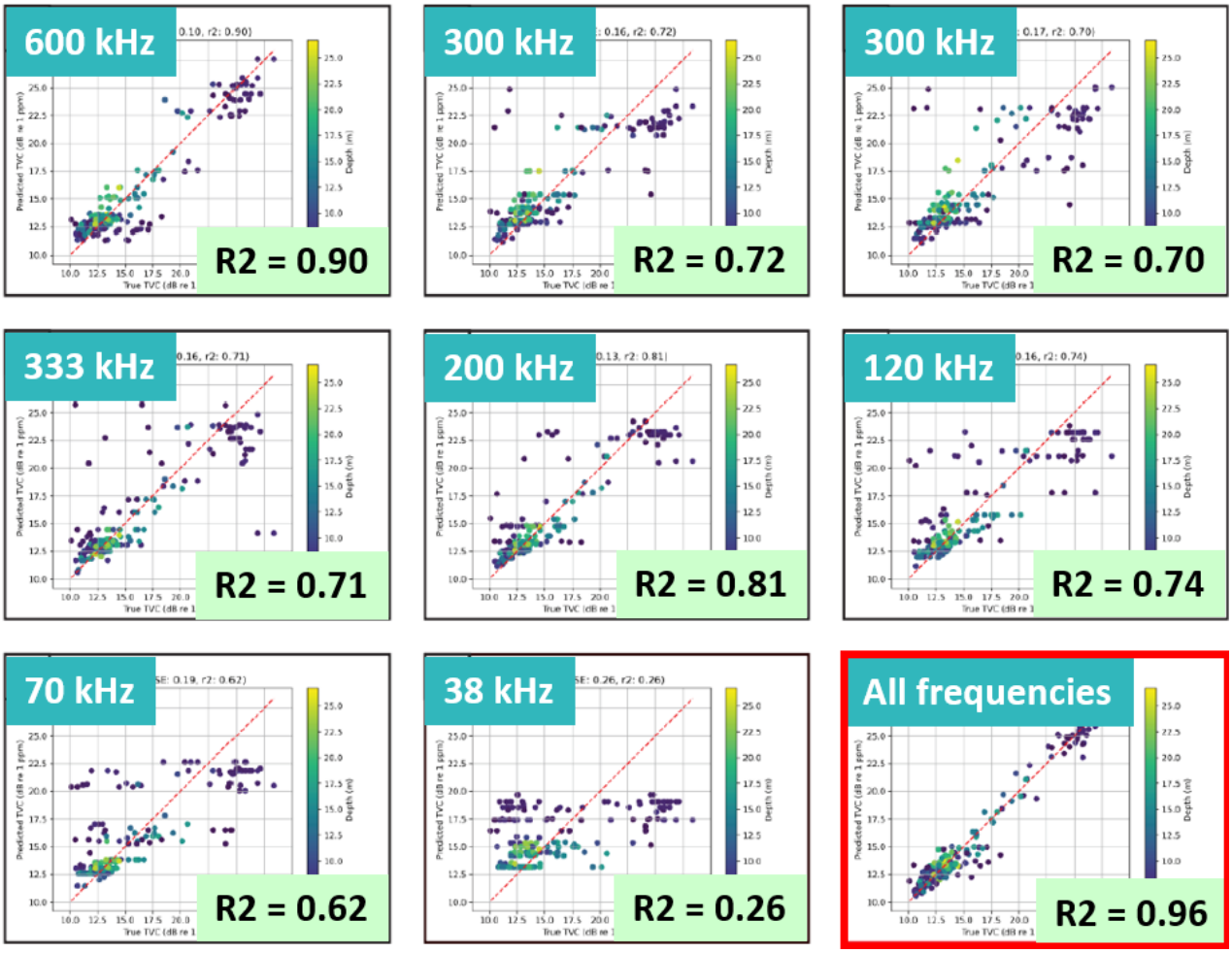

Figure 5: Correlation coefficients (r^2) between measured (LISST) and predicted Total Volume Concentration (TVC). ADCP: 600 kHz; MBES: 300 kHz (transducer 1 & 2); 333, 200, 120, 70 & 38 kHz: SBES data.

3. SPM characteristics using plankton imaging tools

The relative abundances of SPM with biological (zooplankton, phytoplankton, faecal pellets, ...), sedimentological (primary particles, floculli, flocs, fibers, minerals,...) and unknown origin (for size ranges >150 µm and 55-300 µm) are shown in Figure 6. It is clear that sedimentological particles vastly outnumber biological particles, both close to shore (MOW01) and offshore (W05 and W08). This implies that the plankton imaging tools have a lot of potential for the identification of SPM.

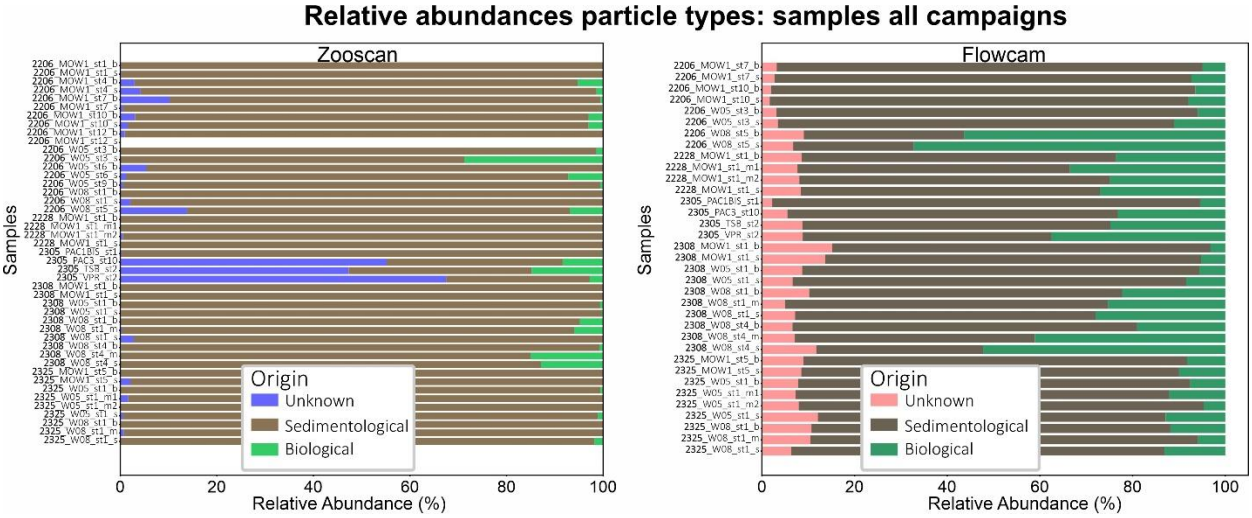

Figure 6: Relative abundances of particle types in the BPNS

Conclusion

TURBEAMS is still an ongoing project in which both the software and the methods are still being developed. PING still needs to implement export options and will see some processing upgrades in the coming year. The machine learning approaches will be further refined by using the calibrated multibeam data that is now available and by testing the generalization of the model between stations and campaigns. Moreover, the data obtained during the project are being used in the framework of sediment plume detection studies, ensuring the usage of both the data and methods in societal-relevant projects. Despite the project being unfinished business, some striking intermediary results pop out

1. Multibeam water column data tend to take a lot of storage space and consequently require a lot of processing power. Software dedicated to these data are needed in order to keep the datasets manageable. PING is an open-access software allowing to load, visualize and export multibeam water column data efficiently. Future improvements will render the software even better suited and invite other expert-users to contribute to its development.
2. Multi-frequency acoustic data are the way forward. Statistics indicate that the usage of multiple frequencies to detect particles in the water column significantly improves the

predictor capabilities. Moreover, since the combination of visual, optical and acoustic methods allow the detection of particles of different sizes and nature, combining methods is key.

3. Devices built for the detection of living plankton are evenly well suited to detect particles with sedimentological origin. Within this project, we visualized and classified for the first time a larger size range of SPM (~1µm -1 cm), including plankton as well as non-living particles. Refining the classification is the next logical step to improve this method.

References

FROMANT, G., LE DANTEC, N., PERROT, Y., FLOC'H, F., LEBOURGES-DHAUSSY, A., & DELACOURT, C. 2021. Suspended sediment concentration field quantified from a calibrated MultiBeam EchoSounder. Applied Acoustics, 180, 108107.

DOGLIOTTI, A. I., RUDDICK, K. G., NECHAD, B., DOXARAN, D. & KNAEPS, E. 2015. A single algorithm to retrieve turbidity from remotely-sensed data in all coastal and estuarine waters. Remote Sensing of Environment, 156, 157-168.

DUBELAAR, G. B. J., GERRITZEN, P. L., BEEKER, A. E. R., JONKER, R. R. & TANGEN, K. 1999. Design and first results of CytoBuoy: A wireless flow cytometer for in situ analysis of marine and fresh waters. Cytometry, 37, 247-254.

ELEVELD, M. A., PASTERKAMP, R., VAN DER WOERD, H. J. & PIETRZAK, J. D. 2008. Remotely sensed seasonality in the spatial distribution of sea-surface suspended particulate matter in the southern North Sea. Estuarine, Coastal and Shelf Science, 80, 103-113.

FETTWEIS, M., BAEYE, M., VAN DER ZANDE, D., VAN DEN EYNDE, D. & JOON LEE, B. 2014. Seasonality of floc strength in the southern North Sea. Journal of Geophysical Research: Oceans, 119, 1911-1926.

FETTWEIS, M. & LEE, B. J. 2017. Spatial and Seasonal Variation of Biomineral Suspended Particulate Matter Properties in High-Turbid Nearshore and Low-Turbid Offshore Zones. Water, 9, 694.

FROMANT, G., LE DANTEC, N., PERROT, Y., FLOC'H, F., LEBOURGES-DHAUSSY, A. & DELACOURT, C. 2021. Suspended sediment concentration field quantified from a calibrated MultiBeam EchoSounder. Applied Acoustics, 180, 108107.

GROSJEAN, P., PICHERAL, M., WAREMBOURG, C. & GORSKY, G. 2004. Enumeration, measurement, and identification of net zooplankton samples using the ZOOSCAN digital imaging system. ICES Journal of Marine Science, 61, 518-525.

HERMANS, T. 2017. Prediction-Focused Approaches: An Opportunity for Hydrology. Groundwater, 55, 683-687.

MAWET, S. 2024. Unlocking the potential of sonar data to predict sea turbidity using machine learning - An innovative approach for marine monitoring. 2024.

PRAET, N., COLLART, T., OLLEVIER, A., ROCHE, M., DEGRENDELE, K., DE RIJCKE, M., URBAN, P. & VANDORPE, T. 2023. The Potential of Multibeam Sonars as 3D Turbidity and SPM Monitoring Tool in the North Sea. Remote Sensing [Online], 15.
ROBIN, T. 2023. Machine Learning for Bayesian Experimental Design in the Subsurface. PhD, Ghent University.
URBAN, P., PRAET, N., VANDORPE, T. & HERMANS, T. On (cross-)calibration of multibeam and singlebeam water column data, accounting for near-field effects.
SIERACKI, C. K., SIERACKI, M. E. & YENTSCH, C. S. 1998. An imaging-in-flow system for automated analysis of marine microplankton. Marine Ecology Progress Series, 168, 285-296.
SIMMONS, S. M., PARSONS, D. R., BEST, J. L., OBERG, K. A., CZUBA, J. A. & KEEVIL, G. M. 2017. An evaluation of the use of a multibeam echo-sounder for observations of suspended sediment. Applied Acoustics, 126, 81-90.
SIMMONS, S. M., PARSONS, D. R., BEST, J. L., ORFEO, O., LANE, S. N., KOSTASCHUK, R., HARDY, R. J., WEST, G., MALZONE, C., MARCUS, J. & POCWIARDOWSKI, P. 2010. Monitoring Suspended Sediment Dynamics Using MBES. Journal of Hydraulic Engineering, 136, 45-49.
VAN DIJK, T. A. G. P., ROCHE, M., LURTON, X., FEZZANI, R., SIMMONS, S. M., GASTAUER, S., FIETZEK, P., MESDAG, C., BERGER, L., KLEIN BRETELER, M. & PARSONS, D. R. 2024. Bottom and Suspended Sediment Backscatter Measurements in a Flume—Towards Quantitative Bed and Water Column Properties. Journal of Marine Science and Engineering, 12, 609.
VAN LANCKER, V. & BAEYE, M. 2015. Wave Glider Monitoring of Sediment Transport and Dredge Plumes in a Shallow Marine Sandbank Environment. PLOS ONE, 10, e0128948.

Intra-annual variability of marine floc morphology in southern North Sea coastal waters using *in-situ* high-resolution underwater imaging and the SANDI Python package

Louise Delhaye[a], Céline Taymans[a], Paul van Kan[b] and Michael Fettweis[a]

[a] Royal Belgian Institute of Natural Sciences, OD Nature, Rue Vautier 29, 1000 Brussels (Belgium)

[b] HAN University of Applied Sciences, P.O. Box 2217, NL-6802 CE, Arnhem (the Netherlands)

Intra-annual variability of marine floc morphology in southern North Sea coastal waters using *in-situ* high-resolution underwater imaging and the SANDI Python package

Louise Delhaye[a], Céline Taymans[a], Paul van Kan[b] and Michael Fettweis[a]

[a] Royal Belgian Institute of Natural Sciences, OD Nature, Rue Vautier 29, 1000 Brussels (Belgium)

[b] HAN University of Applied Sciences, P.O. Box 2217, NL-6802 CE, Arnhem (the Netherlands)

Corresponding author: Louise Delhaye, ldelhaye@naturalsciences.be

Introduction

Marine suspended particulate matter (SPM), composed of mineral and organic particles that aggregate into flocs, plays a fundamental role in coastal and oceanographic processes such as sediment transport, carbon cycling, and water clarity (e.g. Fettweis et al., 2006, 2012; Giering et al., 2020b). Before the availability of an instrument capable of measuring the particle size distribution *in-situ* at high frequency and over long time periods (Agrawal & Pottsmith, 2000), the study of SPM mainly relied on optical devices such as back- or side scatter sensors or transmissometers, providing data on turbidity and after calibration, SPM concentration. Instruments like the LISST-100/200x (Laser In-situ Scattering and Transmissometry), have greatly changed our science, however, they provide 'blind' measurements of particle size distributions (PSDs), and are based on the assumption that particles are spherical. While size distribution is an essential metrics, it does not fully capture the complexity of natural particles, which vary in shape, density and composition, parameters that strongly influence settling velocity and transport dynamics (Markussen, 2020; Many et al., 2019; Giering et al., 2020a).

Shape characterization is especially important for understanding particle behavior, yet many studies and instruments still assume spherical geometry (Shen and Maa, 2016). Such assumption leads to errors in estimating dynamics, especially for flocs larger than 60 µm (Vahedi, 2010; Ye et al., 2024). Furthermore, LISST instruments are limited by a narrow size detection range (with a maximum size detection of 250 or 500 µm) and reduced accuracy at the minimum and maximum bins (Andrews et al., 2010).

Floc morphology remains understudied primarily due to the challenges of analyzing fragile, heterogeneous aggregates. Extreme fragility of such flocs requires *in-situ* study as sampling would likely break them down. Laboratory approaches (e.g. gel capture, microscopy, lab-based laser diffraction) are time-intensive, often disruptive, and can lead to unrepresentative sampling (e.g. Jarvis et al., 2005; Ye et al., 2024).

In the past decades, high-resolution *in-situ* underwater imaging has emerged as a non-invasive solution to overcome many of these challenges (e.g. Giering et al., 2020a,b; Many et al., 2019). This approach remains non-destructive while enabling almost continuous measurement. However, underwater imaging still faces several challenges: including inconsistency in metrics terminology (Russ, 2011; Zhu et al., 2023), variability in sensor systems (Osborn et al., 2021), and lack of standardized image processing protocols. These factors firstly make datasets

comparison difficult between different imaging systems and secondly make comparisons with other techniques (e.g. laser diffraction, sedigraphy, camera sieving) challenging.

To address the first limitations, we developed an open-source, user-friendly software that is intended at creating more standardized underwater particle analysis workflows and results regarding both particle size and morphology. In this study, we present the structure of the software and use it on a dataset of images collected using a particle camera (PCam3). The goal was to verify if the results of the PCam3 using the software could be used as an effective tool to investigate intra-annual variability in floc morphology in the Belgian Part of the North Sea (BPNS).

Methods

Study area

The study area is located ~4 km offshore from Nieuwpoort in the BPNS, near the Westdiep aquaculture site. It is within a very dynamic environment, influenced by tidal currents and strong seasonal variations, but characterized by low SPM concentrations.

Data collection

As part of the Westdiep aquaculture environmental monitoring, images were collected using a particle camera (PCam3, developed by Herbst Environmental Science) during six oceanographic campaigns on board the *RV Belgica* between April 2023 and March 2024. The camera was attached to the rosette which was profiling the water column every hour for several hours. Before processing, images were manually sorted in order to only retain sharp and high-quality images and excluding those where particles were visibly distorted by water movement or containing semi-transparent particles (likely phytoplankton).

Data processing

In this presentation, we will present SANDI (Sediment ANalysis and Delineation through Images), an open-source Python package developed for automated image-based analysis of flocs, available on GitHub and PyPI. Based on the workflow developed by Markussen (2016), SANDI integrates additional image enhancement options, that can be adapted in a user-friendly interface and generates several shape and size metrics for detected particles. The software supports both single image and batch processing, enabling users to optimize the parameters on a test image before applying it to the entire dataset.

In the present study, the image processing workflow consisted of (1) denoising, (2) histogram stretching, (3) morphological reconstruction, (4) background illumination correction and (5) image resampling at a resolution of 1 µm. Preliminary to the processing of the *in-situ* data, the effect of each of these steps and of their parameters' values was tested on lab samples in order to find the optimal workflow. Particles were then extracted using Otsu's method for thresholding and the ones smaller than 7 adjacent pixels or touching the border of the image were discarded. For each extracted particle, size metrics (e.g. area, perimeter, equivalent spherical diameter, volume) and shape indicators (e.g. roundness, sphericity, aspect ratio, solidity, extent, form factor) were automatically computed.

Statistical analyses

Particles were then classified into flocculi (10-50 µm), microflocs (50-200 µm) and macroflocs (> 200 µm), following standard classifications (Lee et al, 2012). To identify natural groups of flocs, automatic clustering methods were used on micro- and macroflocs based on their size and shape metrics.

Results & discussion

In the preliminary results, the automatic clustering method grouped flocs into four distinct clusters, ranging from highly irregular and elongated to nearly spherical shapes. The seasonal distribution of these clusters showed clear trends in the morphology of marine suspended flocs: irregular, elongated flocs dominate in early spring probably pointing to the presence of phytoplankton, especially in March, while more regular, rounder ones became increasingly prevalent in autumn and winter, probably indicating the occurrence of mineral-dominated flocs. This suggests that seasonal variables (phytoplankton, marine gel production and flocculation, organic matter content) influence floc morphology.

Conclusion

These preliminary results tend to confirm that underwater high-resolution images processed through the SANDI python software can successfully give insights into the morphological variations of suspended particles, enabling to have a better understanding of SPM dynamics in the Belgian part of the North Sea. However, our preliminary results must still be investigated further before any statistically significant conclusion can be drawn.

References

Andrews, S., Nover, D., & Schladow, S. Using laser diffraction data to obtain accurate particle size distributions: The role of particle composition, Limnol. Oceanogr. Meth. 8, 507–526 (2010).

Fettweis M., Francken F., Pison V. and Van den Eynde D., 2006. “Suspended particulate matter dynamics and aggregate sizes in a high turbidity area”. Marine Geology 235, 63-74. https://doi.org/10.1016/j.margeo.2006.10.005

Fettweis M., Baeye M., Lee B.J., Chen P. and Yu J.C.S., 2012. “Hydro-meteorological influences and multimodal suspended particle size distributions in the Belgian nearshore area”, Geo-Marine Letters. https://doi.org/10.1007/s00367-011-0266-7

Giering S.L.C., Hosking B., Briggs N. and Iversen M.H, 2020a. “The Interpretation of Particle Size, Shape, and Carbon Flux of Marine Particle Images Is Strongly Affected by the Choice of Particle Detection Algorithm”. Frontiers in Marine Science 7:564. https://doi.org/10.3389/fmars.2020.00564

Giering S.L.C., Cavan E.L., Basedow S.L., Briggs N., Burd A.B., Darroch L.J., Guidi L., Irisson J-O., Iversen M.H., Kiko R., Lindsay D., Marcolin C.R., McDonnell A.M.P., Möller H.O., Passow U., Thomalla S., Trull T.W. and Waite A.M., 2020b. “Sinking Organic Particles in the Ocean-Flux Estimates Fom in-situ Optical Devices”, Frontiers in Marine Science 6:834. https://doi.org/10.3389/fmars.2019.00834

Graham, G.W., Davies, E.J., Nimmo-Smith, W.A.M., Bowers, D.G. & Braithwaite, K.M. Interpreting LISST-100X measurements of particles with complex shape using digital in-line holography. J. Geophys. Res. 117, C05034 (2012).

Jarvis P., Jefferson B. and Parsons S.A., 2005. “Measuring floc structural characteristics”, School of Water Sciences, Cranfield University, Cranfield, 45p.

Lee, B. J., M. Fettweis, E. Toorman, and F. J. Molz (2012), Multimodality of a particle size distribution of cohesive suspended particulate matters in a coastal zone, J. Geophys. Res., 117, C03014, doi:10.1029/2011JC007552.

Many G., Durieu De Madron X., Verney R., Bourrin F., Renosh P., Jourdin F. and Gangloff A., 2019. “Geometry, fractal dimension and settling velocity of locs during flooding conditions in the Rhône ROFI”, Estuarine, Coastal and Shelf Science 219, 1-13. https://doi.org/10.1016/j.ecss.2019.01.017

Markussen T.N., 2016. “Parchar - Characterization of Suspended Particles Through Image Processing in Matlab”, Journal of Open Research Software 4: e26. http://dx.doi.org/10.5334/jors.114.

Markussen T.N., Konrad C., Waldmann C., Becker M., Fischer G. and Iversen M.H., 2020. “Tracks in the Snow – Advantage of Combining Optical Methods to Characterize Marine Particles and Aggregates”, Frontiers in Marine Science 7:476.

Osborn R., Dillon B., Tran D., Abolfazli E., Dunne K.B.J., Nittrouer J.A. and Strom K., 2021. “FlocARAZI: An In-Situ, Image-Based Profiling Instrument for Sizing Solid and Flocculated Suspended Sediment”, Journal of Geophysical Research: Earth Surface, 126

Shen X. and Maa J. P.-Y., 2016. “A camera and image processing system for floc size distributions of suspended particles”, Marine Geology 376, 132-146.

Russ J.C., 2011. “The image processing handbook”. CRC Press.

Vahedi A., 2010. “Predicting the Settling Velocity of Lime Softening Flocs using Fractal Geometry”, PhD thesis, Department of Civil Engineering, University of Manitoba, Canada.

Ye L., Chen Z., Chen L., Ren J., Wu J., Chen Y., Huang X., Chen H. and Guo Y., 2024. “Volumetric reconstruction of settling mud flocs: A new insight of equilibrium flocculation in saline water”. Water Research 255. https://doi.org/10.1016/j.watres.2024.121512

Zhu Y., Chen Q., Zhang Y., Tang W., Xu C., Li W. and Jia J., 2023. “GraSSAMS: A new instrument designed for the determination of grain size and shape of sand-gravel-sized sediment”, Estuarine, Coastal and Shelf Science 290.

Particle dynamics in marine environments: processes, patterns, and applications

Dr. Brent A. Law

Department of Fisheries and Oceans, Bedford Institute of Oceanography, NS, Canada

Particle dynamics in marine environments: processes, patterns, and applications

Dr. Brent A. Law
Department of Fisheries and Oceans, Bedford Institute of Oceanography, NS, Canada

Floc size and abundance in the ocean are controlled by five basic mechanisms: advection, resuspension, aggregation, disaggregation, and deposition. Changes in floc size or abundance due to advection are recognizable when these parameters are decoupled from bottom stress. Resuspension is distinguishable by coupling between floc abundance and seabed stress. Aggregation occurs when turbulence is low to moderate and particle concentration is large. This co-occurrence occurs most often in a tidally dominated system during slack water, allowing flocs to grow. Disaggregation is the process of floc destruction and occurs under energetic conditions. Its signature is an inverse correlation between floc size and turbulence. Deposition occurs when stress is low enough for flocs to settle from the water column. It is associated with decreases in concentration and overall particle size. This talk will examine water column and seabed particle dynamics to look at these five basic mechanisms. Water column and seabed particle dynamics will be investigated using data from Floc Cameras, a Sequoia Scientific LISST 100X, Size versus Settling Velocity Cameras, current meters, and a process based inverse model that directly uses the seabed grain size. The goal of the talk is to describe the particle dynamics knowledge in a range of applications, including finfish aquaculture in coastal and offshore waters, the interaction of sediment with spilled oil, and studies of meso- and macro-tidal flats.

Concentration and composition of Suspended Particulate Matter along nearshore to offshore transects

Michael Fettweis

Royal Belgian Institute of Natural Sciences, OD Natural Environment, rue Vautier 29, 1000 Brussels, Belgium

Concentration and composition of Suspended Particulate Matter along nearshore to offshore transects

Michael Fettweis

Royal Belgian Institute of Natural Sciences, OD Natural Environment, rue Vautier 29, 1000 Brussels, Belgium

Corresponding author: Michael Fettweis, mfettweis@naturalsciences.be

Suspended particulate matter (SPM) is composed of minerals and organic matter (OM). The interaction between them take place in a variety of ways, from the sorption of organic molecules to surfaces, to intercalation into expandable clay minerals, the inclusion of smaller organic particles (bacteria, small phytoplankton, detritus) into small clay mineral aggregates (flocculi), the incorporation of organic particles (phytoplankton, bacteria, detritus) into flocs, and the formation of biofilms. Interactions between minerals and OM are driven by physical, chemical and biological processes that vary along the land-ocean transition, leading to significant spatial and temporal variability in the size, shape, composition, concentration, vertical distribution and transport pathways of the SPM.

SPM concentration and composition is an indicator for the relative importance of physical and biogeochemical processes. A characteristic feature of the SPM is that the composition becomes more organic and the floc size larger with decreasing SPM concentration. The shape of both relationships and their variability are caused by spatio-temporal variations in biogeochemical and physical processes. Flocs largely consist of minerals in estuarine and nearshore turbidity maximum zones, while they contain gradually more organic matter when turbidity decreases. High turbidity zones are characterized by strong tidal currents, intensive resuspension and settling, flocculation in phase with the tides and high primary production. In oligotrophic environments, the SPM consists mostly of large, organic rich and fluffy aggregates. In this regime, physical processes are less important and flocculation occurs on seasonal time scales.

We explain the processes leading to these relationships, and discuss the current understanding of the characteristics, dynamics and interactions of OM and minerals along the continuum from land to ocean. Further we will discuss the role of SPM in biogeochemical cycles as well as the effects of climate change and human activities on SPM characteristics.

Vertical dynamics of suspended particulate matter and chlorophyll-a in a well-mixed coastal turbid system

Saumya Silori1, Xavier Desmit1, Rolf Riethmüller2, Markus Schartau3, Nathan Terseleer1, Michael Fettweis1

1 OD Natural Environment, Royal Belgian Institute of Natural Sciences, rue Vautier 29, 1000 Brussels, Belgium
2 Institute of Carbon Cycle, Helmholtz Centre Hereon, Max-Planck-Str. 1, 21502 Geesthacht, Germany
3 GEOMAR, Helmholtz Centre for Ocean Research, Wischhofstr. 1-3 24148 Kiel, Germany

Vertical dynamics of suspended particulate matter and chlorophyll-a in a well-mixed coastal turbid system

Saumya Silori[1], Xavier Desmit[1], Rolf Riethmüller[2], Markus Schartau[3], Nathan Terseleer[1], Michael Fettweis[1]
[1]*OD Natural Environment, Royal Belgian Institute of Natural Sciences, rue Vautier 29, 1000 Brussels, Belgium*
[2]*Institute of Carbon Cycle, Helmholtz Centre Hereon, Max-Planck-Str. 1, 21502 Geesthacht, Germany*
[3]*GEOMAR, Helmholtz Centre for Ocean Research, Wischhofstr. 1-3 24148 Kiel, Germany*

Introduction

Coastal hydrodynamics are a result of interacting physical forces (tidal currents, waves, density-driven currents, etc.), which significantly influence suspended particulate matter (SPM; Jones et al., 1998) dynamics. SPM composition, more specifically particulate organic matter (POM) content of SPM (POM/SPM; hereafter referred to as POM content), changes characteristically with the SPM concentrations (Liénart et al., 2017; Schartau et al., 2019). SPM typically becomes more organic with decreasing concentrations offshore, due to reduced resuspension and differential settling of mineral versus organic particles (Schartau et al., 2019; Fettweis et al., 2022). Seasonal shifts in SPM composition also occur, especially during phytoplankton blooms, when biologically exuded organic matter enhances aggregation and deposition. While cross-shore and seasonal patterns in SPM composition are relatively well studied, vertical and tidal variations remain poorly resolved. We hypothesize that POM content is higher in surface waters than near the bottom due to the SPM concentration gradient in the water column, analogous to cross-shore patterns. Among the organic fraction, phytoplankton, though minor by mass, play a key role in SPM dynamics (Fetweiss et al., 2022). Our preliminary data from the Belgian coastal zone suggest that the vertical association between Chl*a* and SPM varies seasonally, with strong coupling in winter and decoupling in spring. To investigate this, we analyse vertical profiles of Chl*a* and SPM concentrations to infer the phytoplankton–SPM association. In parallel, we use organic matter quality indicators (POC/PON and POC/Chl*a* ratios) to assess whether the composition of SPM differs between surface and bottom layers. Together, these insights reveal how phytoplankton interact with SPM in well-mixed turbid systems.

Methods

MOW1 (51.36°N, 3.13°E), located within the Belgian coastal turbidity maximum, was sampled over 29 tidal cycles between 2019 and 2022. Hourly water samples were collected ~2 m below the surface and ~2 m above the seabed using a Sea-Bird SBE09 CTD carousel equipped Niskin bottles. Samples were filtered on board and later analysed for SPM, POC, PON, Chl*a*, and Phaeophytin-*a* (Pheo*a*). In 2019, hourly sensor-based profiles were also recorded during each tidal cycle. An OBS3+ backscatter sensor, mounted on the CTD, provided continuous turbidity measurements. The SPM and Chl*a* vertical profiles were calculated assuming a linear regression between the water depth and the logarithm of the

SPM or Chl*a* concentrations (Dyer, 1986). The depth of the photic layer was estimated using light attenuation coefficients derived from SPM concentrations, following the empirical relationship proposed by Devlin et al. (2008). These fitted profiles were used to quantify the mass of SPM and Chl*a* within the euphotic zone to assess their vertical distribution.

Results

SPM, POC, and Chla concentrations showed significant tidal and seasonal variability, with SPM ranging from 8 to 990 mg/l and POC from 0.38 to 34 mg/l across seasons. On average, SPM, POC, and Chl*a* concentrations were higher near the bottom than at the surface, though POC and Chl*a* content were relatively higher in surface waters. Highest Chl*a* concentrations occurred during spring and summer (up to 65 µg/l). Analysis of the expanded dataset (2012–2018), revealed a positive linear relationship between SPM and Chl*a* concentrations in both spring and winter (Fig. 1a). However, the bootstrapped distribution of regression slopes showed greater variability in spring (standard deviation = 0.01) compared to winter (standard deviation = 0.001) (Fig. 1b).

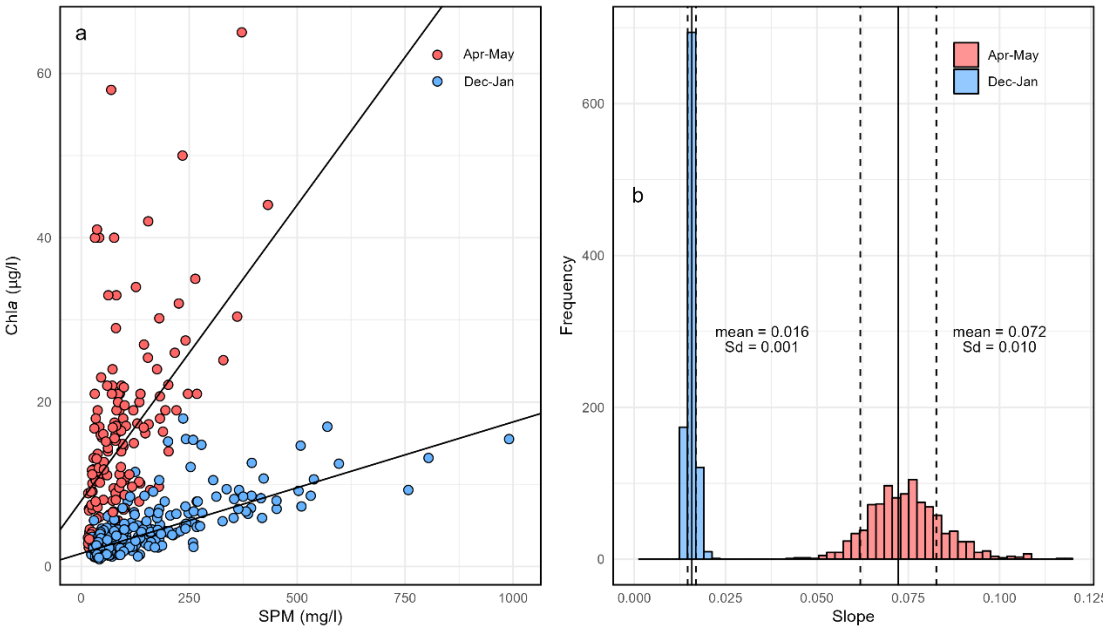

Figure 1: (a) Robust Linear Regression between SPM (mg/l) and Chl*a* (µg/l) in winter (Dec-Jan) and spring (Apr-May).The slope and intercept of the linear fit are mean values of these coefficients derived from bootstrapping. (b) Histograms of bootstrapped sampling distribution of slopes of the robust linear regression between SPM (mg/l) and Chl*a* (µg/l) in winter (Dec-Jan) and spring (Apr-May). The solid black lines represent the mean of the bootstrap slopes, the dashed black lines give the boundaries of one standard deviation (Sd) above and below the mean.

The vertical variation in the Chl*a* content (Chl*a*/SPM) was notably more pronounced than the variation in the POC content. We observed significantly higher Chl*a* content in the upper water column during spring and summer, and occasionally in autumn. Additionally, this evidence for vertical differences in the organic content of the SPM in the water column is supported by significantly lower POC/Chl*a* and POC/PON ratios in surface waters, with

concomitant higher Chl*a*/Pheo*a* ratios. These ratios may serve as potential proxies indicating the quality of organic matter (Savoye et al., 2003; Bouillon et al., 2011), and our results suggest that the surface waters are generally enriched in organic matter of higher trophic quality.

Analysis of hourly profiles of SPM and Chl*a* concentrations during tidal cycles in spring (April 2019) and winter (November 2019) revealed notable disparities between the two seasons (Fig. 2). Throughout both tidal cycles, SPM concentrations exhibited a tendency to increase towards the bed during periods of maximum current velocities, whereas they remained relatively constant on the vertical exhibiting lower values on average during the slack periods . Concurrently, Chl*a* profiles in November (Fig. 2a) closely mirrored the corresponding SPM patterns which was not the case in April. About half of the Chl*a* profiles in April exhibited inversions, where concentrations decreased towards the bed (Fig. 2b). To better quantify the accumulation of Chl*a* in the surface waters, we attempted to determine the average mass of SPM and Chl*a* within the estimated photic layer. The depth-integrated concentration of SPM ([g m^{-2}]) within the photic layer during a tidal cycle remains conservative across seasons. However, the mass of Chl*a* within the photic layer during a tidal cycle exhibits seasonal variation, being higher during spring and summer compared to winter and autumn, yet it remains constant within each of these seasons. Further we calculate the percentage of SPM and Chl*a* within the photic layer and the analysis reveals that the percentages of Chl*a* and SPM within the photic layer are identical during a tidal cycle in winter. However, during spring, the Chl*a* percentage in the photic layer approaches 10%, while the SPM percentage is notably lower at 3%. Similarly, in summer, the Chl*a* percentage increases up to 30%, whereas the percentage of SPM in the photic layer rises to 18%.

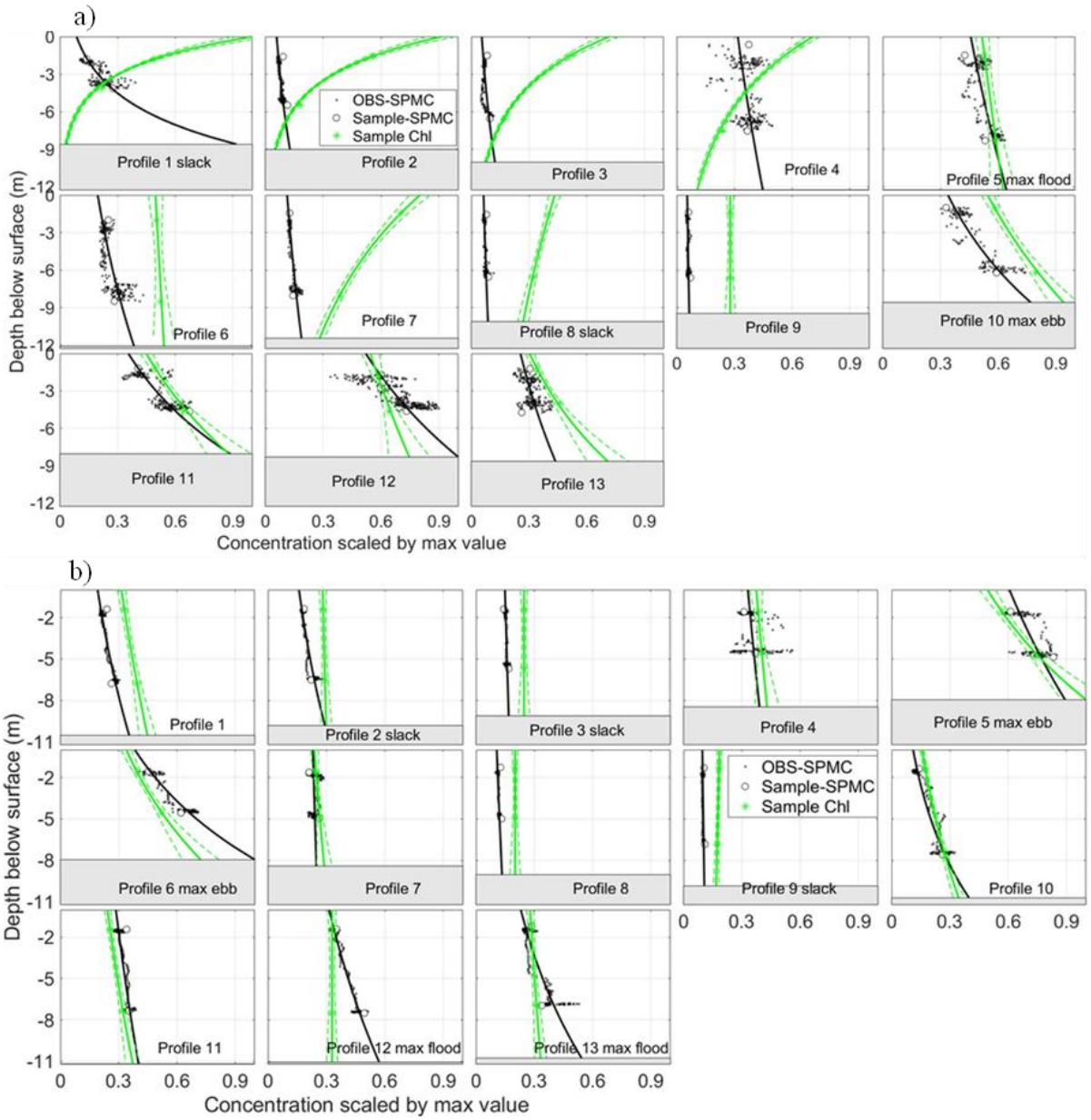

Figure 2: Hourly vertical profiles of SPM (black line) and Chl*a* (green line) concentrations scaled by the maximum value during the tidal cycle in April 2019 (SPM: 366 mg/l, Chl*a*: 33 µg/l) (a) and November 2019 (SPM: 272 mg/l, Chl*a*: 11 µg/l) (b). The Chl*a* profile uncertainty (expressed as a standard deviation is shown as dashed lines. The SPM profile uncertainty, expressed as R^2, is between 0.5-0.9, except for profiles 4, 8, 9 and 13 in April and profiles 4, 7 and 9 in November). The light gray box represents the sea bed.

Discussion

During the spring bloom, the accumulation of Chl*a* in the surface layer diverges from the more uniform SPM distribution, indicating a seasonal decoupling of phytoplankton and sediment dynamics in an otherwise well-mixed water column. We attribute this divergence to the presence of two functional types of phytoplankton: floc-associated types that follow SPM dynamics and dominate most of the year, and free, buoyant phytoplankton that are decoupled from mineral SPM and dominate during bloom periods. The latter's independent vertical

distribution, likely driven by differences in density and settling behavior, helps explain sustained phytoplankton production in turbid, mixed waters with light limitation. Enhanced turbulence during spring may contribute to fragmentation of larger flocs and promote surface accumulation of buoyant, POC-rich aggregates, especially in species like *Phaeocystis globosa* and lightly silicified diatoms. These findings provide insight into the mechanisms that allow phytoplankton to thrive in dynamic, light-limited environments and highlight the complex interplay between biological and physical processes in coastal ecosystems.
In the turbid Belgian nearshore waters, high surface Chl*a* concentrations during the early spring bloom occur simultaneously with elevated SPM concentrations, highlighting the employment of mechanisms that help retain phytoplankton in the photic zone. Despite smaller variations in SPM concentrations from winter to early spring, Chl*a* concentrations increase in March, suggesting that bloom initiation is triggered by the relaxation of winter light limitation and not by improved water clarity. Free-floating phytoplankton, due to slower settling velocities, may have distinct advantage in early spring, remaining longer in the shallow photic layer. As spring progresses and SPM levels decline, the photic depth increases, reducing this advantage. Vertical profiles show that the probability of Chl*a* being in the photic zone increases from ~2% in January to ~12% in April, peaking in summer when SPM is lowest. Conversely, this probability declines in late summer and autumn as SPM rises. Importantly, Chl*a* consistently shows a higher probability than SPM of being within the photic layer, suggesting that water clarity, modulated by SPM concentration and composition, significantly affects phytoplankton retention and productivity.

Conclusion

Our results demonstrate that the enrichment POC content at the surface is driven by similar processes as the horizontal nearshore-offshore gradient, primarily differential settling of mineral versus organic particles. Seasonal differences in POC quality between surface and bottom waters peak in summer, emphasizing the need for sampling both depths even in well-mixed waters. While tidal currents largely shape vertical gradients in SPM and Chl*a* concentrations, higher surface Chl*a* concentrations during the growing season suggests phytoplankton adapt by shifting from floc-attached to free-living forms to remain longer in the photic zone under low light. Understanding phytoplankton strategies affecting buoyancy and particle association is crucial for improving models of organic carbon dynamics in coastal systems.

References

1. Jones, S. E., Jago, C. F., Bale, A. J., Chapman, D., Howland, R. J. M., & Jackson, J. (1998). Aggregation and resuspension of suspended particulate matter at a seasonally stratified site in the southern North Sea: physical and biological controls. Continental Shelf Research, 18(11), 1283-1309. https://doi.org/10.1016/S0278-4343(98)00044-2
2. Liénart, C., Savoye, N., Bozec, Y., Breton, E., Conan, P., David, V., ... & Sultan, E. (2017). Dynamics of particulate organic matter composition in coastal systems: A spatio-temporal study at multi-systems scale. Progress in Oceanography, 156, 221-239. https://doi.org/10.1016/j.pocean.2017.03.001

3. Schartau, M., Riethmüller, R., Flöser, G., van Beusekom, J. E. E., Krasemann, H., Hofmeister, R., & Wirtz, K. (2019). On the separation between inorganic and organic fractions of suspended matter in a marine coastal environment. Progress in Oceanography, 171, 231-250. https://doi.org/10.1016/j.pocean.2018.12.011
4. Fettweis, M., Schartau, M., Desmit, X., Lee, B. J., Terseleer, N., Van der Zande, D., ... & Riethmüller, R. (2022). Organic matter composition of biomineral flocs and its influence on suspended particulate matter dynamics along a nearshore to offshore transect. Journal of Geophysical Research: Biogeosciences, 127(1), e2021JG006332. https://doi.org/10.1029/2021JG006332
5. Dyer, K. R. (1986). Coastal and estuarine sediment dynamics. John Wiley & Sons, Chichester, 258p.
6. Devlin, M. J., Barry, J., Mills, D. K., Gowen, R. J., Foden, J., Sivyer, D., & Tett, P. (2008). Relationships between suspended particulate material, light attenuation and Secchi depth in UK marine waters. Estuarine, Coastal and Shelf Science, 79(3), 429-439. https://doi.org/10.1016/j.ecss.2008.04.02
7. Bouillon, S., Connolly, R. M., & Gillikin, D. P. (2011). 7.07 Use of stable isotopes to understand food webs and ecosystem functioning in estuaries. Treatise on estuarine and coastal science, 7. https://doi.org/10.1016/B978-0-12-374711-2.00711-7
8. Savoye, N., Aminot, A., Tréguer, P., Fontugne, M., Naulet, N., & Kérouel, R. (2003). Dynamics of particulate organic matter δ15N and δ13C during spring phytoplankton blooms in a macrotidal ecosystem (Bay of Seine, France). Marine ecology progress series, 255, 27-41. https://www.int-res.com/articles/meps2003/255/m255p027.pdf

Multi-sensor observations of suspended particulate matter in a tidal coastal environment

Benjamin Van Roozendael[a], Matthias Baeye[a], Duc Tran[a], Romaric Verney[b], Michael Fettweis[a]

[a] Royal Belgian Institute of Natural Sciences, Rue Vautier 31, 1000 Brussels, Belgium
[b] Ifremer, 1625 Route de Sainte-Anne, CS 10070, 29280 Plouzané, France

Multi-sensor observations of suspended particulate matter in a tidal coastal environment

Benjamin Van Roozendael[a], Matthias Baeye[a], Duc Tran[a], Romaric Verney[b], Michael Fettweis[a]

[a]Royal Belgian Institute of Natural Sciences, Rue Vautier 31, 1000 Brussels, Belgium
[b]Ifremer, 1625 Route de Sainte-Anne, CS 10070, 29280 Plouzané, France

Corresponding author: Benjamin Van Roozendael; bvanroozendael@naturalsciences.be

Introduction

Turbidity, or the cloudiness of water, is primarily determined by the amount and type of suspended particulate matter (SPM) in the water column. In coastal environments such as the Belgian part of the North Sea (BPNS), SPM is generated through a combination of biological processes and sedimentary processes. These particles influence light penetration and are therefore a key factor in monitoring water quality (Capuzzo et al., 2015). As such, understanding and measuring SPM is important for both scientific research and effective environmental management.

The BPNS is characterized by a semi-diurnal tidal regime, with average tidal ranges of 4.3 m during spring tides and 2.8 m during neap tides at Zeebrugge. This predictable alternation between high and low tides, together with strong wind-driven flows, creates constantly shifting SPM conditions. Northeasterly winds tend to increase SPM concentrations by resuspending sediments from the seabed, while south-westerly winds often bring in clearer waters from the English Channel, pushing the turbidity maximum towards the Westerschelde estuary. During persistent northeasterly wind events, dense mud suspensions can remain in the water column for several tidal cycles, leading to sustained reductions in water clarity (Baeye et al., 2011). In these waters, SPM concentrations typically range from 20 to 70 mg l^{-1} in the water column near the coast, reaching up to 3,000 mg l^{-1} near the seabed during energetic conditions. Offshore, concentrations are generally lower, usually below 10 mg l^{-1}, reflecting the influence of both hydrodynamic and sedimentary processes (Baeye et al., 2011; Fettweis et al., 2022).

Human activities further complicate SPM dynamics in the BPNS. This area is a busy maritime region, with activities such as navigation, commercial and recreational fishing, dredging, and the development and operation of offshore windfarms. Vessel traffic and fishing gear can disturb seabed sediments, while dredging and sand extraction operations directly release sediments into the water column (Fettweis et al., 2011, 2016; Martens et al., 2018; Van Lancker & Baeye, 2015). Offshore windfarms also alter local hydrodynamics and create new habitats for marine life, influencing the production and movement of biological SPM (Baeye & Fettweis, 2015;

Vanhellemont & Ruddick, 2014). These human activities combine with natural processes to produce a highly variable and dynamic suspended particulate environment that can be challenging to measure and monitor accurately.

To address these complexities, this study investigates how SPM concentrations change under these dynamic conditions and how different sensors perform in capturing these variations. Our findings aim to contribute to more accurate SPM monitoring and better environmental management in this active coastal area.

Methods

To monitor SPM in both nearshore and offshore areas of the BPNS, we conducted several field campaigns at three stations (Fig. 1). These campaigns covered multiple tidal cycles, different weather conditions, and various seasons. This comprehensive approach ensured that we captured the full range of hydrodynamic and sedimentary environments present in the study area.

Acoustic measurements played a central role in these campaigns. We used an Acoustic Doppler Current Profiler (ADCP) to record both water currents and acoustic backscatter intensity (Kim & Voulgaris, 2014), alongside an EK80 echosounder and a multibeam echosounder (MBES) (Praet et al., 2023), which focused on measuring backscatter intensity in the water column. Operating at different frequencies, these instruments allowed us to assess how various types of particles respond to different acoustic signals and to capture the dynamic distribution of suspended sediments.

To complement the acoustic observations, we also collected optical measurements using a range of instruments. Optical backscatter sensors (OBS) were used to measure turbidity, while the LISST-200 (Laser In Situ Scattering and Transmissometry) instrument provided in situ data on particle size distributions and volume concentrations (Creed et al., 2001; Downing, 2006). Both sensors were installed on a rosette that was lowered frequently to take vertical profiles of the water column. A Hach turbidity sensor offered standard turbidity measurements, adding further detail to the dataset. In addition, imaging systems were deployed to visually characterize the suspended particles, including flocs, organic matter, and sediments. To validate and refine these sensor-based observations, we collected water samples at various depths and locations throughout the study area. In the laboratory, these samples were filtered to determine mass concentrations of SPM and analyzed for other parameters such as salinity, particulate organic carbon (POC), particulate organic nitrogen (PON), chlorophyll, and transparent exopolymer particles (TEP).

The combined dataset from the acoustic and optical sensors, together with the laboratory results, allowed us to evaluate the strengths and limitations of each measurement approach. By integrating these diverse data sources, we gained a comprehensive view of how each sensor performed under the dynamic and often complex conditions typical of the Belgian coastal waters.

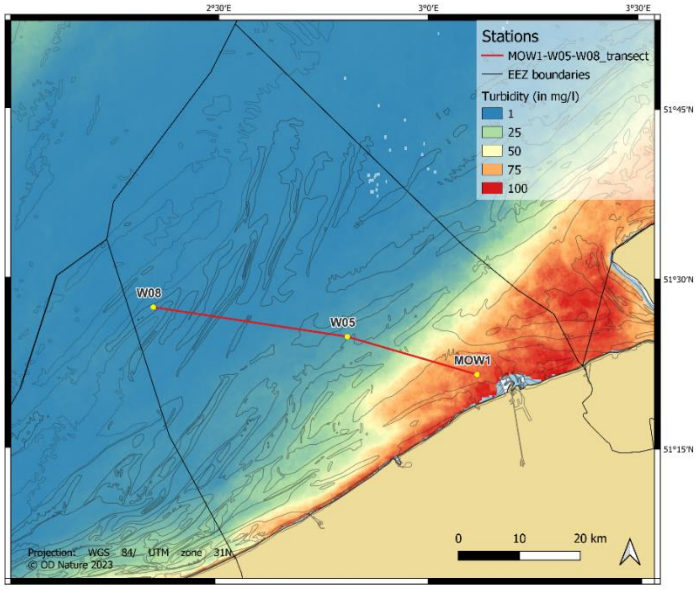

Figure 1. Map of the BPNS displaying the locations of experiments conducted. The background on the map features the average surface SPMC for the winter period of 2019, derived using the algorithm by (Nechad et al., 2010) to the standard Sentinel-3/OLCI remote sensing reflectance product (RRS) provided by EUMETSAT water processor.

Results

Our observations showed that SPM concentrations and compositions varied strongly with tidal, weather, and seasonal conditions. Near the shore, SPM levels fluctuated significantly in response to changes in tidal currents and wind events. During high-energy tidal phases, larger sand grains and other particles were resuspended, leading to higher acoustic backscatter signals in the bottom water layers. In contrast, periods of calm weather and slack tide were marked by lower SPM concentrations, with fine cohesive particles and flocs dominating the water column.

Acoustic sensors demonstrated a strong response to these dynamic conditions, particularly in detecting periods of intense resuspension when coarser particles were present. However, we noted that these sensors tended to overestimate SPM concentrations when larger particles or flocs dominated the particle assemblage, due to the strong acoustic reflections associated with such materials.

Optical sensors, on the other hand, provided reliable measurements of SPM when fine cohesive particles were the main contributors to turbidity. However, they tended to underestimate concentrations during resuspension events dominated by larger sand grains or aggregates, due to the lower optical scattering efficiency of these coarser particles.

The LISST-200 instrument proved especially useful for monitoring changes in particle size distributions throughout the tidal cycle. It consistently showed that during calmer periods such as slack tide, larger flocs formed as a result of particle aggregation, and these larger particles settled more quickly. In contrast, during peak flood and ebb currents, higher turbulence broke up the flocs, resulting in smaller particle sizes.

Overall, integrating data from multiple sensors revealed the strong variability of SPM in the study area and demonstrated the complementary strengths of different measurement approaches for capturing these dynamics (see Fig.2).

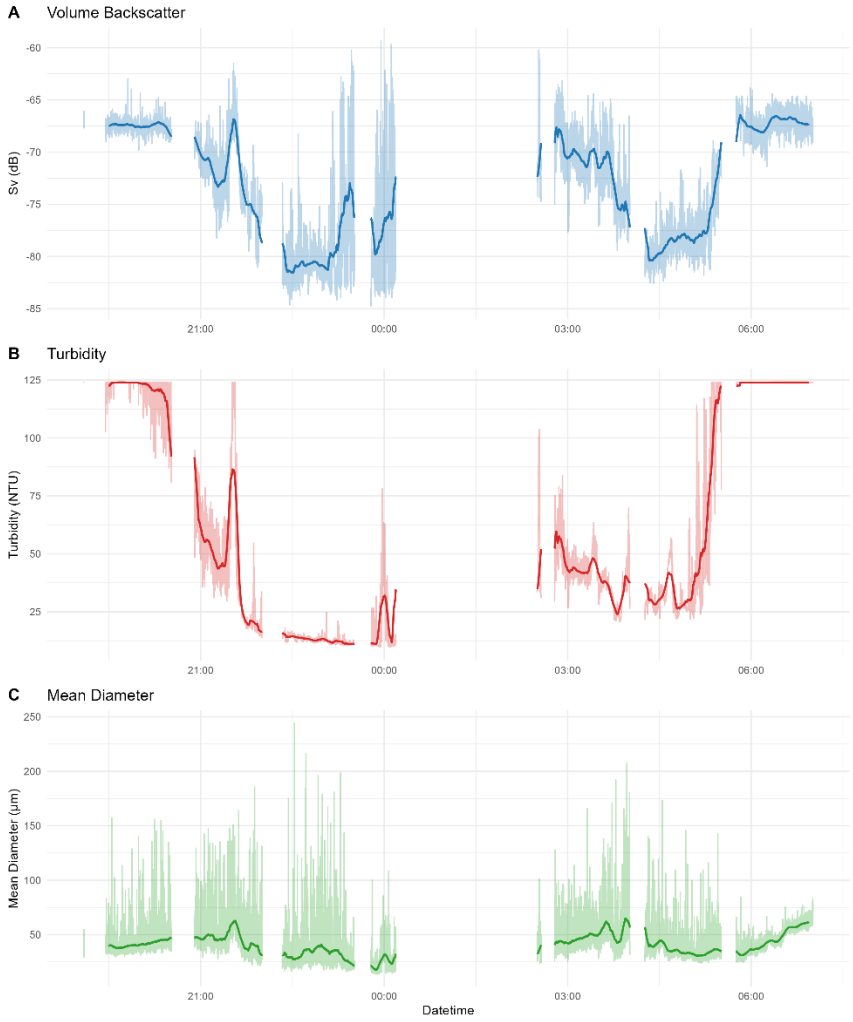

Figure 2. Example of a time-series of volume backscatter strength (Sv), mean particle diameter (µm), and turbidity (NTU) recorded at station MOW1. Raw data are shown with shaded lines, while smoothed trends highlight the main variations. Data gaps exceeding five minutes are excluded to avoid artificial connections.

Discussion

Our study confirms that no single sensor can fully capture the complex variations of SPM in tidal environments. The differences in sensor responses highlight the importance of understanding the physical principles behind each measurement technique. Acoustic backscatter data, depending on their frequency, are influenced by both the size and density of particles, making these sensors particularly sensitive to larger, denser grains. In contrast, optical sensors rely on light scattering, which is more effective for detecting fine, cohesive particles. These differences create challenges when SPM composition shifts rapidly in response to tides and wind-driven resuspension. By integrating data from both sensor types, we obtained a more complete picture of SPM dynamics. Acoustic measurements helped identify energetic resuspension events and the presence of sand in suspension, while optical sensors provided precise measurements of fine sediment concentrations during calmer periods. The LISST-200's particle size data were essential for interpreting these patterns and reconciling differences between sensor readings. The combined dataset also revealed that SPM in the study area is highly variable in time and space, requiring flexible and adaptive monitoring strategies. This variability is driven not only by tidal currents but also by wind-induced flows and episodic events, such as storms and persistent wind conditions, algal blooms, or human activitiets.

Conclusion

Our observations and analyses show that combining acoustic and optical sensors is essential for accurate and comprehensive monitoring of suspended particulate matter in dynamic tidal environments. Each sensor type provides complementary insights into SPM concentration and composition, and together, they offer a robust approach to characterizing particle dynamics.

This work emphasizes the need for multi-sensor approaches in coastal monitoring programs, especially in regions like the BPNS, where tidal and wind forcing create complex and rapidly changing SPM conditions. These findings have implications for environmental monitoring, ecosystem management, and understanding sediment transport in coastal areas. Future work will focus on refining calibration procedures for different sensors under varying conditions, and developing data fusion methods to produce more reliable and spatially comprehensive SPM maps. Such efforts will contribute to improved water quality assessments and better management of coastal environments.

References

Baeye, M., & Fettweis, M. (2015). In situ observations of suspended particulate matter plumes at an offshore wind farm, southern North Sea. Geo-Marine Letters 2015 35:4, 35(4), 247–255. https://doi.org/10.1007/S00367-015-0404-8

Baeye, M., Fettweis, M., Voulgaris, G., & Van Lancker, V. (2011). Sediment mobility in response to tidal and wind-driven flows along the Belgian inner shelf, southern North Sea. Ocean Dynamics 2011 61:5, 61(5), 611–622. https://doi.org/10.1007/S10236-010-0370-7

Capuzzo, E., Stephens, D., Silva, T., Barry, J., & Forster, R. M. (2015). Decrease in water clarity of the southern and central North Sea during the 20th century. Global Change Biology, 21(6), 2206–2214. https://doi.org/10.1111/GCB.12854

Creed, E. L., Pence, A. M., & Rankin, K. L. (2001). Inter-comparison of turbidity and sediment concentration measurements from an ADP, an OBS-3, and a LISST. Oceans Conference Record (IEEE), 3, 1750–1754. https://doi.org/10.1109/OCEANS.2001.968098

Downing, J. (2006). Twenty-five years with OBS sensors: The good, the bad, and the ugly. Continental Shelf Research, 26(17–18), 2299–2318. https://doi.org/10.1016/j.csr.2006.07.018

Fettweis, M., Baeye, M., Cardoso, C., Dujardin, A., Lauwaert, B., Van den Eynde, D., Van Hoestenberghe, T., Vanlede, J., Van Poucke, L., Velez, C., & Martens, C. (2016). The impact of disposal of fine-grained sediments from maintenance dredging works on SPM concentration and fluid mud in and outside the harbor of Zeebrugge. Ocean Dynamics, 66(11), 1497–1516. https://doi.org/10.1007/S10236-016-0996-1/METRICS

Fettweis, M., Baeye, M., Francken, F., Lauwaert, B., Van den Eynde, D., Van Lancker, V., Martens, C., & Michielsen, T. (2011). Monitoring the effects of disposal of fine sediments from maintenance dredging on suspended particulate matter concentration in the Belgian nearshore area (southern North Sea). Marine Pollution Bulletin, 62(2), 258–269. https://doi.org/10.1016/J.MARPOLBUL.2010.11.002

Fettweis, M., Schartau, M., Desmit, X., Lee, B. J., Terseleer, N., Van der Zande, D., Parmentier, K., & Riethmüller, R. (2022). Organic Matter Composition of Biomineral Flocs and Its Influence on Suspended Particulate Matter Dynamics Along a Nearshore to Offshore Transect. Journal of Geophysical Research: Biogeosciences, 127(1). https://doi.org/10.1029/2021JG006332

Kim, Y. H., & Voulgaris, G. (2014). Estimation of suspended sediment concentration in estuarine environments using acoustic backscatter from an ADCP. https://www.researchgate.net/publication/228780627

Martens, C., Van den Eynde, D., Lauwaert, B., Van Hoey, G., Devriese, L., Sterckx, T., Malherbe, B., & Vantorre, M. (2018). Dredging and dumping.

Nechad, B., Ruddick, K. G., & Park, Y. (2010). Calibration and validation of a generic multisensor algorithm for mapping of total suspended matter in turbid waters. Remote Sensing of Environment, 114(4), 854–866. https://doi.org/10.1016/j.rse.2009.11.022

Praet, N., Collart, T., Ollevier, A., Roche, M., Degrendele, K., De Rijcke, M., Urban, P., & Vandorpe, T. (2023). The Potential of Multibeam Sonars as 3D Turbidity and SPM Monitoring Tool in the North Sea. Remote Sensing, 15(20), 4918. https://doi.org/10.3390/RS15204918/S1

Van Lancker, V., & Baeye, M. (2015). Wave Glider Monitoring of Sediment Transport and Dredge Plumes in a Shallow Marine Sandbank Environment. PLOS ONE, 10(6), e0128948. https://doi.org/10.1371/JOURNAL.PONE.0128948

Vanhellemont, Q., & Ruddick, K. (2014). Turbid wakes associated with offshore wind turbines observed with Landsat 8. Remote Sensing of Environment, 145, 105–115. https://doi.org/10.1016/J.RSE.2014.01.009

Exploring (micro)plastic pollution in European ports: Antwerp and Rotterdam case studies

Xiebe Stiers, Mariana N. Miranda, Gert Everaert, Ana I. Catarino

Flanders Marine Institute (VLIZ), Jacobsenstraat 1, 8400, Oostende, Belgium

Exploring (micro)plastic pollution in European ports: Antwerp and Rotterdam case studies

Xiebe Stiers[a], Mariana N. Miranda[a], Gert Everaert[a], Ana I. Catarino[a]

[a]Flanders Marine Institute (VLIZ), Jacobsenstraat 1, 8400, Oostende, Belgium
Corresponding author: Xiebe Stiers; xiebestiers@gmail.com

Introduction

Plastic pollution has emerged as a major global environmental issue due to the high abundance of microplastics in the ocean, and the potential negative effects to organisms and ecosystems. Plastic items and particles which have been accidentally introduced in waters start to degrade, followed by fragmentation, due to the action of weather and physical-chemical stressors. This results in the introduction of macro- (> 2.5 cm), meso- (5 mm – 25 mm), micro- (1 μm – 5000 μm), and nanoplastics (1 - 1000 nm) in the ocean and in the environment[1,2]. Although awareness on this matter is increasing, there still is an urgent need to expand the knowledge on the abundance, distribution and fate of these plastics, specifically in places such as estuaries and ports, where plastic litter tends to accumulate[3]. In addition, it is estimated that the number of plastic particles in the ocean will triple in the next twenty years, if no action is taken[4]. In this context the project "Innovative solutions for plastic free European rivers" (INSPIRE) [Horizon Europe] aims to contribute to the Green Deal targets and the European Commission Mission to restore the ocean and inland waters by 2030[5].

INSPIRE is a four-year project (2023 – 2027) with the goal to develop, implement, test and validate a set of solutions to assist in mitigating the increasing aquatic plastic pollution[5,6]. It brings different technologies and actions together with a focus on three main aspects: detection, collection, and prevention. Detection is about identification, quantification and characterization of litter pollution in rivers and transitional waters, such as finding the type and number or mass of macro-, meso-, and microplastics that are present in the water or sediment. Collection covers retrieval of litter and plastic from rivers. This results in a minimal lifetime of this pollutant in the river, preventing further fragmentation of these particles. Finally, prevention is about implementing different strategies that reduce the inputs of litter, macro-, meso-, and microplastics being introduced in the aquatic environment. This includes research towards technologies that enable the collection of litter before it reaches rivers, ports and estuaries or the development of alternatives for the currently used products that are responsible for plastic pollution. The INSPIRE project makes use of six rivers (demo cases) across Europe to conduct research on this topic: the Rhine, Scheldt, Danube, Kamniska Bistrica, Po, and Douro[5]. In the context of the INSPIRE project, the objective of this study was to assess the microplastic,

mesoplastic, and litter abundance from Doeldok (port of Antwerp; Scheldt, BE) and Londenhaven (port of Rotterdam; Rhine, NL), and to characterize the particles diversity.

Methods

The samples used for analysis were obtained using different sampling methods. The first method relied on sampling using a Ferrybox (Fig. 1.a)[5], a semi-automated device that collects (sea)water and retains microplastics and other microlitter, at a specific water depth. It consists of a collection module that uses a series of sieves to sort the plastics within different size fractions, which is then connected to the Ferrybox system itself that is onboard a research vessel or connected to a submerged pump. In addition, the volume of filtered water and flow rate within the collection module can be recorded[5]. A second sampling method used was the manta net (Fig 1.b)[5], a device designed to sample plankton, but now adapted for the collection of microlitter and microplastics that are floating or are within the first few centimeters of the water column. The microplastics were extracted from the obtained samples using established standard operating procedures[7] and the analysis of the particles was performed using an automated decision-making model, that detects and identifies plastic particles using images taken with a fluorescent microscope under different filters[7,8]. Following this, the microplastics presence and the polymer identification were verified using μ-Fourier transform infrared (FTIR) spectroscopy[7].

Figure 1. Sampling methodologies used in this study, to assess microplastics abundance in various matrices: (a) the Ferrybox sampling system, (b) the manta net, (c) the riverbank quadrat. (source: INSPIRE)

Additionally, quadrat (20 x 20 cm) sampling along a transect was performed to collect larger microplastic (1 - 5 mm), mesoplastic particles, and litter in general, in the riverbanks of the selected sampling locations (Fig. 1.c), using metal tweezers[5]. At both sites, sampling was performed at the beginning, middle and end of three different transects of 100 m (Doeldok, BE) or 30 m (Londenhaven, NL). The collected pellets were counted to determine the particle concentrations at each transect, followed by analysis using Fourier transform infrared/attenuated total reflection (FTIR/ATR) spectroscopy, after a cleaning step using ethanol and miliQ-water.

Results

The mean concentration of particles and litter items was estimated after using both the automated model and FTIR analysis, and the mean abundance of items varied between 0.47 and 19.63 particles / m^3 (Table 1). When comparing the decision-making model to the FTIR analysis, we observed that the model underestimates the number of particles for all measurements. We have further observed that the manta net samples show lower particle concentrations than the Ferrybox samples. The Ferrybox measurements indicated a higher particle abundance for Doeldok than for Londenhaven.

Table 1. Mean (± SD, n = 3) plastic particle concentrations with standard deviations, as observed by the decision-making model and FTIR analysis.

	Automated model: (particles / m^3)	**FTIR: (particles / m^3)**
Doeldok (Port of Antwerp) - Ferrybox	16.58 ± 21.53	19.63 ± 22.59
Doeldok (Port of Antwerp) - Manta net	0.47 ± 0.31	1.87 ± 1.35
Londenhaven (Port of Rotterdam) - Ferrybox	5.36 ± 4.48	9.34 ± 5.99

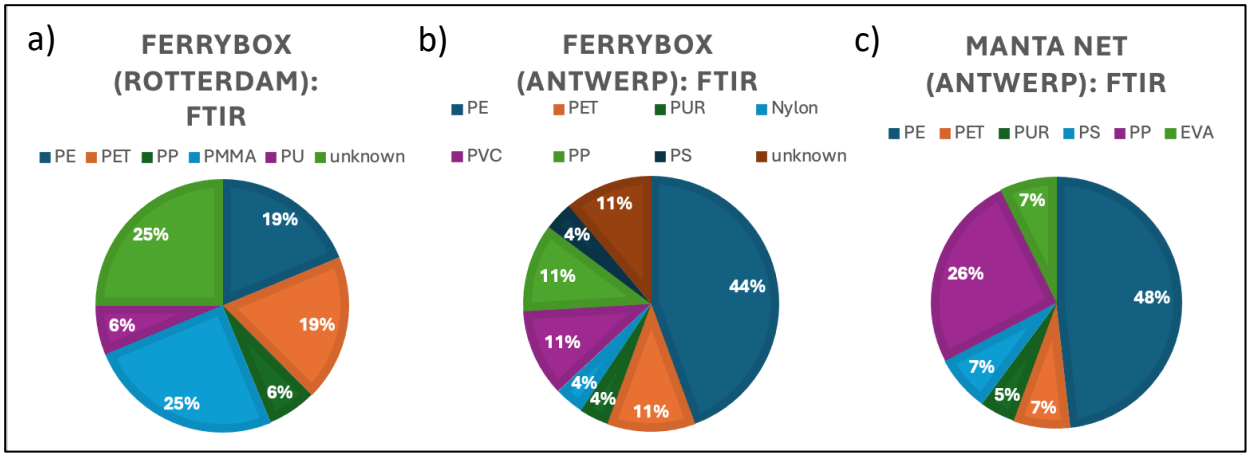

Figure 2. Proportion of particles observed from each polymer type at the different sites: (a) Ferrybox samples collected in Rotterdam, (b) Ferrybox samples collected in Antwerp, (c) manta net samples collected in Antwerp.

The most common polymer type observed varied between compartment sampled: PMMA was the most common polymer observed in samples acquired in Rotterdam using the Ferrybox, while PE was the most common polymer observed for samples acquired both using the Ferrybox and manta net in Antwerp (Fig. 2). For the Ferrybox samples at both sites, the polymer types of some

particles remained unknown, as the FTIR results did not have a sufficient correlation to the spectrum of a certain polymer type. This can be an indication that the material was not a plastic but cannot be confirmed as such.

Table 2. Overview of the collected litter particles in Doeldok (port of Antwerp, BE) and Londenhaven (port of Rotterdam, NL), using 20 x 20 cm quadrats.

	Doeldok: particle number per sample	Doeldok: concentration (particles / m^2)	Londenhaven: particle number per sample	Londenhaven: concentration (particles / m^2)
Transect 1: beginning	20	500	257	6425
Transect 1: middle	10	250	218	5450
Transect 1: end	5	125	94	2350
Transect 1: 15m	71	1775	NA	NA
Transect 1: weighted mean	31.6	790	279.67	4741.67
Transect 2: beginning	2	50	NA (sample too large, and so not quantified)	NA
Transect 2: middle	2	50	208	5200
Transect 2: end	4	100	40	1000
Transect 2: weighted mean	2.67	66.67	> 124*	> 3100*
Transect 3: beginning	0	0	15	375
Transect 3: middle	4	100	19	475
Transect 3: end	1	25	473	11825
Transect 3: weighted mean	71	1775	169	4225

**The sample at the beginning of transect 2 was too large, it was not counted and not considered when calculating the average.*

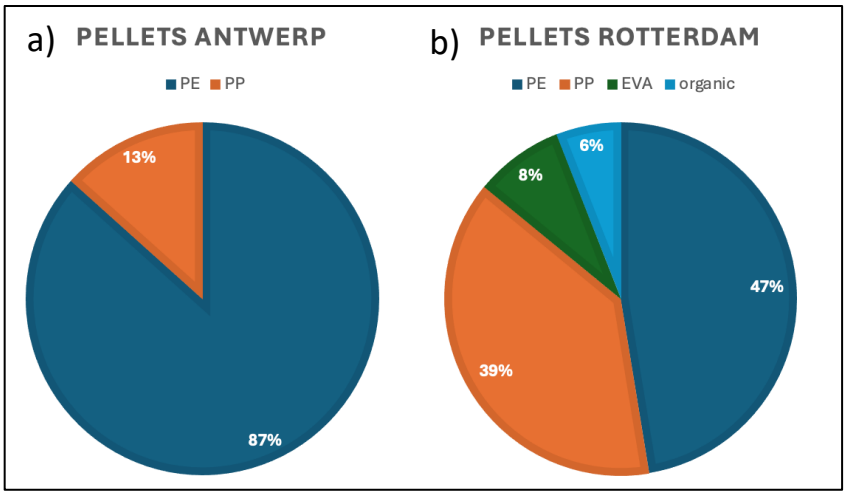

Figure 3. Proportion of pellets from each polymer type observed at the different sites: (a) Doeldok (port of Antwerp, BE), (b) Londenhaven (port of Rotterdam, NL).

The highest concentration of litter was observed in the Port of Rotterdam (11,825 particles / m^2), exceeding the highest concentration observed in the port of Antwerp (1,775 particles / m^2) (Table 2). The polymer types of the pellets in both sampled locations were mainly PE and PP, with the former being most common polymer type.

Discussion

High concentrations of litter particles were recorded in Doeldok and Londenhaven, across all sampling methods, with mean concentrations ranging from 0.47 particles / m^3 to 4,741.67 particles / m^3. Manta net and Ferrybox sampling indicated the presence of microplastics in both the water surface and on the water column, which varied between 0.47 particles / m^3 and 19.63 particles / m^3, respectively. Furthermore, micro- and mesolitter collection using quadrat sampling revealed a high concentration of plastics and other litter at both sites, with concentrations ranging from 0 particles / m^3 (Doeldok; BE) up to 11,825 particles / m^3 (Londenhaven; NL) being reported.

The analysis of the abundance of particles revealed a large variation depending on the location and sampling method (which reflects the sampling depth in the water column). The lowest concentrations observed correspond to manta net samples (0.47 particles / m^3). As the manta net samples were taken at the water surface, this is an indication that more particles were located in the water column, where Ferrybox samples were taken. This suggests a moderate to high flux was occurring during sampling. In contrast, a low flux typically associated with the turn of the tide would lead to accumulation of particles at the surface, resulting in a higher abundance of particles in the manta net samples. Furthermore, the concentration of particles sampled using the Ferrybox was higher in Doeldok (BE) than in Londenhaven (NL), and therefore we suggest that these results should be further investigated by additional sampling over multiple time points, to analyze if there is a specific trend linked to this observation.

Polyethylene (PE) and polypropylene (PP) were amongst the most abundant polymers observed in the microlitter for both Antwerp and Rotterdam. In addition, Rotterdam showed a remarkable 25% share of polymethylmethacrylate (PMMA). In contrast to these results, the microplastics collected using the manta net were almost exclusively PE and PP particles. The polymer types from the Ferrybox samples indicated that different locations contain a diverse range of categories, with certain polymers occurring exclusively at one of the two sites, such as polyvinylchloride (PVC) and polystyrene (PS) for Doeldok, and the abundant PMMA for Londenhaven. Furthermore, the results suggest turbulence was present during sampling, as low-density polymers, such as PE and PP, were detected in the Ferrybox samples. Additionally, the presence of high-density polymers, such as polyethylene terephthalate (PET), in the manta net samples further supports this observation. These are important observations, as these unique

patterns for the different sampling sites establish new developments towards finding the origins of these different types of microplastics.

The abundance of large micro- and mesolitter by the riverbank quadrats showed high concentrations at both sampling sites, with substantially higher levels observed for Londenhaven, where concentrations reached up to 11,825 particles / m^2. From the observed litter types, pellets were the most abundant at both sites. This indicates that these materials are within the most important sources of plastic pollution in the riverbanks around these large port areas. Furthermore, the pellets predominantly are PE and PP, with PE being more abundant than PP on both sites. In Rotterdam, NL, some pellets were categorized as organic material, and several pellets were ethylene/vinyl acetate copolymer. The results of this study provide a first step towards monitoring the origin of these pellets, indicating whether the pellet loss is related to production and an important mismanagement of transport in the port areas or transport.

Conclusion

In this study, the particle abundance of micro- and mesolitter has been assessed at the ports of Antwerp (BE) and Rotterdam (NL), the two largest industrial and commercial ports in Europe. The Ferry box and manta net sampling methods were used, and our samples have indicated the presence of a variety of microplastics within the water column (largest concentrations) and at the water surface. Furthermore, we used quadrat sampling along transects in riverbanks, and our observations indicate a very high abundance of large microlitter and mesolitter, with the concentrations for Londenhaven (NL) being significantly higher than for Doeldok (BE). The FTIR analysis on the different litter particles contributed to a deeper insight on the polymer types present at both sites, indicating a unique variety of compositions at the different locations, with the most abundant polymers observed being PE and PP. The results of this study have produced key data that will be incorporated into the analysis of plastic particles transport and fate, and will be incorporated into baseline analysis on prevention actions.

References

(1) Hartmann, N. B.; Hüffer, T.; Thompson, R. C.; Hassellöv, M.; Verschoor, A.; Daugaard, A. E.; Rist, S.; Karlsson, T.; Brennholt, N.; Cole, M.; Herrling, M. P.; Hess, M. C.; Ivleva, N. P.; Lusher, A. L.; Wagner, M. Are We Speaking the Same Language? Recommendations for a Definition and Categorization Framework for Plastic Debris. *Environ. Sci. Technol.* **2019**, *53* (3), 1039–1047. https://doi.org/10.1021/acs.est.8b05297.

(2) *ISO 24187:2023(en), Principles for the analysis of microplastics present in the environment*. https://www.iso.org/obp/ui/#iso:std:iso:24187:ed-1:v1:en (accessed 2025-03-19).

(3) Schreyers, L. J.; van Emmerik, T. H. M.; Bui, T.-K. L.; van Thi, K. L.; Vermeulen, B.; Nguyen, H.-Q.; Wallerstein, N.; Uijlenhoet, R.; van der Ploeg, M. River Plastic Transport Affected by Tidal Dynamics. *Hydrol. Earth Syst. Sci.* **2024**, *28* (3), 589–610. https://doi.org/10.5194/hess-28-589-2024.

(4) *Plastic Pollution Around the World | Plastics and the Environment Series*. https://www.genevaenvironmentnetwork.org/resources/updates/plastic-pollution-around-the-world/ (accessed 2025-03-17).
(5) *Inspire Europe*. Inspire Europe. https://inspire-europe.org/ (accessed 2025-03-17).
(6) *Innovative Solutions for Plastic Free European Rivers | INSPIRE | Projekt | Fact Sheet | HORIZON*. CORDIS | European Commission. https://cordis.europa.eu/project/id/101112879 (accessed 2025-06-10).
(7) Meyers, N.; Bouwens, J.; Catarino, A.; Witte, B. D.; Everaert, G. Standardised Operating Procedure for the Extraction of Microplastics from Marine Seawater Samples.
(8) Meyers, N.; Catarino, A. I.; Declercq, A. M.; Brenan, A.; Devriese, L.; Vandegehuchte, M.; De Witte, B.; Janssen, C.; Everaert, G. Microplastic Detection and Identification by Nile Red Staining: Towards a Semi-Automated, Cost- and Time-Effective Technique. *Sci. Total Environ.* **2022**, *823*, 153441. https://doi.org/10.1016/j.scitotenv.2022.153441.

Microplastic pollution in the inner Ría de Arousa: seasonal variability and transport pathways from riverine, urban, and industrial sources

Marisela Des[a], Juan Santos-Echeandía[b], Patricia Bernardez[b], Maite de Castro[a], Jesús Gago[b], Moncho Gómez-Gesteira[a]

[a]Centro de Investigación Mariña, Universidade de Vigo, Environmental Physics Laboratory (EPhysLab), Campus As Lagoas s/n, 32004 Ourense, Spain

[b]Centro Oceanográfico de Vigo (IEO, CSIC), Subida a Radio Faro 50, Vigo, 36390, Spain e

Microplastic pollution in the inner Ría de Arousa: seasonal variability and transport pathways from riverine, urban, and industrial sources

Marisela Des [a], Juan Santos-Echeandía[b], Patricia Bernardez[b], Maite de Castro[a], Jesús Gago[b], Moncho Gómez-Gesteira [a]

[a]Centro de Investigación Mariña, Universidade de Vigo, Environmental Physics Laboratory (EPhysLab), Campus As Lagoas s/n, 32004 Ourense, Spain
[b]Centro Oceanográfico de Vigo (IEO, CSIC), Subida a Radio Faro 50, Vigo, 36390, Spain

Corresponding author: Marisela Des; mdes@uvigo.gal

Introduction

Microplastic contamination has become a prominent environmental concern in marine and estuarine ecosystems due to its persistence, ubiquity, and potential ecological and toxicological impacts. Defined as plastic particles smaller than 5 mm, microplastics originate from both primary sources, such as industrial pellets and synthetic fibers, and secondary sources, primarily through the degradation of larger plastic debris. Once in the aquatic environment, their transport, accumulation, and bioavailability are strongly influenced by hydrodynamic conditions and the location and intensity of input sources.

The Ría de Arousa, located on the northwestern Atlantic coast of the Iberian Peninsula, is the largest of the Galician rias and represents a highly productive estuarine system of ecological and economic significance. The inner sector of the ria is subject to intense anthropogenic pressure due to the presence of urban centers, aquaculture facilities, mainly mussel rafts, and industrial activity. It also receives freshwater input primarily from the Ulla River, which has a catchment area of 2,769 km² and a mean discharge of 79.3 m³/s, making it by far the most significant fluvial contributor among the rivers discharging into the Galician rias. For comparison, other major rivers in the region, such as the Tambre (54.1 m³/s), Umia (16.4 m³/s), Lérez (21.2 m³/s), and Verdugo–Oitavén (17.0 m³/s) present substantially lower discharge values. The inner Ría de Arousa is a particularly dynamic and sensitive area to study microplastic input and transport because of the hydrological dominance of the Ulla River and the proximity of several potential pollution sources.
Among the key sources of microplastic entry into this system are the Ulla River itself, the municipal wastewater outfall of Vilagarcía de Arousa, multiple stormwater overflow points, and several industrial discharge outlets located along the shoreline.

This study examines the abundance, typology, and dispersion dynamics of microplastics in the inner Ría de Arousa using a dual approach: field sampling campaigns and numerical simulations.

Sampling was conducted under contrasting hydrometeorological conditions, during a dry period in September 2023 and following the first major autumn rainfall events in November 2023. Microplastic samples were collected along three transects in the vicinity of the Ulla estuary, quantified, and classified by polymer type. To complement the field data, a hydrodynamic simulation was conducted using the Delft3D 4 FLOW model, coupled with the Lagrangian particle-tracking module PART.

By combining empirical observations and numerical modeling, this study aims to elucidate the mechanisms governing microplastic transport and accumulation in the inner Ría de Arousa. Special emphasis is placed on the role of variable hydrological inputs and the influence of anthropogenic point sources, including both municipal and industrial discharges.

Methods

Two microplastic sampling campaigns were carried out in the inner Ría de Arousa, Galicia, Spain, under contrasting hydrometeorological conditions. The first took place on September 19, 2023, during a dry period, and the second on November 9, 2023, following the first significant autumn rainfall events. Sampling was conducted along four transects strategically located in the inner ria: two transverse transects were positioned directly in front of the mouth of the Ulla River and one longitudinal transect extended seaward from the Ulla estuary, and another longitudinal transect was located along the southern coastline, in front of the urban area of Vilagarcía de Arousa.

Microplastics were collected using a manta trawl net, which was towed at the sea surface in accordance with standardized methodologies for microplastic surface sampling. After collecting, the samples were filtered and dried before being sorted and analyzed in the laboratory. Particles were classified by polymer type and then quantified in terms of the number of items per km^2. Additionally, each microplastic item was classified by morphology into one of five types: fragment, film, filament, foam, or fiber.

To assess the hydrodynamic behavior of the inner Ría de Arousa and simulate the dispersion of microplastics during the study period, the Delft3D 4 FLOW model, previously calibrated and validated by Des et al. (2019), was employed. The simulation period extended from September 1 to November 16, 2023, including a 15-day spin-up period to allow the model to reach hydrodynamic equilibrium before the start of the first sampling campaign.

The FLOW module was coupled with the PART module to simulate Lagrangian particle transport. Particles were assigned the physical properties of polyethylene (PE), including density

and settling behavior, since PE was by far the most abundant polymer found in both sampling campaigns.

Three main sources of microplastic input were included in the model: i) the Ulla River, modeled with a continuous input of particles scaled by river discharge data; ii) the municipal wastewater outfall of Vilagarcía de Arousa, where microplastic input was modulated by precipitation-dependent treatment efficiency of the wastewater treatment plant (WWTP); iii) numerous urban and domestic stormwater overflow points, whose discharges were activated in the model based on precipitation events.

In all cases, the temporal variation of microplastic inputs was implemented using continuous time series, with concentration levels dynamically adjusted according to the flow regime. For the Ulla River, inputs varied proportionally with daily river discharge. For the wastewater outfall, inputs were linked to WWTP capacity and overflows, which are known to occur during heavy rainfall. For stormwater overflows, particle release events were directly tied to rainfall intensity and frequency.

The model outputs included spatial and temporal maps of particle concentrations, residence times, and transport pathways, allowing for the assessment of microplastic behavior under realistic hydrodynamic and meteorological conditions.

Results

Microplastics were detected in all transects during both sampling campaigns, confirming the widespread presence of plastic debris in the inner Ría de Arousa. Overall concentrations were higher in the November campaign, following the onset of autumn rainfall, compared to the September campaign, which was conducted during a prolonged dry period. This seasonal difference suggests a direct influence of increased runoff and overflow events on microplastic loading in the estuary.

In both campaigns, polyethylene (PE) was the dominant polymer, accounting for almost half of the total particles collected during the first campaign and more than half of the total particles collected during the second campaign. Other polymers were also present in smaller proportions. In terms of particle morphology, fragments were the most abundant category.

Contrary to initial expectations, the highest concentrations of microplastics were not recorded near the Ulla River mouth, despite it being the primary freshwater input to the estuary; rather, they were found along the southern coastal transect, directly in front of the urban area of

Vilagarcía de Arousa. This pattern was observed in both campaigns and became even more pronounced in November. The elevated presence of particles in this area is consistent with proximity to urban and industrial drainage infrastructure, including stormwater overflows and wastewater outfalls.

The Lagrangian particle tracking simulations showed that microplastic particles introduced from the Ulla River predominantly followed the main longitudinal axis of the estuary, moving westward under the combined influence of river flow and tidal mixing. However, a consistent lateral drift toward the northern shoreline was observed, likely influenced by residual circulation patterns.

Particles released from the municipal outfall and stormwater/industrial overflows near Vilagarcía de Arousa, showed more localized dispersion patterns, with high residence times and accumulation in nearby coastal zones, especially under low-wind, neap tide conditions. During rainfall events, these sources contributed intense pulses of microplastics, which remained concentrated in the southern coastal zone due to limited transport and high residence times. The model indicates that under specific hydrodynamic conditions, this area can become a persistent hotspot for microplastics.

Discussion

The results of this study offer insight into the spatial and temporal variability of microplastic pollution in the inner Ría de Arousa. The predominance of polyethylene (PE) across all sampling sites and both campaigns is consistent with global findings, as PE is one of the most widely produced and used polymers, with high buoyancy and environmental persistence.

The seasonal contrast between the dry (September) and wet (November) campaigns underscores the key role of hydrological forcing in driving microplastic input and dispersion. The increased concentrations observed after the first autumn rainfall events suggest that surface runoff, combined sewer overflows, and reduced wastewater treatment efficiency under high precipitation are critical pathways for land-based microplastic input into the estuary. This seasonal pulse is typical in estuarine systems where episodic events dominate pollutant loading, and highlights the need to consider non-continuous, precipitation-driven emissions in monitoring and management efforts.

The numerical model provided valuable information on transport dynamics and retention zones. The simulation showed that particles originating from the Ulla River, the main freshwater source to the estuary, followed the estuarine axis but exhibited a consistent lateral shift toward the northern shoreline.

However, the highest particle retention and accumulation occurred near the southern coastal zone, close to the urban discharge points, especially during high-rainfall periods. The model confirmed that these sources, under conditions of limited flushing, can result in persistent contamination hotspots.

These findings have important environmental implications. Microplastic accumulation in shallow coastal zones near urban areas increases the risk of exposure for benthic organisms, filter feeders, and aquaculture species, particularly relevant in the Ría de Arousa, where shellfish farming is economically and ecologically significant. Furthermore, the localized retention of particles under certain conditions suggests that management actions could be targeted geographically, focusing on urban infrastructure upgrades, overflow control, and rainwater management.

Conclusion

This study investigated the presence, distribution, and transport of microplastics in the inner Ría de Arousa, integrating field sampling and numerical modeling to characterize spatial patterns and potential sources. The main conclusions are as follows:

- Microplastics were present throughout the inner estuary in both sampling periods, with higher concentrations observed in November, following the onset of autumn rainfall. This highlights the role of seasonal hydrological dynamics in modulating microplastic loads.

- Contrary to expectations, the highest concentrations were not found near the Ulla River mouth, despite its dominant discharge, but rather along the southern coastal area in front of Vilagarcía de Arousa, an urbanized and industrialized zone. This indicates that urban runoff, stormwater overflows, and wastewater discharges are likely the main contributors to microplastic pollution in this part of the estuary.

- Polyethylene (PE) was the most abundant polymer in both campaigns, consistent with its ubiquity and buoyancy, while PET and synthetic fibers were especially prevalent near urban outfalls, supporting their attribution to domestic and industrial wastewater sources.

- Numerical modeling using Delft3D-FLOW coupled with the PART module confirmed the role of combined sewer overflows and wastewater effluents as key point sources, particularly during rainfall events. The model also showed that microplastics from the Ulla River tended to follow the main estuarine axis, with a lateral drift toward the northern shoreline, whereas particles from urban outfalls tended to accumulate locally in the southern coastal zone.

These results emphasize the need to expand pollution control strategies beyond major riverine sources to include urban infrastructure, particularly in regions with frequent rainfall and combined sewer systems. Targeted mitigation efforts in urbanized estuarine zones could significantly reduce local microplastic contamination. Moreover, this study demonstrates the utility of combining in situ monitoring with high-resolution hydrodynamic modeling to identify priority sources and zones of accumulation. The findings are particularly relevant for coastal management and water quality policy, especially in estuaries with high ecological and economic value, such as the Ría de Arousa.

References

Des, M., DeCastro, M., Sousa, M. C., Dias, J. M., & Gómez-Gesteira, M. (2019). Hydrodynamics of river plume intrusion into an adjacent estuary: The Minho River and Ria de Vigo. Journal of Marine Systems, 189, 87-97. https://doi.org/10.1016/j.jmarsys.2018.10.003

Understanding the Settling Behavior of Microplastics with Fine Sediments

Vania Ruiz-Gonzalez[a,b], Sophie Defontaine[c,d], sabel Jalon-Rojas[a]

[a] **Univ. Bordeaux, CNRS, Bordeaux INP, EPOC, UMR 5805, Pessac, France**

[b] **Universidad Autonoma de Sinaloa, Facultad de biologia, Mexico**

[c] **Cerema, RHITME Research Team, Margny Les Compiegne, France**

[d] **University Rouen Normandie, Universite Caen Normandie, CNRS, Normandie University, M2C UMR 6143, Rouen, France**

Understanding the Settling Behavior of Microplastics with Fine Sediments

Vania Ruiz-Gonzalez[ab], Sophie Defontaine[cd], sabel Jalón-Rojas[a]

[a] Univ. Bordeaux, CNRS, Bordeaux INP, EPOC, UMR 5805, Pessac, France
[b]Universidad Autónoma de Sinaloa, Facultad de biología, México
[c]Cerema, RHITME Research Team, Margny Les Compiègne, France
[d]University Rouen Normandie, Université Caen Normandie, CNRS, Normandie University, M2C UMR 6143, Rouen, France

Corresponding author: Sophie Defontaine; sophie.defontaine@cerema.fr

Introduction

Plastic pollution is ubiquitous in aquatic environments, including in previously considered "pristine" environment such as deap sea location (Peng et al., 2020; Van Cauwenberghe et al., 2013). Microplastics (MP), i.e. plastic particles of the longest dimension being below 5mm, represent a large part of the global plastic pollution. They can originate from primary source (i.e. be produced for industrial use) or secondary source (i.e. by mechanical, photochemical and/or biological degradation of larger plastic debris).

Understanding of MPs behavior is crucial for predicting accumulation, identifying potential areas of ecological risk and managing/preventing plastic pollution. MP transport dynamics has received increasing attention in recent years. Several studies have focused in measuring the settling velocity of individual MP, with different physical characteristics (e.g. shape, size, density, pristine/aged particles) under controlled conditions. Several semi-empirical formulation taking into account shape factors have been derived from such laboratory experiments (Bagheri & Bonadonna, 2016; Francalanci et al., 2021; Waldschläger et al., 2019). However, in natural aquatic environments, significant interactions with other suspended particles may occur, especially in estuaries with high suspended sediment concentration.

This study set out to investigate the settling velocity of small MPs (below 150 µm) of different characteristics (size, shape, density) in clear and turbid salty waters, under controlled conditions.

Methods

Three types of MP particles were selected for our experiments: spheres of polyethylene (1,2 g/cm^3), irregular particles of poly(methyl methacrylate) (1,18 g/cm^3) and fragments of polystyrene (1,05 g/cm^3). They were suspended in seawater (Certified filtered Atlantic Seawater, OSIL) with or without natural sediments from the Gironde Estuary characterized by size ranging from 4-17 µm and low organic content (POC<2%).

Three different treatments were applied to suspensions of MP with sediments before settling velocity measurements: (I) no treatment; (ii) orbital shaker agitation during 20hrs; (iii) 5 months resting at low temperature and no light.

Measuring settling velocities under highly turbid conditions preclude classical measuring techniques (e.g. holography, optic, video). An innovative optical settling column named SCAF, previously successfully deployed in hyper turbid environment, has been used to estimate settling velocity in the present study.

Results

Settling velocity distributions of individual particles in saline waters reveal that the size, shape and density impacts settling velocity of MP particles differently. For example, the size has a bigger influence on spherical particles settling velocity than other irregular particles and fragments settling velocity. Shape and density have stronger impacts on the settling velocities of bigger particles. A comparison with Stokes formula, generally used for natural sediment, indicate that settling behavior of small MPs is comparable to the one of natural sediments (Figure 1).

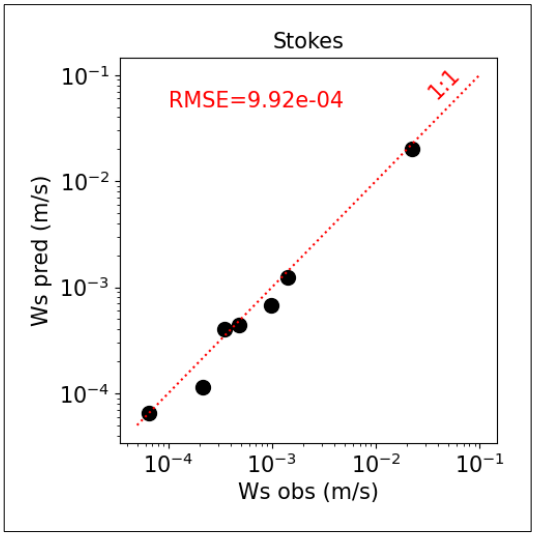

Figure 1. Comparison between measured median settling velocity and predictions based on Stokes formula.

When MP are suspended in saline turbid waters (SSC=500 mg/L), we can observe significant modification of the settling velocity distributions with or without any pre-treatment (agitation or resting), indicating flocculation between MP and suspended sediment. Regular spherical MPs seems less prone to enhance flocculate than irregular particles and fragments. Such results can be

explained by the fact that surface roughness ease binding between MP and sediments. Agitation and resting largely favor flocculation between MPs and sediments by enhancing collision/contact between particles.

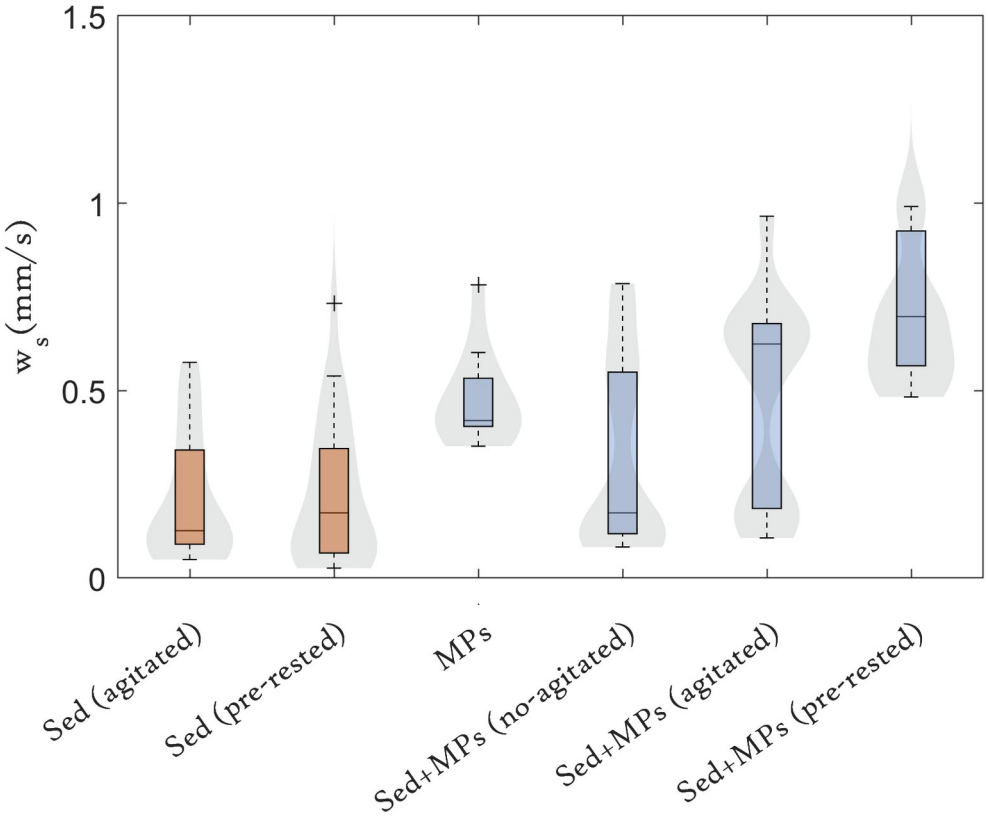

Figure 2. Settling velocity distributions of suspension of sediments and/or microplastics.

Conclusion

The study showed that Stokes formula well predicts small MP individual settling velocity, as it does for natural sediment. Therefore, settling dynamic of small MP seems to have comparable behavior as natural particles. However, semi-empirical formulations dedicated to MPs have been recently developed for MP particles due to shape effect, which may be necessary for bigger particles, as our study shows that the shape of the particles seems to have a greater influence on settling velocities of particles above 100µm.

Flocculation significantly modifies settling dynamics of MPs in turbid conditions, especially when long period of resting are considered allowing burial of MP in the sediments. That needs to be considered for management of plastic pollution in turbid environment such as estuaries.

References

Bagheri, G., & Bonadonna, C. (2016). On the drag of freely falling non-spherical particles. Powder Technology, 301, 526-544.

Francalanci, S., Paris, E., & Solari, L. (2021). On the prediction of settling velocity for plastic particles of different shapes. *Environmental Pollution*, *290*, 118068.

Peng, G., Bellerby, R., Zhang, F., Sun, X., & Li, D. (2020). The ocean's ultimate trashcan: Hadal trenches as major depositories for plastic pollution. Water research, 168, 115121.

Van Cauwenberghe, L., Vanreusel, A., Mees, J., & Janssen, C. R. (2013). Microplastic pollution in deep-sea sediments. Environmental pollution, 182, 495-499.

Waldschläger, K., & Schüttrumpf, H. (2019). Effects of particle properties on the settling and rise velocities of microplastics in freshwater under laboratory conditions. *Environmental science & technology*, *53*(4), 1958-1966.

Transport of alien particles in sand beds mobilised by waves

Otto Neshamar, Dominic van der A, Jos Derksen, Tom O' Donoghue

University of Aberdeen, King' s college, Aberdeen, UK

Transport of alien particles in sand beds mobilised by waves

Otto Neshamar[a], Dominic van der A[a], Jos Derksen[a], Tom O'Donoghue[a]

[a]University of Aberdeen, King's college, Aberdeen, UK
Corresponding author: Otto Neshamar; o.neshamar@abdn.ac.uk

Introduction

Coastal sand beds often contain discrete particles which differ from the native sand in terms of particle size, density and shape. These "alien particles" range from low-density microplastics to high-density industrial waste particles. As the sand is mobilised by waves or currents, the alien particles are transported and may spread throughout the surrounding region. Understanding the mechanisms governing the transport of alien particles is essential for assessing the impact of pollutants of various forms on the coastal environment.

A density-dependence of the wave-induced transport of particles has long been observed in sedimentological studies (Komar, 2007). However, due to the difficulty of direct observation, this was only described on a long-term basis, and detailed mechanisms have not been quantified. Recent wave flume studies have focused on microplastic particles on a sloped sand bed (e.g. Guler et al., 2022; Laksanalamai & Kobayashi, 2023), measuring net particle movement as a function of size, shape and density. However, due to the complexity of the problem, including progressive wave transformation and a changing and evolving bed morphology, generalising their observations is challenging. For bulk sand transport under waves, much understanding has derived from experiments in oscillatory flow tunnels (OFTs, see e.g. van der A, (2013)). These facilities create purely horizontal oscillatory flows similar to near-bed conditions under full-scale coastal waves; by varying the shape of the oscillatory velocity timeseries, different nonlinear waves can be represented in a controlled manner.

The aim of the present study was to conduct a systematic investigation of alien particle transport in sand beds mobilised oscillatory flows representative of large coastal waves. Alien particles in the 2-10 mm size range with a range of different densities and shapes are considered.

Methods

Experiments were conducted in the Aberdeen Oscillatory Flow Tunnel (AOFT, Figure 1(a)). The AOFT is a 16 m long, 0.3 m wide U-tube facility capable of producing horizontal oscillatory flows representative of near-bed conditions under large waves. A 6 m long, 0.25 m deep sand bed was placed in the middle test section of the tunnel. Experiments involved placing a small number of alien particles on a flat sand bed, after which it was exposed to a short, controlled sequence of oscillatory flow. Particles were colour-coded by type, allowing many particles to be tested in each experiment. Net movement of particles was recorded by measuring their position

before and after each experiment. In addition, particle motions were recorded using an array of four CMOS colour cameras (2 MP, 50 fps) installed in the tunnel lids, imaging a continuous region of approximately 2 m near the middle of the test section. A monochrome high-speed camera was used to simultaneously record the experiment from the side, imaging a ~0.3 m long region of the test section at 250-300 fps. Figure 1(b) shows the arrangement of cameras relative to the sand bed. The colour cameras were installed in custom-made viewports in the tunnel lid, with dome-shaped acrylic windows for minimal optical distortion. Around each viewport, arrays of high-intensity white LED strips were placed in sealed enclosures on the underside of the lid to achieve uniform illumination. Viewports and LED arrays are pictured in Figure 1(c).

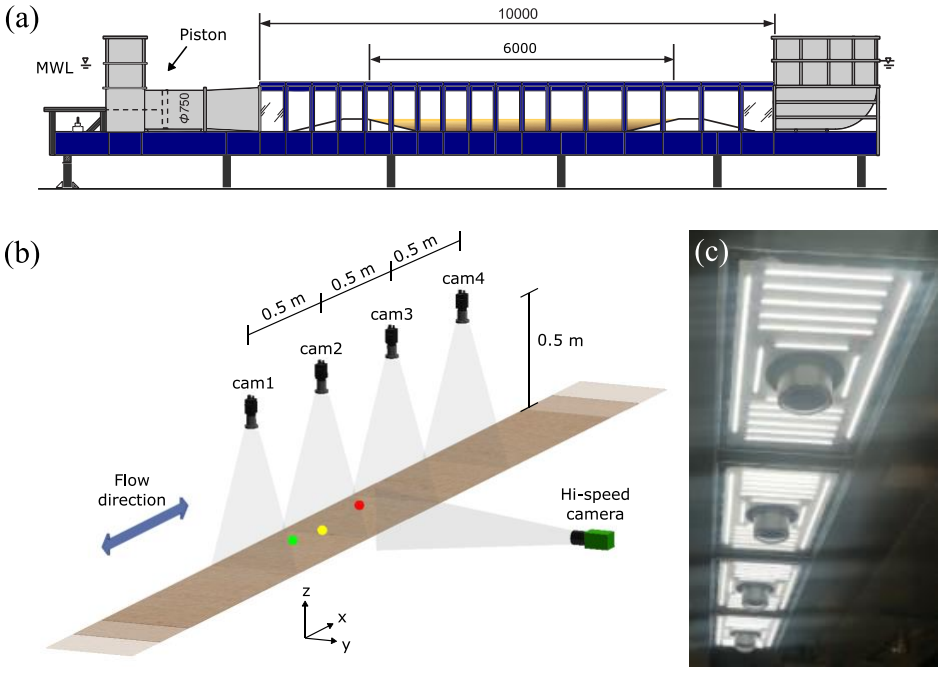

Figure 1. (a) AOFT with a 6 m sand bed. (b) Camera arrangement relative to the sand bed. (c) Camera viewports with surrounding LED strip lights on the underside of the tunnel lid.

Table 1 lists the flow conditions tested, all of which were conducted with a constant flow period of $T = 6$ s. U_{RMS} denotes root-mean-square velocity in the free-stream, $U_{\max}$ and $U_{\min}$ are maximum and minimum velocities, respectively, and Sk and As are flow skewness and asymmetry, defined by (Malarkey & Davies, 2012):

$$Sk = \frac{\overline{u^3}}{U_{\mathrm{RMS}}^3} \qquad As = \frac{\overline{\mathcal{H}(u)^3}}{U_{\mathrm{RMS}}^3}, \tag{1,2}$$

where u is flow velocity in the free-stream, the overbar denotes a time-average, and $\mathcal{H}(u)$ denotes the Hilbert transform of u. Each experiment was conducted for a short series of 3, 6 or

10 flow cycles in order to avoid particles travelling past the edges of the test section; in most cases, results showed convergence in net movement after 6 flow cycles.

Table 1. Flow conditions

Name	Flow shape	U_{RMS} [m/s]	$U_{\max}$ [m/s]	$U_{\min}$ [m/s]	Sk	As
075S	Skewed	0.66	1.30	-0.67	0.79	-0.06
110S	Skewed	0.99	1.98	-0.97	0.87	0.04
075N	Near-sinusoidal	0.65	0.89	-0.92	-0.05	-0.01
110N	Near-sinusoidal	0.98	1.34	-1.39	-0.03	-0.02
075A	Asymmetric	0.66	0.99	-0.94	0.09	-0.67

Experiments were conducted for two different, well-sorted sand beds: a coarse sand bed, grain size d_{50} = 0.44 mm, and a fine sand bed, d_{50} = 0.16 mm. Sand sizes were selected to represent two different transport domains: Under large nearshore waves, where both sands are transported as sheet flow, coarse sand is generally transported in the onshore direction, while fine sand is transported in the offshore direction (van der A et al., 2013). Two categories of alien particles were tested: (a) Spherical particles and (b) irregular, "naturally" shaped particles. 11 different types of spherical particles were tested, covering three diameters (3, 6, 9 mm) and four densities ($\rho_p^* = 1.36, 2.55, 3.27, 4.00$), where $\rho_p^* = \rho_p/\rho_w$ is the normalised density, with ρ_p and ρ_w being the densities of the particle and the fluid respectively. 11 types of irregular particles were also tested, with densities between $2.5 < \rho_p^* < 4$ and average diameters between 2-10 mm, covering a range of different "natural" shapes. Experiments were performed using 8-10 particles of each type, for a total of ~100 alien particles per experiment (spherical or irregular); each experiment was repeated 2-5 times to establish convergence.

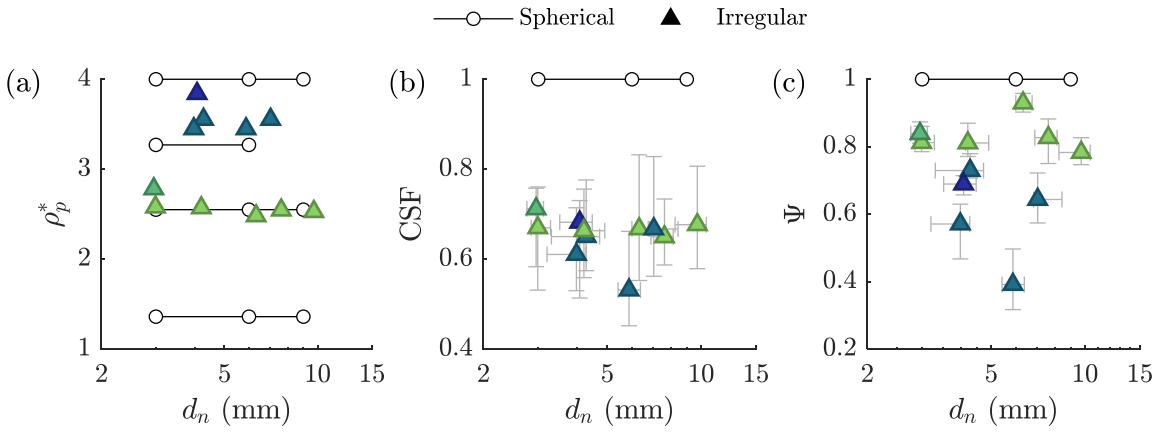

Figure 2: Properties of alien particles used in the experiments. (a) density, (b) Corey shape factor, (c) sphericity. Irregular particles are colour-coded by density for better readability.

Figure 2 shows properties of the alien particles tested, showing (a) density, (b) Corey shape factor, and (c) sphericity Ψ, against nominal diameter d_n. Nominal diameter is taken as the diameter of an equivalent sphere, i.e. $d_n = \sqrt[3]{6V/\pi}$, where V is particle volume, and CSF and Ψ follow their conventional definitions (e.g. Blott and Pye, 2008). The particle properties were measured by micro-CT scanning; error bars in Figures 2(b) and (c) show the 16th and 84th percentile values.

Results

Results from experiments involving skewed flow (flows 075S and 110S) are presented here. Figure 3 shows a short sample sequence of images from a colour camera (cam2, middle row), as well as simultaneous images from the high-speed camera (bottom row), during an experiment involving spherical particles on coarse sand with flow 075S. The images are taken at (a) $u = 0$, (b) $u = U_{\max}/2$, and (c) $u = U_{\max}$, as indicated in the top row. Coloured particles are visible in the top-down view and can be observed moving left-to-right between images. Particles are aligned in rows at the beginning of each experiment; over time, their increasing variation in relative position can be observed. The sand bed appears stationary in Figure 3(a). In Figure 3(b), some movement of sand particles is seen; spherical alien particles are also visible in the side view. Finally, Figure 3(c) shows the highest degree of mobilisation of the sand bed. Alien particles are no longer visible from the side view, as they are occluded by the mobilised sand.

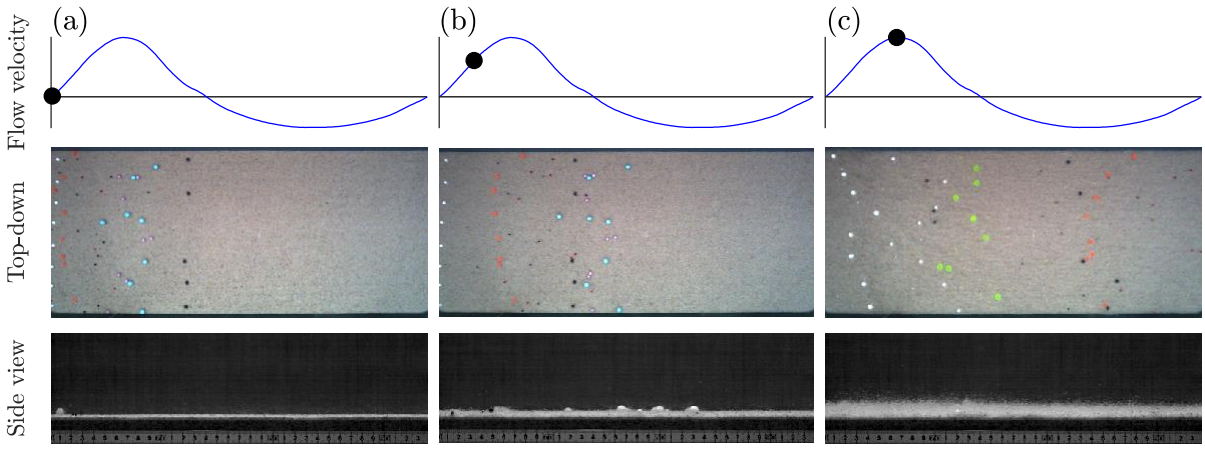

Figure 3: Sample sequence of images from coarse bed experiments. Top row: Phase within the flow cycle. Middle row: Top-down view from cam2. Bottom row: Side view from the high-speed camera.

Figure 4 shows an equivalent sequence as that shown in Figure 3, this time for the fine sand bed. An immediate difference is that the high-speed camera already shows a cloud of suspended sand in the first image (suspended during the flow ramp-up period). Despite this, alien particles are still partially visible in the top-down image. Between Figures 4(a-b), some movement in the alien

particles can be seen, similar to the coarse-bed case. In Figure 4(c), the bed appears strongly mobilised in both camera views, and as a result, particles are entirely occluded.

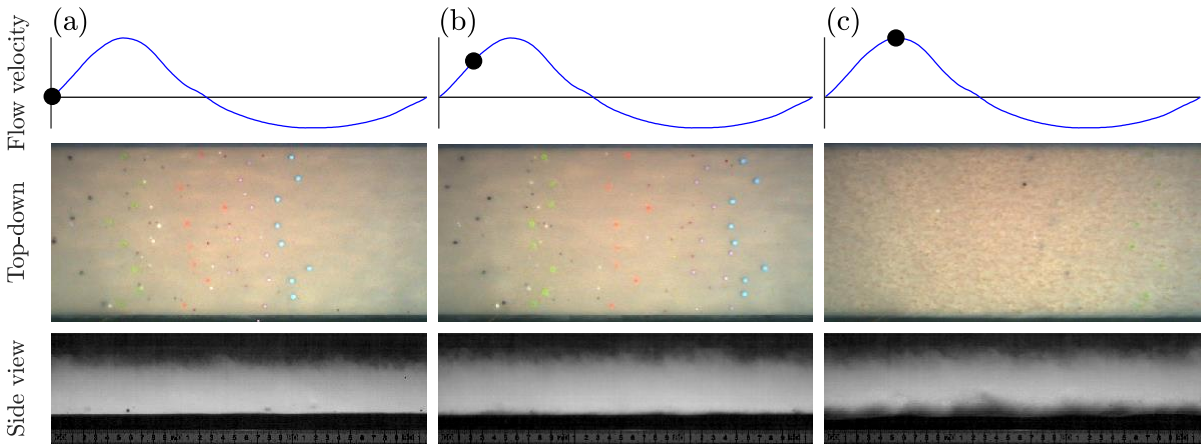

Figure 4: Sample sequence of images from fine bed experiments.

The average velocity of an alien particle, $\bar{u}_p$, is defined as the net distance travelled by the particle in the direction of flow divided by the duration of the experiment. Figure 5 shows average velocities from all experiments with spherical particles under skewed flow, showing results for (a) 075S on coarse sand, (b) 110S on coarse sand, (c) 075S on fine sand, and (d) 110S on fine sand. Each plot shows the non-dimensional particle velocity $\bar{u}_p^*$ against the mobility number ψ, where:

$$\bar{u}_p^* = \frac{\bar{u}_p}{U_{\mathrm{RMS}}} \qquad \psi = \frac{U_{\mathrm{RMS}}^2}{(\rho_p^* - 1) g d_n}, \tag{3,4}$$

and g is gravitational acceleration. The mobility number is a nondimensional representation of the ratio between disturbing and stabilising forces on the particle. For the flow shapes tested, positive $\bar{u}_p$ represents transport in the onshore direction, while negative $\bar{u}_p$ denotes offshore transport. The markers in the Figure represent average transport velocities over multiple experiments, with error bars representing 16$^{\mathrm{th}}$ and 84$^{\mathrm{th}}$ percentile values.

On coarse sand, the alien particle velocities are always positive, indicating consistent transport in the onshore direction; this is also the direction in which the sand is transported. Alien particle velocity magnitudes appear to be a function of the particle density, with high-density particles transported onshore at greater velocities than low-density particles. The dependence of alien particle velocity on ψ also varies with density, with low-density particles ($\rho_p^* = 1.36$) showing little variation in velocity with ψ. On fine sand, the alien particle velocities are significantly different from the velocities on coarse sand. For 075S (Figure 5(c)), lower-density particles are

transported offshore, and higher-density particles are transported onshore, while for 110S (Figure 5(d)) nearly all particles travel offshore. This correlates with the native sand transport, which is weakly offshore for 075S and strongly offshore for 110S. The tendency for higher-density particles to travel onshore under waves has previously been identified in studies of coastal mineral deposits (Komar, 2007).

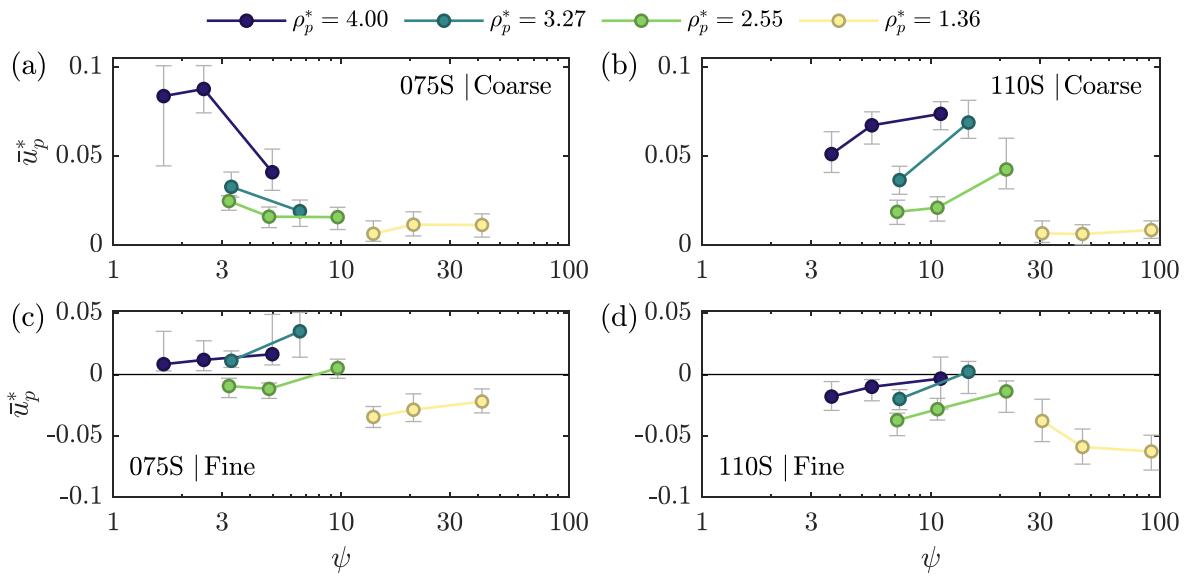

Figure 5: Average velocities of spherical alien particles under skewed flows 075S and 110S.

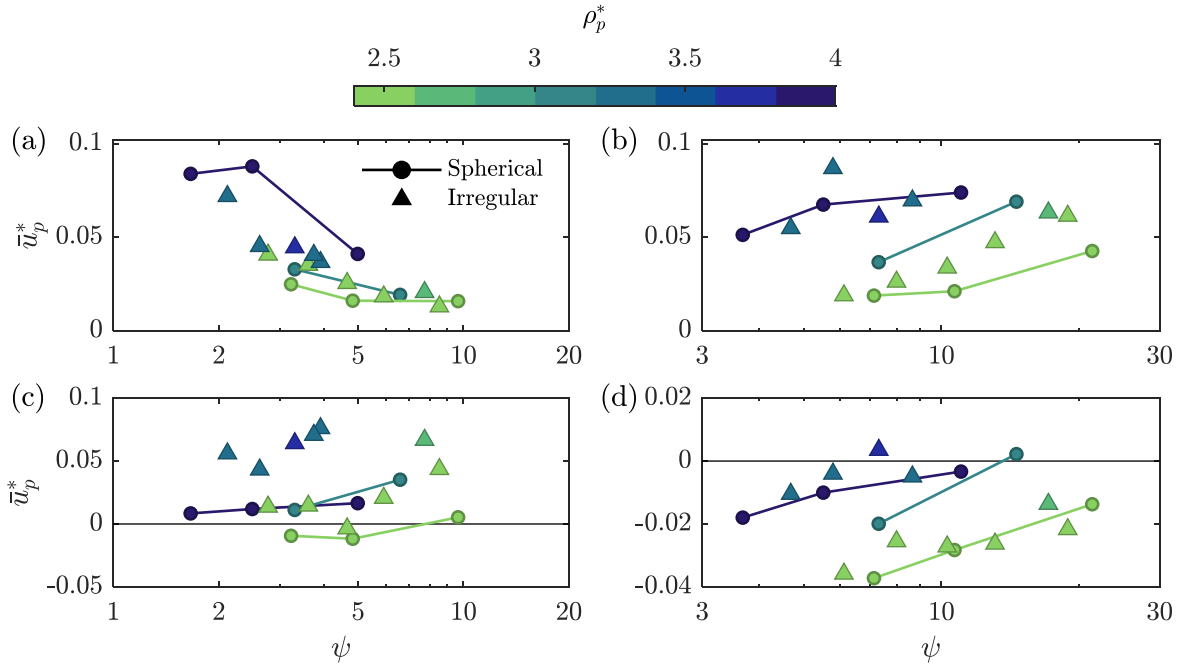

Figure 6: Average velocities of irregular alien particles under skewed flows 075S and 110S. Velocities of spherical particles from Figure 5 are included for comparison (excluding $\rho_p^* = 1.36$).

Figure 6 shows alien particle velocity measurements from experiments involving irregular particles under skewed flow. Results are arranged in the same manner as in Figure 5, and velocities of spherical particles are included for comparison. Markers are colour-coded by density as indicated at the top of the Figure. For legibility, error bars are excluded from the Figure; variations were slightly larger for irregular particles than those shown for spherical particles in Figure 5. The results show that alien particle velocities are similar between irregular and spherical particles of equal density and size. This indicates that, for the set of conditions tested, alien particle shape does not have a strong influence on net transport. It is noteworthy that Guler et al. (2022) saw a strong shape effect for microplastics on a sloped bed, where spherical particles show a strong tendency to roll down the slope. Present results suggest that in the absence of a bed slope, this effect is much less pronounced, and the behaviour of spherical particles is representative of a wide range of shapes.

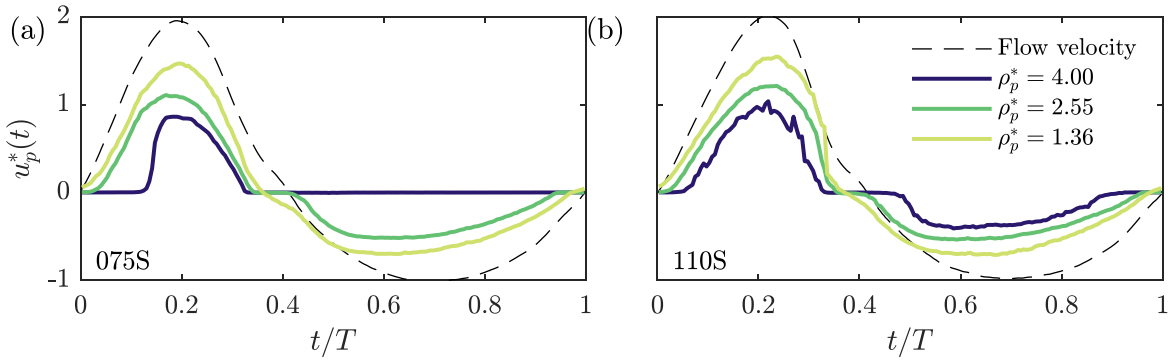

Figure 7: Time-varying velocities of 6 mm spherical particles at three different densities on a coarse sand bed under skewed flows (a) 075S and (b) 110S.

Figure 7 shows example results from applying particle tracking methods to the plan-view images to measure the time-varying velocities of alien particles. The figure shows time-dependent particle velocities (normalised by U_{RMS}) of three different density particles, all with $d_n = 6$ mm, on a coarse sand bed under (a) 075S and (b) 110S flow. The velocities are obtained by tracking several particles of the given type in repeated experiments and taking the median values. Time-averages of $u_p^*(t)$ are approximately equal to the $\bar{u}_p^*$ values shown in Figure 5. Figure 7(a) shows that high-density particles ($\rho_p^* = 4.00$) are only mobilised in the forward flow half-cycle, while lower-density particles are transported in both directions; this explains the high average velocity of high-density particles in Figure 5(a). Figure 7(b) shows that under flow 110S, high-density particles become mobilised in both half-cycles, resulting in lower net movement. The other two particles show little difference between Figures 7(a) and (b); the small differences which do appear are linked to the increased turbulence under the higher-intensity flow.

Conclusion

This work presents a systematic, experimental investigation of the transport of alien particles on sand beds under high-energy oscillatory flow conditions. The experiments involved a range of alien particle sizes, densities and shapes, placed on two different-sized sand beds, and mobilised by five flows with different shape and intensity. The main factor influencing transport is particle density, with a general tendency towards onshore-directed transport for high-density particles and offshore transport for low-density particles. The experiments indicate that, on a flat bed, particle shape does not have a strong influence on net transport.

The results presented are a subset of a rich dataset. In addition to the skewed-flow results shown, experiments were conducted involving near-sinusoidal and asymmetric flows. Statistical variations in particle motions were characterised, including rates of particle burial, and time-varying velocities were analysed for most of the particles in coarse sand experiments. High-speed camera recordings were also obtained in all experiments, providing detailed views of particle motion characteristics. Results from these analyses will be presented at the conference.

References

Blott, S. J., & Pye, K. (2008). Particle shape: A review and new methods of characterization and classification. Sedimentology, 55(1), 31–63. https://doi.org/10.1111/j.1365-3091.2007.00892.x

Guler, H. G., Larsen, B. E., Quintana, O., Goral, K. D., Carstensen, S., Christensen, E. D., Kerpen, N. B., Schlurmann, T., & Fuhrman, D. R. (2022). Experimental study of non-buoyant microplastic transport beneath breaking irregular waves on a live sediment bed. Marine Pollution Bulletin, 181, 113902. https://doi.org/10.1016/j.marpolbul.2022.113902

Komar, P. D. (2007). Chapter 1 The Entrainment, Transport and Sorting of Heavy Minerals by Waves and Currents. In Developments in Sedimentology (Vol. 58, pp. 3–48). Elsevier. https://doi.org/10.1016/S0070-4571(07)58001-5

Laksanalamai, J., & Kobayashi, N. (2023). Tracking of Small Discrete Objects Submerged in Surf and Swash Zones on Sand Beaches. Journal of Waterway, Port, Coastal, and Ocean Engineering, 149(6), 04023017. https://doi.org/10.1061/JWPED5.WWENG-1987

Malarkey, J., & Davies, A. G. (2012). Free-stream velocity descriptions under waves with skewness and asymmetry. Coastal Engineering, 68, 78–95. https://doi.org/10.1016/j.coastaleng.2012.04.009

van der A, D. A., Ribberink, J. S., Van Der Werf, J. J., O'Donoghue, T., Buijsrogge, R. H., & Kranenburg, W. M. (2013). Practical sand transport formula for non-breaking waves and currents. Coastal Engineering, 76, 26–42. https://doi.org/10.1016/j.coastaleng.2013.01.007

Particle dynamics in coastal ecosystems

Teresa Serra

Department of Physics. University of Girona. Carrer de la Universitat de Girona, 4. 17003-Girona (Spain).

Particle dynamics in coastal ecosystems

Teresa Serra
Department of Physics. University of Girona. Carrer de la Universitat de Girona, 4. 17003-Girona (Spain).

Coastal aquatic vegetation like seagrasses modify the vertical distribution of sediment particles; especially when particles come from allochthonous sources. River plumes, coastal runoff, and spontaneous resuspension are a few examples of the natural sources of the allochthonous sediment input. Seagrasses can capture suspended particles trapping them on their leaves, remaining in suspension within the canopy and enhancing the deposition onto the seabed. Seagrasses' ability to capture sediment particles was proved in laboratory studies carried out in a flume with a variety of hydrodynamic conditions and canopy densities that mirrored actual field conditions. Samples of suspended sediment were pipetted above and within the meadow for being measured with the Lisst-100X. Also, at the end of experiments ten plants were gently removed from different evenly separated positions within the meadow and introduced into a beaker with a volume of 80 mL of water to remove particles deposited on their blades. The concentration of particles was then measured with the Lisst-100X, from which the total mass of particles deposited on the blades could be calculated. Seagrasses decreased the amount of suspended sediment by capturing the sediment on the blades of the seagrass and by enhancing particle sedimentation on the seabed. However, particles trapped by the blades of seagrass in the whole canopy increased with canopy density and reduced the number of particles in suspension within the canopy. The ecological implications were noteworthy because a bottom covered with vegetation reduced the suspended sediment particles within the canopy, improving water clarity, in contrast to bare soil. Additionally, seabed sedimentation was facilitated by canopies as opposed to bare substrates, and the denser the canopy, more particles were deposited on the seabed.

Seasonal characteristics of flocculation and Bio-flocculation across the Belgian near-shore region

Chih-Hao Hsu[a], Koenraad Muylaert[b], Christian Schwarz[a]

[a] Hydraulics and Geotechnics, Department of Civil Engineering, KU Leuven
[b] Department of Biology, KU Leuven

Seasonal characteristics of flocculation and Bio-flocculation across the Belgian near-shore region

Chih-Hao Hsu[a], Koenraad Muylaert[b], Christian Schwarz[a]

[a]Hydraulics and Geotechnics, Department of Civil Engineering, KU Leuven
[b]Department of Biology, KU Leuven

Corresponding author: Chih-Hao Hsu, chih-hao.hsu@kuleuven.be

Introduction

Sediment transport governed by the balance between gravitational settling and turbulent resuspension is a crucial process influencing ecological (e.g. light climate) and physical ecosystem (e.g. morphodynamics) properties of fine sedimentary coastal and estuarine ecosystems. In natural systems suspended particulate matter (i.e. SPM) can be broadly classified into living particles (e.g., bacteria, phytoplankton) and non-living particles (e.g., non-cohesive and cohesive sediments). Especially in nearshore regions, SPM concentrations are relatively high, and these particles readily adhere together to form aggregates known as flocs.

SPM undergo seasonal variation in respect to particle properties (e.g. presence of extra polymeric substance, EPS, and particulate organic carbon, POC) and particle quantities (e.g. concentration of cohesive and non-cohesive mineralogic sediments). Previous studies have revealed that average floc sizes are smaller in winter than in summer. This phenomenon may result from bio-flocculation processes. In the Belgian coastal zone, spring blooms triggered by seasonal increases in sea surface temperature and solar radiation are promoted by increased nutrient inputs, particularly nitrogen and phosphorus, from rivers during winter and early spring. Improving light conditions further contributes to rapid colony formation and bloom development from March to mid-May. During these blooms, phytoplankton releases sticky substances, more specifically extracellular polymeric substances (EPS) and transparent exopolymer particles (TEPs), which facilitate the formation of larger flocs. Specifically, *Phaeocystis sp.* colonies frequently form large phytoplankton blooms along the Belgian coastal area from March to mid-May (Breton et al., 2021). The onset of these blooms leads to increased production of fresh and sticky organic matter, particularly TEP, which plays an important role in promoting the aggregation of suspended sediment and organic particles into bioflocs (Fettweis et al., 2022). In addition, Fettweis et al. (2022) indicated that floc size increases during the bloom period, enhancing the settling velocity of particles and thereby reducing suspended particulate matter (SPM) concentrations in the water column. However, the interaction between biological processes and flocculation remains unclear. This study aims to investigate the interaction between algae and sediment to elucidate the flocculation process through field measurements and laboratory experiments.

Study Area

The study area is located in the Belgian coastal region near the Scheldt estuary, situated in the Southern Bight of the North Sea. The hydrodynamics of the Belgian Coastal Zone are dominated by tides as well as by prevailing wind and wave conditions. The Belgian coastal area is shallow, with water depths of approximately 10 m nearshore and around 20 m offshore during spring tides. Within the coast turbidity maximum SPM concentrations vary widely, ranging from 20 to 250 mg/L at the surface and from 100 mg/L to more than a few g/L near the bottom (Fettweis et al., 2014; Fettweis and Lee, 2017) (Figure.1 station MOW1).

Methods

Field Measurement

Re-occuring field campaigns on board the RV Simon Steven were carried out visiting three stations; from the nearshore (MOW1), transition zone (W05), and to offshore (W08). These stations are repeatedly sampled throughout the year in January, April, May and September (Figure 1). Turbulence and floc size were measured by a Nortek Acoustic Doppler Velocimeter (ADV) and Sequoia LISST-200x, all mounted on a CTD (Figure.1a). In addition to the point measurement on the CTD, velocity profiles are measured consecutively by Workhorse Acoustic Doppler Current Profiler (ADCP). All sensor measurements were continuously conducted for 13 hours. Additionally regular water samples were taken, quantifying, ChlA, SPM, POC and EPS concentrations.

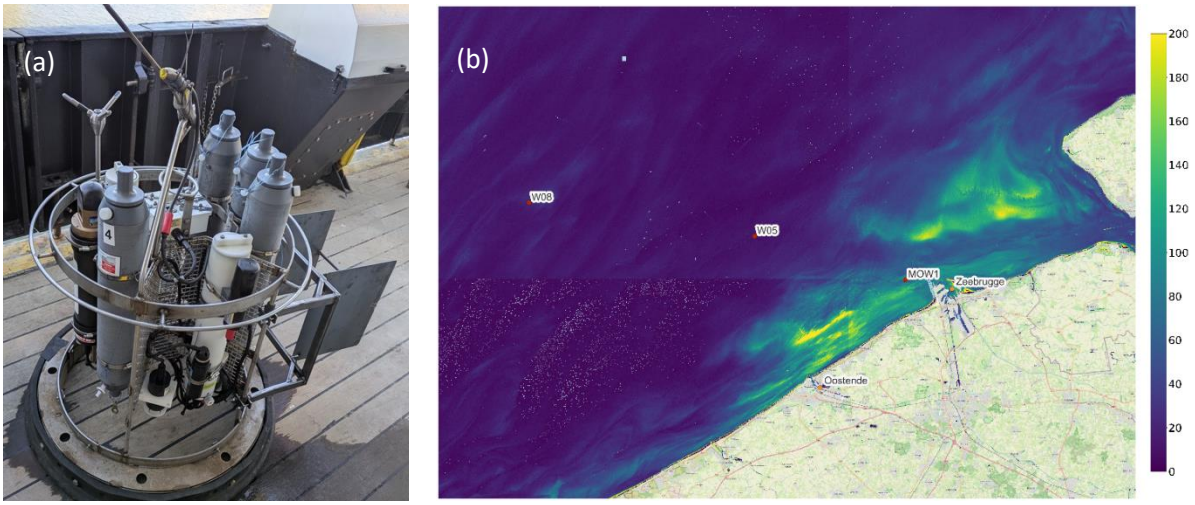

Figure 1. (a) measurement setup, including, a CTD, PAR-sensor, LISST-200X, ADV, OBS, Niskin-bottles for water sampling. (b) Map of sampling stations MOW1, W05, and W08 at Belgium coastal area. The background displays the surface SPM data on April 29 2025 derived from Sentinel 2 (Pahlevan et al., 2019).

Results

First data analysis reveals a varying relationship in turbulence (e.g. TKE) and median floc size (D_{50}) over the seasonal measurements, indicating the importance of bio-flocculation. We, moreover, see that not only temporal but also spatial difference can be observed with increasing distance from the Belgian coast.

Next steps

In order to untangle the relationships observed during the field measurements, flocculation experiments will be conducted using a flocculator-floc-camera setup. Flocs are quantified using a non-intrusive camera system linked to an image processing workflow. The image processing workflow includes grayscale conversion, background removal, image contrast enhancement, and Otsu's thresholding. A critical step, as described by Keyvani & Strom (2013) and Shen & Maa (2016), is the identification and removal of out-of-focus flocs. Pre-experiments were conducted to first investigate the most suitable flocculator setup based on a comparison of spatio-temporal turbulence distribution between the field and the flocculators (e.g. Taylor–Couette. Padel, Hybird). Subsequently a cross-calibration between the floc-camera-system and the LISST-200X are carried. And finally a factorial experiment is carried out, varying turbulence, SPM-concentration and quality.

References

Breton, E., Christaki, U., Sautour, B., Demonio, O., Skouroliakou, D.-I., Beaugrand, G., Seuront, L., Kléparski, L., Poquet, A., Nowaczyk, A., Crouvoisier, M., Ferreira, S., Pecqueur, D,. Salmeron, C., Brylinski, J.-M., Lheureux, A. & Goberville, E. (2021) Seasonal Variations in the Biodiversity, Ecological Strategy, and Specialization of Diatoms and Copepods in a Coastal System With *Phaeocystis* Blooms: The Key Role of Trait Trade-Offs. *Front. Mar. Sci.* 8:656300. doi: 10.3389/fmars.2021.656300.

Coufort, C., Bouyer, D., & Liné, A. (2005). Flocculation related to local hydrodynamics in a Taylor–Couette reactor and in a jar. *Chemical Engineering Science*, *60*(8-9), 2179-2192. https://doi.org/10.1016/j.ces.2004.10.038.

Dyer, K. R. (1989). Sediment processes in estuaries: Future research requirements. *Journal of Geophysical Research*, 94, 14327–14339. https://api.semanticscholar.org/CorpusID: 128566642.

Dyer, K. R. (1995). Chapter 14 sediment transport processes in estuaries. *Developments in sedimentology*, 53, 423–449. https://api.semanticscholar.org/CorpusID:140597036.

Fettweis, M., M. Baeye, D. Van der Zande, D. Van den Eynde, and B. J. Lee (2014), Seasonality of floc strength in the southern North Sea, *J. Geophys. Res. Oceans*, 119, 1911–1926, doi:10.1002/2013JC009750.

Fettweis M, Lee BJ. Spatial and Seasonal Variation of Biomineral Suspended Particulate Matter Properties in High-Turbid Nearshore and Low-Turbid Offshore Zones. *Water*. 2017; 9(9):694. https://doi.org/10.3390/w9090694.

Fettweis, M., Schartau, M., Desmit, X., Lee, B. J., Terseleer, N., Van der Zande, D., et al. (2022). Organic matter composition of biomineral flocs and its influence on suspended particulate matter dynamics along a nearshore to offshore transect. *Journal of Geophysical Research: Biogeosciences*, 127, e2021JG006332. https://doi.org/10.1029/2021JG006332.

Guérin, L., Coufort-Saudejaud, C., Liné, A., & Frances, C. (2017). Dynamics of aggregate size and shape properties under sequenced flocculation in a turbulent Taylor-Couette reactor. *Journal of colloid and interface science*, *491*, 167-178. http://dx.doi.org/10.1016/j.jcis.2016.12.042.

Keyvani, A., & Strom, K. (2013). A fully-automated image processing technique to improve measurement of suspended particles and flocs by removing out-of-focus objects. *Computers & Geosciences*, 52, 189–198. https://doi.org/https://doi.org/10.1016/j.cageo.2012.08.018.

Nosaka Y, Yamashita Y and Suzuki K (2017) Dynamics and Origin of Transparent Exopolymer Particles in the Oyashio Region of the Western Subarctic Pacific during the Spring Diatom Bloom. *Front*. *Mar. Sci.* 4:79. doi: 10.3389/fmars.2017.00079.

Mercier, C. K., & Delhez, É. J. M. (2007). Diagnosis of the sediment transport in the belgian coastal zone. *Estuarine Coastal and Shelf Science*, 74, 670–683. https://api.semanticscholar.org/CorpusID:18404172.

Muylaert, K., Gonzales, R., Franck, M., Lionard, M., Van der Zee, C., Cattrijsse, A., Sabbe, Lei Chou, K., & Vyverman, W. (2006). Spatial variation in phytoplankton dynamics in the Belgian coastal zone of the North Sea studied by microscopy, HPLC-CHEMTAX and underway fluorescence recordings. *Journal of Sea Research*, *55*(4), 253-265.

Pahlevan, N., Chittimalli, S. K., Balasubramanian, S. V., & Vellucci, V. (2019). Sentinel-2/Landsat-8 product consistency and implications for monitoring aquatic systems. *Remote sensing of Environment*, *220*, 19-29.

Passow, U., & Alldredge, A. L. (1995). Aggregation of a diatom bloom in a mesocosm: The role of transparent exopolymer particles (TEP). *Deep Sea Research Part II: Topical Studies in Oceanography*, *42*(1), 99-109.

Shen, X., & Maa, J. P.-Y. (2016). A camera and image processing system for floc size distributions of suspended particles. *Marine Geology*, 376, 132–146. https://doi.org/https://doi.org/10.1016/j.margeo.2016.03.009

Shen, X., Toorman, E. A., Lee, B. J., & Fettweis, M. (2018). Biophysical flocculation of suspended particulate matters in Belgian coastal zones. *Journal of Hydrology*, *567*, 238-252. https://doi.org/10.1016/j.jhydrol.2018.10.028

van Rijn, L. C. (1997). Sediment transport and budget of the central coastal zone of holland. *Coastal Engineering*, 32, 61–90. https://api.semanticscholar.org/CorpusID:129836271

Tidal Dynamics of In Situ PSD in the Southern German Bight and the Weser Estuary

Julián E. Cortese[a], Marius Becker[a], Frank Kösters[b], Anna Zorndt[b], and Chirstian Winter[a]

[a] Christian-Albrechts University zu Kiel, Kiel, Germany.

[b] Bundesanstalt für Wasserbau, Hamburg, Germany.

Zooplankton and Phytoplankton Time Series Analysis for the Belgian North Sea

Annika Eske[a,b], Ilias Semmouri[b], Jonas Mortelmans[a], Colin Janssen[c], Carlota Muñiz[a], Klaas Deneudt[a], Pascal I. Hablützel[a,d]

[a] **Flanders Marine Institute (VLIZ), Jacobsenstraat 1, 8400 Ostend, Belgium**

[b] **Ghent University, Laboratory of Environmental Toxicology and Aquatic Ecology, Faculty of Bioscience Engineering, 9000 Ghent, Belgium**

[c] **Blue Growth Research Lab, Ghent University, Bluebridge Building, Ostend Science Park 1, 8400 Ostend, Belgium**

[d] **Biology Department, Vrije Universiteit Brussel, Pleinlaan 2, 1050 Elsene, Belgium**

Zooplankton and Phytoplankton Time Series Analysis for the Belgian North Sea

Annika Eske[ab], Ilias Semmouri[b], Jonas Mortelmans[a], Colin Janssen[c], Carlota Muñiz[a], Klaas Deneudt[a], Pascal I. Hablützel[ad]

[a] Flanders Marine Institute (VLIZ), Jacobsenstraat 1, 8400 Ostend, Belgium

[b] Ghent University, Laboratory of Environmental Toxicology and Aquatic Ecology, Faculty of Bioscience Engineering, 9000 Ghent, Belgium

[c] Blue Growth Research Lab, Ghent University, Bluebridge Building, Ostend Science Park 1, 8400 Ostend, Belgium

[d] Biology Department, Vrije Universiteit Brussel, Pleinlaan 2, 1050 Elsene, Belgium

Corresponding author: Annika Eske; Annika.eske@vliz.be

Introduction

In marine ecosystems, plankton compose the foundation of trophic webs. Factors that influence plankton can therefore have cascading effects across the ecosystem (Kim et al., 2024; Zeldis and Décima, 2020). In responding to changes in the environment, the plankton community may even amplify environmental signals. For instance, Taylor et al. (2002) used a model of the relationship between Gulf Stream latitude and plankton dynamics to demonstrate that the plankton community can respond to relatively subtle and diffuse meteorological changes. This sensitivity to environmental factors positions plankton in a crucial role for monitoring efforts. While plankton monitoring has previously been conducted using techniques such as microscopy, the more recent and expansive observation networks often take advantage of particle imaging techniques as well. Imaging serves as an important tool for generating interoperable, high-throughput plankton monitoring data. Furthermore, when used jointly, imagers such as the FlowCam and ZooScan offer coverage for much of the plankton size range (Lombard et al., 2019).

Plankton monitoring efforts could be vital for understanding the impacts of extreme climate events associated with climate change. Recent years have seen a 54% increase in annual marine heatwave (MHW) days from 1925 to 2016, with heatwaves becoming more frequent as well as longer in duration (Oliver et al., 2018). Temperature is already considered a key variable underlying plankton abundance trends (Deschutter et al., 2017; Lüskow et al., 2022), but research should now also consider the effects of rapid-onset extreme temperatures. Laboratory-based experiments have demonstrated that steady temperature increases have different effects on phytoplankton compared to sudden temperature spikes and cooling phases (Wolf et al., 2024). Furthermore, higher MHW

intensity and longer MHW duration have more pronounced effects on plankton (Remy et al., 2017; Semmouri et al., 2019). Given that MHW effects often include changes in community composition (Arteaga and Rousseaux, 2023), the present research provides an initial assessment of existing FlowCam and ZooScan time series data from the Belgian part of the North Sea (BPNS), with particular focus on blooms and community composition shifts. The results from these time series are analyzed in the context of two more severe MHW events that were detected in 2018 and 2022.

Methods

Plankton samples were collected on the RV *Simon Stevin* at 9 coastal stations monthly, with an additional 8 offshore stations sampled seasonally. Zooplankton sampling began in 2014 while phytoplankton samples are available from 2017 onwards. Zooplankton were collected using vertical tows of a 200 µm Working Party 2 (WP2) net. To sample phytoplankton, 50-70 L of surface water were collected using a steel bucket and filtered through a 55 µm Apstein net (Amadei Martínez et al., 2020). These samples were imaged using the ZooScan and FlowCam for WP2 net samples and Apstein net samples, respectively. Images were classified using convoluted neural networks to recognize key image categories based on learning datasets. Images were then manually validated. Based on availability of validated FlowCam and ZooScan data, an initial analysis was conducted for plankton abundances from 2017-2023 and 2014-2023, respectively. Using classified and quantified imaging data, plankton abundances were analyzed for community composition and abundance trends over time, in particular with regard to MHWs. The heatwaveR package (Schlegel and Smit, 2018) was used to generate a 30-year climatology baseline using the National Oceanic and Atmospheric Administration Optimum Interpolation Sea Surface Temperature dataset (NOAA OI SST V2 High Resolution Dataset) (Huang et al., 2021). Events surpassing the 90th percentile of this climatology baseline for at least 5 days were considered MHWs (Hobday et al., 2018). MHW features and plankton community composition were compared by year to identify possible relationships between temperature shifts and biological shifts.

Results

Both FlowCam and ZooScan image datasets highlighted years of drastic community shifts (Fig. 1). In the FlowCam data, the years 2022 and 2023 had notably higher fractions of Hemiaulales diatoms (driven by *Bellerochea* spp.) than in previous years. For plankton detected by the ZooScan, shifts in community composition occur most prominently in 2014, 2018, and 2022. The 2014 community displayed a relatively even spread of taxa, while 2018 and 2022 were dominated by high abundance of *Bellerochea* spp. In years when the *Bellerochea* spp. colonies did not dominate the ZooScan images, *Noctiluca* spp. cells were dominant. Certain FlowCam-detected taxa, such as the Rhizosoleniales order, exhibited high cell densities as well as consistent seasonal dynamics. While ZooScan community compositions were categorized using all possible

groupings, FlowCam data was more taxonomically resolved and was therefore grouped at the order level (which was available for 72.9% of FlowCam observations).

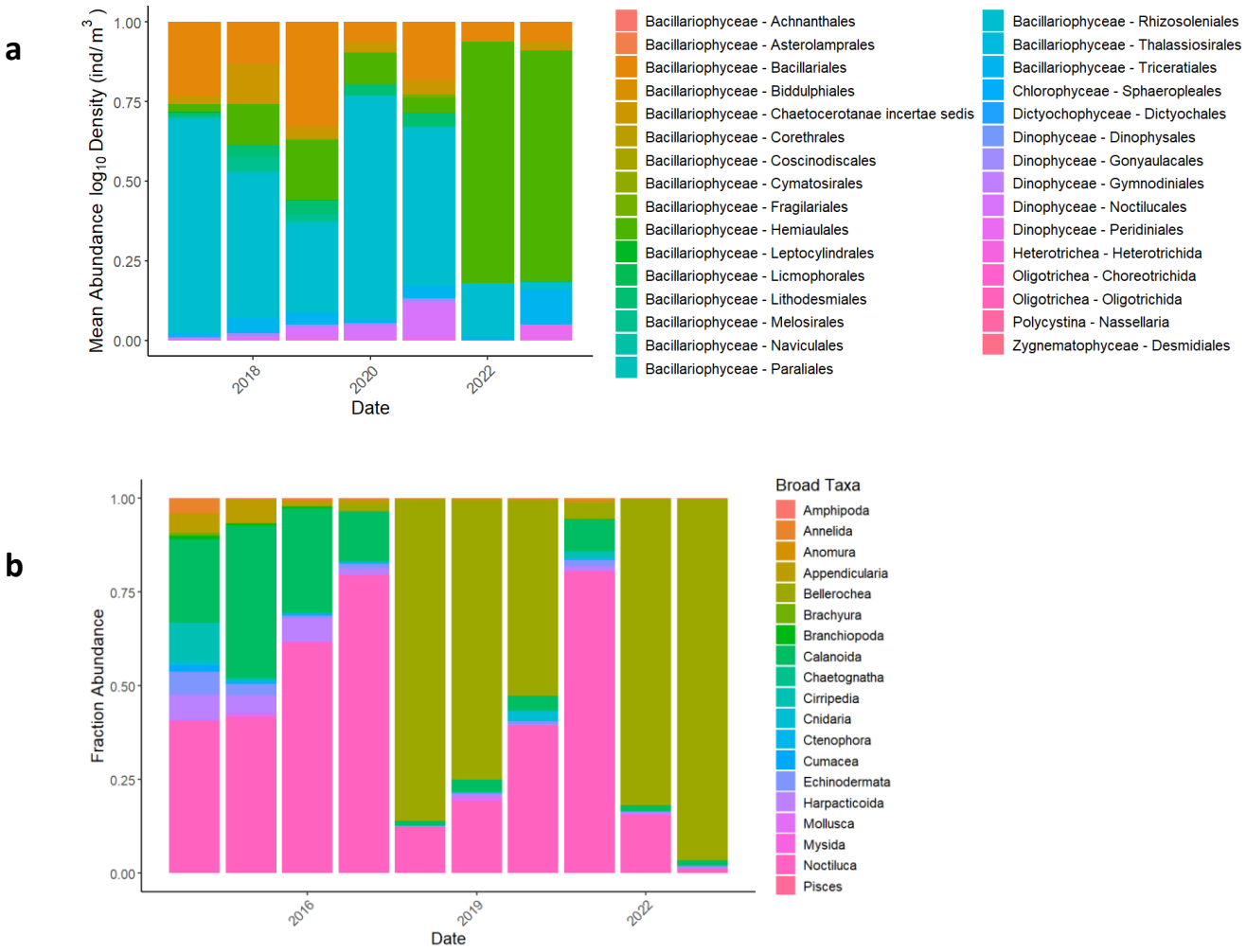

Figure 1. Fraction-based summer community composition for phytoplankton detected by the FlowCam at the order level (a) and for zooplankton and certain larger phytoplankton cells/colonies detected by the ZooScan (b). The community compositions are calculated using 9 coastal LifeWatch stations in the BPNS (see Mortelmans et al., 2019) in the months June-September. All years for which data was available and validated have been included.

Alongside the biological analysis, MHW detection and feature analysis in the heatwaveR package revealed that the years with maximum temperatures were 2018 (21.34°C) and 2022 (21.25°C). The year 2022 was also notable for having the greatest cumulative intensity (°C x days) of MHWs in the studied time frame (2014-2023).

Discussion

The data from the FlowCam and ZooScan revealed trends at the community level and suggest an association between MHW events and community composition shifts. Phytoplankton communities

exhibited couplet and triplet years wherein the communities were more closely related. This pattern seems to be visible for the groups 2017-2019, 2020-2021, and 2022-2023 in the FlowCam data and for groups 2015-2017, 2018-2020, and 2022-2023 in the ZooScan data. In agreement with the analysis of Mortelmans et al. (2024), the *Bellerochea* spp.-driven community shifts starting in 2018 and 2022 align with years exhibiting maximum MHW temperatures. The biological changes in 2022 may also have been influenced by the 91-day length of the summer heatwave that year. The strikingly long duration of the 2022 MHW meant that its cumulative intensity was the greatest of the last nine years. Although the FlowCam and ZooScan data agreed on some of these patterns, there are a few discrepancies that are likely unrelated to MHW effects. The lack of evidence of a 2018 *Bellerochea* spp. (Order Hemiaulales) bloom in the FlowCam data is likely due to the long chain-forming nature of these diatoms. Other organisms, such as *Phaeocystis globosa*, are also known for aggregating and causing clogs in the FlowCam (Aubert et al., 2022).

Despite their many advantages, automated imagers like the FlowCam and ZooScan can also lack taxonomic resolution, and each instrument covers only part of the plankton size range. A review by Lombard et al. (2019) noted that, because the concentration of plankton decreases with plankton size, it is not feasible to sample the full plankton system using one technique only. Hence, observations using only 1-2 methodologies provide an incomplete picture. Multifaceted plankton observation therefore offers the best insight into the status of a plankton community, and future studies would benefit from incorporating molecular observation techniques as well as classical microscopy (Aubert et al., 2022; Lombard et al., 2019). Using a variety of methods would also allow for more in-depth analysis of the relationship between MHW features and plankton densities. Next steps will therefore include the application of DNA metabarcoding on newly collected samples, which will complement the imaging data from the existing time series.

Conclusion

The FlowCam and ZooScan data from the Belgian contribution to LifeWatch capture several prominent trends in community composition and taxon-specific seasonal dynamics. There is some agreement in the data from the two imaging instruments, particularly driven by taxa that are present in both imaging datasets. Discrepancies between the FlowCam and ZooScan are likely due to technical differences such as phytoplankton inducing clogs in the FlowCam. Some key years highlighted by this preliminary assessment include 2016, 2018, and 2022 – these years showed marked shifts from adjacent years before (in the case of 2018 and 2022) or afterward (in the case of 2016). Unusually high temperatures reached during the summer MHWs of 2018 and 2022 may help explain the lasting plankton community shifts of those years. The cumulative intensity of the 2022 MHW may also have allowed it to affect the temporal dynamics of the summer plankton community that year, and such impacts of MHW features should be further investigated.

References

Amadei Martínez, L., Mortelmans, J., Dillen, N., Debusschere, E., Deneudt, K., 2020. LifeWatch observatory data: phytoplankton observations in the Belgian Part of the North Sea. Biodiversity Data Journal 8, e57236. https://doi.org/10.3897/BDJ.8.e57236

Arteaga, L.A., Rousseaux, C.S., 2023. Impact of Pacific Ocean heatwaves on phytoplankton community composition. Commun Biol 6, 263. https://doi.org/10.1038/s42003-023-04645-0

Aubert, A., Beauchard, O., de Blok, R., Artigas, L.F., Sabbe, K., Vyverman, W., Martínez, L.A., Deneudt, K., Louchart, A., Mortelmans, J., Rijkeboer, M., Debusschere, E., 2022. From Bacteria to Zooplankton: An Integrative Approach Revealing Regional Spatial Patterns During the Spring Phytoplankton Bloom in the Southern Bight of the North Sea. Front. Mar. Sci. 9. https://doi.org/10.3389/fmars.2022.863996

Deschutter, Y., Everaert, G., De Schamphelaere, K., De Troch, M., 2017. Relative contribution of multiple stressors on copepod density and diversity dynamics in the Belgian part of the North Sea. Marine Pollution Bulletin 125, 350–359. https://doi.org/10.1016/j.marpolbul.2017.09.038

Hobday, A.J., Oliver, E.C.J., Gupta, A.S., Benthuysen, J.A., Burrows, M.T., 2018. Categorizing and Naming Marine Heatwaves. Oceanography 31, 162–173. https://doi.org/10.5670/oceanog.2018.205

Huang, B., Liu, C., Banzon, V., Freeman, E., Graham, G., Hankins, B., Smith, T., Zhang, H.-M., 2021. Improvements of the Daily Optimum Interpolation Sea Surface Temperature (DOISST) Version 2.1. https://doi.org/10.1175/JCLI-D-20-0166.1

Kim, J.O., Dimitriou, A., Forster, I., Tseng, M., 2024. Heatwave-mediated decreases in phytoplankton quality negatively affect zooplankton productivity. Functional Ecology 38, 778–791. https://doi.org/10.1111/1365-2435.14530

Lombard, F., Boss, E., Waite, A.M., Vogt, M., Uitz, J., Stemmann, L., Sosik, H.M., Schulz, J., Romagnan, J.-B., Picheral, M., Pearlman, J., Ohman, M.D., Niehoff, B., Möller, K.O., Miloslavich, P., Lara-Lpez, A., Kudela, R., Lopes, R.M., Kiko, R., Karp-Boss, L., Jaffe, J.S., Iversen, M.H., Irisson, J.-O., Fennel, K., Hauss, H., Guidi, L., Gorsky, G., Giering, S.L.C., Gaube, P., Gallager, S., Dubelaar, G., Cowen, R.K., Carlotti, F., Briseño-Avena, C., Berline, L., Benoit-Bird, K., Bax, N., Batten, S., Ayata, S.D., Artigas, L.F., Appeltans, W., 2019. Globally Consistent Quantitative Observations of Planktonic Ecosystems. Front. Mar. Sci. 6. https://doi.org/10.3389/fmars.2019.00196

Lüskow, F., Christiansen, B., Chi, X., Silva, P., Neitzel, P., Brooks, M.E., Jaspers, C., 2022. Distribution and biomass of gelatinous zooplankton in relation to an oxygen minimum zone and a shallow seamount in the Eastern Tropical North Atlantic Ocean. Mar Environ Res 175, 105566. https://doi.org/10.1016/j.marenvres.2022.105566

Mortelmans, J., Goossens, J., Amadei Martínez, L., Deneudt, K., Cattrijsse, A., Hernandez, F., 2019. LifeWatch observatory data: Zooplankton observations in the Belgian part of the North Sea. Geoscience Data Journal 6, 76–84. https://doi.org/10.1002/gdj3.68

Mortelmans, J., Semmouri, I., Perneel, M., Lagaisse, R., Martínez, L.A., Rommelaere, Z., Hablützel, P.I., Deneudt, K., 2024. Temperature-induced copepod depletion and the associated wax of *Bellerochea* in Belgian coastal waters: Implications and shifts in plankton dynamics. Journal of Sea Research 201, 102523. https://doi.org/10.1016/j.seares.2024.102523

Oliver, E.C.J., Donat, M.G., Burrows, M.T., Moore, P.J., Smale, D.A., Alexander, L.V., Benthuysen, J.A., Feng, M., Sen Gupta, A., Hobday, A.J., Holbrook, N.J., Perkins-Kirkpatrick, S.E., Scannell, H.A., Straub, S.C., Wernberg, T., 2018. Longer and more frequent marine heatwaves over the past century. Nat Commun 9, 1324. https://doi.org/10.1038/s41467-018-03732-9

Remy, M., Hillebrand, H., Flöder, S., 2017. Stability of marine phytoplankton communities facing stress related to global change: Interactive effects of heat waves and turbidity. Journal of Experimental Marine Biology and Ecology 497, 219–229. https://doi.org/10.1016/j.jembe.2017.10.002

Schlegel, R.W., Smit, A.J., 2018. heatwaveR: A central algorithm for the detection of heatwaves and cold-spells. Journal of Open Source Software 3, 821. https://doi.org/10.21105/joss.00821

Semmouri, I., Asselman, J., Van Nieuwerburgh, F., Deforce, D., Janssen, C.R., De Schamphelaere, K.A.C., 2019. The transcriptome of the marine calanoid copepod *Temora longicornis* under heat stress and recovery. Marine Environmental Research 143, 10–23. https://doi.org/10.1016/j.marenvres.2018.10.017

Taylor, A.H., Allen, J.I., Clark, P.A., 2002. Extraction of a weak climatic signal by an ecosystem. Nature 416, 629–632. https://doi.org/10.1038/416629a

Wolf, K.K.E., Hoppe, C.J.M., Rehder, L., Schaum, E., John, U., Rost, B., 2024. Heatwave responses of Arctic phytoplankton communities are driven by combined impacts of warming and cooling. Sci Adv 10, eadl5904. https://doi.org/10.1126/sciadv.adl5904

Zeldis, J.R., Décima, M., 2020. Mesozooplankton connect the microbial food web to higher trophic levels and vertical export in the New Zealand Subtropical Convergence Zone. Deep Sea Research Part I: Oceanographic Research Papers 155, 103146. https://doi.org/10.1016/j.dsr.2019.103146

The role of sediment transport dynamics in ocean-based climate change mitigation technologies

Chloe Leach, Jaclyn E Cetiner, Hailey Hayes, Thi Tran, M. Grace Andrews, Emilia Jankowska, Cheyenne Moreau, Devon B. Cole

Hourglass Climate, Montclair, NJ, United States

The role of sediment transport dynamics in ocean-based climate change mitigation technologies

Chloe Leach[a], Jaclyn E Cetiner[a], Hailey Hayes[a], Thi Tran[a], M. Grace Andrews[a], Emilia Jankowska[a], Cheyenne Moreau[a], Devon B. Cole[a]

[a]Hourglass Climate, Montclair, NJ, United States

Corresponding author: Chloe Leach; chloe@hourglassclimate.org

Introduction

To limit Earth's climate warming to 2°C by 2100 requires widespread greenhouse gas emission reductions in conjunction with large-scale carbon dioxide removal (CDR) (National Academies of Sciences, Engineering, and Medicine, 2021). The ocean can store 100's of billions of tons of CO2 as alkalinity (dissolved carbon), which simultaneously offers the co-benefit of localized ocean acidification reduction. As such, Ocean Alkalinity Enhancement (OAE) technologies have significant promise for scaled climate change mitigation.

OAE technologies commonly provide alkalinity to seawater via the addition, and dissolution, of alkaline minerals. Transport of these minerals particles can be divided into two main categories; suspended load and bedload. The relative proportion of feedstock in these two reservoirs depends on many factors including sediment characteristics and hydrodynamics, but nevertheless, a significant proportion will be in suspension particularly during and immediately after mineral release. The transport fate of the feedstock dictates all relevant outcomes for these projects, including CDR efficiency (Zhou et al., 2025) and environmental impact. The suspended and bedload fractions can have different outcomes in each of these categories and so should be analysed as distinct portions, and later combined to determine overall project outcomes.

Here, we present preliminary findings from an OAE field trial deployed offshore of the Town of Duck, North Carolina, USA executed in May and June, 2024. Approximately 8,200 tonnes of sand, made from the alkaline mineral olivine (d50 = 0.17 mm, 5.8% fines), was placed as a set of three nearshore mounds in 7.6 m of water ~620 m offshore (Figure 1). The nearshore mounds were deployed on three separate days; Placement 1, 2 and 3 on 16 May 2024, 2nd June 2024 and 13th June 2024 respectively.

We report on the initial fate of the released sediment and describe the suite of methods used to track its transport and behavior. Based on these observations, we provide recommendations for robust carbon removal and environmental impact quantification (so called "Monitoring, Reporting, and Verification" (MRV)) of the suspended fraction in mineral-based OAE projects.

Our findings are applicable not only to olivine deployments but also to other mineral feedstocks currently being explored for marine carbon dioxide removal (mCDR).

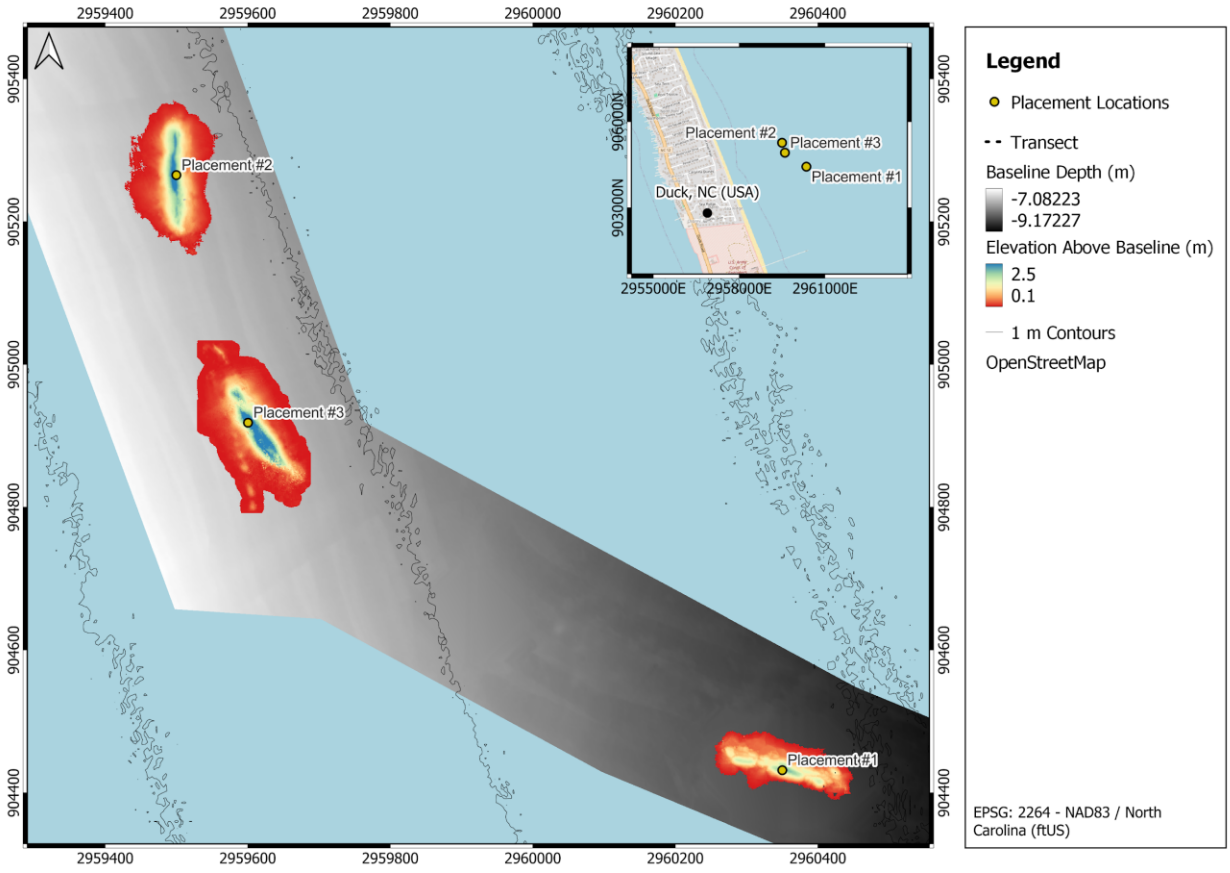

Figure 1. Location and extent of the three nearshore olivine mounds deployment off the coast of Duck, NC, during an OAE field trial

Methods

Multibeam bathymetric surveys were conducted over the project site, before and after the release of sediments using a Norbit 400 kHZ multibeam system. The surveys were differenced and the volume of each nearshore mound computed to determine the volume of material that settled on the seafloor versus the portion that remained in suspension.

A vertical array of YSI EXO2 Sondes was used during each olivine placement to monitor short-term, localized turbidity changes across the water column at a fixed location directly over the olivine mound. The three sondes were tethered to a floating buoy, recording data (1) just below the surface of the water, (2) in the mid-water column and (3) on the seafloor.

An AquaTROLL 500 water quality sonde was deployed from a moving vessel to collect data across the larger project area. Prior to the release of sediment, data was collected to represent conditions across the project area. After placement, the vessel was instructed to follow the pathway of any plume generated from the release of material. It was raised and lowered in the water column to determine any variations with depth.

Aboard the monitoring vessel, 5 L Niskin bottles and 2 L Van Dorn samplers were used to collect discrete water column samples intermittently at the surface and bottom of the water column. Samples were processed to determine Total Suspended Sediment (TSS) concentration, by filtering with 1 μm Sterlitech Corporation Glass Fiber Membrane Filters. Mineralogical analyses of the TSS samples are currently being conducted at QMineral (Leuven, Belgium) using x-ray diffraction (XRD) on a Bruker D8 Advance with XE-T detector and Cu-Kα radiation. Grain size analyses are also being conducted at QMineral using laser diffraction.

Wave and current measurements were derived from the U.S. Army Corps of Engineers (USACE) Field Research Facility (FRF) devices deployed adjacent to the project site. Near real-time wave conditions were recorded by a Waverider buoy located approximately 3.7 km offshore in -17.8 m of water (Station ID: 44056). Ocean current speeds and directions were derived from a bottom mounted Nortek Signature1000 Acoustic Doppler Current Profiler (ADCP) located approximately 600 m offshore at a depth of approximate -6.7 m.

Real-time aerial drone surveys were also conducted during each olivine berm placement to document plume dynamics at the surface.

Results

The bathymetries of difference show that all three mounds represent between 62-71% of the released material during each placement day, with the remainder considered to be transported in suspension. However, there are large error margins on this calculation due to factors such as survey accuracy, void space, and whether the force of the sediment release created a concave profile on the seafloor beneath the mounds.

A turbidity plume was generated from all three placements. The plumes were visible from aerial imagery and dispersed in the direction of the dominant flow path; towards the southeast during placement 1 and the northwest during placement 2 and 3 (Figure 2). The direction of transport and degree of dispersion of suspended sediments varied between placements, reflecting differences in local hydrodynamic conditions on each placement day. Specifically, there were more energetic conditions on the day of placement 1, compared to placement 2 and 3. Placement 1 experienced higher wave heights (0.86 m), longer wave periods (7.2 s), and more onshore-directed waves (60°) compared to placements 2 (0.33 m, 5.8 s, 100°) and 3 (0.53 m, 6.9 s, 110°),

which had lower, more northward-directed waves. Currents during placement 1 were faster (0.33 m/s) and flowed southward (160°), while those during placements 2 and 3 were slower (0.1–0.18 m/s) and flowed northward (335°–339°).

The stationary sondes deployed directly over each olivine placement showed that turbidity increased following the release of material, with peak values for placement 2 and 3 occurring within 30 minutes of release (Figure 3). The greatest increases were consistently found at the bottom of the water column. While placements 2 and 3 showed similar turbidity patterns, placement 1 showed high pre- and post-placement turbidity concentrations that remained elevated for the remainder of the monitoring day that concluded 7 hours and 40 minutes after placement.

Turbidity measurements across the larger project area collected from the vessel demonstrated that across all placements, turbidity (Figure 4) and total suspended solids (TSS) increased following release, concurrent with observations at the placement sites. Placement 1 showed the smallest turbidity response (max 32.85 NTU), with maximum values the furthest in space (107 m) and time (126 minutes) from the release. TSS concentrations were also the lowest overall (average 13.96 + 3.29 mg/l). Placement 2 recorded the highest peak (285.86 NTU) from the lowest baseline (0.11 NTU), observed within 30 minutes and 75 m from the placement site. Placement 3 exhibited moderate turbidity increases (max 79.62 NTU) from a higher baseline, similar in space (70 m) and closer in time (18 m) to observations during placement 2. TSS increased to a similar concentration during placements 2 and 3, from 4.67 ± 0.68 mg/l to 25.47 ± 6.29 mg/l, and from 18.59 ± 5.49 mg/l to 30.11 ± 5.93 mg/l respectively.

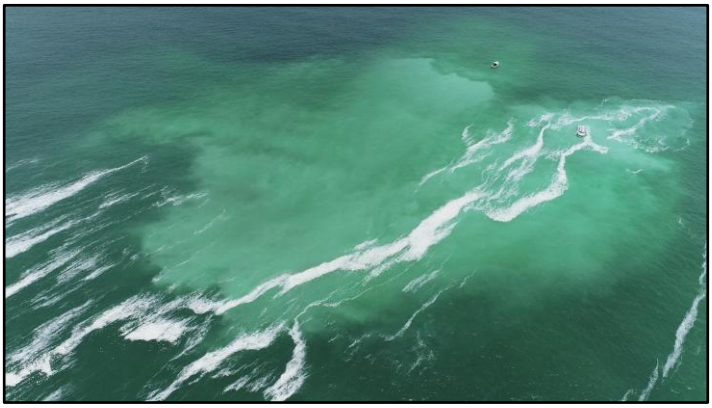

Figure 2. Aerial imagery taken during Placement 3 (13 June 2024, 13:49)

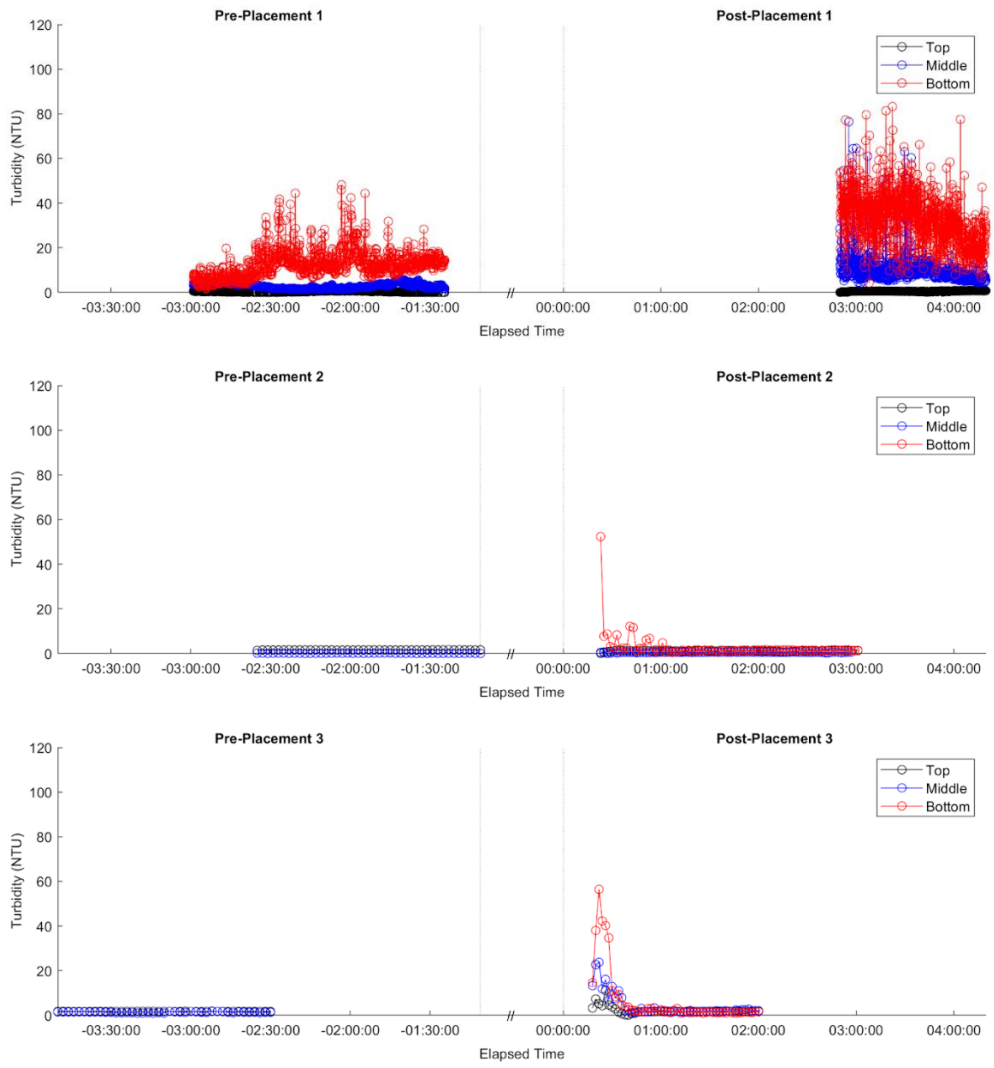

Figure 3. Turbidity (NTU) values pre- and post-placement, recorded using three EX02s at different depths in the water column at the deployment site. Top: Placement 1, middle: Placement 2, bottom: Placement 3.

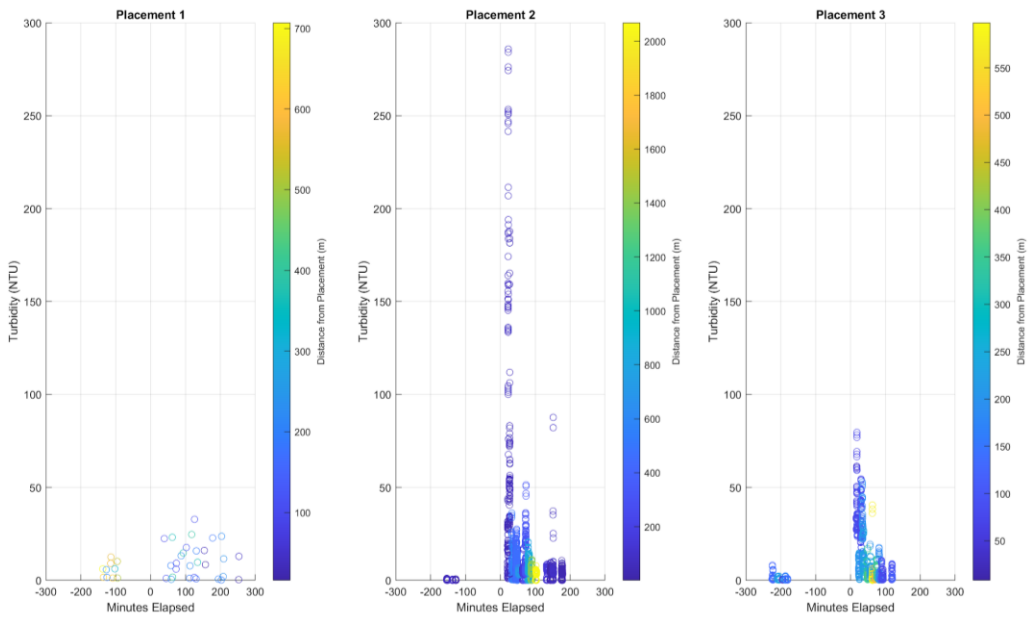

Figure 4. Turbidity (NTU) values pre- and post-deployment, recorded with the AquaTROLL 500 water quality sonde

Discussion

We deployed and evaluated a range of techniques designed to monitor the suspended sediment fraction from an OAE field trial with olivine sand. We take learnings from where we had successes, failures and gaps in data collection that will help to inform how future monitoring programs for the suspended sediment fraction could be designed.

Numerical modelling could be used to predict the fate of the suspended sediment fraction, which could be used to inform design decisions for the project and guide monitoring plans. In turn, data collected during the field-trials could be used to feedback and improve the model predictions for ongoing monitoring, subsequent placement and future projects. While extensive bedload sediment transport was conducted for this trial, suspended sediment transport modelling was not. This could have proven useful in predicting potential rates of plume dispersal and informed a monitoring strategy that was adaptable to dispersion rates, with the potential for a greater sampling success rate within the plume, particularly after placement 1.

Establishing a comprehensive baseline is critical for determining whether observed changes in suspended sediment are attributable to material release. Samples should be collected on the day of placement before any material release, to characterise the environment immediately before impact. The number of samples considered sufficient is driven by the minimum required for robust statistical analysis, and factors that influence the spatial extent of impact such as the energy of the system and the amount of material released. Although day-of baseline samples

were collected here, it was evident during data analysis that additional samples would have yielded a more robust statistical analysis and assessment of the natural heterogeneity at the site..

The bathymetry surveys were used to estimate the volume of sediment on the seafloor and infer the volume in suspension. Whilst this provided a useful first-order approximation, the associated errors are large which ultimately leads to greater uncertainty in CDR calculations and in relating suspended sediment concentrations of the feedstock to environmental impacts. High precision multibeam surveys are a primary way of reducing the error. Collection of sediment cores through to the native sediment layer could then estimate void ratios, compression effects on the seafloor and confirm presence of feedstock. Further methods of identifying the mineralogy of the substrate (e.g. backscatter) would also allow for validation of mineral extent on the seafloor, rather than relying on inference from bathymetric change.

Aerial imagery proved useful in the field for identifying the real-time extent of the sediment plume and directing the monitoring vessel into its path. However, reconciling this imagery with turbidity and TSS concentrations was challenging due to time gaps in imagery and the fact that it only reflected surface conditions. The sensor data showed that turbidity varied with depth, particularly near the placement site, meaning that surface imagery alone provides an incomplete picture. Complementary observations from the water column could enhance plume identification and characterisation, for example, through the use of underwater imagery where background turbidity is sufficiently low or imagery generated from backscatter.

Sampling the suspended fraction of the feedstock posed several challenges due to its heterogeneity and dynamic behaviour. Differences in hydrodynamic conditions between placements influenced plume detectability and behaviour, with stronger currents during placement 1 leading to rapid dispersion and a weaker mobile monitoring signal, while calmer conditions during placements 2 and 3 enabled collection of more samples within a less rapidly dispersing plume. To capture both the intensity and spatial extent of the plume, a combination of fixed sondes near the release site, mobile sensors and water column TSS samples proved successful during this field trial. We recommend this multipronged approach as part of a robust MRV strategy. We further suggest that multiple fixed sensor arrays could prove additive in identifying rates of transport and dispersion, and that UAVs be used to capture real-time baseline conditions beyond the extent of the plume and the suspended sediment gradient within the plume.

Key sediment parameters, including grain size and mineral composition must be characterised from the suspended material to support accurate CDR estimates. This includes quantifying the relative proportion of the feedstock versus native material. The number of samples collected

should be determined based on the minimum required for robust statistical analysis, the expected spatial extent of the plume according to the local hydrodynamics and quantity of sediment released, and the timeframe for post-placement monitoring. The water sample volumes should be determined based on the quantity of sediment required for analysis and expected sediment concentration in the water column. On average, the 5 L niskins used here collected a quantity of sediment that was more than sufficient for further analysis. However, the filters used to extract the sediment were principally selected based on their suitability for measuring TSS. We recommend that separate samples be collected for mineralogy and grain size analysis as this allows for customized filter material and mesh sizes.

Conclusion

This paper reports on the initial fate of sediment related from a mineral-based OAE field trial. Our monitoring strategy focused on tracking the fate of the feedstock across space and time, including the use of bathymetric surveys to estimate deposited versus suspended material, mobile and fixed sensors to monitor turbidity concentrations and transport, water column samples to quantify and characterise suspended sediment and aerial imagery to evidence the presence of a surface plume. The results demonstrated the complexity of robust monitoring strategies, challenges faced in collecting a comprehensive dataset and gave insights into potential improvements to the monitoring program.

References

National Academies of Sciences, Engineering, and Medicine (2021). A Research Strategy for Ocean-based Carbon Dioxide Removal and Sequestration. Washington,DC: The National Academies Press. doi:10.17226/26278

Zhou, M., Tyke, M.D., Ho, D.T., Yankovsky, E., Bachman, S., Nicholas, T., Karspeck, A.R., and Long, M.C (2025). Mapping the global variation in the efficiency of ocean alkalinity enhancement for carbon dioxide removal. Nature Climate Change, 15, 59-65, doi: 10.1038/s41558-024-02179-9

Effects of SPM concentration, composition, size characteristics and optical properties on hyperspectral reflectance signatures in a coastal estuary

Eurico D' Sa[a], Ishan Joshi[b], Christopher Osburn[c] Bingqing Liu[d]

[a] **Louisiana State University, Department of Oceanography and Coastal Sciences, Baton Rouge, LA, USA**
[b] **University of California, Scripps Institution of Oceanography, San Diego, CA, USA**
[c] **North Carolina State University, Department of Marine, Earth and Atmospheric Sciences, Raleigh, NC, USA**
[d] **University of Louisiana at Lafayette, School of Geosciences, Lafayette, LA, USA**

Effects of SPM concentration, composition, size characteristics and optical properties on hyperspectral reflectance signatures in a coastal estuary

Eurico D'Sa[a], Ishan Joshi[b], Christopher Osburn[c] Bingqing Liu[d]

[a]Louisiana State University, Department of Oceanography and Coastal Sciences, Baton Rouge, LA, USA
[b]University of California, Scripps Institution of Oceanography, San Diego, CA, USA
[c]North Carolina State University, Department of Marine, Earth and Atmospheric Sciences, Raleigh, NC, USA
[c]University of Louisiana at Lafayette, School of Geosciences, Lafayette, LA, USA
Corresponding author: Eurico D'Sa; ejdsa@lsu.edu

Introduction – Estuaries represent transitional zones between terrestrial and marine environments, where the mixing of freshwater from rivers and streams with oceanic waters often result in strong gradients in salinity, suspended particulate and dissolved materials along the freshwater-marine continuum (Bianchi et al. 1999) that further contribute to the highly dynamic nature of suspended particulate matter (SPM) in coastal waters and influences water transparency, light availability and primary productivity, including sediment and pollutant transport with implications for coastal ecosystems. With highly productive coastal estuaries such as Barataria Bay in the Gulf of Mexico facing increased impacts of climate and anthropogenic pressures, elucidating the dynamics and characteristics of SPM such as particle size distribution, composition and optical properties (Agrawal and Pottsmith 2000; Reynolds et al. 2010; Naik et al. 2011; Loisel et al. 2023; D'Sa et al. 2025) will contribute to better understanding of this important aquatic constituent and support water quality studies and provide insights for improving bio-optical algorithms for the new generation of hyperspectral ocean color sensors such as PACE-OCI in estuarine environments.

Methods

Study area: Barataria Bay (BB), a semi-enclosed estuary (~1670 km^2) located between the Mississippi River and Bayou Lafourche (an abandoned river channel), is bounded to the south by a chain of barrier islands with tidal passes connecting the estuary to the Gulf of Mexico. It is a well-mixed, microtidal estuary with an average depth of 2 m. The constructed levees along the Mississippi River have significantly reduced freshwater and riverine sediment input to the estuary. The northern part of the bay receives freshwater from rainfall, run-off and from the Davis Pond Freshwater Diversion (~150 m^3 s^{-1}), while the lower bay is influenced seasonally by the magnitude of the river discharge and coastal currents due to its proximity to the Mississippi River (Fig. 1).

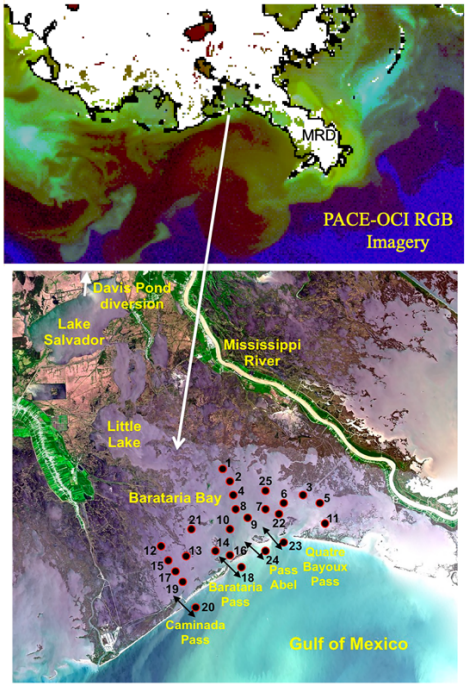

Figure 1. Location of Barataria Bay (BB) in the Mississippi River dominated Louisiana coast with sampling stations shown.

Field sampling and data collection -Surface water samples were collected for measurements of biogeochemical and bio-optical properties during three field surveys conducted in summer 2015 (20–21 July), spring 2016 (13–15 April) and fall 2016 (4–6 October) (Figs. 1, 2).

LISST measurements - A LISST-100X (Type C, 2.5-500 µm range, 1Hz; Sequoia Scientific Inc.) was used to estimate the PSD in the surface water samples.

Satellite ocean color data - Cloud free imagery from the Plankton, Aerosol, Cloud, and ocean Ecosystem (PACE) Ocean Color Instrument (OCI) launched 8 February 2024 (PACE-OCI Level-2 version 3.0 Regional Apparent Optical Properties) of estuary were downloaded from NASA's Earthdata portal (https://search.earthdata.nasa.gov/search) during spring (April 4), summer (August 14), and fall (October 13) of 2024. These data were used to examine time-gapped surface spectral remote sensing reflectance, $R_{rs}(\lambda)$, at selected sampling locations for comparison with in situ $R_{rs}(\lambda)$.

Results and discussions

Located to the west of the Mississippi River is the shallow and broad Barataria estuary that is connected to the Gulf of Mexico through four tidal passes (Fig. 1). Due to its proximity to the Mississippi River Birdsfoot Delta, the coastal section of the estuary is influenced by discharges from the Mississippi River (Fig. 2a). The Davis Pond diversion with its maximum design capacity of 300 m^3s^{-1} (Fig. 2b), is the estuary's primary though limited freshwater source with discharge relatively uniform (21 m^3 s^{-1} to 35 m^3 s^{-1}) corresponding to river discharges of 28,880

m^3 s^{-1} (summer 2015), 23,080 m^3 s^{-1} (spring 2016) and 10,365 m^3 s^{-1} (fall 2016), respectively. Synoptic weather patterns such as cold fronts (about 30 – 40; defined as periods of average wind speed >5 m s^{-1} lasting more than one day) passing through the Louisiana coastline between October and April have been observed to contribute to wave-induced bottom sediment resuspension in the estuary.

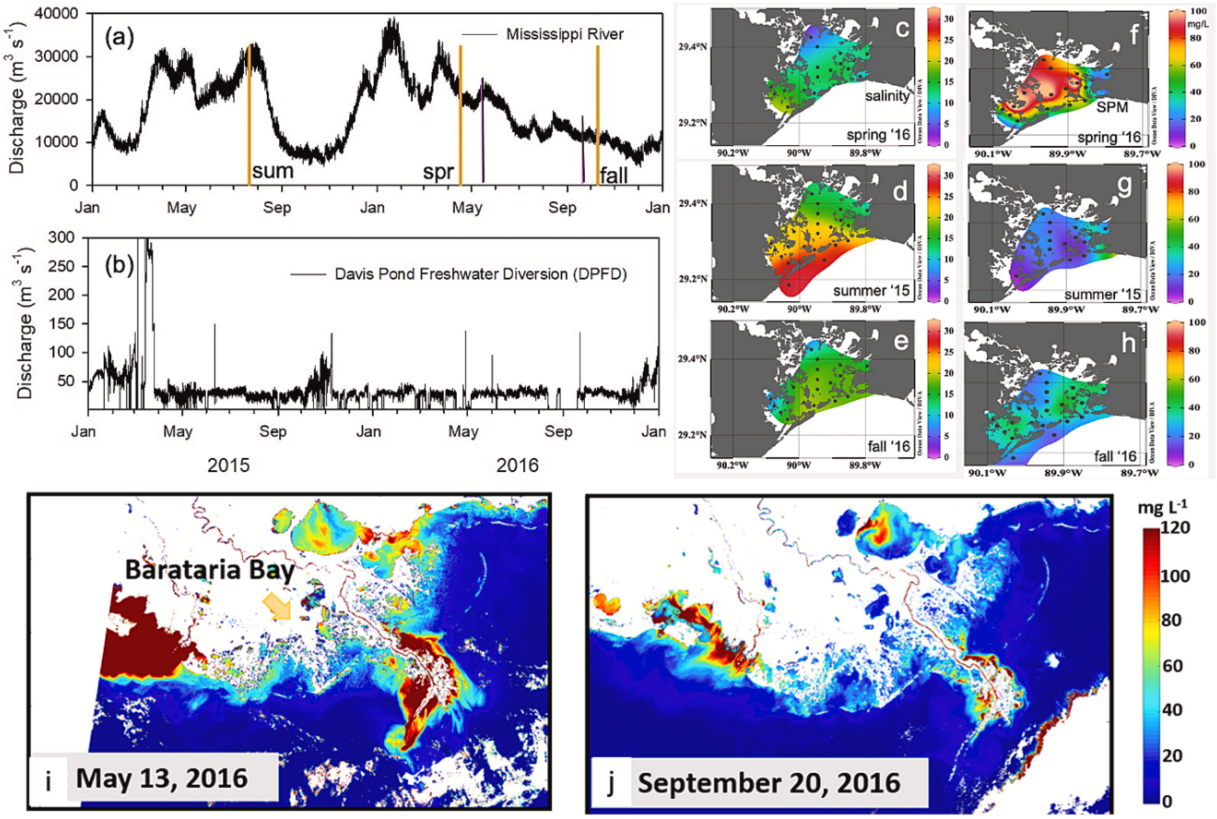

Figure 2. (a) Mississippi River discharge and (b) Davis Pond diversion freshwater discharge conditions during 2015 and 2016 (vertical orange lines denote the field campaigns in Barataria Bay (BB) in summer 2015, and spring and fall of 2016; black lines denote satellite imagery dates. Surface salinity (c-e) and SPM (f-h) distributions in BB during summer 2015 and spring and fall of 2016. Sentinel-3 OLCI SPM imagery of river delta and BB on 13 May and 20 September of 2016 (adapted from D'Sa et. Al. 2025).

Although discharge from the Mississippi River (Fig. 2a) does not directly influence the Barataria Bay, diversions, siphon points and runoff including exchange with the low salinity shelf waters, especially during high river discharge have an impact on the bay's salinity (Fig. 2c–e). Average salinity was low in the spring of 2016 (13.44 ± 3.02) due to elevated river discharge during the winter/spring period and the normally westward current flows; salinity increased to 16.33 ± 3.41 in the fall of 2016 as the river discharge decreased. Corresponding SPM concentrations varied between 19.66 and 115.50 mg L^{-1} in spring of 2016 (mean 66.36 ± 29.17 mg L^{-1}) and between 5.6 and 59.2 mg L^{-1} in the fall of 2016 (mean 21.62 ± 12.81 mg L^{-1}), respectively, showing large spatial variability in SPM distribution within the estuary (Figure 2f–h). The high SPM in spring

(Fig. 2f) could be attributed to the river discharge and to sediment resuspension associated with elevated wind events (cold fronts) which occur frequently in spring. In the summer of 2015, salinity was lower (mean 20.59 ± 4.82) compared to spring despite higher river discharge (Fig. 2a). Winds are the primary driver of upper circulation along the Louisiana coast with westward or downcoast flow during fall and winter. However, during summer the downcoast current weakens and disappears due to wind shift from easterly to southerly and southwesterly, and an upcoast current develops which can contribute to dispersal of plume waters; this dispersal of shelf waters likely contributed to higher salinity in the southwestern part of the Barataria Bay (Fig. 2d) and to overall lower SPM (mean 30.54 ± 8.2 mg L^{-1}; Fig. 2g). Sentinel 3-OLCI satellite derived estimates of SPM concentrations for the deltaic region including BB for May 13 (spring) and September 20 (fall) of 2016 (Fig. 2i, j) reveal the generally high SPM in the Mississippi and Atchafalaya River deltas.

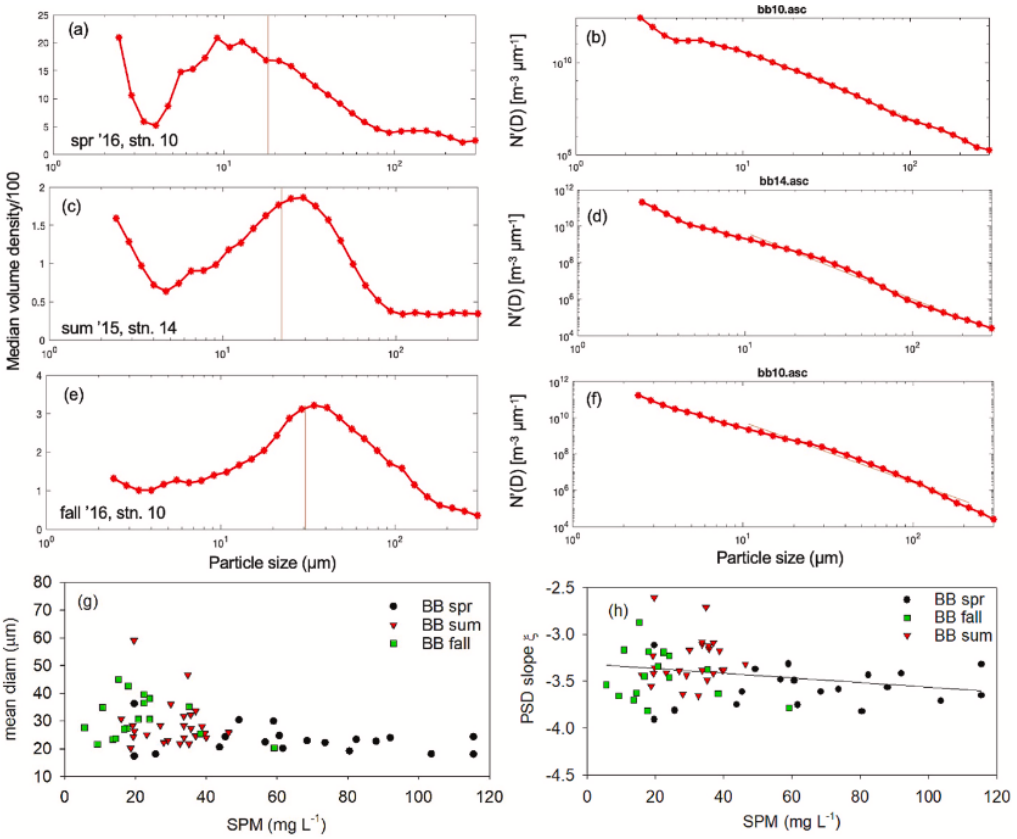

Figure 3. (a, c, e) Volume concentration density of each size class V′(D) (ppm µm^{-1}) normalized by 100 times total volume of all size classes and corresponding (b, d, f) number density N′(D) as a function of particle size for typical surface samples obtained during spring (stn. 10), summer (stn. 14) and fall (stn. 10) in BB. Relationships between SPM (mg L^{-1}) and (g) mean diameter (µm) and (h) PSD slope (ξ) in BB during spring, summer and fall of 2015/2016, respectively. Stations representing field campaigns in the spring, summer, and fall seasons are depicted as black circles, red inverted triangles, and green squares, respectively.

Particle size distribution (PSD) characteristics that include volume and number concentration densities were examined at three representative stations during spring 2016 (stn. 10), summer 2015 (stn. 14) and fall 2016 (stn. 10) located in the lower estuary (Fig. 3a–f) along with the mean particle diameter and PSD slopes for all stations sampled during the three field campaigns (Fig. 3g, h).

During spring 2016, high mass concentrations and low POC/SPM ratio were observed at most stations, as indicated by stn. 10 (SPM 103.6 mg L^{-1}, POC/SPM 0.05), with volume density concentration (Fig. 3a) showing the presence of particles with a minor peak at ~150 μm and major peaks between ~6 μm and 20 μm, that was however not well resolved by the LISST sensor, and ~7 orders of magnitude range in particle number concentration (Fig. 3b). A strong rising tail at the lowest end of the PSD estimated volume concentration followed by a minimum in the other small size classes (e.g., Fig. 3a) can be attributed to particles smaller than 2.5 μm and an artifact created by LISST (Fabris et al. 2021). Further, such strong rising tails in the size distribution that is also reflected in a steep slope in N′(D) (Fig. 3b) have been attributed to the presence of inorganic natural particles (Ahn and Grant, 2007) and supported by the low POC/SPM ratio (0.05) (Loisel et al. 2023).

A sharp rising tail also observed at stn. 14 (Fig. 3c) sampled during summer of 2015 (salinity 25.39, SPM 32.57 mg L^{-1}, POC/SPM 0.08) indicated the presence of particles smaller than 2.5 μm in the particle size spectrum. In comparison, at stn.10 (Fig. 3e) sampled during fall of 2016 (salinity 18.88, SPM 20.80 mg L^{-1}), the POC/SPM ratio and particulate absorption coefficients along with a slow rising tail suggested the presence of mixed inorganic/organic particle field with a smaller fraction of particles <2.5 μm and the likely presence of three distinct phytoplankton populations of sizes ~30 μm (major peak), ~100 μm and ~7 μm (minor peaks). Worth noting is that despite SPM mass concentrations being significantly higher at stn. 14 (32.57 mg L^{-1}) than at stn. 10 (20.80 mg L^{-1}), total VC was much lower at stn. 14 (29 μl/l) compared to stn. 10 (50 μl/l) indicating the greater contribution by phytoplankton to VC at stn. 10 (fall 2016), with enriched stable isotope values of POM also indicating a strong phytoplankton contribution (Arellano et al. 2019). For all stations sampled, mean particle diameter (23.12±4.49 μm) and PSD slope (-3.57±0.19) were the lowest in spring compared to summer and fall (Fig. 3g, h) indicating the presence of fine-grained resuspended inorganic particles in the water column linked to frequent frontal passages during spring.

The dimensionless POC/SPM ratio (Loisel et al. 2023) was used to describe the seasonal variability in particulate matter composition in BB (Fig. 4 horizontal dash lines denote the POC/SPM ratio thresholds for mineral dominated (<0.08), organic dominated (>0.2) and mixed

(between 0.08 to 0.2) waters. Phytoplankton absorption coefficient at 676 nm, $a_{phy}676$ is used as an optical proxy for phytoplankton biomass (Roesler and Barnard, 2015).

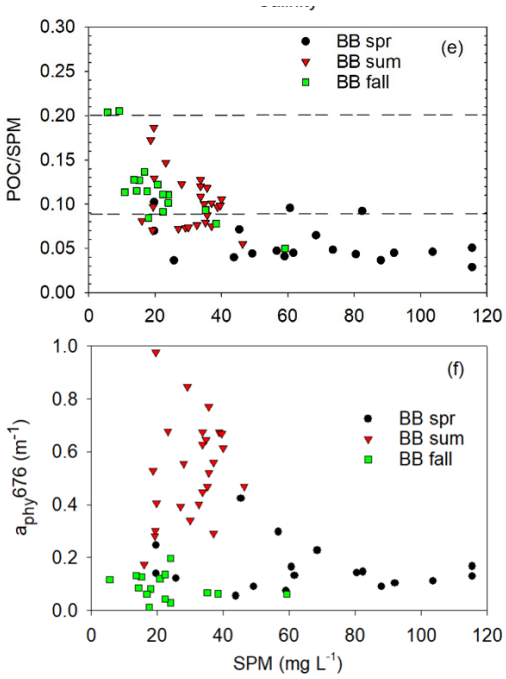

Figure 4. Seasonal relationships between, (e) SPM vs. POC/SPM ratio, and (f) SPM vs. $a_{phy}676$ for BB. Stations representing field campaigns in the spring, summer, and fall seasons are depicted as black circles, red inverted triangles, and green squares, respectively. The upper and lower dashed lines in the middle panel represent thresholds distinguishing organic from mixed classes (POC/SPM = 0.2) and inorganic from mixed classes (POC/SPM = 0.08), respectively (adapted from D'Sa et al. 2025).

Suspended particulate matter was high in BB with clear seasonal differences in particulate composition (Fig. 4). During spring 2016, under low salinity and high SPM conditions (Fig. 2c,f), particulate composition was mineral dominated (mean POC/SPM: 0.06 ± 0.02) despite elevated $a_{phy}676$ (0.14 ± 0.08 m^{-1}). In comparison, in the fall, under lower river discharge conditions and relatively higher salinity in the estuary (Fig. 2a,e), particulate composition was mixed with relatively higher POC/SPM ratio (0.12 ± 0.04) and lower $a_{phy}676$ (0.09 ± 0.05 m^{-1}; Fig. 4) indicating greater contribution by detrital organic matter or smaller sized autotrophic population. During summer of 2015, POC/SPM ratio (0.10 ± 0.03) suggested a mixed particulate assemblage with high $a_{ph}676$ (0.53 ± 0.19 m^{-1}) indicating increased contribution by phytoplankton to the particulate assemblage.

Dissolved and particulate matter interact with the underwater light by absorption and scattering to influence the remote sensing reflectance. The three main non-water constituents, namely CDOM, phytoplankton and nonalgal matter that contribute to the absorption were examined using a ternary plot to aid the interpretation of in situ hyperspectral $R_{rs}(\lambda)$ (Fig. 5) collected concurrently at the sampling stations in the two estuaries. Further, the seasonal (spring, summer

and fall) hyperspectral $R_{rs}(\lambda)$ from the recently launched PACE-OCI satellite sensor were also examined for comparison (Fig. 6) to assess the atmospherically corrected reflectance signatures characteristic of the two contrasting estuarine systems.

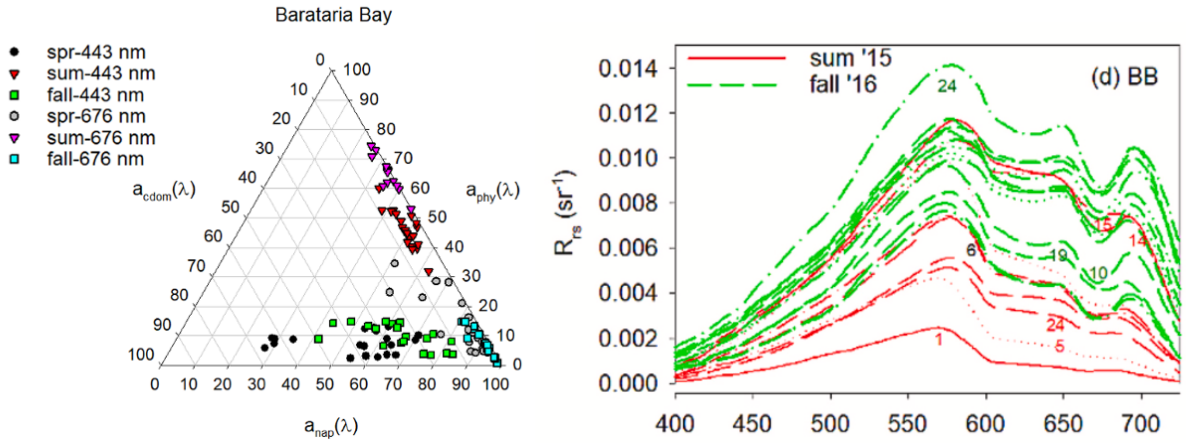

Figure 5. Ternary plots showing relative contribution of absorption by CDOM, phytoplankton and non-algal particles at 443 nm and 676 nm for BB. Remote sensing reflectance spectra, $R_{rs}(\lambda)$, obtained from field measurements in BB. The numbered labels on the spectra correspond to station locations in Fig. 1 (adapted from D'Sa et al. 2025).

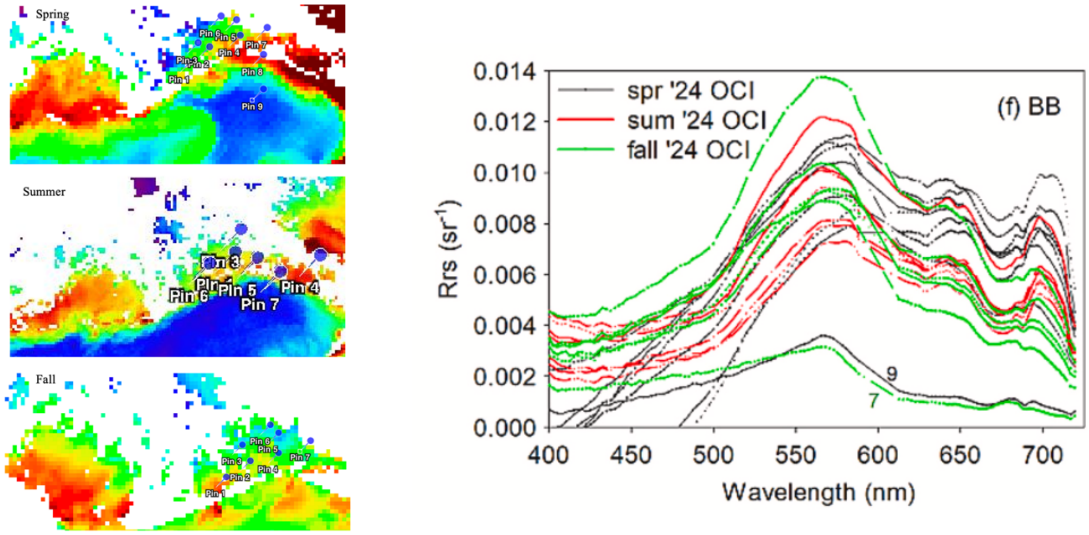

Figure 6. PACE-OCI derived $R_{rs}(\lambda)$ in Barataria Bay (left). The numbered labels on the spectra correspond to pin locations in the PACE-OCI imagery (adapted from D'Sa et al. 2025).

Conclusion

This study which aimed to elucidate the seasonal dynamics and characteristics of SPM in Barataria Bay demonstrates that field observations of suspended matter particle concentration, composition and size characteristics could contribute to better understanding of the biogeochemical cycling and transformation of this important aquatic constituent and support

water quality and biogeochemical studies using the new generation hyperspectral ocean color sensors such as the PACE-OCI.

References

Agrawal, YC, Pottsmith, HC (2000) Instruments for particle size and settling velocity observations in sediment transport. Marine Geology 168, 89-114.

Ahn, JH, Grant, SB (2007) Size distribution, sources, and seasonality of suspended particles in Southern California marine bathing waters. Environmental Science and Technology 41 (3), 695–702.

Bianchi TS, Pennock JR, Twilley RR (1999) Biogeochemistry of Gulf of Mexico Estuaries. John Wiley & Sons.

D'Sa EJ, Joshi ID, Osburn CL, Liu, B (2025) Suspended particulate matter distribution, composition and size characteristics in two coastal estuaries (Gulf of Mexico): seasonal variability and influence on hyperspectral reflectance signatures. Science of the Total Environment 987, 179801.

Fabris, AS, Larouche, P, Montero-Serrano, JC (2021) Characterization of suspended matter size and composition in the St. Lawrence Estuary (eastern Canada). Regional Studies of Marine Science 45, 101838.

Loisel, H, Duforêt-Gaurier, L, Tran, TK, Schaffer Ferreira Jorge, D, Steinmetz, F, Mangin, A, Bretagnon, M, Hembise Fanton d'Andon, O (2023) Characterization of the organic vs inorganic fraction of suspended particulate matter in coastal waters based on ocean color radiometry remote sensing. State of Planet 1-osr7, 11.

Naik, P., D'Sa, E.J., Grippo, M., Condrey, R., Fleeger, J., 2011. Absorption properties of shoal-dominated waters in the Atchafalaya shelf, Louisiana, USA. Int. J. Remote Sens. 15, 4383–4406.

Reynolds, RA, Stramski, D, Wright, VM, Wozniak, SB (2010) Measurements and characterization of particle size distributions in coastal waters. Journal of Geophysical Research 115, C08024.

Roesler, CS, Barnard, AH (2013) Optical proxy for phytoplankton biomass in the absence of photophysiology: Rethinking the absorption line height. Methods in Oceanography. 7, 79–94.

A visual survey of the Atlantic: Particle size distributions from the imaging sensors

Marika Takeuchi[a], Zonghua Liu[b], Mojtaba Masoudi[a], Thanga Thevar[c], Sarah L.C. Giering[a]

[a] National Oceanography Centre, European Way, Southampton, UK
[b] Robert Gordon University, School of Engineering, Aberdeen, UK
[c] University of Aberdeen, King's College, Aberdeen, UK

A visual survey of the Atlantic: Particle size distributions from the imaging sensors

Marika Takeuchi[a], Zonghua Liu[b], Mojtaba Masoudi[a], Thanga Thevar[c], Sarah L.C. Giering[a]

[a] National Oceanography Centre, European Way, Southampton, UK
[b] Robert Gordon University, School of Engineering, Aberdeen, UK
[c] University of Aberdeen, King's College, Aberdeen, UK
Corresponding author: Marika Takeuchi; marika.takeuchi@noc.ac.uk

Introduction

Particle sinking is a major pathway to transfer particulate organic carbon (POC) from the surface to the deep ocean. This carbon transfer process is called biological carbon pump (BCP) and has a large contribution to the global ocean carbon storage (Falkowski et al. 1998). Suspended particles that are consisting of miscellaneous organic and inorganic matter called marine aggregates (hereafter aggregates) have remarkable roles in BCP. Large aggregates with fast sinking speed accelerate BCP, however, once aggregates are grazed by organisms in higher trophic levels such as zooplankton and fish, POC is captured in the upper ocean food web and may cause delay in POC transfer to the deeper ocean (Ducklow 2001). Furthermore, grazing by organisms can also cause fragmentation of aggregates, resulting in decreasing size and sinking speed. Thereby, the contribution of aggregates to BCP varies depending on the size and remains unclear. To fully understand the roles of aggregates in BCP, further investigation of *in-situ* aggregate size distributions that shows micrometre scale (small slow-sinking aggregates) to centimetre scale (large fast-sinking aggregates) is required.

Methods

To construct in-situ aggregate size distributions, it was essential to develop observational methods capable of capturing a broad particle size range—from micrometres to centimetres. Numerous underwater imaging instruments are available, each optimized for different size classes, but individually limited in their size coverage. To overcome this, we integrated two complementary high-resolution imaging systems—the LISST-HOLO2 (holographic imaging, micrometre to sub-millimetre scale) and the UVP5 (optical imaging, sub-millimetre to centimetre scale)—on a single frame to enable simultaneous, co-located measurements across several orders of magnitude. During a 2023 Atlantic Ocean transect, we conducted 27 vertical profiles spanning a range of oceanographic regimes. In this study, I present the resulting particle size distributions and discuss how the combined system improves resolution and continuity across size ranges compared to using a single instrument alone.

Results

Preliminary observations from the 27 transect stations indicate a latitudinal trend in particle size distribution. Larger aggregates were generally more abundant at higher latitudes in both hemispheres, while smaller particles with lower overall concentrations were more commonly observed near the equator. These patterns were consistent across multiple depth layers, suggesting a link between particle size structure and regional biogeochemical conditions. The combined use of LISST-HOLO2 and UVP5 enabled characterization of particle distributions across a wide size range, revealing vertical and horizontal variability along the Atlantic transect. Ongoing analysis will further refine these trends and explore their relationship with environmental parameters such as productivity and water column structure.

Conclusion

The combination of LISST-HOLO2 and UVP5 provided a robust method for capturing in-situ particle size distributions across a broad range of sizes. Preliminary results suggest clear latitudinal and vertical patterns in particle abundance and size, with potential implications for understanding regional differences in particle dynamics and carbon export. Further analysis will help link these patterns to underlying oceanographic processes.

References

Ducklow, H. W. 2001. Upper Ocean Carbon Export and the Biological Pump. Oceanography **14:** 50-54.

Falkowski, P. G., R. R. Barber, and V. Smetacek. 1998. Biogeochemical Controls and Feedbacks onOcean Primary Production. Sceince **281:** 200-206.

N. Otsu, "A Threshold Selection Method from Gray-Level Histograms," in *IEEE Transactions on Systems, Man, and Cybernetics*, vol. 9, no. 1, pp. 62-66, Jan. 1979, doi: 10.1109/TSMC.1979.4310076.

Use of a Lagrangian Particle Model to Characterise a New Acoustic Backscatter Profiler

Andy Smerdon[a,b], Dominic van der A[b], Tom O' Donoghue[b]

[a] Aquatec Group, Aquatec House, Stroudley Road, Basingstoke, RG24 8FW, UK

[b] University of Aberdeen, School of Engineering, Aberdeen, AB24 3UE, UK

Use of a Lagrangian Particle Model to Characterise a New Acoustic Backscatter Profiler

Andy Smerdon[a,b], Dominic van der A[b], Tom O'Donoghue[b]

[a]Aquatec Group, Aquatec House, Stroudley Road, Basingstoke, RG24 8FW, UK
[b]University of Aberdeen, School of Engineering, Aberdeen, AB24 3UE, UK
Corresponding author: Andy Smerdon; asmerdon@aquatecgroup.com

Introduction – Acoustic backscatter measurement is a proven technique for monitoring suspended matter in aquatic environments. When multiple acoustic frequencies are used, analysis of the acoustic responses can reveal detailed vertical profiles of suspended sediment concentration and mean particle size (Thorne and Hanes, 2002). Instruments such as the AQUAscat® 1000, developed by Aquatec, have been widely used for this purpose (Smerdon and Caine, 2007).

Evaluating new acoustic instruments typically involves time-consuming and uncertain field experiments. Experimental processes can introduce sufficient uncertainty to hinder full performance verification. Moreover, while electronics hardware is being validated, it is also useful to evaluate new signal processing algorithms independently from the electronics. Numerical models offer a faster and more controlled alternative for exploring instrument behaviour under a variety of environmental conditions.

In this paper, we describe the application of a Lagrangian particle model designed to assess the expected performance of a new evolution of the AQUAscat instrument over a range of suspensions, concentrations and hydrodynamic conditions.

Acoustic Suspension Models

Particle suspension models are widely applied in coastal and river modelling to predict the dynamics of sediment concentration at a macro scale. At such scales, physical observations are made with a typical spatial resolution in the order of 1 m to 10 m using techniques such as satellite remote sensing and acoustic Doppler current profilers. This aligns well with Eulerian modelling approaches, which can generally model suspensions efficiently at these broader scales.

On the finer scale needed to model boundary layer processes, such as erosion, deposition and resuspension, observations are frequently made with spatial resolution in the order of 1 cm. For the most part, Eulerian models have also been used to describe the acoustic backscatter response of these small volumes. However, to be effective, they must assume that particle positions between observations are uncorrelated. While that is convenient for measurements of particle

concentrations in a dynamic environment, it does not allow for the simulation of particle velocities or turbulence, where knowledge of the relative positions of particles from one observation to the next is essential to derive such dynamic parameters.

Recently Fromant *et al.* (2024) described a point-particle Lagrangian simulation. This was run on a high-performance computing cluster and used to evaluate the performance of a bistatic coherent Doppler acoustic backscatter instrument. A range of concentrations of particles of a single radius at different constant advection velocities were modelled. Use of the model highlighted the opposing demands of simultaneous velocity and particle load observations. The former requires coherent measurements for accuracy, while the latter requires independent, uncorrelated measurements. The model results show how this leads to statistical bias errors in the measurement of particle concentration and time resolved flux, based on the residence time of particles in a measurement sample volume.

In this paper, we describe an alternative point-particle Lagrangian model that has initially been developed in MATLAB and optimised for the monostatic configuration of the AQUAscat instrument, where the acoustic transmitting and receiving transducers are at the same location. The model generates a particle population with a specified size distribution and concentration, to which can be applied horizontal and gravity-driven flows, random motions, and turbulent velocity spectra. For higher concentrations, the model granularity can be reduced to allow it to run on a standard laptop PC.

Acoustic System

The instrument model currently generates a sequence of up to four single-frequency transmission voltages, with configurable timing, digital quantisation levels, and gain. These are processed through transducer models with experimentally derived transfer functions to obtain the transmitted acoustic signal (Figure 1). The receiver model also incorporates a transducer transfer function, configurable gain and quantisation, and the ability to introduce input-referred noise. The model includes quadrature data acquisition at a configurable rate and digital down-sampling to generate acoustic backscatter profiles at the chosen spatial resolution.

The model has been designed to support various particle types. It currently includes sand and glass beads but is also intended to be used to simulate marine biota, frazil ice, oil droplets, and bubbles. For each particle type, an appropriate scattering equation is used.

A simplified sample volume is created to incorporate only the extent of the main acoustic beam of each transducer, derived from their theoretical near field distance and far field main beam angle. The sample volume is split into bins that correspond to the simulated instrument acoustic range bins. For this simulation, each bin is populated independently, meaning there is no

relationship between the particles that leave one bin and those that arrive in an adjacent bin. The bins are chosen to be arranged vertically down from the transducers.

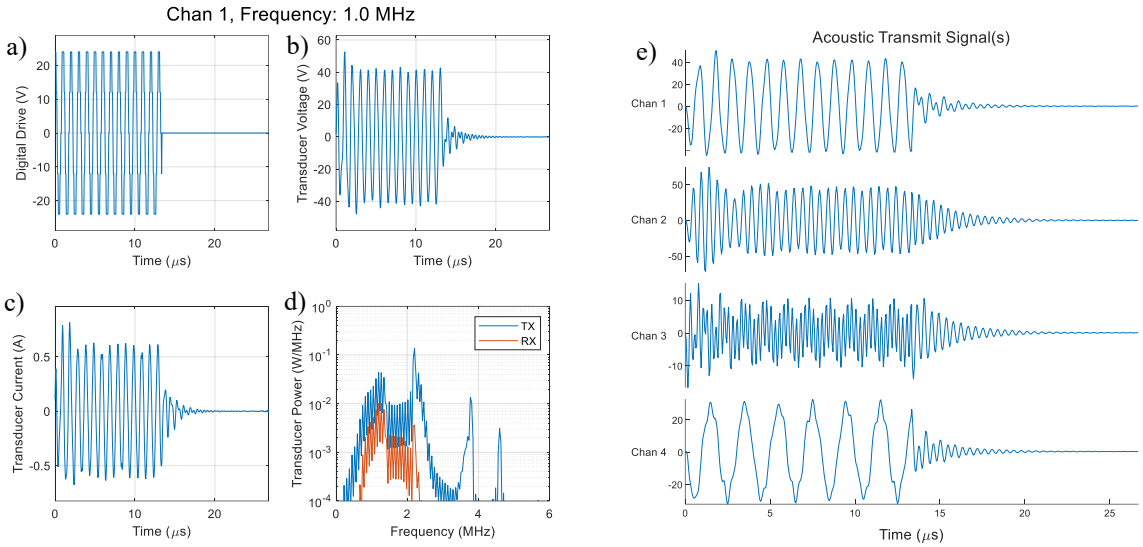

Figure 1: Signal generation waveforms. a) Quantised drive; b) Transducer voltage; c) Transducer current; d) Tx and Rx spectra; e) Transmitted waveforms for Channels 1 to 4 at 1 MHz, 2 MHz, 4 MHz, and 0.5 MHz

A population of *n* particles is created, where *n* is the maximum granularity of the model. The particles are created with a chosen size distribution (uniform, normal, or log normal), mean and standard deviation. Based on the chosen mass concentration and mean particle size, the number of particles in each bin is calculated. For low concentrations, this number may be less than one, so it is then used as the probability of a particle being present or absent in the bin. When the number is greater than *n*, the number of particles is set to *n* and a scale factor is applied to the backscattering strength later in the calculation, thus placing an upper limit on the number of particle calculations. Every particle within the bin is assigned random coordinates. Figure 2 provides further information.

Environmental Variables

The water environment is defined by user-selected temperature, depth, salinity and pH, and other parameters such as speed of sound, water density, dynamic and kinematic viscosity, and sound absorption are all calculated from these. The density of each particle population is also provided by the user.

a)

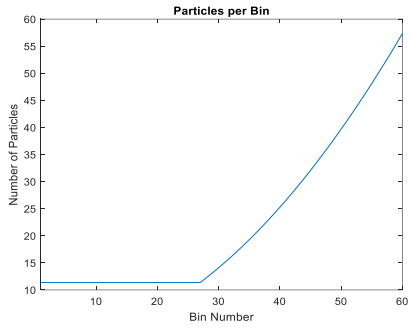

b)

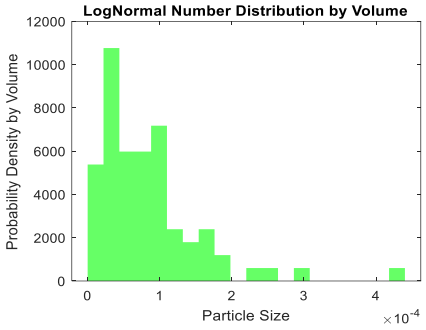

c)

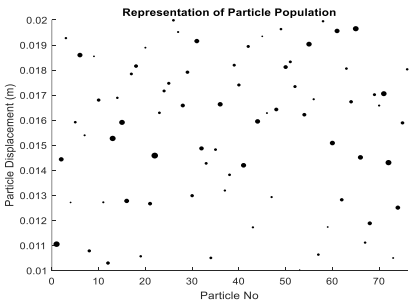

d)

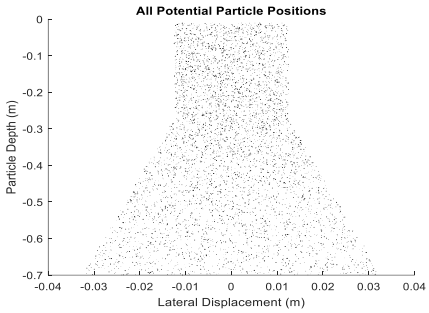

Figure 2: Particle Population (mass concentration 5 mgL-1, mean radius 59 µm, relative standard deviation 0.9)
a) Number of particles per 1 cm bin, bin 1 closest to transducer; b) Particle size distribution
c) Visual representation of particle population in one bin; d) Initial model particle distribution (transducers at top)

Particle Dynamics

Four dynamic effects can currently be applied to the particle populations, either individually or in combination. In each case, when a particle crosses a bin boundary because of its motion, it is replaced by a new randomly chosen particle that enters the bin from the boundary opposite. As the acoustic instrument analyses each bin independently, it is a statistical simplification to not move particles from one bin to the next and assume a constant supply of random new particles to maintain concentration.

Particles can be displaced with random vertical displacements to reduce or remove the correlation between consecutive acoustic transmissions. A constant horizontal velocity can be applied to advect particles across the beam, thereby controlling the particle residency. Stokes settling can be applied to particles, so that they descend vertically according to their weight and drag. Finally, a one-dimensional turbulence velocity spectrum can be applied to the particles.

As the measurement of velocity in a monostatic system can only be along the axis of the beam, there is no need to complicate the model by applying turbulence velocity components perpendicular to the beam. Any analysis using this approach must assume that the turbulent environment is locally homogeneous and isotropic. The turbulence simulation creates an idealised Kolmogorov energy spectrum with -5/3 slope for length scales appropriate to the

modelled acoustic profile, bin size and user-selected Total Kinetic Energy (TKE) and TKE Dissipation Rate to suit the environment (Figure 3a). This is then converted to velocities in each bin (Figure 3b).

Model Execution

The current version of the model is written as a MATLAB Live Script. After establishing the environmental variables and particle populations, a sequence of simulated acoustic transmissions is executed at the chosen timing intervals. Between each transmission, the hydrodynamic motions are applied to every particle, replacing those particles that leave a bin due to motion with new randomly generated particles from the same population.

The model stores the coherently summed and down-sampled backscatter in a file with a format that mimics the standard AQUAscat instrument data, so that it can be processed using existing tools.

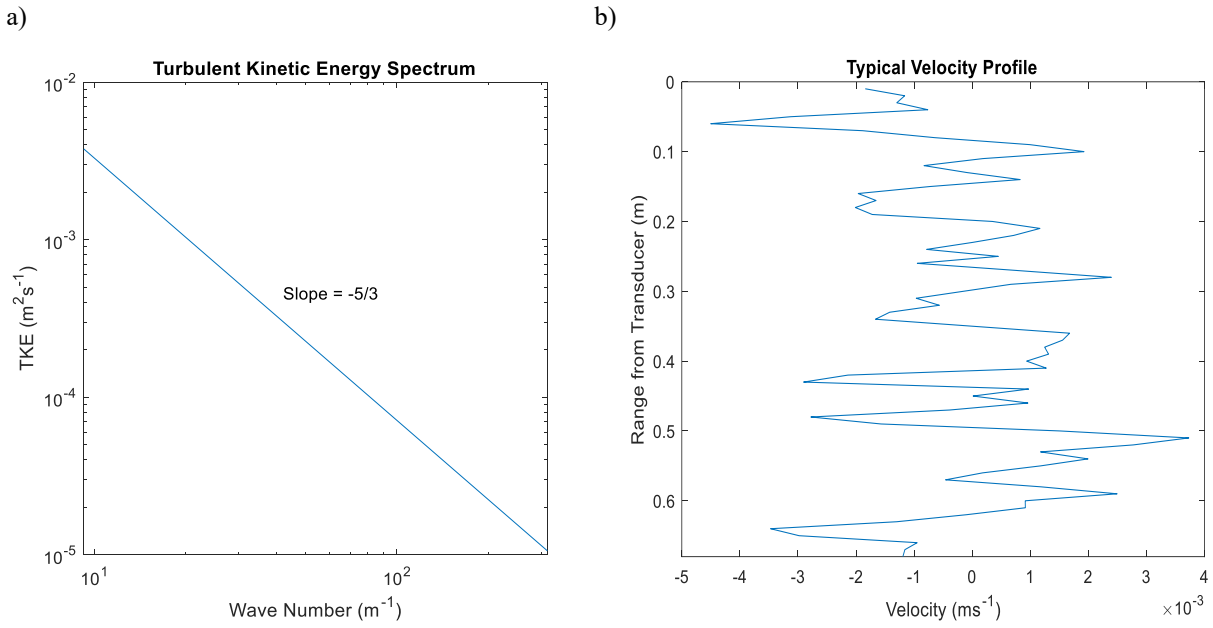

Figure 3: a) Turbulent Kinetic Energy Spectrum. b) Typical Turbulent Velocity Profile

Model Testing and Further Work

The model is currently undergoing testing. Model outputs for a range of sediment concentrations and size distributions and varying hydrodynamic conditions are being generated and loaded into the AQUAscat Toolkit, a commercial software package for analysing multi-frequency acoustic backscatter files from the AQUAscat 1000, to process and compare output results against input conditions. Further results and comparisons with data from a typical instrument will be presented at the conference.

The current version has some necessary simplifications to aid in reducing processing time. This includes the use of a simplified acoustic beam model, the assumption of locally isotropic turbulence to allow the use of a single axis of turbulence velocity, and some assumptions about the steady state motion of particles. However, it is anticipated that it will be a valuable tool in evaluating planned new processing algorithms exploring settling velocity, turbulence, and detection of bubbles within the suspension.

Acknowledgments

Some of the work described is supported by funding from the European Union's Horizon 2020 research and innovation program under Grant agreement No 101000825 — NAUTILOS.

References

Fromant, G., Thorne, P. D., & Hurther, D. (2024). An examination of point-particle Lagrangian simulations for assessing time-resolved hydroacoustic particle flux measurements in sediment-laden flows. *The Journal of the Acoustical Society of America*, *155*(4), 2817–2835. https://doi.org/10.1121/10.0025766

Smerdon, A. M., & Caine, S. J. (2007). A commercial multi-frequency acoustic backscatter instrument for profiling of suspended sediment size distribution and load. *Proceedings of the Hydraulic Measurements and Experimental Methods Conference*.

Thorne, P. D., & Hanes, D. M. (2002). A review of acoustic measurement of small-scale sediment processes. *Continental Shelf Research*, *22*(4), 603–632. https://doi.org/10.1016/S0278-4343(01)00101-7

On Acoustic Backscatter Systems (ABS) calibration for suspended sediment concentration estimation in turbulent flows

Guillaume Fromant[a], Maxime Lernould[a], Benoît Becquet[b], Ghislain Poncin[b], Fabien Flahaut[b], Georges Stienne[a]

[a] **Laboratoire d' Informatique Signal et Image de la Côte d' Opale, ULCO, 50 rue Ferdinand Buisson, 62228 Calais**

[b] **Ecole d' Ingénieurs du Littoral Côte d' Opale, ULCO, 50 rue Ferdinand Buisson, 62228 Calais**

On Acoustic Backscatter Systems (ABS) calibration for suspended sediment concentration estimation in turbulent flows

Guillaume Fromant[a], Maxime Lernould[a], Benoît Becquet[b], Ghislain Poncin[b], Fabien Flahaut[b], Georges Stienne[a]

[a]Laboratoire d'Informatique Signal et Image de la Côte d'Opale, ULCO, 50 rue Ferdinand Buisson, 62228 Calais
[b] Ecole d'Ingénieurs du Littoral Côte d'Opale, ULCO, 50 rue Ferdinand Buisson, 62228 Calais

Corresponding author: Guillaume Fromant; Guillaume.fromant@univ-littoral.fr

Introduction

The need to monitor and model their transport has lead scientists to design more efficient methods of SPM content estimations based on the physical properties of the suspended matter in the water column. Among a large number of surrogate techniques, acoustical methods have the advantage of providing nonintrusive measurements, with high spatial and temporal instrumental resolutions (Gray & Gartner 2009). This led to the development of Acoustic Backscatter Systems (ABS), designed to insonify the water column and retrieve volume backscattering coefficients S_v (Maclennan et al. 2002) at multiple frequencies of the order of the MHz over complete profiles (Thorne & Hanes 2002). Through the measurement of the volume backscattering coefficients (linked to the mean backscattered echo intensity) and given a specific backscattering model that describes the scattering properties of a particle (mineral or organic), acoustic inversion methods have been designed and successfully applied to retrieve both the concentration and size distribution of a suspension (eg. Greenlaw & Johnson 1983, Thorne & Hurther 2014).

Carrying out the acoustic inversion however requires accurate calibration of such ABS systems. The role of the calibration procedure is to convert the backscattered voltage into S_v, thus accounting for the sampled volume size, and transducers sensitivity (Betteridge et al. 2008). This calibration can be carried out by measuring the transmit and receive sensitivity as well as the transducers beampatterns, which in practice requires significant resources (human, material, financial). A common alternative to such a procedure is to measure the backscattering from a suspension with know scattering properties (eg. Sand like particles of known size distribution) under controlled conditions in dedicated tank facilities, sometimes guaranteeing a homogeneous suspended sediment concentration over the instrument profiling range (Thorne & Hanes 2002, Betteridge et al. 2008, Vergne et al. 2021). This calibration procedure has become standard on monostatic or bistatic ABS systems dedicated to suspended sediment concentration monitoring, from which a particle-independent calibration constant can be estimated for each frequency

(Betteridge et al. 2008). Yet, a few experiments suggest a potential bias in such procedures, linked to the scattering of turbulent microstructures formed by passive additive quantities such as temperature of particulate concentration fluctuations (Lhermitte & Lemmin 1993, Shen & Lemmin 1997, Vergne et al. 2023). Under the assumption of incoherent scattering, the final mean echo intensity recoreded in a calibration tank would then become the sum of the intensities produced by the particles and turbrulent microstructures, consequently leading to an overestimation of the calibration coefficients of each ABS frequencies (Figure 1). Owing to the large range of turbulent scales in environmental flows, the question of the validity of this calibration procedure arises.

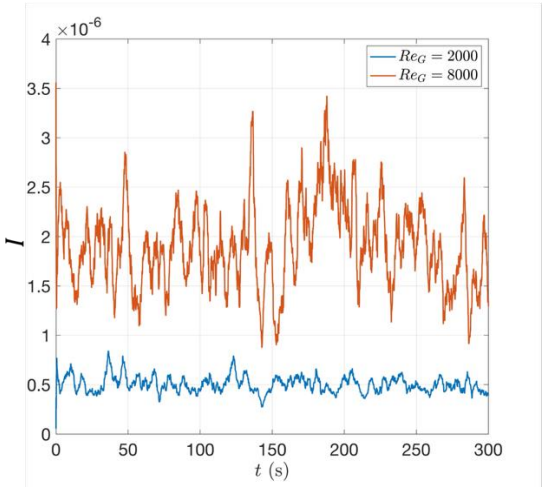

Figure 1: Quasi-instantaneous (uncalibrated) intensity recorded using a 1 MHz ABS system deployed in a micro-bubble suspension in an oscillating grid turbulence tank under two different turbulent conditions (Grid Reynolds number Re_G of 2000 and 8000). The micro bubble concentration remains the same for both turbulent conditions.

The present work reports on an attempt to observe and quantify the impact of turbulence on the standard calibration procedure. A series of measurements involving two bistatic ABS systems have been conducted in a rectangular tank equiped with a standard oscillating grid (OGT) and a micro-air bubble generator.

Methods

Three different turbulent regimes were produced in the OGT system by setting the frequency $f_g = [1; 3.2; 5]$ Hz with a fixed amplitude $S = 4.5$ cm of the grid in the tank, leading to grid Reynolds number $Re_G = f_g S^2/\nu = [2000; 6400; 10000]$, with ν the kinematic viscosity of water. The ABS systems (two UBFlow-2C bistatic systems from Ubertone ©, based on the

Acoustic Concentration and Velocity Profiler technology - ACVP) were equiped with broad-band transducers, covering the frequency range [0.7 – 1.5 MHz] and [1.5 – 3 MHz] respectively. Both systems were tilted at 45° (Figure 2). Each transducer was equipped with small water jets powered by a pump to prevent bubbles from attaching to their active surface. The micro-air bubble generator produced non-inertial bubbles of mean radius $a_0 = 16$ µm with a normalized standard deviation $\sigma = 0.4$. A steady homogeneous bubble volume fraction of $3.10^{-6}\ m^3.m^{-3}$ could be reached in the tank.

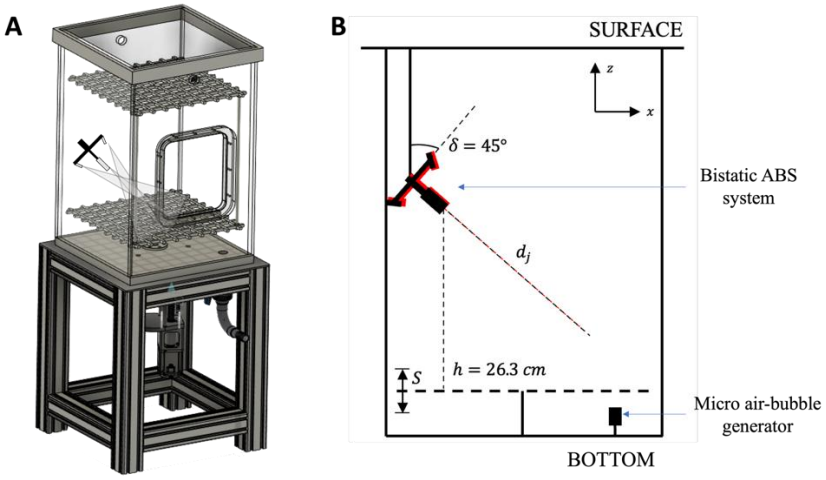

Figure 2: (A) – 3D view of the OGT system (B) Schematics of the present experiment set-up showing the ABS bistatic system tilted at 45° and the position of the air bubble generator below the system grid.

The ABS systems recorded the intensity I scattered by both turbulent micro structures and micro air bubbles at a rate of 1000 Hz over a profile of 20 cm, with a vertical resolution of 2.2 mm.

$$I = A_j \left(M_b A_b e^{-2\int_0^r \zeta M_b dr} + S_\theta \right) \quad (1)$$

Here A_j is a calibration coefficient accounting for the system sensitivity and directivity in bistatic configuration (Hurther et al. 2011). A_b is the angle dependent scattering coefficient accounting for the bubble scattering properties (Hurther et al. 2011, Gaunaurd et Uberall 1983), ζ is the total scattering attenuation coefficient (event though no attenuation was observed for such low bubble volume fractions) and M_b is the bubble mass concentration. S_θ here accounts for the scattering coming from turbulent microstructures. Note that the term A_j has been estimated for each frequency in a previous experiment under very low turbulent conditions ($S = 1$ cm, $f_G = 1$ Hz) so that S_θ could be neglected.

In a turbulent velocity field, passive scalars θ such as micro-bubble concentration produce sound-velocity fluctuations from which incident sound pressure waves are scattered. Tatarski (1971) and Ishimaru et al. (1978) show that, under isotropic turbulent conditions, the volume backscattering cross-section from these microstructures is linked to the 3D wavenumber spectrum $\Phi(K)$ of the medium variability (here expressed in terms of sound velocity fluctuations), itself linked to the 3D energy spectrum of the passive scalar fluctuations $E_\theta(K)$ evaluated at the Bragg wave number $K = 2k\sin(\gamma/2)$. Here, k is the wavenumber of the incident wave and γ the angle formed between the emission and reception axis ($\gamma = \pi$ in monostatic configuration) (Shen & Lemmin 1997). The volume scattering cross section of turbulent microstructures then writes:

$$\sigma_\theta = \frac{S_{n\theta}^2 \, k^2}{8\sin(\gamma/2)} E_\theta(K) \tag{2}$$

Where $S_{n\theta}$ is a transforming constant linking the sound velocity fluctuation to the passive scalar fluctuations (Shen & Lemmin 1997). With frequencies of the order of the MHz, and turbulent kinetic energy dissipation rates of the order $\epsilon = [10^{-6} - 10^{-3}]$, the Bragg wave number lies beyond the inertial subrange where $E_\theta(k)$ should take the form of a Batchelor scalar spectrum (Batchelor 1959). Finally, $E_\theta(k)$ should be a function of (among other) the r.m.s of the passive scalar fluctuations $\sqrt{\overline{\theta'^2}}$ (which in the case of concentration is approximately to the actual mean concentration) (Shen & Lemmin 1997).

Results

From Eq. 1, and neglecting scattering attenuation due to micro air-bubbles, S_θ is expressed as follows :

$$S_\theta = \frac{I}{A_j} - A_s M_b \tag{3}$$

Average profiles of the quantity S_θ are then observed in the tank and represented in Figure 3. It is seen that S_θ increases as approaching the grid (here, $z = 0$ m indicates the grid mean position), consistent with the increasing turbulent intensities near the grid (u_{RMS} prfiles) as it is generally observed in such vertically decaying turbulence systems (Poulain-Zarcos et al. 2022). We also see that S_θ increases with Re_G regardless of the acoustic frequency. Note that negative

values of S_θ can be observed at high z away from the grid as a probable consequence of the use of the mean concentration profile estimed over all runs in Eq. 3.

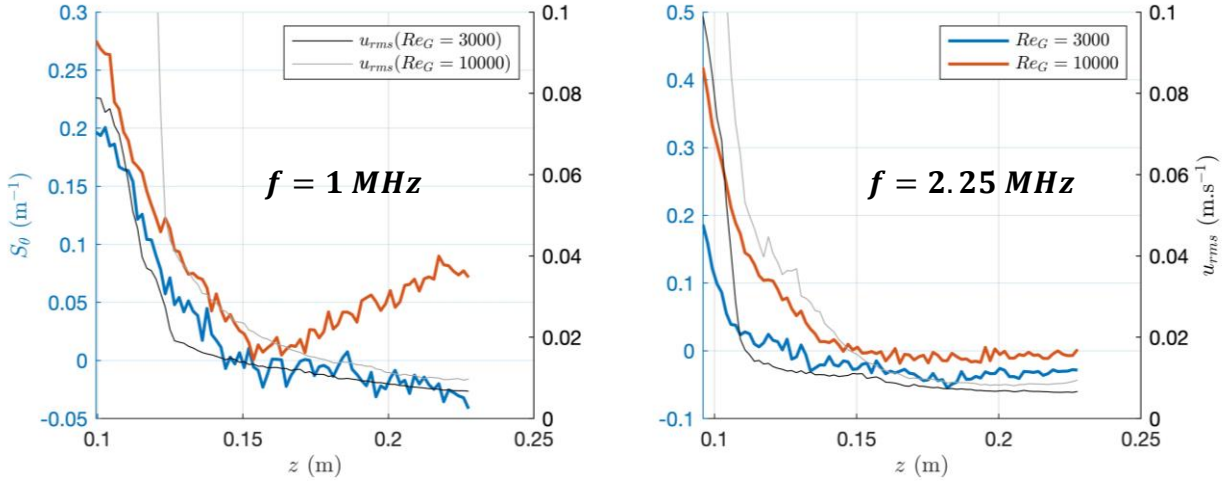

Figure 3: S_θ as a function of the turbulent regime (Re_G) and instrument carrier frequency (f) in the tank and compared to the turbulent intensity profiles u_{rms} measured in the tank.

Discussion

Passive scalars in a turbulent medium scatter sound, the amount of which is linked to the ABS frequency, the passive scalars fluctuations, as well as the turbulent regime. In the present experiment, most of the scattering produced by passive scalar quantities is hypothesized to be coming from the micro air-bubble concentration fluctuations, although a few percents might be attributed to temperature fluctuations as well (Shen & Lemmin 1997).

These turbulent microstructures can be problematic when it comes to the calibration of ABS systems (monostatic of bistatic) using the known scattering properties of a suspension in a controlled environment (in terms of size distribution and mass concentration). Most of the time, natural sandy particles are used, as ABS are generally deployed above sandy beds in the marine environment (Thorne & Hanes 2002); Perfect spherical glass beads are also an interesting choice as the scattering properties of spherical objects are much better described by theory (Betteridge et al. 2008). Low concentrations are generally targeted to avoid attenuation effects. Nevertheless, water mixing using pumps or grids is almost always necessary to ensure homogeneous concentration in these calibration tanks (eg. Betteridge et al. 2008, Vergne et al. 2021) due to the highly inertial nature of sand-like particles. Unless the water from the tank is properly degassed from its naturally present air bubbles, and the agitation system does not introduce micro air

bubbles in the suspension (through cavitation for instance), the final calibration coefficient could become biased. As an example, Figure 4 shows the volume scattering coefficient of a sand suspension of fixed mass concentration (0.5 g/L) for three mean particle radii as a function of incident frequency. The volume scattering from turbulent microstructures coming from bubbles with volume fraction as low as 3.10^{-7} (which is of the order of the volume fractions of air bubbles naturally present in suspension in a tilted flume) and 3.10^{-6} (which is of the order of the volume fractions of air bubbles present in suspension in the present OGT system) are superimposed, suggesting the potential impact on the final calibration coefficient estimate.

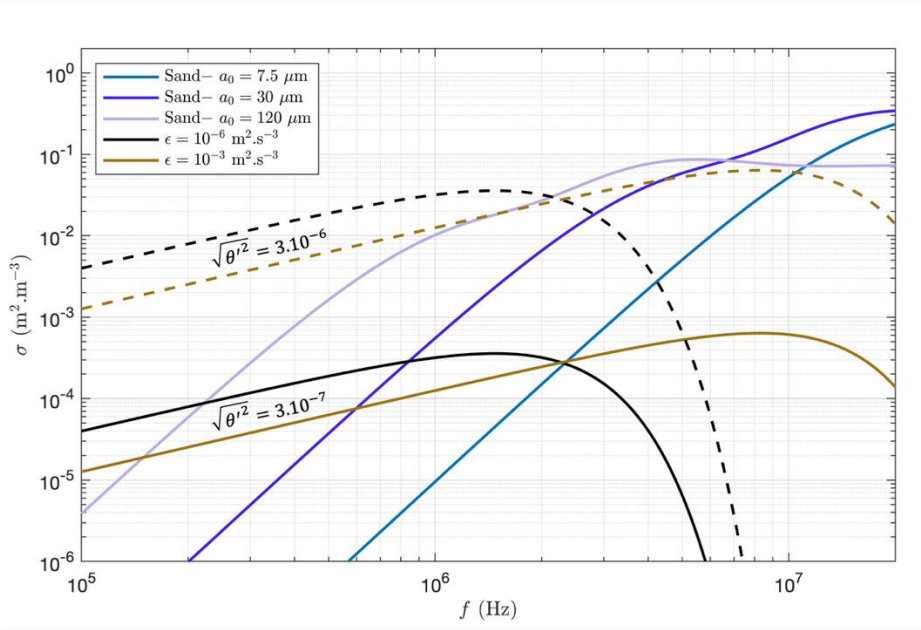

Figure 4: Modeled volume backscattering coefficient as a function of frequency (monostatic case) for sandy suspensions of fixed mean radii and steady mass concentration M=0.5 g/L. Predicted volume scattering from turbulent micro structures formed by micro bubbles concentration fluctuations (Eq. 2) is also displayed for fixed volume fraction of 3.10^{-7} (plain lines) and 3.10^{-6} (dotted line) and two different turbulent regimes.

Apart from the calibration procedures, this could also affect the quality of field acoustic measurements. There is no way to predict the occurrence of scattering due to turbulent microstructures, even with a good evaluation of the turbulent intensities as velocity fluctuations themselves do not contribute to scattering like passive scalars do (Shen & Lemmin 1997). Complementary optical measurements might be needed to assess the presence of micro air-bubbles in the field. Given the large range of turbulent scales observed in natural flow conditions (eg. river floods, coastal surges vs. open ocean mixing layers), ABS carelessly calibrated under turbulent conditions (eg. strongly agitated by water pumps) could potentially lead to biased estimates of suspended sediment concentrations in the field.

To conclude, further experiments need to be carried out to assess the scattering properties of turbulent microstructures from passive additive quantities although several theoretical descriptions have already been formulated (Shen & Lemmin 1997, Tatarski 1971, Lavery et al. 2003). Tatarski (1971) and Ishimaru (1978) underline the importance of a large sampled volume size, as their theoretical description relies on the occurrence of multiple turbulent scales within the sampled volume. If turbulent microstructures scattering measurements have often been carried out over large volumes in open ocean (eg. Lavery et al. 2003), this is generally not the case for high resolution ABS systems, for which the sampled volumes are much smaller, of the order of 10^1-10^2 mL.

Conclusion

A series of acoustic measurements involving multiple frequencies bistatic ABS systems has been carried out in a tank equipped with an oscillating grid at different turbulent conditions where a homogeneous micro air bubble suspension has been maintained. The resulting volume backscattering coefficient profiles reveal the presence of an excess scattering, that is attributed here to the presence of turbulent microstructures formed by passive additive quantities such as temperature and microbubbles concentration fluctuations. The potential impact of such scattering effects on standard ABS calibration procedures generally carried out under turbulent conditions is discussed. Implications for in situ measurements in various environmental flows is also discussed.

References

Betteridge, K. F., Thorne, P. D., & Cooke, R. D. (2008). Calibrating multi-frequency acoustic backscatter systems for studying near-bed suspended sediment transport processes. Continental Shelf Research, 28(2), 227-235.

Gaunaurd, G. C., & Überall, H. (1983). RST analysis of monostatic and bistatic acoustic echoes from an elastic sphere. The Journal of the Acoustical Society of America, 73(1), 1-12.

Gray, J. R., and J. W. Gartner. (2009). Technological advances in suspended-sediment surrogate monitoring. Water Resources Research, 45, W00D29, doi:10.1029/2008WR007063.

Greenlaw, C. F., and R. K. Johnson. (1983). Multiple-frequency acoustical estimation. Biological Oceanography, 2, 227–252, doi:10.1080/01965581.1983.10749460.

Ishimaru, A. (**1978)**. Wave Propagation and Scattering in Random Media (Academic, New York), Vol. 2

Lavery, A. C., Schmitt, R. W., & Stanton, T. K. (2003). High-frequency acoustic scattering from turbulent oceanic microstructure: the importance of density fluctuations. The Journal of the Acoustical Society of America, 114(5), 2685-2697.

Lhermitte, R., & Lemmin, U. (1993). Turbulent flow microstructures observed by sonar. Geophysical Research Letters, 20(9), 823-826.

Maclennan, D. N., P. G. Fernandes, and J. Dalen, 2002: A consistent approach to definitions and symbols in fisheries acoustics. ICES J. Mar. Sci., 59, 365–369, doi:10.1006/jmsc.2001.1158.

Poulain-Zarcos, M., Mercier, M. J., & Halle, A. (2022). Global characterization of oscillating grid turbulence in homogeneous and two-layer fluids, and its implication for mixing at high Peclet number. *Physical Review Fluids*, *7*(5), 054606.

Shen, C., & Lemmin, U. (1997). Ultrasonic scattering in highly turbulent clear water flow. Ultrasonics, 35(1), 57-64.

Tatarski, V. I. **1961**. Wave Propagation in a Turbulent Medium McGraw-Hill, New York .

Thorne, P. D., and D. M. Hanes, 2002: A review of acoustic measurement of small-scale sediment processes. Cont. Shelf Res., 22, 603–632, doi:10.1016/S0278-4343(01)00101-7.

Thorne, P. D., & Hurther, D. (2014). An overview on the use of backscattered sound for measuring suspended particle size and concentration profiles in non-cohesive inorganic sediment transport studies. Continental Shelf Research, 73, 97-118.

Vergne, A., Berni, C., Le Coz, J., & Tencé, F. (2021). Acoustic backscatter and attenuation due to river fine sediments: Experimental evaluation of models and inversion methods. Water Resources Research, 57(9), e2021WR029589.

Vergne, A., Le Coz, J., & Berni, C. (2023). Some Backscatter Modeling Issues Complicating the Sonar-Based Monitoring of Suspended Sediments in Rivers. Water Resources Research, 59(6), e2022WR032341.

The complexity of calibrating indirect sediment measurement techniques in the Schelde-estuary

Yves Plancke[a,b], Sven Smolders[a]

[a] Flanders Hydraulics, Berchemlei 115, 2140 – Antwerpen, Belgium
[b] Hasselt University, Agoralaan gebouw H, 3590 Diepenbeek, Belgium

The complexity of calibrating indirect sediment measurement techniques in the Schelde-estuary

Yves Plancke[a,b], Sven Smolders[a]

[a]Flanders Hydraulics, Berchemlei 115, 2140 – Antwerpen, Belgium
[b]Hasselt University, Agoralaan gebouw H, 3590 Diepenbeek, Belgium

Corresponding author: Yves Plancke, Yves.Plancke@mow.vlaanderen.be

Introduction

Sediment transport is important for several estuarine functions. The morphology determines both the tidal penetration in the estuary and the port accessibility (Smolders et al. 2015). Suspended sediment influences the light penetration in the water column and therefore it is crucial for ecology (Meire et al., 2005). In order to guarantee the accessibility towards the Port of Antwerp-Bruges, regular maintenance dredging works are necessary. In the Westerschelde, dredged sediment consist mainly of very fine and fine sands (d50 ~ 150 – 230 µm). The dredged sediments are relocated within the estuary, in order to minimize the influence on the sediment budget.

The maritime access division, who is responsible for the maintenance dredging works, receive dredging and relocation license for a limited period (5 to 7 years) during which they are allowed to relocated the dredged sediment according to a certain sediment strategy. The present strategy (2022-2028) includes disposal of sand in both main and secondary channels, in combination with disposal along sandbars. To optimize the sediment strategy preparatory research is ongoing at this moment, using numerical models (Smolders et al., 2018). To validate these models, field measurements are used, focusing on both hydrodynamics, sediment transport and morphology. This paper describe the challenges of calibrating indirect techniques that were used during a 3-day field campaign in May 2025 in the Westerschelde.

Study site

The Schelde-estuary is macro-tidal estuary with a length of 180 km (Meire et al., 2005). It stretches from the North Sea up until Gent, and consists of an open mouth area (Vlakte van de Raan, KM -20 until KM 0), a multiple channel system (Westerschelde, KM 0 until KM 60) and a (pseudo-)meandering one channel system (Zeeschelde, KM 60 until KM 160). The estuary is fully protected within the European Bird and Habitat Directive and consists out of different ecological valuable habitats.

This paper focuses on a part of the Westerschelde, which is characterized by a vertical tide of 4.5 m (up to 5.5 m at spring tide) and horizontal tides with ebb currents up to 1.5 m/s and flood

currents up to 2.0 m/s. The morphology is complex, characterized by multiple channels (main and secondary) surrounding intertidal sandbars, and tidal flats and brackish marshes along the edges. Bed sediments consist of fine sand, with limited mud fractions (mainly at intertidal areas). The sediment transport is characterized by both non cohesive (sand) and cohesive sediment (mud). The measurements were performed near Hansweert (Figure 1), with water depths varying from ~6 m (at LW) to ~10 m (at HW).

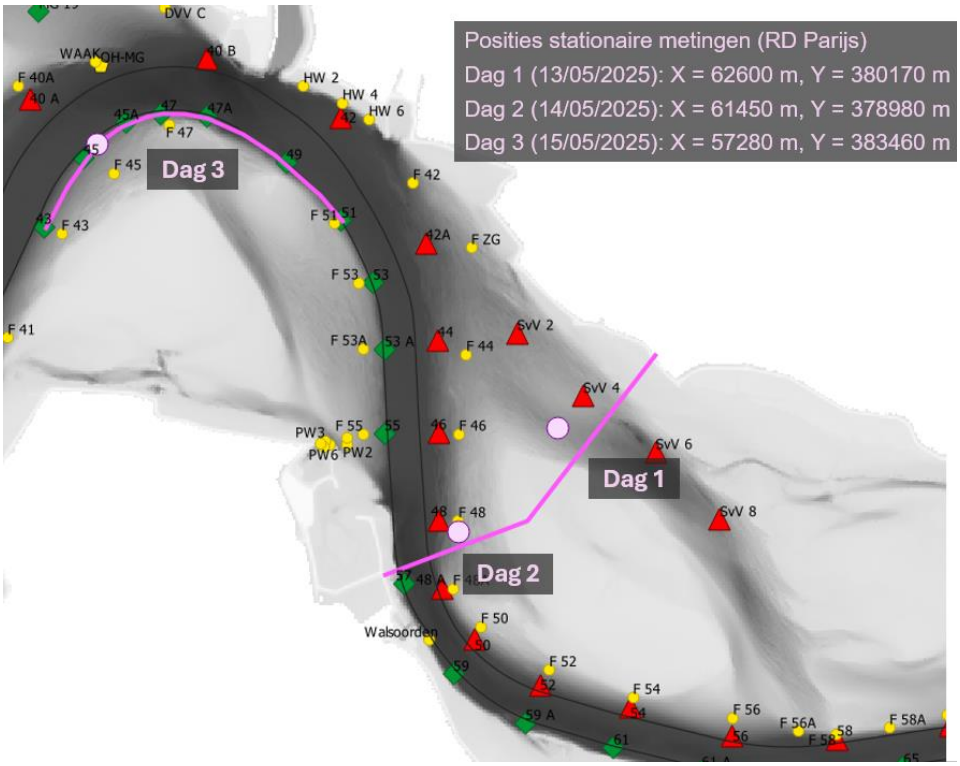

Figure 1 - Measurements locations in the area of interest in the Schelde-estuary, pink markers indicates measurement location

Methods

During the field campaign several measurement techniques were used to measure the sediment transport. A survey vessel was put at a fixed position monitoring different parameters. An ADCP was used to measure flow conditions. Both optical (OBS, YSI) and acoustic (ABS, ADCP and AquaScat) backscatter, optical transmission (OT, LISST-100X), Delft Bottle (DB) and pump sampling were used to measure the suspended sediment concentration (SSC). The LISST-100X also provided grain size distributions during the campaigns. Each campaign took place over a time span of ~ 6 hours, covering the full flood phase, starting 1 hour after LW (slack LW) until 0.5 hour after HW (slack HW). During the campaign, one measurement frame - with multiple devices (Figure 2) - profiled the water column every ~10 minutes. The DB was placed at the bed

measuring the near bed transport every ~10 minutes for a period of ~5 minutes (depending on transport rates). The AquaScat was installed on a second frame that was positioned on or close to the bed. An overview of all used devices and settings can be found in Table 1.

Table 1 - Overview of measured parameters and set-up resolution
Devices in gray were used but won't be discussed in this paper

Parameter	***Device***	***Spatial resolution***	***Temporal resolution***
Current	ADCP	Vertical profile (50 cm cell size)	Continuous (1/4 s)
SSC	YSI-OBS *Frame 1*	Point measurement + vertical profiles	Continuous (1/s) + 1 vertical profile/ ~10'
SSC	LISST-optical transmission *Frame 1*	Point measurement + vertical profiles	Continuous (1/s) + 1 vertical profile/ ~10'
SSC	AquaScat *Frame 2*	Near bed vertical profiles	Continuous (1 minute bursts of 30 s)
SSC	Pump *Frame 1*	Point measurement 3 samples/ profile	Ad hoc
Sediment transport	Delft Bottle *Frame 3*	Point measurement Bed + 10 cm Bed + 30 cm	One measurement every 5 to 10 minutes
Grain size	LISST-laser diffraction *Frame 1*	Point measurement + vertical profiles	Continuous (1/s) + 1 vertical profile/ ~10'

SSC is determined using filtration on the pump samples. These results were used to calibrate indirect (ABS, OBS, OT) techniques. For the optical measurements a direct relation between the measured signal and the SSC was made. For the ABS, the post-processing according to Landers et al. (2016) was used.

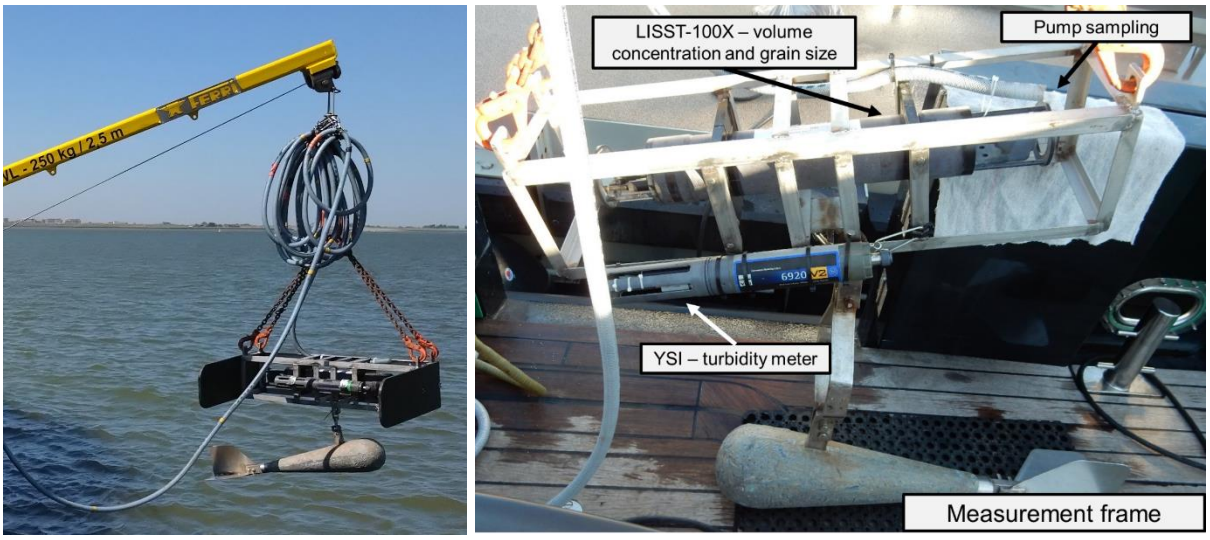

Figure 2. Measurement frame used during field campaigns, with detail of measurement instruments (right).

Results

Figure 3 presents the calibration of both the optical backscatter (YSI) and the LISST-100, where all samples from the 3 days are included. Both figures also include 2 theoretical calibration lines, one for sand, one for mud or flocs.

With regard to the optical backscatter the relation between mass concentration (SSC) and turbidity (T) according to Sutherland *et al.* (2000) was used:

$$SSC = \frac{2}{3}.\frac{\rho_s.d_{50}.T}{Q_c} \quad (1)$$

With d_{50} the median grain size (respectively 15 µm and 150 µm for mud and sand), ρ_s the density of the sediment (fixed 2650 kg/m³) and Q_c a sediment characteristics (color, shape) parameters (respectively 0.022 and 0.014 for mud and sand, derived from in lab calibration experiments).

With regard to the optical transmission of the LISST-100 the relation between mass concentration (SSC) and volume concentration was given for pure sand density (2650 kg/m³) on the one side, and flocs (density of 1200 kg/m³) on the other side.

From Figure 3 it is clear that all points are situated between the 2 lines (sand and mud/flocs), indicating the presences of both sediment types during the measurement campaign.

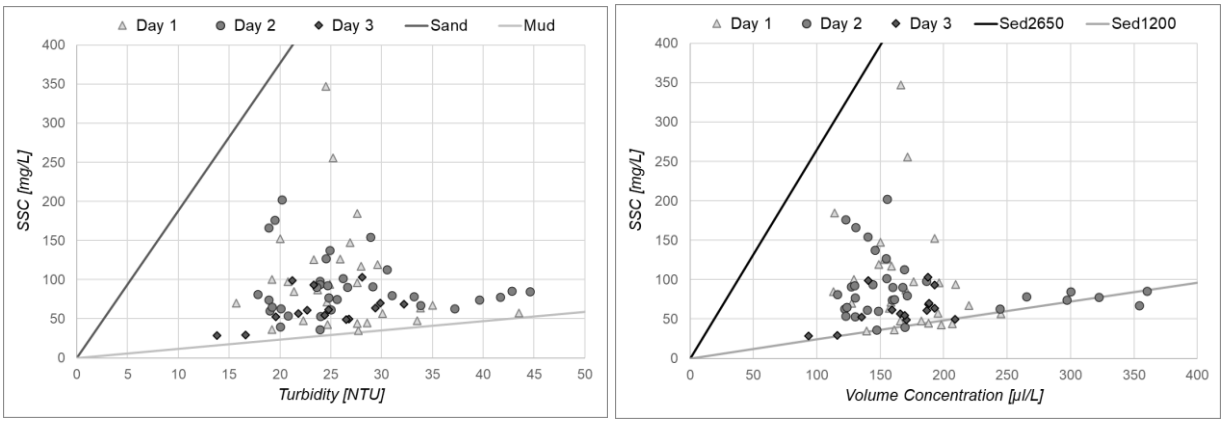

Figure 3. Calibration of YSI-OBS (left) and LISST-100 (right) with pump samples

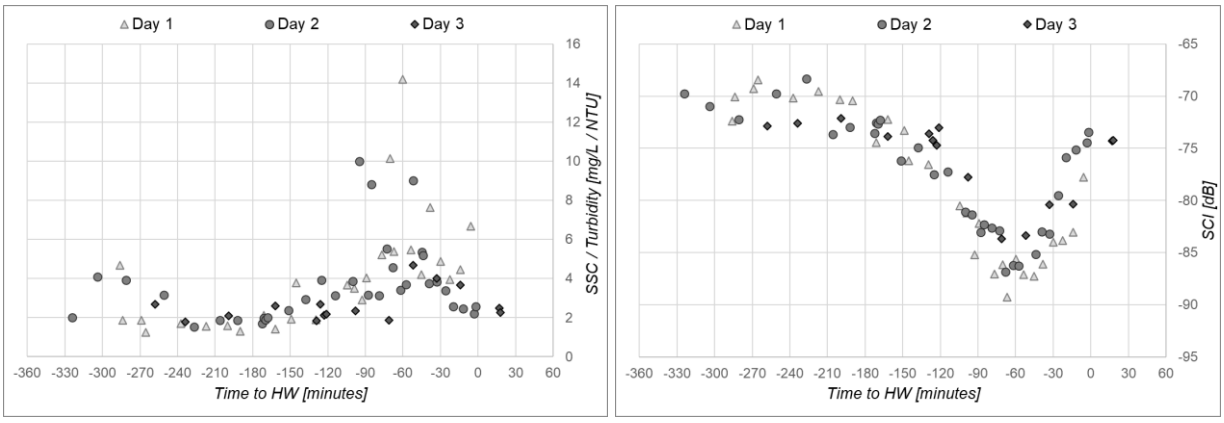

Figure 4. Temporal variation of ratio between SSC and turbidity (left) and sediment composition index SCI (right)

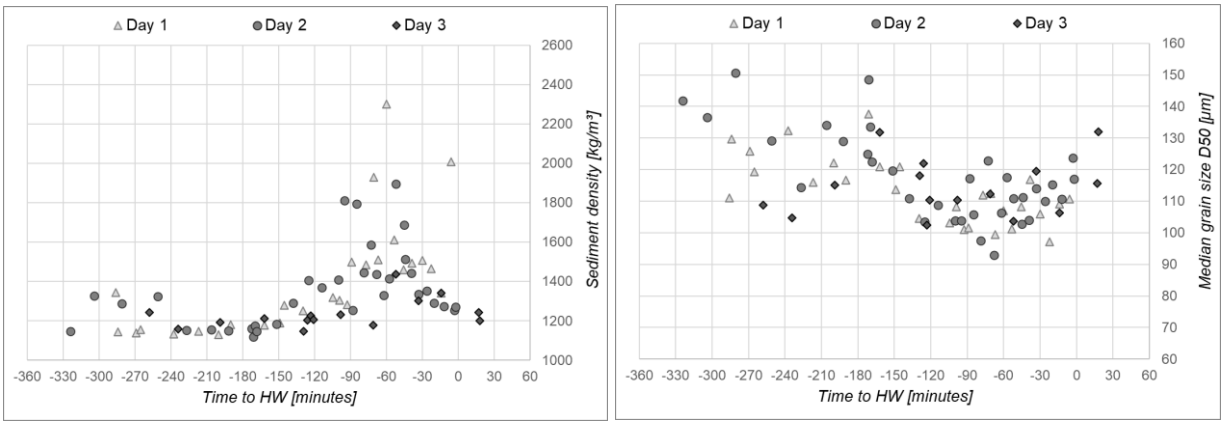

Figure 5. Temporal variation of sediment density (left) and median grain size D50 (right) [LISST-100 measurements]

In order to get an idea of the temporal variation of the sediment composition, additional parameters are presented/derived, with temporal variation (in relation to the moment of high water (HW)) shown in Figure 4 and Figure 5.

Figure 4 (left) gives the variation during the flood phase of the ratio between the SSC and the turbidity. Higher values occur in the period of HW-90' to HW-30'. In addition the sediment composition index (SCI) was calculated, combining the measurements of the optical and acoustic backscatter. It is known (eg. Pearson *et al.*, 2021) that optical sensors tend to be more sensitive to finer sediments, while acoustic sensor are more sensitive to sandy material. From Figure 4 (right) it can be seen that lower values are found in the period of HW-90' to HW-30', indication a dominance of sandy material, while in the other periods of the flood phase more muddy sediments are dominant.

Figure 5 (left) gives the variation during the flood phase of the sediment density derived from the LISST-100 volume concentration and the mass concentration from pump samples. Also here we see higher values during the period of HW-90' to HW-30', indicating pure sediment grains, while the lower values during the rest of the flood phase give an indication the flocs are dominant. From Figure 5 (right) it can be seen that lower values in d_{50} are found in the period of HW-90' to HW-30', while in the other periods of the flood phase higher values are found. Probably this is related to the variation in sediment composition (sand vs. flocs), which is in agreement with earlier observations.

Conclusion

In order to improve both the system understanding and supply datasets for model validation, field campaigns play an crucial role. During 3 field campaigns in the Westerschelde, the presence of both mud and sand created challenging conditions for the calibration of optical and acoustic backscatter sensors that were deployed during the measurements. It was found that during the first phase of the flood, sediment transport was dominated by mud, with also flocs being present. During the tidal phase of maximum flood currents, sediment transport was dominated by sand transport. This temporal variation of sediment composition makes it hard to convert the indirect measurement techniques to sediment concentration.

At this moment research is ongoing how to implement the variation in sediment composition in the calibration of the devices. Probably the SCI, which can be calculated directly from the OBS and ABS signal, will be used to vary to calibration parameters over the flood phase.

Acknowledgement

The measurements were made possible with the help of different colleagues, both in the preparation phase (HIC field team) as during the execution of the field campaigns (in particular crew members from the vessel MS Pierre Petit) and the post-processing (in particular sediment lab colleagues).

References

Meire, P., T. Ysebaert, S. Van Damme, E. Van Den Bergh, T. Maris, and E. Struyf, 2005. "The Scheldt estuary: A description of a changing ecosystem." Hydrobiologia 540 (1–3): 1–11. https://doi.org/10.1007/s10750-005-0896-8.

Pearson, S. G., Verney, R., van Prooijen, B. C., Tran, D., Hendriks, E. C. M., Jacquet, M., & Wang, Z. B. (2021). Characterizing the composition of sand and mud suspensions in coastal and estuarine environments using combined optical and acoustic measurements. Journal of Geophysical Research: Oceans, 126, e2021JC017354. https://doi.org/10.1029/2021JC017354

Smolders, S., Y. Plancke, S. Ides, P. Meire, and S. Temmerman, 2015. "Role of intertidal wetlands for tidal and storm tide attenuation along a confined estuary: A model study." Nat. Hazards Earth Syst. Sci. 15 (7): 1659–1675. https://doi.org/10.5194/nhess-15-1659-2015.

Smolders, S.; Bi, Q.; Maximova, T.; Vanlede, J. (2018). Modelling cohesive sediments in the Scheldt estuary (Belgium) with SEDI-3D, in: Bacon, J. et al. (Ed.) Proceedings of the XXVth TELEMAC-MASCARET User Conference, 9th to 11th October 2018, Norwich. pp. 53-60

Sutherland, T. F., Lane, P. M., Amos, C. L., & Downing, J. (2000). The calibration of optical backscatter sensors for suspended sediment of varying darkness levels. Marine Geology, 162(2–4), 587–597. https://doi.org/10.1016/S0025-3227(99)00080-8.

Comparing the determination of Suspended solids concentration (SSC) by use of Optical Backscatter (OBS) and Acoustic Backscatter (ABS) Sensors

Alisa Spriet, Jelle Malschaert, Pieter Mallants, Kris Van Troos, Jan Claus

IMDC, Van Immerseelstraat 66 2018 Antwerp, Belgium

Comparing the determination of Suspended solids concentration (SSC) by use of Optical Backscatter (OBS) and Acoustic Backscatter (ABS) Sensors

Alisa Spriet[a], Jelle Malschaert[a], Pieter Mallants[a], Kris Van Troos[a], Jan Claus[a]

[a]IMDC, Van Immerseelstraat 66 2018 Antwerp, Belgium
Corresponding author: Pieter Mallants; pieter.mallants@imdc.be

Introduction

Two commonly used techniques to determine turbidity in the water column are Optical Backscatter (OBS) and Acoustic Backscatter (ABS) Sensors. An OBS measures turbidity by means of detecting the backscattered infrared signal from suspended sediment. An ABS emits sound pulses with a sonar transducer and registers the reflected sound waves to determine the suspended particle concentration. Due to the nature of their working principles, ABS is more tolerant to fouling compared to OBS. Another notable difference between both types of measurement techniques is the range of particle sizes they are more sensitive to. In general, the response of an OBS is greater to finer particles, whereas ABS sensors are more sensitive to larger and wider range of particles.

During a long term monitoring campaign on the river Scheldt, both types of sensors were deployed on a bottom frame and collected data at an equal measurement interval. In this way, an attempt was made to compare the workings of optical and acoustic sediment sensors in conditions close to the river bed in a geomorphologically highly dynamic setting.

Methods

For a measurement campaign with a total period of twelve months, a measurement frame was deployed on the river Scheldt. The measurement setup was equipped with multiple instruments that were serviced during a monthly maintenance visit. One of the focus points of this study were the ABS sensor (type LISST-ABS from Sequoia Scientific) and the OBS sensor (type EXO3 from YSI) (Figure 1). These instruments were installed near the bottom of the frame where they registered the water conditions and sediment behavior near the river bed. The ABS and OBS were deployed with a measurement interval of 20 minutes and the sensors successfully collected data simultaneously for a total period of four months. Besides the instruments that were installed in the bottom frame, an extra OBS sensor was mounted ca. one meter under the water surface on a marker buoy, measuring the conditions at the top of water column.

Figure 1. ABS (center) and OBS (right) sensors installed on the bottom frame.

In addition to the OBS, also measurements of suspended sand concentration were conducted within the bottom frame using the acoustic LISST-ABS sensor. Calibration of the instrument was performed by the manufacturer, who provided a calibration sheet with corresponding weighting factors. As a result, the calibration of the LISST-ABS remains virtually constant across a wide range of grain sizes. Outliers (sand concentrations > 5 g/L) and unreliable data were removed during the semi-automated processing procedure.

To convert the turbidity values measured by the optical turbidity sensor (in FNU) of the YSI EXO3 to suspended sediment concentration (in mg/L), water samples were collected. These samples were analyzed in the laboratory for suspended sediment concentration in accordance with the NBN standard (NBN, 2005). The resulting data were subsequently used as a calibration to convert the turbidity values recorded by the YSI EXO (in FNU) to suspended sediment concentration (in mg/L).

Results

The figure below shows an example of the time series of the total sediment concentration as measured by the OBS sensor near the river bed (*YSI bed* in Figure 2) and the sand concentration measured by the ABS sensor (*LISST ABS* in Figure 2). The dashed blue line is the tide.

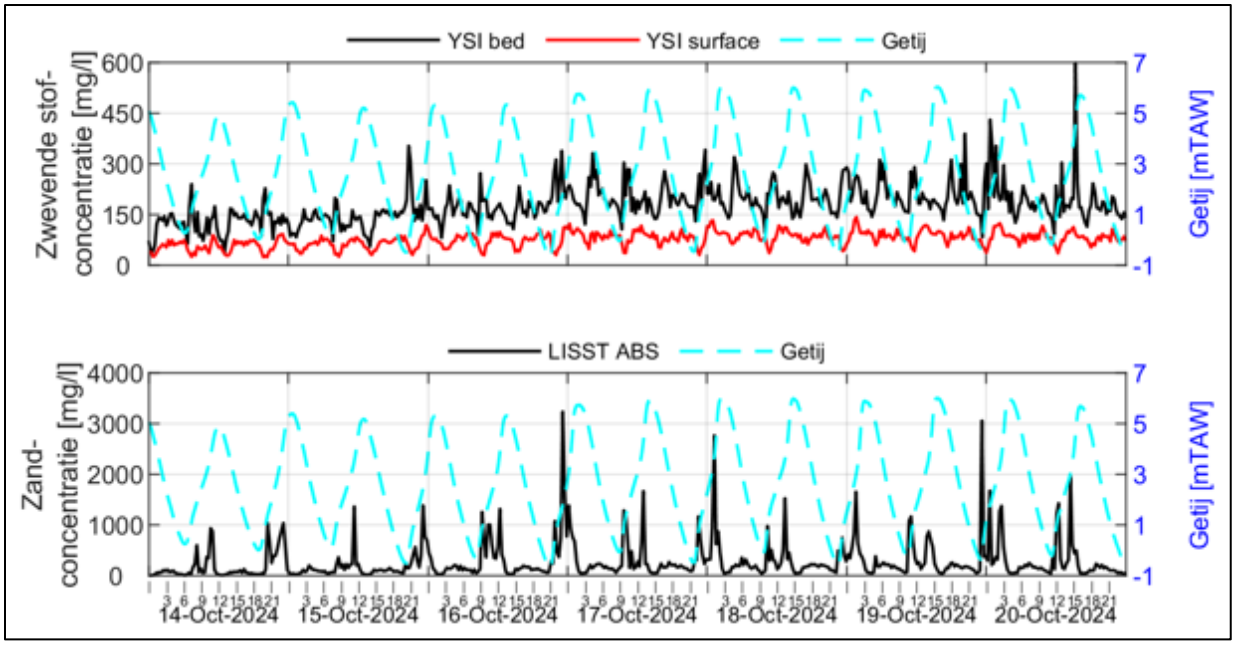

Figure 2. Time series for the suspended sediment concentration and the sand concentration as measured by the OBS and ABS sensors.

With regard to the suspended sediment concentration as measured by the OBS sensor, the highest values are registered during the winter months (December – January – February) and at the end of summer (August – September). During this period there was a maximum sediment concentration of ca. 1 800 mg/L and an average concentration of ca 275 mg/L near the river bed. The influence of the tides is clearly visible on the measurement results. The sediment concentration near the river bed increases during the flood phase followed by a peak in concentration near the high water slack tide.

Next to suspended sediment concentration, the bottom transport was also monitored by measuring the sand concentration with the ABS sensor. The maximum measured sand concentration in the months March – April – May is ca. 1 000 mg/L and ca. 3 500 mg/L in the month of October. The average concentrations for those periods are 97 and 198 mg/L respectively. The influence of the tide can also be seen in the observed sand concentrations. An increase in concentration has been observed during flood phase and especially during spring tide conditions. In general, minimum concentrations are reached during high and low water slack tide.

As was described above, an additional OBS sensor was installed near the water surface. The resulting registered sediment concentration can be seen on Figure 2 (*YSI surface*). Generally, the concentrations at this depth are lower than those measured near the river bed. Also, the influence

of the tides on the sediment concentrations are less pronounced than is the case for the concentrations measured at the bottom of the water column.

Discussion

In general, measured particle concentrations between OBS and ABS sensors reach their maximum during a different moment in the tidal cycle. The OBS reaches its maximum values in general around slack water, whereas the ABS mainly reaches maximum values during maximum flood flow conditions. This highlights the difference in response of both sensors to the type of sediment. During slack water, when there is little to no current, the settling particles near the bed are mainly finer grains (materials mainly consisting silt particles), and are registered by the OBS. Contrary, during the start of the flood phase, the sediment transport near the bed contains larger grains (materials mainly consisting of sand), which is the main focus of the ABS and is less observed by the OBS. The installation of the ABS sensor provides better insights into the sand transport near the bed.

Average concentration values for both sensors are relatively comparable (275 mg/L for OBS and 97-198 mg/L for ABS), however, the concentration range in which both sensors measure differs largely. During the measurement period, maximum concentrations registered by the OBS reach up to 1 800 mg/L whilst the ABS registered concentrations up to 3 500 mg/L. The largest differences in concentrations are obtained during autumn, where outliers are more prominent. Here again, a difference in the measurement principle between both sensors is highlighted. The ABS is more reliable in sand rich waters, compared to the OBS. The use of both measurement principles provide an added value to this campaign and a better determination of the sediment transport of near the bed.

Conclusion

Over the course of this one-year measurement period, a comparison is made between an Optical Backscatter (OBS) and Acoustic Backscatter (ABS) sensor. Both sensors were installed on a measurement frame on the bottom of the river Scheldt. Results show highest OBS concentrations during winter and at the end of summer. ABS was measured during March-April-May and in October. Tidal influences are visible for both sensors, the OBS registered an increase in concentrations during the flood phase with maximum around high water slack tide. For the ABS, an increase in concentration is registered during both ebb and flood phase with maximum during peak flow velocities.

In conclusion, differences in measurement principle and focus of both sensors are clearly highlighted in this study. Where the OBS sensor performs better in areas with smaller particles and lower turbidity zones, the ABS sensor is best to use in areas with larger particles and in sand

rich waters. Depending on the application of research, one sensor is thus preferred over the other. However, when one wants to measure in a highly variable environment, as for example the river Scheldt, the use of both of these sensors has a large advantage. During the sediment laden water dominated by fines, the OBS registers data, whereas the ABS takes over during the more sand-rich sediment transport. In future research, a combination of OBS and ABS data into one total concentration value could provide further insight into the comparability of both sensors.

References

NBN (2005) Waterkwaliteit - Bepaling van het gehalte aan zwevende stoffen - Methode door filtratie over glasvezelfilters. Bureau voor Normalisatie België, NBN EN 872:2005.

Assessment of the settling velocity measurement procedures of sediment particles in laboratory conditions

Kris Dumont[a], Lander Bruylandt[b], Thomas Neirinckx[b], Renaat De Sutter[b], Bernard Malherbe[a], Jan Fordeyn[a]

[a] Jan De Nul NV, Tragel 60, 9308 Aalst, Belgium

[b] Ghent University, UGent, Sint-Pietersnieuwstraat 25, 9000 Ghent, Belgium

Assessment of the settling velocity measurement procedures of sediment particles in laboratory conditions

Kris Dumont[a], Lander Bruylandt[b], Thomas Neirinckx[b], Renaat De Sutter[b], Bernard Malherbe[a], Jan Fordeyn[a]

[a]Jan De Nul NV, Tragel 60, 9308 Aalst, Belgium
[b]Ghent University, UGent, Sint-Pietersnieuwstraat 25, 9000 Ghent, Belgium

Corresponding author: Kris Dumont; kris.dumont@jandenul.com

Introduction

Sediment transport models are applied on numerous dredging projects all over the world to assess dredging production, sediment budgets, and to investigate the impact of dredging activities on the environment. An essential parameter to calibrate these models is the settling velocity of these sediment particles in still water for low suspension-concentrations. Over the past decades various settling velocity laboratory measurement procedures have been developed and applied (Hasler 2007, van Rijn et al. 2023 and Deltares 2016).

Comparison of the settling velocity distributions of samples investigated during the MUSA project (van Rijn et al., 2023) shows that the results of two different measurement methodologies on cohesive sediment samples are similar for high initial concentrations (>2gds/l) with settling velocities of 0.1mm/s. Nevertheless, the settling velocities deviate significantly for low initial concentrations (<2gds/l) ranging between 0.1-7 mm/s.

Based on these findings, JDN initiated a practical program to (re)gain confidence in the use of settling velocities measured in laboratory environments. The final aim is to assess the impact of different physical phenomena on the settling velocity of sediment particles, such as particle size, particle shape, particle density, concentration, temperature, salinity, and flocculation. In the first phase two different laboratory methodologies were selected and compared for non-cohesive sediments, allowing to focus on the basic theory for the determination of settling velocity based upon the particle size and shape. The sediment samples are collected from various dredging projects and for a median-diameter range between D50= 0,080 mm to 0,330 mm. The testing conditions are fresh-water (no salinity), room temperatures (20°C), still water and low suspension-concentrations (<2gds/l).

The research also allows to determine the margins of uncertainties and to elaborate a sound measurement protocol to be applied on different JDN sites all over the world.

Methods

The measurements methods that were investigated in this research (see Figure 1) are i) the settling tube or cylinder with side-tap at the bottom of the cylinder (subsample method) ii) and the settling tube with (digital) underwater balance (balance method).

With the subsample method, samples are taken from the large cylinder at t=0s, 10s, 30s, 60s, 90s, 120s, 300s, 900s, 1800s and 3600s. For each subsample dry-solids concentration is measured; this enables to draw a time-evolution graph of the suspension concentration and deduce the average settling velocity of sediment particles in the water-column. Depending on the particle size distribution (PSD) and derived median particle diameter (D50), the sampling frequency can be increased or decreased to improve the accuracy and efficiency of the measurements.

The balance method measures settled material with a frequency of 1Hz, by using a digital balance (type: "Ohaus AX423"). Both applied laboratory methods therefor measure the gradual settling of sediment particles over time in the settling tube or cylinder. The obtained values are considered as representative for the settling velocity of the sediment particles in still water and for low suspension concentrations.

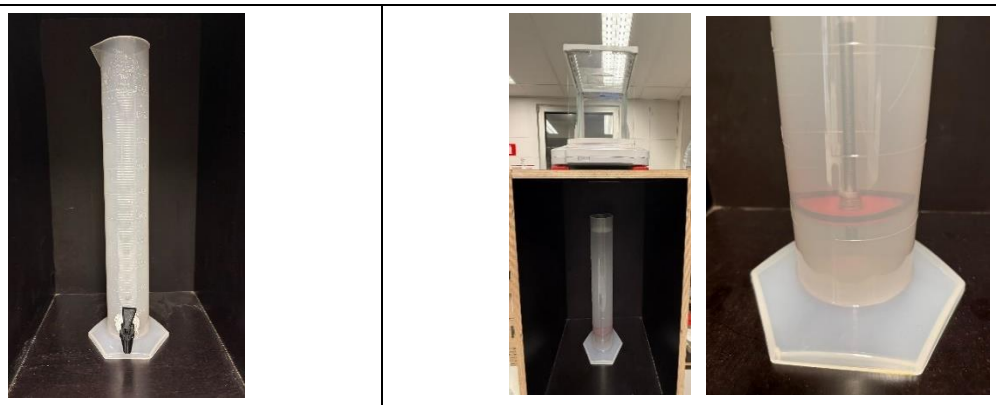

Side-Tap Sample Withdrawal Method Methodology based on van Rijn et al., 2023.	Settling Tube with Underwater Balance Methodology based on Deltares 2016.

Figure 1: Settling tube measurement setup with tap (left) and with underwater balance (right).

In the first phase of the research, the laboratory measurements were limited to non-cohesive sediment in non-saline water to avoid potential flocculation of the fines. All measurements are repeated for different concentrations of the sediment samples, and for two sizes of the settling tube: (i) a large tube (25 litre, height=2.4m), and (ii) a small tube (2 litre, height=0.45m). For the large tube a release device with a sediment container and valves (see Figure 2) was designed and printed in polymer. For the small cylinder, the sediment is released 'manually' (with a small cup or folded paper) at the top of the cylinder.

Four sand samples were tested: (1) commercial white quartz sand, (2) sand from Posorja-beach in Ecuador, (3) sand from the Meghna delta in Bangladesh and (4) a sample from a (dredging) siltation pond in the Bahamas (see Table 1). Initial dry solids suspension concentrations were varied from 0.4-2.0 gds/l (in 5 steps). PSD-data were obtained via bulk sediment samples (no prior preparation) tested in a Mastersizer laser diffraction device (Mastersizer 3000+ Ultra - Particle Size Analyzer Malvern Panalytical).

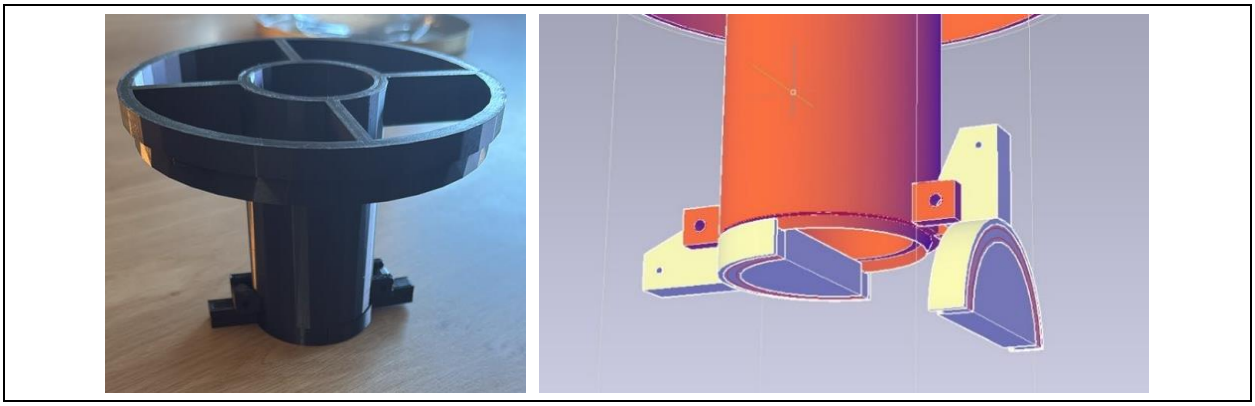

Figure 2: Sediment container and its release mechanism applied at the top of the large settling tube measurement setup.

There are several empirical - and complicated - equations to determine the settling velocities of sediment particles for the entire range of viscous to turbulent conditions (particle Reynolds number < 20,000) (Cheng 2008). Sand grains are small enough that viscous forces still play an important role in their settling behavior, but large enough that the deviation from the Stokes' Law is significant and wake turbulence cannot be ignored (Hagemeier 2021). We have chosen the formula of Ferguson and Church (2004) for its simplicity:

$$w_0 = \frac{Rgd^2}{C_1\nu + \sqrt{0.75C_2Rgd^3}}$$

where w_0 denotes the particle's fall velocity [m/s], d its diameter [m], R its submerged specific gravity (for quartz sand in fresh water this is 1.65) [-], g the gravitational acceleration [m/s²], ν the kinematic viscosity [m²/s], C_1 [-] and C_2 [-] the parameters dimensionless parameters related to viscous and turbulent regime respectively.

For small particles, the left term in the denominator is much larger and the equation is equivalent to Stokes' Law. For large particles, the second term in the denominator dominates, and the settling velocity converges to the solution of the turbulent drag equation. In between the formula predicts the transitional area.

The research of Ferguson and Church (2004) concludes that for smooth spheres these parameters take values 18 and 0.4, respectively. For typical natural sands, values of C1=18 and C2=1.0 where

sieve diameters are used, or 20 and 1.1 where nominal diameters are used. A limit for very angular grains as reported by Ferguson and Church (2004) is C1 = 24, C2 = 1.2.

Table 1: summary of 4 sand samples (D50, and % fines).

Sample name	%fines <63µm	D50	Number of Measurements			
			Large Cylinder	Large Cylinder	Small Cylinder	Small Cylinder
	%	µm	Subsample Method	Underwater Balance Method	Subsample Method	Underwater Balance Method
Quartz Sand	0	330	2	10	-	-
Ecuador (Posorja)	2	270	2	10	2	2
Bangladesh	13	122	3	12	2	2
Bahamas silt pond	38	69.5	2	12	2	4

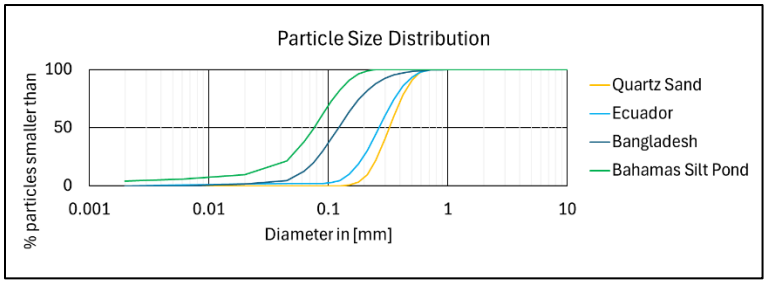

Figure 3: Particle Size Distributions of the samples in scope of the study. PSDs are determined with the Mastersizer Laser Diffraction Particle Distribution analyser.

Results

Figure 4 shows a microscopic view of the particle shape of all samples. It can be observed that the sediment particles of Bangladesh are much more angular, heterogeneous with flaky particles than the other sand samples (white quartz sand, and Ecuador sand). In the Ecuador sample some shell fragments can be seen, but overall, the shape of the particles is quite uniform. The particle shape of the white quartz sand is clearly most uniform. The Bahamas samples show smaller particle diameters with a more irregular shape. Based upon the shape of the particles the sand samples (quartz sand, and Ecuador sample) can be labelled as typical subangular sand, while for the Bangladesh and Bahamas samples, the particles are angular (thus C1=22 & C2=1.15 or even C1=24 & C2=1.2).

Figure 5 summarizes the settling velocity results measured for the Bangladesh sample. Very similar conclusions can be drawn for the other sand samples. The left panel of Figure 5 shows settling velocities (w0) for the full range of particle diameters for sediment concentrations of 1.2gds/litre. It can be observed that the settling velocities are in the same range as the settling velocities derived with the empirical formula of Ferguson and Church (with C1=22, C2=1.15). For a few measurements there is a discrepancy found for the tails of the settling velocity curves (thus for the smallest and largest sediment fractions). The median settling velocity (ws50) is well aligned with the empirical formula. This conclusion is also confirmed in the right panel, showing a box

plot of the median settling velocity ws50 = 0.0088 m/s for all lab measurements (avg ws50=0.0092m/s, based on 19 measurements on the Bangladesh sample), and compared with a settling velocity of 0.0089 m/s calculated with the empirical formula of Ferguson and Church.

Comparison of all results also showed that there was no impact of the concentration of the sediment particles, which can be explained by the low concentrations and non-cohesive properties of the samples tested.

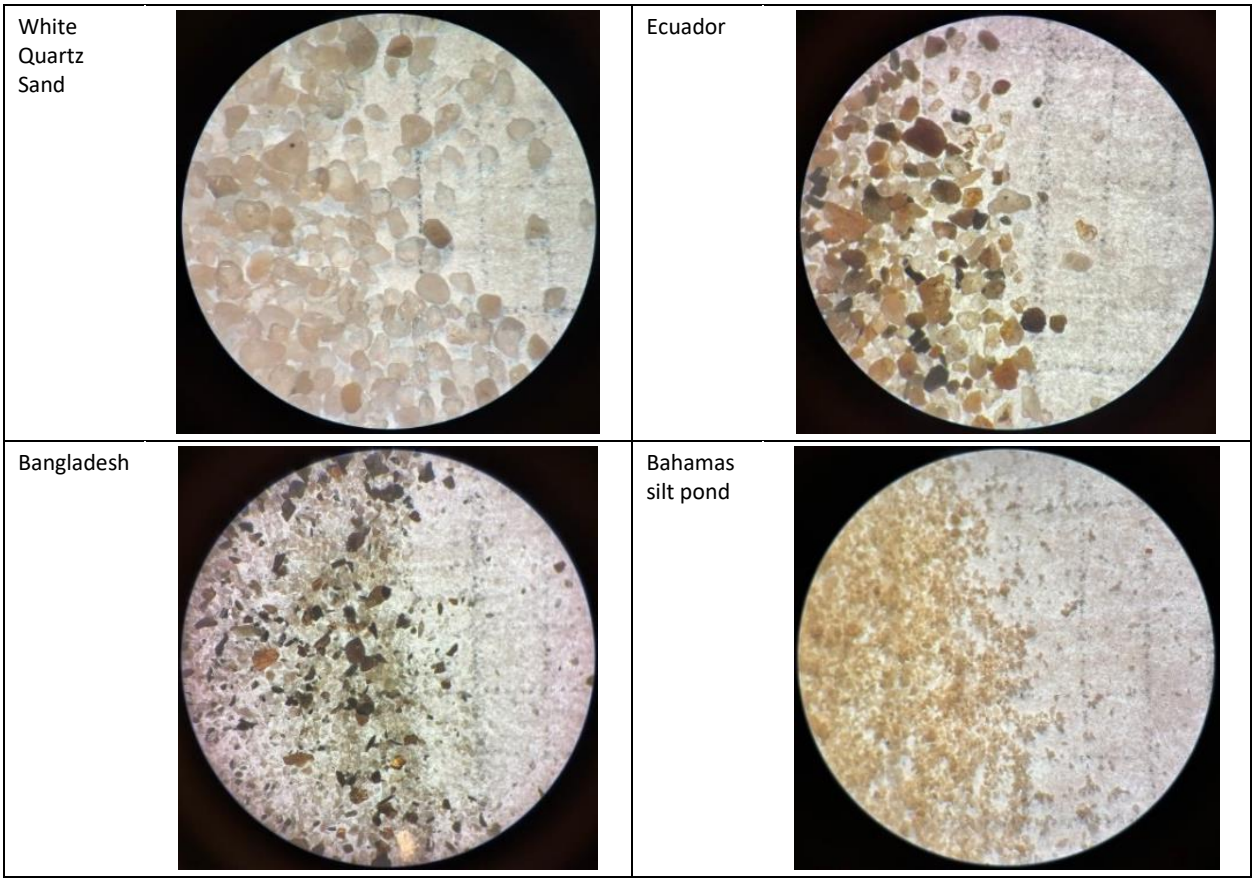

Figure 4: Picture of the particle shape for the three sand samples (white quartz sand, Ecuador and Bangladesh, Bahamas).

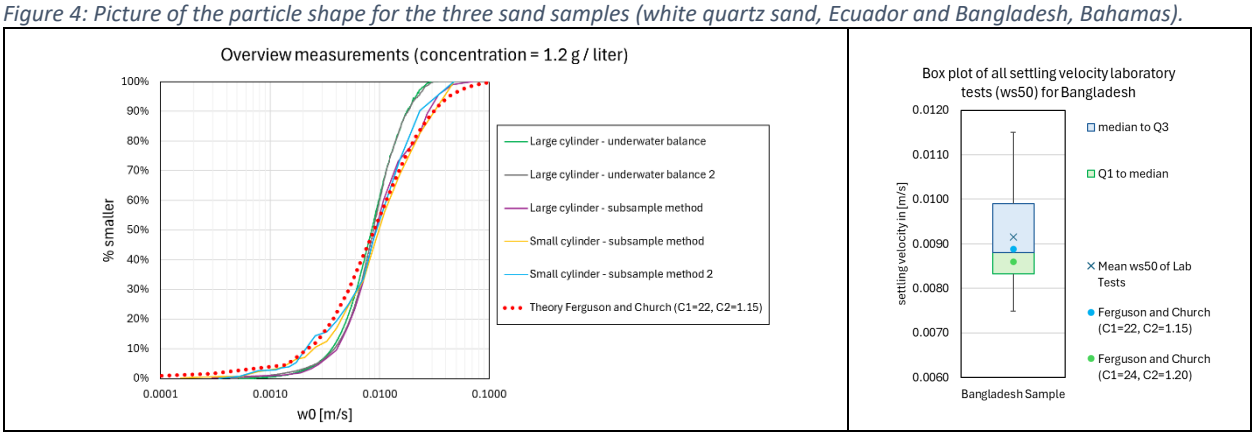

Figure 5: Settling velocity results for the Bangladesh sample. Left panel: full range of settling velocities w0 for 5 laboratory measurements for c=1.2g/litre, right pane: median settling velocity ws50 for all lab measurements (19 measurements), compared with empirical formula of Ferguson and Church.

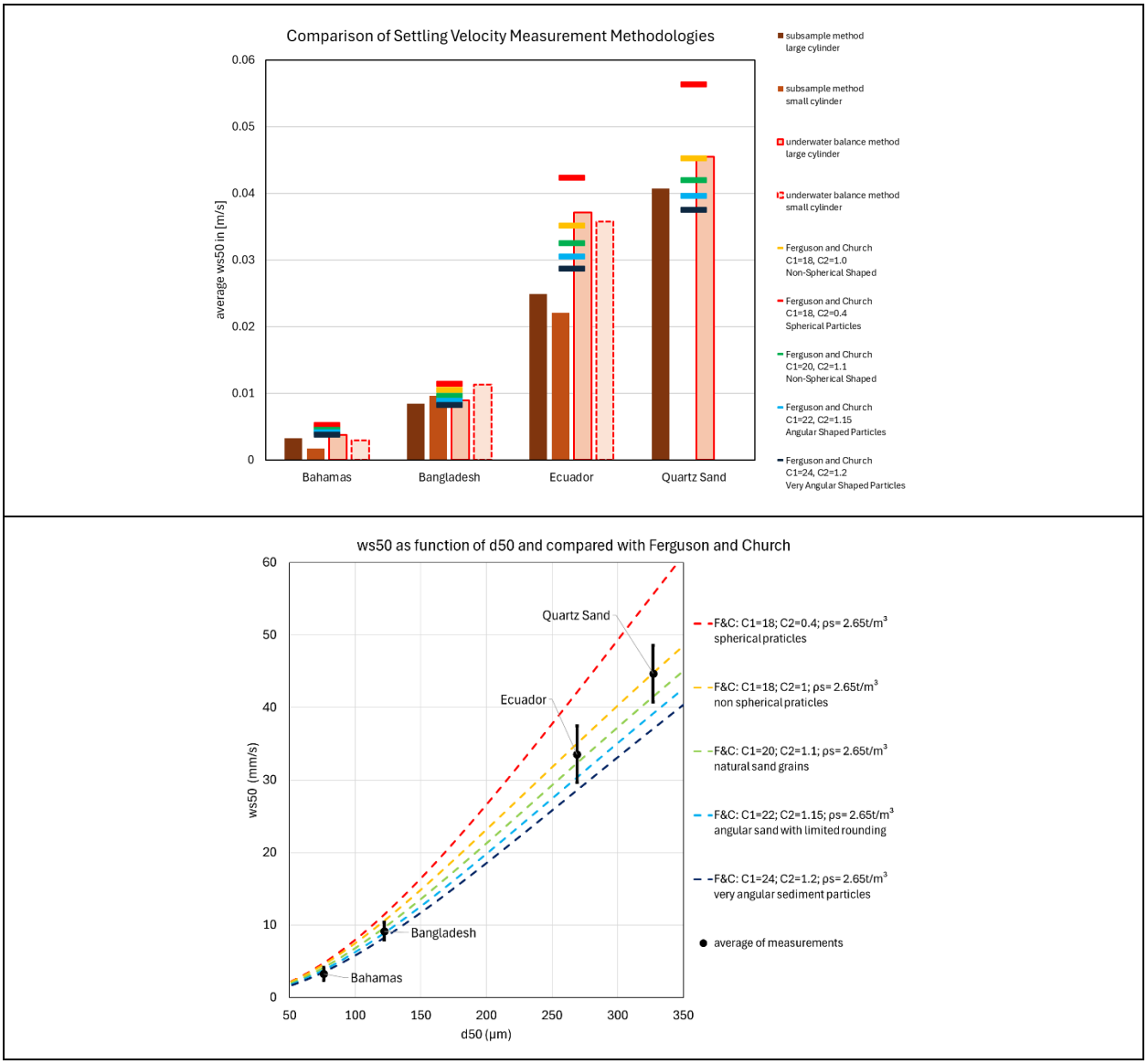

Figure 6: Settling velocity results for all available laboratory tests compared with the empirical formula of Ferguson and Church.

Finally, Figure 6 summarizes the settling velocity results for all available laboratory tests. The upper panel compares the measurement methodologies per sample. Based on the available measurements it seems that the method based on subsamples taken with the side tap results in somewhat lower settling velocities. This is particularly the case for the Ecuador sample, which might be due to the presence of some larger shell fragments settling more quickly (and which are absent in the water subsamples as they never reach the side tap). The settling velocities determined

with the underwater balance seem to give the best results for all sample locations. The lower panel compares all measurement ws50 results with the empirical formula.

Discussion

The median fall-velocity measured corresponds well with the values from the Ferguson & Church equation, provided correct assumptions are made for the C1 and C2 parameters. However, deviations between measurements and calculated values occur for the tails of the full settling velocity curve (left pane of Figure 5). These deviations are caused by 'density flow' phenomena at the start of the settling test, and boundary turbulence effects which play a role during the full extent of the test. In addition, the measurement method of the PSD based on the Mastersizer might lead to an under/overestimation of the settling velocity for larger/smaller sediment particles, especially for more angular particles.

When comparing the different methods to estimate the median settling velocity of particles, we observe (for the methods and sediment samples used in this research) a standard deviation between 10 % and 40 % (see Figure 6). Based upon this graph, it seems also reasonable to assume that the particle density for the sediment sample (crushed limestone) of the Bahamas is lower than 2.65 t/m^3 (to be confirmed by additional lab measurements).

The subsample method is a workload and resource intensive methodology. For one measurement 10-20 subsamples (50-200 ml of water with sediment in suspension) are taken. The samples are filtered and dried. In the final step, the weight of the sediment particles in the subsamples is determined. In all steps measurement errors can be made. For this reason, the method with the underwater balance seems to offer numerous advantages. When comparing the results of the different methodologies, the study seems to confirm that the method with the underwater balance is sufficiently accurate even with the small cylinder, which makes it an efficient method to be applied on a project site.

Based upon the graphical comparison with the empirical formula results given in Figure 6, it seems a correct conclusion that the sample of Bangladesh consists of more angular particles (and in consequence that the following values are to be adopted for C1=22 and for C2=1.15). The particles of the other two sand samples are more uniform and hence other parameter-values are recommended (C1=18, C2=1.0). For the samples from the Bahamas two elements seem to play a role, which is the particle shape, and the lower particle density. The shape of the particles will be further analysed with the Morphology 4 laboratory instrument to confirm the above conclusion.

Conclusion

All applied laboratory measurements allow to derive the settling velocity in line with empirical formulas. Provided the correct choices are made for the parameters (C1 and C2) in the Ferguson and Church equation, this formula provides a reasonably good approximation of the measured (still water) median settling velocity.

The 3D printed release mechanism was applied in the large settling tube, as this allowed to reduce measurement uncertainties. All measurements are repeated with the small and large cylinder and no deviations are found due to the absence of the release mechanism in the small tube. In addition, the method with the underwater balance avoids workload intensive analyses on water samples and increases the accuracy of the measurement. This allows to conclude that the laboratory methodology with the small settling tube, and with the balance method can be applied to derive qualitative settling velocity values (ws50) for non-cohesive sediment samples, and for low concentrations.

As the laboratory measurements and results are consistent with the results derived with the empirical formula of Ferguson and Church, it is worthwhile to invest in the extension of the settling velocity database with numerous samples tests on samples collected from all over the world. In addition, during the next phases additional complexity will be added in the studies, such as studying the impact of flocculation and increased concentrations of mud.

References

Cheng NS. 2008. Comparison of Settling-Velocity-Based Formulas for Threshold of Sediment Motion. Journal of Hydraulic Engineering, Vol. 134, Issue 8, 1136-1141.

Hagemeier T, Thévenin D, Richter T. 2021. Settling of spherical particles in the transitional regime. International Journal of Multiphase Flow. Volume 138(6).

Hasler M. 2007. Field and laboratory experiments on settling process in stormwater storage tanks. Master thesis, Graz University of Technology, 1-212.

van Rijn LC, Boechat Albernaz M, Manning AJ. 2023. Field measurements of settling velocities and floc sizes in the ferry channel near Holwerd, TKI MUSA project, 1-49.

Deltares, 2016a. Analysis tidal channel Holwerd-Ameland; Overview laboratory analyses. Report 1230378.002.

Stokes GG. 1851. On the effect of internal friction of fluids on the motion of pendulums. Transactions of the Cambridge Philosophical Society. 9, part ii: 8–106.

Ferguson FI, Church M. 2004. Simple universal equation for grain settling velocity. Journal of Sedimentary Research. Vol. 74, No. 6, 933-937.

Understanding the optical behaviour and spectral signature of dredginginduced plumes in coastal waters

Liesbeth De Keukelaere[a], David Doxaran[b], Robrecht Moelans[a], Niels Verdoodt[c], Els Knaeps[a]

[a] VITO, Boeretang 200, Belgium
[b] Laboratoire d' Océonographie de Villefranche, 181 chemin de Lazaret, 06230 Villefranche-sur-Mer, FR
[c] DEME Group, Scheldedijk 30, 2070 Beveren-Kruibeke-Zwijndrecht, BE

Understanding the optical behaviour and spectral signature of dredging-induced plumes in coastal waters

Liesbeth De Keukelaere[a], David Doxaran[b], Robrecht Moelans[a], Niels Verdoodt [c], Els Knaeps[a]

[a]VITO, Boeretang 200, Belgium
[b] Laboratoire d'Océonographie de Villefranche, 181 chemin de Lazaret, 06230 Villefranche-sur-Mer, FR

[c] DEME Group, Scheldedijk 30, 2070 Beveren-Kruibeke-Zwijndrecht, BE

Corresponding author: Liesbeth De Keukelaere; liesbeth.dekeukelaere@vito.be

Introduction

Based on past experience from monitoring dredging sites using satellite and drone data, it has become clear that the optical behavior of dredge plumes can differ significantly from those of naturally occurring turbidity. As a result, currently available turbidity algorithms tend to underperform, they can struggle to identify dredge plumes accurately and to quantify turbidity levels effectively.

The PLUMES project addresses this issue by developing dedicated prototype algorithms specifically designed to monitor these dredge plumes in coastal waters. In parallel, it will enhance our understanding of the unique optical properties of these plumes. The purpose is to more precisely delineate the spatial extent of dredge plumes and to distinguish them from natural turbidity, a distinction that is critical for environmental assessments in dredging operations.

Currently, environmental monitoring in dredging projects typically relies on a network of CTD sensors mounted on seabed frames or buoys. These setups are not only labor-intensive to install and maintain but also often fail to provide a comprehensive picture of the turbidity impact across a site. In recent years, VITO has increasingly been asked to support such assessments by integrating satellite and drone images with in situ measurements across various international sites. While these Earth Observation (EO) data sources have proven valuable, our experience also highlights a key limitation: existing, validated turbidity algorithms often fall short when applied to dredge plumes, underscoring the need for tailored solutions like those being developed in PLUMES.

Methods

Field data collection

Water samples were collected at three dredging sites: two in Europe and one in Africa. The sites were selected based on the duration of the dredging activity, the availability of personnel to perform the sampling and the possibility for transport of the samples. Due to the sensitivity of the data, the exact locations of these sites are not disclosed in this report. Sampling was carried out

using a bucket, either directly inside the hopper or at the water surface near the hopper, with the aim of analyzing the optical properties of the dredged materials.
It is important to note that while samples taken from inside the hopper are not representative in absolute terms, high turbidity and SPM concentrations will be encountered due to the continuous discharge of water, they are considerably easier to collect. Despite this limitation, these samples are valuable for deriving the specific optical absorption and backscattering properties of the dredged material.

Immediately after collection, four clean 1-liter dark plastic sampling bottles were filled. The bottles were placed in a cool box with cold packs and transported to the laboratory in France for further analysis.

Table 1. Field samples

Site	Sample number	Date of field data collection	comment
Dredging Site 1 Europe	Sample 1	19/11/2024	Only sample in the hopper
	Sample 2	17/12/2024	Only sample in the hopper
	Sample 3	11/02/2025	Inside and outside hopper
	Sample 4	17/03/2025	Inside and outside hopper.
Dredging Site 2 Africa	Sample 1	30/11/2024	Inside the hopper 2x Outside the hopper 4x Before the dredging to have a reference 1x
	Sample 2	13/02/2025	Inside hopper 4x outside hopper 4x

Laboratory sample analysis

On the day the water samples were delivered, they were analyzed in LOV laboratory facilities to determine the optical and biogeochemical properties of suspended particles, in order to determine how these properties influence the water reflectance signal.

Atmospheric correction of Sentinel-2 images

The operational ICOR atmospheric correction approach was selected for processing the Sentinel-2 satellite images. However, to quantify the impact of the atmospheric corrections applied to S2-MSI satellite data on the retrieved water-leaving reflectance (Rhow, i.e., the spectral signature notably of the dredge plumes), a selection of S2-MSI satellite images from different test sites were processed using the iCOR (De Keukelaere et al. 2018), ACOLITE-DSF (Vanhellemont 2019) and Sen2Cor processors (Main-Knorn et al. 2017) for intercomparison.. iCOR, ACOLITE and Sen2Cor-derived Rhow spectra on same images were extracted on a number of locations along

and outside identified dredge plumes and compared as spectral signatures and scatterplots over the visible and near-infrared spectral ranges (400 – 900 nm).

Results

Satellite intercomparison

Rhow spectra inside and outside dredge plumes were extracted in various test sites: Altamira (Mexico), Taman (Russia), Lagos (Nigeria), Abu Dhabi (U.A.E.) and Hinkley point (UK). Rhow spectra are typical of moderately to highly turbid waters (Knaeps et al. 2015). Scatterplots show very good agreement between iCOR and ACOLITE products especially at 560 nm (where the water-leaving signal is maximum), with a best-fitted linear relationship having a slope of 1.05, a negligible intercept and a determination coefficient close to 1 (Figure 1). This agreement when considering several S2-MSI images and wavebands in the visible and near-infrared spectral ranges, with differences lower than 8% on average. These results clearly tend to validate the iCOR atmospheric correction processing which allows retrieving Rhow spectra very close to those obtained applying the ACOLITE-DSF approach which was proved to perform well in turbid waters (e.g., Doxaran et al. 2024).

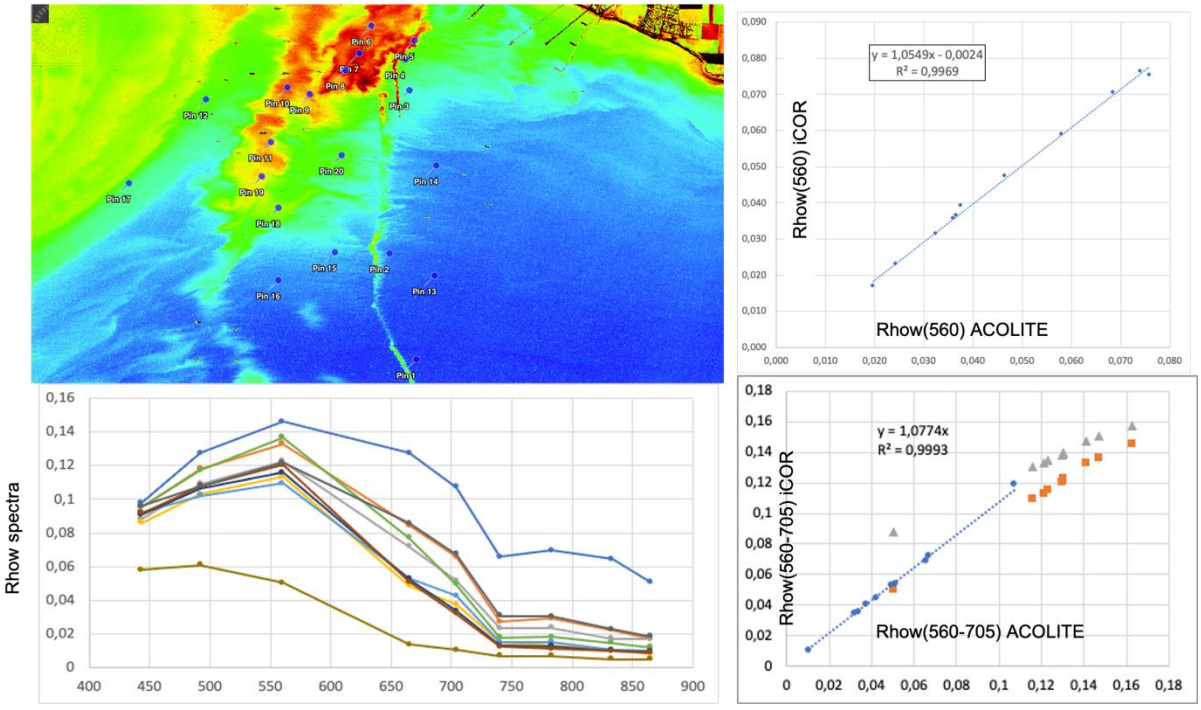

Figure 1. Typical intercomparisons between S2-MSI Rhow values in and outside dredge plumes obtained from iCOR and ACOLITE processors. Spectra and scatterplots Considered test sites are: Altamira Exp2021 (Mexico), TTNG, Russia, EKO (Nigeria), NMDC Spartacus (Abu Dhabi) and Hinkley point C (UK).

The results obtained are clearly not as satisfactory when comparing Sen2cor-derived Rhow values to ACOLITE products (here used as a reference) (Figure 2). The best-fitted linear relationship has a much lower determination coefficient (R^2 = 0,53), and the overall difference is close to 40% on average over the visible and near-infrared spectral regions, with Sen2Cor-derived Rhow values overestimating those retrieved using ACOLITE.

The conclusion at this stage is that both iCOR and ACOLITE processors can be used to retrieve the spectral signature of turbid waters inside and outside dredge plumes, while Sen2Cor products should be avoided at this stage.

The next step is to analyze and compare the spectral signatures of (highly) turbid waters encountered in natural environmental such as estuaries and in dredging plumes

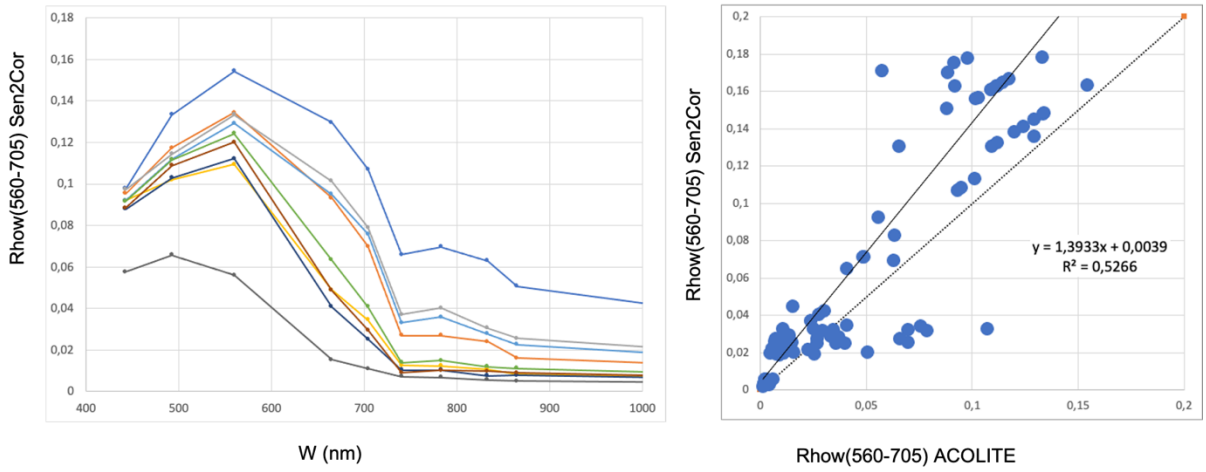

Figure 2. Typical intercomparisons between S2-MSI Rhow values in and outside dredge plumes obtained from Sen2Cor and ACOLITE processors. Spectra and scatterplots. Considered test sites are: Altamira Exp2021 (Mexico), TTNG, Russia, EKO (Nigeria), NMDC Spartacus (Abu Dhabi) and Hinkley point C (UK).

In situ data analysis

From analysis of the biogeochemical and optical properties of suspended particles in suspension in the dredge plumes to most interesting results can be summarized as follows:

The measured contributions of non-algal particles to the total particulate light absorption coefficient in dredge plumes appeared to vary from 90 to 100% at 443 nm (a wavelength corresponding to a peak of light absorption by phytoplankton pigments (Babin et al. 2003)). In surrounding waters, this contribution was observed to be 10 to 30% lower. However, the SPM mass-specific absorption coefficient of non-algal particles at 443 nm ($a_{nap}(443)$, in $m^2.g^{-1}$) did not differ from typical values reported for a wide range of European coastal waters (Babin et al. 2003). By opposition, the spectral slope associated to the measured a_{nap} spectra proved to be peculiar, i.e.,

quite at the extreme limit of values reported by Babin et al. (2003) in natural European coastal waters. The S_{nap} values measured in the dredge plumes actually varied 0,007 to 0,010 nm^{-1}, which is at the extreme lower limit of values reported by Babin et al. (2003). As SPM sampled in the dredge plumes were proved to be mineral-rich, this most probably indicates the presence of coarse SPM not efficient in terms of light absorption at short visible wavelengths but significantly absorbing light in the near-infrared. This peculiar light absorption by non-algal particles in dredge plumes most probably explains the specific spectral signatures (Rhow spectra) observed in dredge plumes compared to that of naturally turbid waters and can represent a way to distinguish and identify dredge plumes from ocean color satellite data.

Analysis of spectra

To evaluate differences in spectral characteristics between naturally occurring sediment plumes and those resulting from dredging activities, we show here the results of an image acquired on 10 February 2021 over Abu Qir, Egypt (Tile ID: 36RTV), which depicts intensive dredging activity involving approximately four hopper dredgers (TSHD) trailing the seabed, generating extensive sediment plumes. Additionally, rainbowing operations are visible near the coastline.

The Sentinel-2 scene of Abu Qir contains a high density of sediment plumes originating from various sources. To enable comparative analysis, spectral data were extracted from 13 visually identified plume types, each representing a distinct suspected source. For each category, five replicate spectra were collected to account for within-class variability. This manual classification and the corresponding extraction locations are illustrated in Figure 4.

Figure 4 : Selected locations for pixel extraction. A total of 13 distinct source types were manually identified. For each category, five spectra were extracted to account for intra-category variability.

Figure 5 presents the reflectance spectra of 13 manually delineated sediment plume categories derived from the Sentinel-2 imagery of Abu Qir. Several observations can be drawn from the spectral profiles for this image:

- The *Dark water* category exhibits uniformly low reflectance across the spectrum, with a slight increase in the blue region. This spectral shape is characteristic of clear water bodies with minimal optically active constituents such as suspended sediments or phytoplankton, suggesting low turbidity and low biological activity.
- Naturally occurring plumes, such as those labeled *River water* and *Plume 3*, display slightly elevated reflectance compared to dark water, particularly in the green and red regions. However, in the blue region, reflectance values drop significantly—reaching near or below zero—which may indicate strong absorption due to phytoplankton. This is further supported by a small observed dip around 665 nm, a known absorption feature associated with chlorophyll-a, suggesting biological influence and a potential presence of algal matter. The visual appearance of these plumes as dark green also aligns with this interpretation.
  Rainbowing plumes display a relatively flat spectral response across the visible spectrum, with elevated reflectance extending into the near-infrared (NIR) region. This pattern suggests a sediment-rich composition—such as mud—rather than a water-dominated one, as water typically exhibits stronger absorption, particularly in the NIR spectral region.
- Hopper dredger plumes, especially *Hopper 1*, exhibit the highest reflectance values in the visible range, indicating a high concentration of suspended sediments and strong scattering. In the case of *Hopper 1 old*, a noticeable decline in reflectance is observed, particularly around 665 and 705 nm, suggesting sediment settling or plume dispersion over time. This temporal change may reflect a reduction in particle concentration or shifts in particle composition as the plume ages.

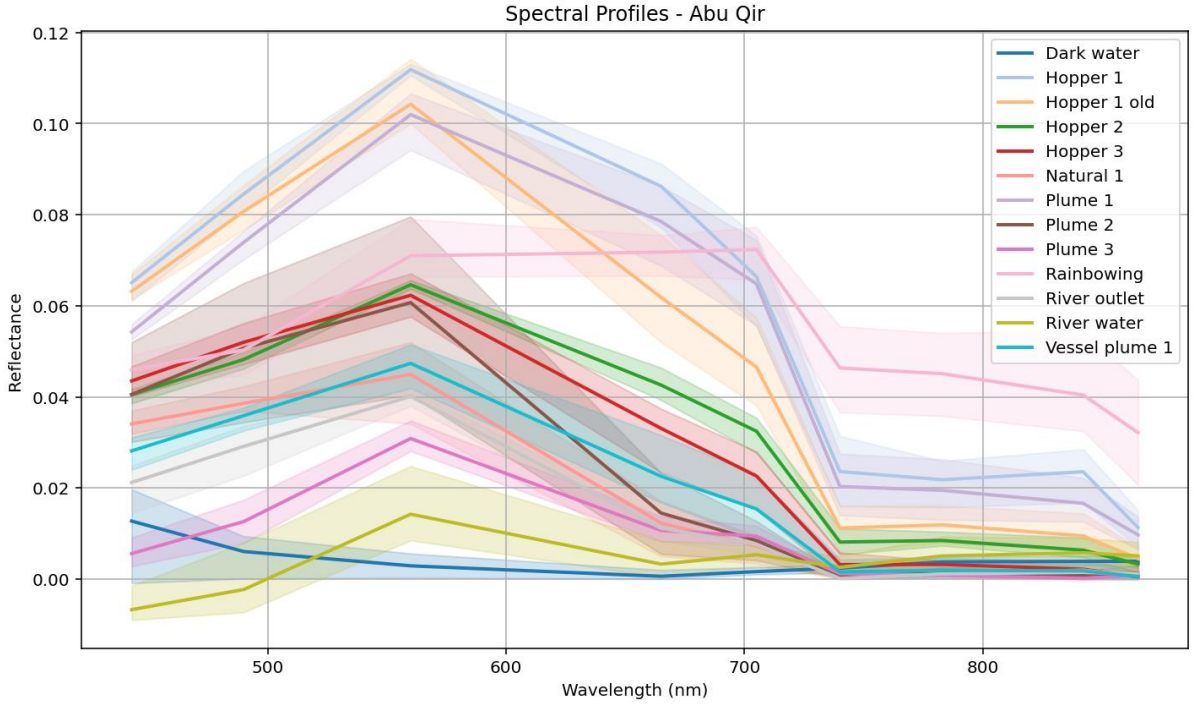

Figure 5. Spectral profiles of the 13 identified sediment categories in the Abu Qir scene. Solid lines represent the mean reflectance for each category, while the shaded areas indicate the range between minimum and maximum values.

Discussion and conclusion

This abstract presents a preliminary assessment of the optical characteristics of dredged sediment plumes, with a focus on distinguishing them from naturally occurring sediment plumes using remote sensing and in situ data. The analysis was carried out at two complementary levels.

First, water and sediment samples were collected in the vicinity of hopper dredging vessels (TSHD) and analysed in the laboratory to characterize their inherent optical properties, specifically their absorption and backscattering coefficients. These measurements provide baseline insights into the spectral behaviour of sediments directly linked to dredging operations.

Second, satellite-derived spectral signatures from Sentinel-2 imagery were analyzed to compare the reflectance profiles of sediment plumes associated with active dredging operations (e.g., trailing, rainbowing, hopper discharge) and those of naturally occurring plumes (e.g., river outflows, resuspension events). To ensure the reliability of the retrieved water-leaving reflectance, a preliminary intercomparison was performed between three established atmospheric correction processors: iCOR, ACOLITE, and Sen2Cor (the default processor provided by ESA). The comparison demonstrated strong agreement between ACOLITE and iCOR—both of which are optimized for aquatic applications—thereby providing confidence in their suitability for coastal and turbid water analyses. Based on these results, one of the two (iCOR or ACOLITE) was selected for subsequent analysis of the spectral signatures.

The remote sensing analysis revealed notable spectral distinctions between dredge-induced and natural sediment dynamics. Plumes generated by rainbowing activities exhibited relatively flat spectral profiles across the visible range and elevated reflectance in the near-infrared (NIR), suggesting a composition dominated by suspended mineral sediments—such as mud—rather than optically deep water. In contrast, hopper dredger plumes showed pronounced peaks in the visible spectrum, with significantly higher reflectance values compared to natural waters, indicating higher concentrations of suspended particles and more intense light scattering.

References

Babin M., Stramsk, D., Ferrari, G.M., Claustre H., Bricaud A., Obolensky, G. and N. Hoepffner (2003). Variations in the Light Absorption Coefficients of Phytoplankton, Non-algal particles, and dissolved organic matter in coastal waters around Europe, J. Geophys. Res., 108, 3211, https://doi.org/10.1029/2001JC000882.

De Keukelaere L., S. Sterckx, S. Adriaensen, E. Knaeps, I. Reusen, C. Giardino, M. Bresciani, P. Hunter, C. Neil, D. Van der Zande & D. Vaiciute (2018) - Atmospheric correction of Landsat-8/OLI and Sentinel-2/MSI data using iCOR algorithm: validation for coastal and inland waters, European Journal of Remote Sensing, 51:1, 525-542, DOI: 10.1080/22797254.2018.1457937

Doxaran D., Ehn J., Bélanger S., Matsuoka A., Hooker S., and M. Babin (2012). Optical characterisation of suspended particles in the Mackenzie River plume (Canadian Arctic Ocean) and implications for ocean colour remote sensing, Biogeosciences, 9, 3213-3229, doi:10.5194/bg-9-3213-2012.

Doxaran, D., ElKilani, B., Corizzi, A., & Goyens, C. (2024). Validation of satellite-derived water-leaving reflectance in contrasted French coastal waters based on HYPERNETS field measurements. Frontiers in Remote Sensing, 4, 1290110.

Knaeps E., Ruddick K.G., Doxaran D., Dogliotti A.I., Nechad B., Raymaekers D. and S. Sterckx (2015). A SWIR based algorithm to retrieve Total Suspended Matter in highly turbid waters, Remote Sensing of Environment, 168, 66–79.

Main-Knorn M., Pflug B., Louis J., Debaecker V., Müller-Wilm U. and G. Ferran. (2017). Sen2Cor for Sentinel-2. 3. 10.1117/12.2278218.

Vanhellemont, Q. (2019). Adaptation of the dark spectrum fitting atmospheric correction for aquatic applications of the Landsat and Sentinel-2 archives. Remote Sensing of Environment 225, 175–192. (https://doi.org/10.1016/j.rse.2019.03.010).

A bio-geo-optically consistent particle model for optical inversion

Xiaodong Zhang[a], Deric Gray[b], Ping Yang[c]

[a] University of Southern Mississippi, Stennis Space Center, Mississippi, USA

[b] Naval Research Laboratory, Washington DC, USA

[c] Texas A&M University, College Station, Texas, USA

A bio-geo-optically consistent particle model for optical inversion

Xiaodong Zhang[a], Deric Gray[b], Ping Yang[c]

[a]University of Southern Mississippi, Stennis Space Center, Mississippi, USA
[b]Naval Research Laboratory, Washington DC, USA
[c]Texas A&M University, College Station, Texas, USA

Corresponding author: Xiaodong Zhang; xiadong.zhang@usm.edu

Introduction – One of motivations for optical observations has been to quantify physical properties of particles suspended in the aqueous environment (Pabst and Gregorova, 2007). Because the scattering of light by suspended particles vary with their size, composition, shape and internal structure (Bohren and Huffman, 1983), measurements of light scattering have been used as an efficient and powerful biogeochemical tool to characterize particles in the environment.

Optical inversion of particles from light scattering requires a kernel function or particle model (Twomey, 1977) that links the scattering function to the particle characteristics to be derived. Upon thoroughly reviewing the earlier efforts in deriving the size distributions and refractive indices of particles in the oceans from the volume scattering functions, Zhang et al. (2011) developed a new particle model using particle subpopulations. A subpopulation represents a particular species, such as a diatom population, or a type of particles, such as silicate frustules in the oceans, which are found to follow lognormal distribution in number-size spectrum (Campbell, 1995; Jonasz, 1987; Lambert et al., 1981; Stramski and Kiefer, 1991). A subpopulation is also assumed to be represented by homogeneous spherical particles. The Zhang et al. (2011) subpopulation particle model was able to retrieve the refractive index and particle size distribution over an extended size ranges from measured volume scattering functions that are consistent with results based on backscattering data (Boss et al., 2004). Twardowski et al. (2012) and Zhang et al. (2012) improved the subpopulation model by using a hexahedral shape instead of spheres to reflect the fact that oceanic particles are seldom spherical. The improved particle model showed better performance in retrieving the organic and inorganic particles (Zhang et al., 2014; Zhang et al., 2017) and particle size distributions over 5 orders of magnitude from 0.02 μm to 2000 μm (Zhang et al., 2023).

The current particle models did not account for the internal structure of oceanic particles, particularly those of living organisms. All the living cells, such as phytoplankton, have membrane and some, such as coccolithophores have scales. The membrane and scales would alter light scattering significantly (Meyer, 1979; Zhai et al., 2013). Indeed, optical properties simulated using shelled spheres to represent phytoplankton agreed better with the observations

than those predicted using homogeneous spheres (Kitchen and Zaneveld, 1992; Organelli et al., 2018).

Hu et al. (2022) simulated polarized scattering using three particle models including homogenous spheres, mix of homogenous/coated spheres, and homogenous asymmetric hexahedra to account for the effects of particle shapes and/or internal structures. With the size distribution that was measured, each of the models can reproduce some of the scattering features observed, but neither of them can reproduce all. The result suggests that accurate simulation of the polarized scattering by oceanic particles needs to account for both their nonsphericity and heterogeneity, in addition to the concentration and size distribution of the particles. The objectives of this study are to 1) present a particle model that embodies predominant morphological features of major types of suspended particles in the aquatic environment; and 2) evaluate the performance of the model in retrieving the bio-geo-optical properties of particles from the volume scattering functions.

Methods

Following Zhang et al. (2011), we adopt the subpopulation concept, where each subpopulation represents a particular species or a type of particle and follows log-normal distribution in its number-size spectrum. The mode sizes of subpopulations are set at 0.04, 0.08, 0.16, 0.4, 0.8, 1.6, 3.2, 6.4, and 20 μm. For mode sizes < 0.2 μm, the standard deviations are set at 0.3, 0.5, and 0.7; for mode sizes between 0.2 and 20 μm, the standard deviation are set at 0.3, 0.5, 0.7, and 0.9; for mode sizes equal to or greater than 20 μm, the standard deviation is set at 1.1. The choices of these values are based on observations of various types of particles in laboratories and the oceans (refer to Table 2 of Zhang et al. (2011)), including nonliving submicron organic matter (Longhurst et al., 1992), colloids (Vaillancourt and Balch, 2000), biological particles (Yamasaki et al., 1998), organic and mineral particles (Lambert et al., 1981; Wells and Goldberg, 1992), cultured phytoplankton species (Campbell and Yentsch, 1989), natural phytoplankton species (Campbell et al., 1989), and bubbles (Zhang et al., 1998). The actual size distributions conveyed by these chosen values of mode and standard deviation encompass nearly all optically significant particles in the oceans (Davies et al., 2014; Stramski and Kiefer, 1991).

Particle subpopulations are further grouped into living and nonliving populations. Nonliving subpopulations include colloids (< 0.2 μm), particulate organic matter (> 0.2 μm), and particulate inorganic matter (0.2 μm). Non-living populations are represented by asymmetric hexahedra to emphasize their optical effect due to non-spherical shape. The refractive index relative to water, $m = n + in_k$, varies for different types of particles and spectrally. For colloidal particles, the real part of relative refractive index n(532 nm) was set at 1.02 and 1.10 to broadly represent organic and inorganic particles, and imaginary part of index n_k was calculated as

$0.010658\exp(-0.007186\lambda)$ (Stramski and Woźniak, 2005), where λ is wavelength in nanometer. For particulate organic matter, n(532 nm) was set at 1.02, 1.04, and 1.07 to represent mixture of protein, lipid and carbohydrate with water at various levels; and n_k was assumed to follow that of chloroplast absorption (Lain et al., 2023). For particulate inorganic matter, n(532 nm) was set at 1.10, 1.14, 1.20 to represent the dominant mineral composition of silicate (1.10), clay (1.14), and calcite (1.20); and n_k was assumed to follow that of mineral particles suggested by Wozniak and Stramski (2004) based on measurements for Saharan aerosol (Patterson et al., 1977). The values of n_k are shown in Fig. 1. Spectral variations of real index arise from normal and abnormal dispersion. As real indices go through normal dispersion for both water and particles, the normal dispersion for relative real index n was ignored in this study. However, the abnormal dispersion, which is caused by interdependence of real and imaginary parts of the index (Bohren and Huffman, 1983), cannot be ignored and was considered in this study. Three examples of spectral variation of n due to abnormal dispersion are shown in Fig. 1.

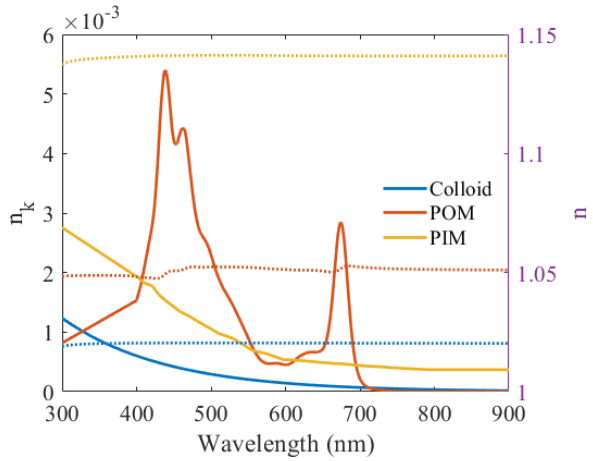

Figure 1. Spectral variation of the relative refractive indices (m = n + ink) for different particles. Solid curves represent n_k; and dashed curves represent three examples of n exhibiting abnormal dispersion in response to the change of n_k.

Another non-living subpopulation is microbubbles, which are represented using coated spheres (Zhang et al., 1998), with a shell of thickness of 0.002 µm and refractive index of 1.20 + i0 to represent a single layer of proteinaceous molecules (Fox and Herzfeld, 1954) and an air core of index = 0.75 + i0.

Living subpopulations or organisms include microbes (< 0.2 µm), bacterio- or pico-plankton (0.2 – 2 µm), and larger phytoplankton (> 2 µm). Living populations are represented by coated spheres to emphasize the dominant cellular structure feature consisting of a membrane and a cellular core. From 3-D mapping of refractive index of various phytoplankton cells measured by a holo-tomographic scanner (NanoLive), Kamowski et al. (2023) deduced that the thickness of phytoplankton cell membrane is of relatively constant thickness (approximated 1.3 µm from their

data) regardless of their sizes. Using coated spheres to represent living organism, we assigned the thickness of the shell for larger phytoplankton a fixed value of 1.0 μm. We extend the fixed-thickness-membrane assumption to smaller living organisms, assuming microbe has a membrane of thickness 0.003 μm (suitable for viruses) and picoplankton 0.01 μm (suitable for bacteria). The real parts of refractive indices measured for various phytoplankton membranes/shell (Kamowski et al., 2023) varied from 1.088±0.016 for silica frustule, 1.153±0.005 for cellulose membrane, to 1.177±0.004 for calcite coccolith. In this study, we assume the refractive index of the shell of a fixed value of m = 1.12 + i0 (with no absorption). The imaginary index n_k for the core is assumed to be that of colloid (blue curve in Fig. 1) for microbes and that of POM (orange curve in Fig. 1) for both pico- and larger phytoplankton. The real index for all living organisms is assumed to be n(532 nm) = 1.04, consistent with (Aas, 1996; Kamowski et al., 2023; Morel and Ahn, 1990) and varies spectrally following anomalous dispersion (exhibited as dotted lines in Fig. 1).

Optical inversion is performed with measured volume scattering functions (β(θ)) following the approach detailed in (Zhang et al., 2011). Basically, the phase functions (P(i,θ)) associated with each subpopulation (i) were computed at the wavelength of measurements and serve as the kernel to the following linear model

$$\beta(\theta) = \sum_i b_i P(i,\theta) \tag{1}$$

where b_i is the scattering coefficient associated with each subpopulation and are the solution of optical inversion. To ensure physical soundness of the solution, the inversion will be carried out using Least Squares with non-negative constraint. The subpopulations with positive b_i values represent those that are identified to contribute significantly to the measured VSF. An example of optical inversion from measured VSF is shown in Fig. 2.

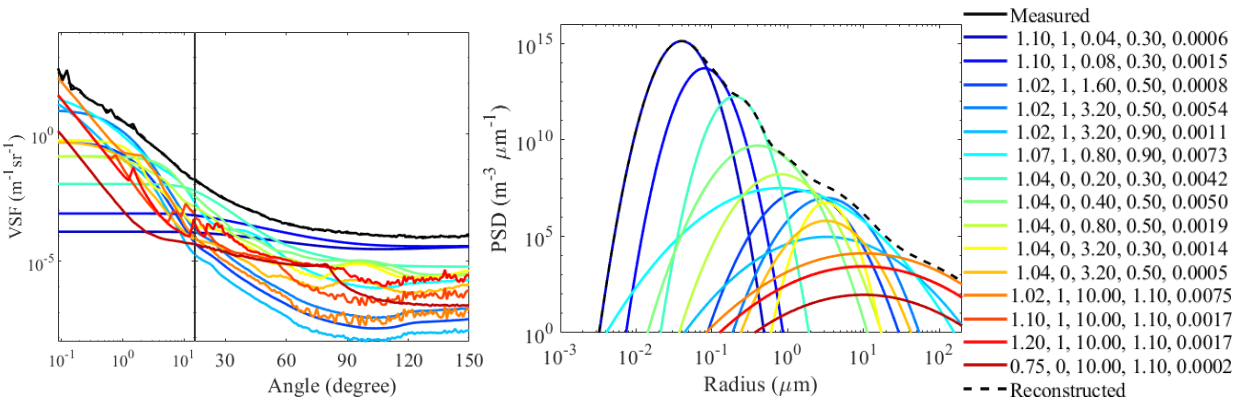

Figure 2. A VSF measured with a LISST-VSF instrument in the North Atlantic Ocean was inverted to derive particle subpopulations following Eq. (1). (a) and (b) The VSFs and particle size distributions of derived subpopulations. Each subpopulation is identified

by 5 values: refractive index, shape (1 for hexahedra and 0 for coated sphere), mode size (radius, μm), standard deviation, and scattering coefficient (m-1).

The identified subpopulations can reconstruct the observed VSF completely. The other optical and biogeochemical properties can then be calculated from these identified subpopulations through forward modelling.

Results

During the NASA EXPORTS field campaign, we measured particle size distributions (PSDs) from 0.2 μm to 2000 μm using a suite of instruments, including ViewSizer for submicron particles, Coulter Counter, Imaging Flow Cytometer (IFCB), LISST and Underwater Video Profiler. The PSDs derived from the VSF-inversion as illustrated in Fig. 1 compared well with the independent measurements at various size sections (Fig. 3) with an overall difference of ~50% over the sizes that span 5 orders of magnitude (Zhang et al., 2023).

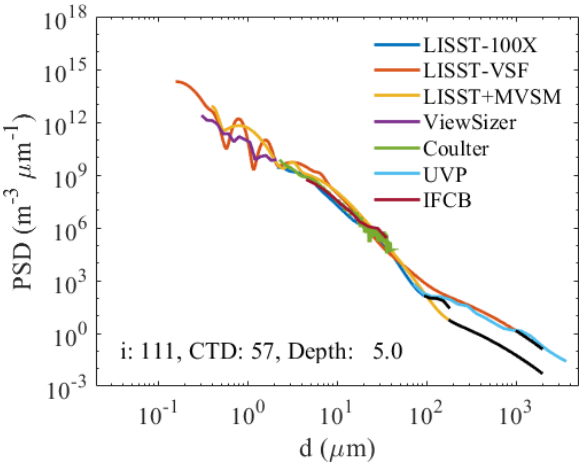

Figure 3. The PSDs derived from the VSF-inversion with LISST-VSF data and MVSM data agreed well with the independent measurements by various instruments (ViewSizer, Coulter Counter, Imaging Flow CytometerBot, and Underwater Video Profiler) at different size sections.

Because refractive index is closely related to the density of particles, mass concentrations of various particle groups can be estimated from the subpopulations that are identified. Figure 4 compares the particulate organic carbon (POC) concentrations between laboratory determination and VSF-inversion. The organic particles are assumed to have refractive indices < 1.10 and their densities

$$\rho = 8.56(n-1). \quad (2)$$

POC is typically measured by filtering water samples through pre-combusted G/F filters of pore sizes 0.4 μm. When organic particles of all sizes were considered, the VSF-inversion results clearly overestimated the POC concentration. However, using only those organic particles of

sizes that match with filtration process, the estimated POC agreed very well with the laboratory determination.

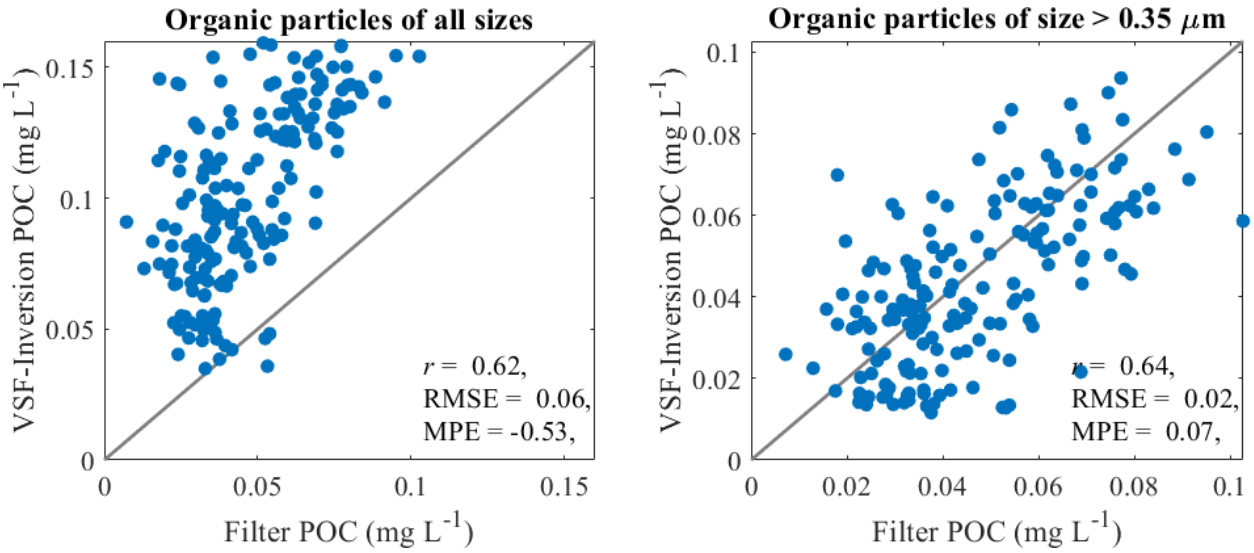

Figure 4. Comparison of POC between laboratory determination and VSF-inversion. Organic particles are assumed to have refractive indices < 1.10. (Left) Organic particles of all sizes; (right) organic particles of sizes > 0.35 µm, the pore size of GF filters used to filter water samples for POC determination.

Both Multispectral Volume Scattering Meter (MVSM) and LISST-VSF were deployed during NASA EXPORTS field campaigns. MVSM measured VSFs at 8 spectral bands while LISST-VSF measures VSFs at 517 nm. We calculated the spectral backscattering coefficient at the 8 bands of MVSM from the particle subpopulations identified from VSF-inversion using the LISST-VSF data (Fig. 5). It is interesting to note that the backscattering coefficient predicted with the particle model that includes living organisms compare much better with the particle model that does not include living organisms. This corroborates that living organisms are the major optically active components in the study site (North Pacific Ocean) and the coated spheres used to represent organisms were able to reproduce their spectral signature well.

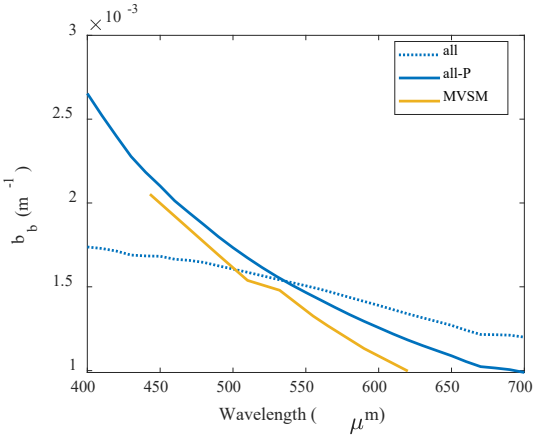

Figure 5. Backscattering coefficients measured by MVSM and inferred from VSF-inversion using LISST-VSF data with (all-P) and without (all) inclusion of living organisms.

The inclusion of living organisms in the particle model also improves the estimate of the polarized components. Figure 6 compares the predicted degree of linear polarization (DoLP, -P12/P11) with the measured values. Prediction without the living organisms overestimated DoLP (Fig. 6-left) by an average of 14%. On the other hand, with the living organisms, the prediction agreed with the measurements extremely well, with a regression slope close to unity (0.98) and a mean difference of 4% (Fig. 6-right).

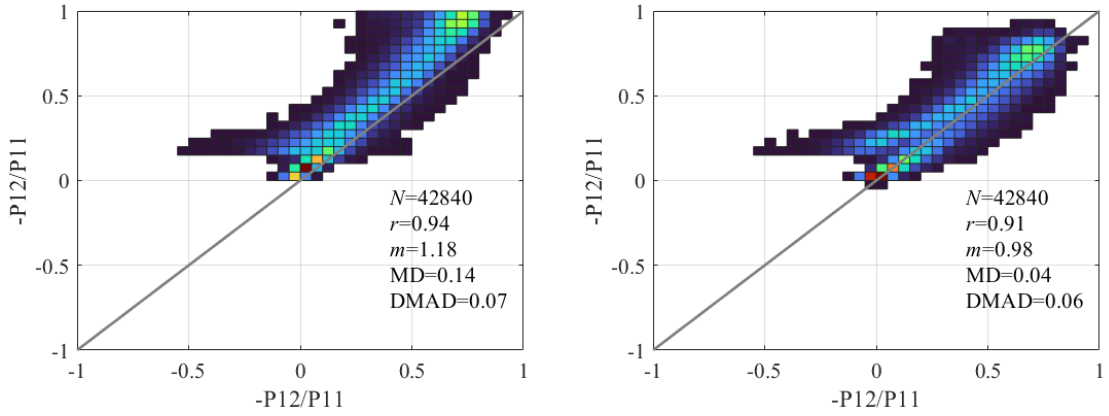

Conclusion

A particle model that accounts for major size distribution and morphological features of marine particles is proposed with an aim to facilitate optical inversion. The particle model improves over an earlier model (Zhang et al., 2011), which is built upon a concept of subpopulations to represent individual species or a specific type of particles. While the earlier model is exclusively built on hexahedra shape to account for the nonspherical feature of marine particles, the new model added coated spheres to represent living organisms whose most salient morphological feature is cellular structure with a membrane and a core. The optical inversion using the particle model is initiated with the volume scattering function, describing the angular distribution of the scattered light and tested with other optical properties and some biochemical properties that were measured concurrently. The results showed that the new particle model was able to retrieve particle size distribution and mass concentration of various particle components very well. In particular, the inclusion of living organisms represented by coated spheres seem to reproduce the spectral and polarized signature much better than the model without living organisms. This suggests living organisms are a major contributor to the spectral and polarized states of the light field in the aquatic environments.

References

Aas, E. 1996. Refractive index of phytoplankton derived from its metabolite composition. *Journal of Plankton Research* **18**(12): 2223–2249. doi:10.1093/plankt/18.12.2223.

Bohren, CF, Huffman, DR. 1983. *Absorption and Scattering of Light by Small Particles*. New York: John Wiley & Sons.

Boss, E, Pegau, WS, Lee, M, Twardowski, M, Shybanov, E, Korotaev, G. 2004. Particulate backscattering ratio at LEO 15 and its use to study particle composition and distribution. *Journal of Geophysical Research* **109**: C01014. doi:10.1029/2002JC001514.

Campbell, JW. 1995. The lognormal distribution as a model for bio-optical variability in the sea. *Journal of Geophysical Research* **100**(C7): 13237–13254.

Campbell, JW, Yentsch, CM. 1989. Variance within homogeneous phytoplankton populations, II: Analysis of clonal cultures. *Cytometry* **10**(5): 596–604.

Campbell, JW, Yentsch, CM, Cucci, TL. 1989. Variance within homogeneous phytoplankton populations, III: Analysis of natural populations. *Cytometry* **10**(5): 605–611.

Davies, EJ, McKee, D, Bowers, D, Graham, GW, Nimmo-Smith, WAM. 2014. Optically significant particle sizes in seawater. *Applied Optics* **53**(6): 1067–1074. doi:10.1364/AO.53.001067.

Fox, FE, Herzfeld, K. 1954. Gas bubbles with organic skin as cavitation nuclei. *Journal of the Acoustical Society of America* **26**: 984–989.

Hu, L, Zhang, X, Xiong, Y. 2022. Contribution of Submicron Particles to the Unpolarized and Linearly Polarized Angular Scattering. *Frontiers in Remote Sensing* **3**. doi:10.3389/frsen.2022.925654.

Jonasz, M. 1987. Nonspherical sediment particles: Comparison of size and volume distributions obtained with an optical and a resistive particle counter. *Marine Geology* **78**(1-2): 137–142.

Kamowski, M, Mojica, K, Lange, K, Zhang, X. 2023. Refractive index and volume fractions of various cellular components of plankton. *Optics Express* **31**(22): 35892-35907. doi:10.1364/OE.502465.

Kitchen, JC, Zaneveld, JRV. 1992. A three-layered sphere model of the optical properties of phytoplankton. *Limnology and Oceanography* **37**(8): 1680–1690.

Lain, LR, Kravitz, J, Matthews, M, Bernard, S. 2023. Simulated Inherent Optical Properties of Aquatic Particles using The Equivalent Algal Populations (EAP) model. *Scientific Data* **10**(1): 412. doi:10.1038/s41597-023-02310-z.

Lambert, CE, Jehanno, C, Silverberg, N, Brun-Cottan, JC, Chesselet, R. 1981. Log-normal distribution of suspended particles in the open ocean. *Journal of Marine Research* **39**(1): 77–98.

Longhurst, AR, Koike, I, Li, WKW, Rodriguez, J, Dickie, P, Kepay, P, Partensky, F, Bautista, B, Ruiz, J, Wells, M, Bird, DF. 1992. Sub-micron particles in northwest Atlantic shelf water. *Deep*

Sea Research Part A Oceanographic Research Papers **39**(1): 1–7. doi:10.1016/0198-0149(92)90016-M.

Meyer, RA. 1979. Light scattering from biological cells: Dependence of backscattering radiation on membrane thickness and refractive index. *Applied Optics* **18**(5): 585–588.

Morel, A, Ahn, Y-H. 1990. Optical efficiency factors of free-living marine bacteria: Influence of bacterioplankton upon the optical properties and particulate organic carbon in oceanic waters. *Journal of Marine Research* **48**: 145–175.

Organelli, E, Dall'Olmo, G, Brewin, RJW, Tarran, GA, Boss, E, Bricaud, A. 2018. The open-ocean missing backscattering is in the structural complexity of particles. *Nature Communications* **9**(1): 5439. doi:10.1038/s41467-018-07814-6.

Pabst, W, Gregorova, E. 2007. *Characterization of Particles and Particle Systems*.

Patterson, EM, Gillette, DA, Stockton, BH. 1977. Complex index of refraction between 300 and 700 nm for Saharan aerosols. *Journal of Geophysical Research (1896-1977)* **82**(21): 3153–3160. doi:10.1029/JC082i021p03153.

Stramski, D, Kiefer, DA. 1991. Light scattering by microorganisms in the open ocean. *Progress in Oceanography* **28**: 343–383.

Stramski, D, Woźniak, SB. 2005. On the role of colloidal particles in light scattering in the ocean. *Limnology and Oceanography* **50**(5): 1581–1591.

Twardowski, M, Zhang, X, Vagle, S, Sullivan, J, Freeman, S, Czerski, H, You, Y, Bi, L, Kattawar, G. 2012. The optical volume scattering function in a surf zone inverted to derive sediment and bubble particle subpopulations. *Journal of Geophysical Research* **117**: C00H17. doi:10.1029/2011JC007347.

Twomey, S. 1977. *Introduction to the mathematics of inversion in remote sensing and indirect measurements*. Amsterdam: Elsevier Scientific Publishing Company. (Developments in Geomathematics).

Vaillancourt, RD, Balch, WM. 2000. Size distribution of marine submicron particles determined by flow field-flow fractionation. *Limnology and Oceanography* **45**(2): 485–492.

Wells, ML, Goldberg, ED. 1992. Marine submicron particles. *Marine Chemistry* **40**(1-2): 5–18.

Wozniak, SB, Stramski, D. 2004. Modeling the Optical Properties of Mineral Particles Suspended in Seawater and their Influence on Ocean Reflectance and Chlorophyll Estimation from Remote Sensing Algorithms. *Applied Optics* **43**(17): 3489–3503.

Yamasaki, A, Fukuda, H, Fukuda, R, Miyajima, T, Nagata, T, Ogawa, H, Koike, I. 1998. Submicrometer particles in northwest Pacific coastal environments: Abundance, size distribution, and biological origins. *Limnology and Oceanography* **43**(3): 536–542.

Zhai, P-W, Hu, Y, Trepte, CR, Winker, DM, Josset, DB, Lucker, PL, Kattawar, GW. 2013. Inherent optical properties of the coccolithophore: Emiliania huxleyi. *Optics Express* **21**(15): 17625–17638. doi:10.1364/OE.21.017625.

Zhang, X, Gray, D, Huot, Y, You, Y, Bi, L. 2012. Comparison of optically derived particle size distributions: Scattering over the full angular range versus diffraction at near forward angles. *Applied Optics* **51**(21): 5085–5099. doi:10.1364/AO.51.005085.

Zhang, X, Huot, Y, Gray, D, Sosik, HM, Siegel, D, Hu, L, Xiong, Y, Crockford, ET, Potvin, G, McDonnell, A, Roesler, C. 2023. Particle size distribution at Ocean Station Papa from nanometers to millimeters constrained with intercomparison of seven methods. *Elementa: Science of the Anthropocene* **11**(1). doi:10.1525/elementa.2022.00094.

Zhang, X, Lewis, MR, Johnson, BD. 1998. Influence of bubbles on scattering of light in the ocean. *Applied Optics* **37**(27): 6525–6536. doi:10.1364/AO.37.006525.

Zhang, X, Stavn, RH, Falster, AU, Gray, D, Gould Jr, RW. 2014. New insight into particulate mineral and organic matter in coastal ocean waters through optical inversion. *Estuarine, Coastal and Shelf Science* **149**: 1–12. doi:10.1016/j.ecss.2014.06.003.

Zhang, X, Stavn, RH, Falster, AU, Rick, JJ, Gray, D, Gould Jr, RW. 2017. Size distributions of coastal ocean suspended particulate inorganic matter: Amorphous silica and clay minerals and their dynamics. *Estuarine, Coastal and Shelf Science* **189**: 243–251. doi:10.1016/j.ecss.2017.03.025.

Zhang, X, Twardowski, M, Lewis, M. 2011. Retrieving composition and sizes of oceanic particle subpopulations from the volume scattering function. *Applied Optics* **50**(9): 1240–1259. doi:10.1364/AO.50.001240.

Developing optical fingerprinting framework for coastal particle source identification

Eero Asmala[a], Joonas Virtasalo[a], Marine Poizat[a], Kristian Spilling[b], Karoliina Koho[a]

[a] Geological Survey of Finland, Espoo, Finland
[b] Finnish Environment Institute, Helsinki, Finland

Developing optical fingerprinting framework for coastal particle source identification

Eero Asmala[a], Joonas Virtasalo[a], Marine Poizat[a], Kristian Spilling[b], Karoliina Koho[a]

[a]Geological Survey of Finland, Espoo, Finland
[b]Finnish Environment Institute, Helsinki, Finland
Corresponding author: Eero Asmala; eero.asmala@gtk.fi

Introduction

Particles in coastal waters play a central role in carbon cycling. They influence microbial processes, serve as carriers of particulate organic matter and contribute to the transfer of carbon from the surface ocean to the sediments. The origin and composition of suspended particles vary substantially over time and space, shaped by riverine inputs, local primary production, resuspension and detrital degradation. In shallow shelf seas such as the northern Baltic Proper, understanding the source, transformation and fate of these particles is essential for improving carbon budgets and assessing the role of coastal systems in long-term carbon storage (Bianchi & Allison 2009).

Recent sedimentological research has indicated that sediment accumulation in these coastal environments may be predominantly driven by lateral near-bottom transport. Rather than settling directly from surface production, organic matter can be advected horizontally along the seafloor and deposited far from its origin. This finding challenges conventional views of vertical particle settling and highlights the importance of distinguishing between vertical and lateral fluxes when evaluating coastal carbon pathways, particularly for phytoplankton-derived material (Jokinen et al. 2015).

However, identifying the sources of particles in situ remains a significant challenge. Traditional laboratory methods for source differentiation are often labor-intensive, time-consuming and unable to capture high-frequency or short-lived events. Episodic phenomena such as phytoplankton blooms, storm-driven resuspension, or sudden increases in river discharge may therefore go unobserved. To address this limitation, synoptic optical measurements offer a promising approach by enabling continuous, real-time characterization of particle properties within the water column. In dissolved organic matter research, multivariate optical fingerprinting techniques are already well established and routinely used to assess DOM source and quality (Wünsch et al. 2018). Extending similar approaches to particulate matter offers a valuable opportunity to resolve suspended particle mixtures with high temporal resolution.

We are developing a classification approach that uses in situ optical measurements to distinguish between dominant suspended particle types. By combining particle size distributions with spectral backscattering data and calibrating these measurements using a broad suite of known reference materials, we aim to identify operational classes such as riverine particles, phytoplankton-derived organic matter, fresh detritus and resuspended surface sediments. The classification is further refined using supporting measurements from chlorophyll fluorescence and FDOM sensors, which help to resolve differences between organic and mineral components.

Our approach also seeks to connect water-column particle characteristics with seafloor processes. Comparisons between optical signals, sediment trap material and samples from the sediment-water interface are used to track changes in the composition and diagenetic quality of organic matter during transport. In particular, this allows us to assess whether the lower water column is influenced predominantly by recent vertical flux or by older, laterally transported material that has undergone degradation en route.

Through this work, we aim to improve our understanding of particle origin and fate in coastal seas. This includes clarifying how particulate carbon is cycled, transformed, or buried in dynamic nearshore environments, which is essential for advancing coastal carbon budgets and for interpreting the role of suspended particles in biogeochemical processes.

Methods

We are developing a classification tool for identifying dominant particle types in natural waters, based on particle size distribution and optical backscattering properties. Particle fingerprints are derived from two in situ instruments: a Sequoia LISST-100X or 200X for laser diffraction-based particle size distribution (1.25–250 µm across 32 bins for 100X and 1 to 500 µm across 36 bins for 200X) and a Sequoia Hyper-bb hyperspectral backscattering sensor measuring 430–700 nm at 5 nm resolution. Both instruments were deployed on a benthic lander during campaigns in autumn 2024 (5 weeks) and in spring 2025 (7 weeks) at 60 m depth in the open coast of the northern Baltic Proper. The instruments on the lander collected continuous particle data under natural environmental conditions. Earlier, the same LISST and Hyper-bb instruments were also run in autumn 2023 on the pumped flow-through system at Tvärminne Zoological Station (University of Helsinki), where coastal surface water is pumped through a sensor array.

We also conducted laboratory experiments using known particulate materials suspended in water, including common clay minerals (kaolinite, montmorillonite, illite+smectite), iron and manganese oxides (goethite, ferrihydrite, birnessite grinded and unground), organic-rich materials (fresh and old peat) and natural surface sediment. These measurements are used to generate characteristic particle fingerprints for each source material.

In future, unsupervised methods such as PCA and functional PCA will be applied to identify dominant patterns and axes of variability across particle types. Information from chlorophyll fluorescence and FDOM sensors and water quality sensors (temperature, salinity, pH, DO etc.) will also be incorporated to further refine the particle fingerprint. This auxiliary data will be used iteratively to enhance the classification of particle types and improve separation between organic and inorganic sources.

Figure 1. Benthic lander recovered after 7-week deployment. Photo credit: J. Virtasalo.

Results

The spectral shapes of the corrected particle backscattering coefficient (β_μ) showed clear and material-specific patterns across the measured wavelength range (Figure 2). Clays (kaolinite, montmorillonite and illite+smectite) exhibited generally decreasing β_μ values with wavelength, but with some concave features. The spectral shape of goethite was concave, especially in the longer wavelengths, while ferrihydrate showed more linear increase throughout the spectrum. Birnessite was analyzed in both grinded and nongrinded forms. Both exhibited broadly similar spectral shapes, with increasing β_μ over the wavelength range. Natural surface sediment from Finnish south coast showed a gradually increasing spectral shape with a subtle flattening toward the higher wavelengths. Its profile was generally smooth but slightly less steep than most mineral materials. Fresh peat showed nearly linear increase with wavelength, whereas old peat exhibited a distinctly concave spectral shape.

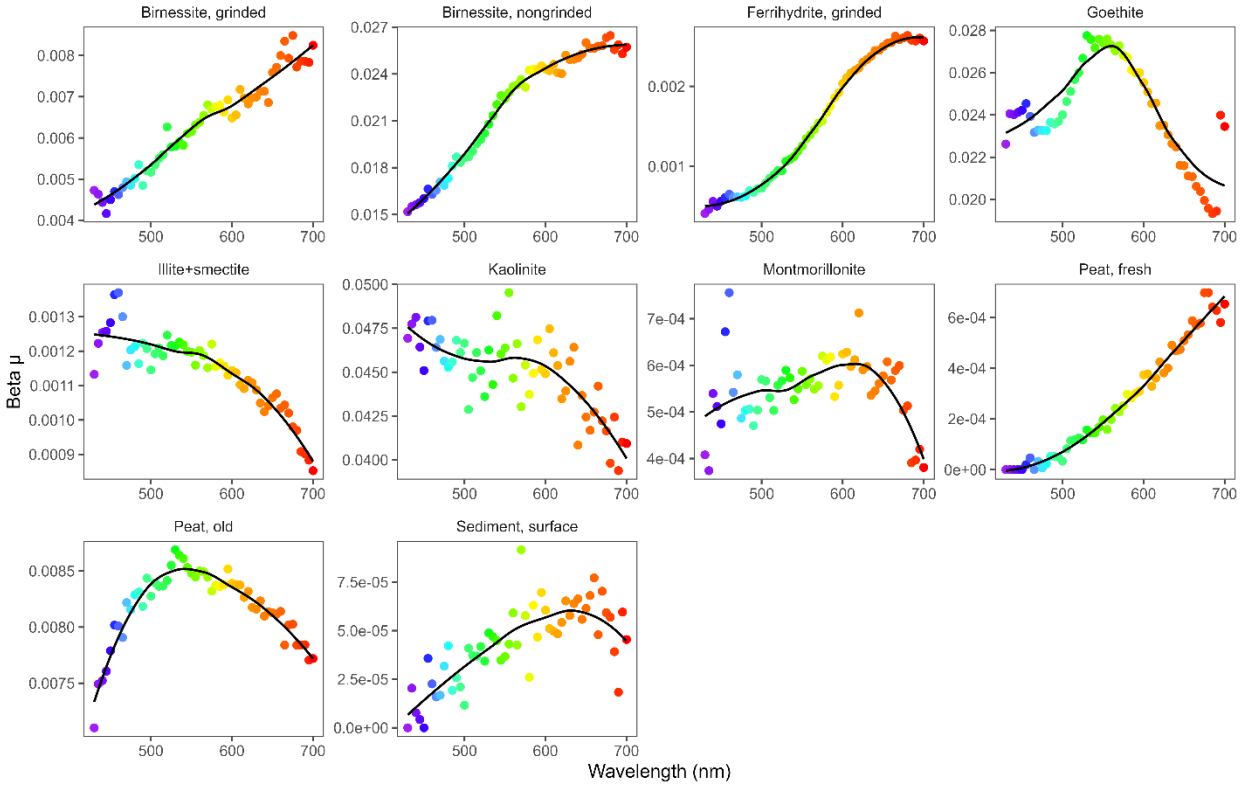

Figure 2. Spectral particle backscattering in the wavelength range 430-700 nm for various source materials.

During the lander deployment in spring 2024, we observed a gradual increase in total particle concentration, with more pronounced increase towards the end of the deployment (Figure 3).

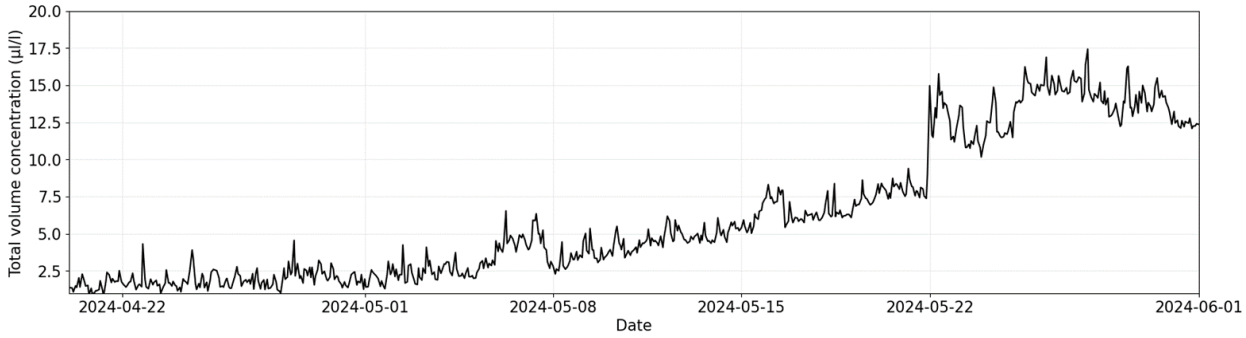

Figure 3. Benthic lander recovered after 7-week deployment. Photo credit: J. Virtasalo.

From the flow-through deployment in autumn 2023, we observed a change in particle backscattering values during the 5 week campaign (Figure 4). In the beginning of this period, most intense backscattering was observed in lower wavelengths, which shifted relatively abruptly midway through the campaign to the higher wavelengths.

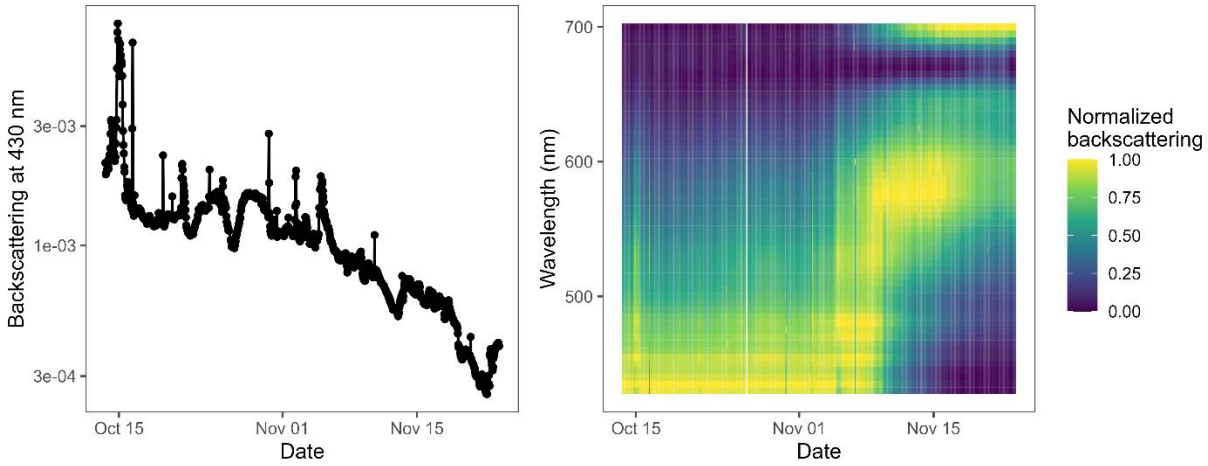

Figure 4. Benthic lander recovered after 7-week deployment. Photo credit: J. Virtasalo.

Discussion

Spectral backscattering properties varied distinctly across particle types, both in laboratory conditions and natural field measurements. Materials such as peat and goethite exhibited concave or non-linear shapes, while clay minerals tended to show more linear or gradually increasing spectra. These differences, although subtle in some cases, provide evidence that spectral shape alone can help distinguish between particle sources. Temporal variability observed during in situ deployments further suggests that shifts in particle composition can be tracked through changes in backscattering spectra. This highlights the potential of optical parameters to serve as indicators of changing particle origin in dynamic coastal environments. The laboratory-based fingerprints

offer a foundation for interpreting field data, although direct comparisons remain a goal for future analysis. Principal component analysis and functional PCA are being used to extract dominant patterns from the combined size and spectral datasets. These multivariate approaches allow for unsupervised classification of particle types and will be refined by integrating supporting data from FDOM and chlorophyll fluorescence sensors. Altogether, the findings point toward a classification tool that can help resolve suspended particle mixtures in real time.

Conclusion

Spectral backscattering shows strong potential for identifying suspended particle types based on their optical properties. Continued development of multivariate fingerprinting approaches will support future efforts to trace particulate carbon sources in aquatic systems.

References

Bianchi, T. S., & Allison, M. A. (2009). Large-river delta-front estuaries as natural "recorders" of global environmental change. *Proceedings of the National Academy of Sciences*, *106*(20), 8085-8092.

Jokinen, S. A., Virtasalo, J. J., Kotilainen, A. T., & Saarinen, T. (2015). Varve microfabric record of seasonal sedimentation and bottom flow-modulated mud deposition in the coastal northern Baltic Sea. *Marine Geology*, *366*, 79-96.

Wünsch, U. J., Acar, E., Koch, B. P., Murphy, K. R., Schmitt-Kopplin, P., & Stedmon, C. A. (2018). The molecular fingerprint of fluorescent natural organic matter offers insight into biogeochemical sources and diagenetic state. *Analytical chemistry*, *90*(24), 14188-14197.

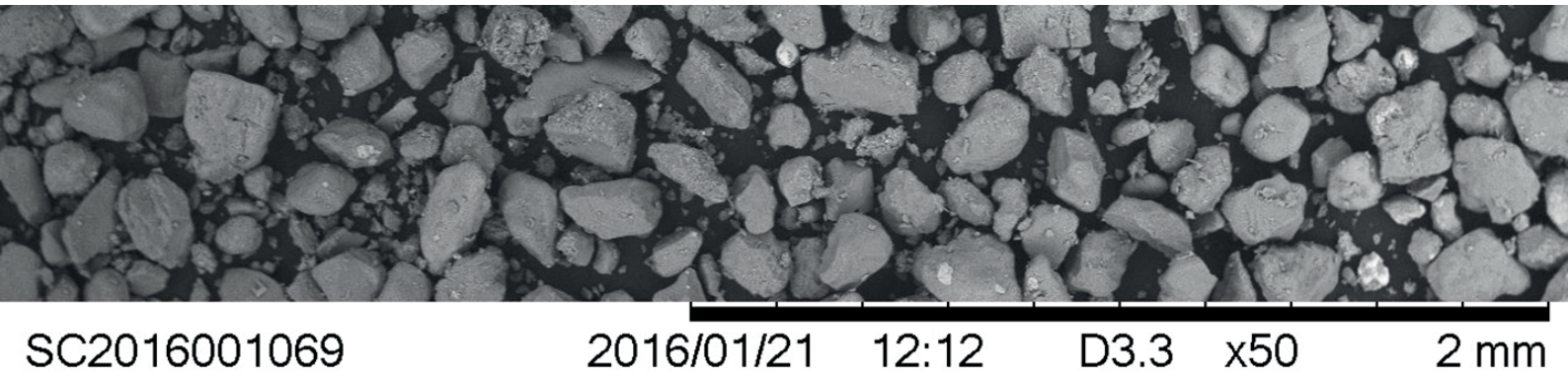
SC2016001069
2016/01/21
12:12
D3.3
x50
2 mm